Characterisation of thermal radiation in the near - wall region of a packed pebble bed

M de Beer

21707588

Dissertation submitted in partial fulfilment of the requirements for the degree *Magister* in Mechanical Engineering at the Potchefstroom Campus of the North-West University

Supervisor: Prof PG Rousseau

Co-supervisor: Prof CG Du Toit

November 2014

Acknowledgements

Firstly, I would like to thank my Heavenly Father for the opportunities, abilities, strength, endurance and His unending love. I know that it is only by His grace that the completion of this study was possible.

I would also like to thank everyone that has supported and assisted me during this study. Prof. P.G. (Pieter) Rousseau and Prof. C.G. (Jat) Du Toit, thank you for your guidance and support throughout the study. I really had a study leader “dream team” and am very grateful for the experience and knowledge gained from such insightful leaders. I learned so much from you, thank you for believing in me, I am eternally grateful. For their countless hours of assistance with the experimental test facility, I would like to thank Mr S. Naude and Mr T. Diobe. Mr Sarel, you were always willing to help with a smile and I learned a great deal from you. My sincere thanks goes to Prof. J. Markgraaff for his advice, insight and assistance, I sincerely appreciate it. I would also like to express my gratitude towards Ms F. Jacobs for the endless moral support and making life a little easier in whichever way she could when the stress levels got high.

Finally, I would like to thank my parents and my partner Adriaan for their unconditional love, support and patience. They always showed an interest in my work and made life a little sunnier in the tough times, by helping in whichever way they could. I could most definitely not have done any of it without their support and love, thus I am extremely grateful and blessed.

This work is based upon research supported by the South African Research Chairs Initiative of the Department of Science and Technology and National Research Foundation. Any opinions, findings and conclusions or recommendations expressed in this material are those of the author(s) and therefore the NRF and DST do not accept any liability with regard thereto.

Abstract

The heat transfer phenomena in the near-wall region of a randomly packed pebble bed are important in the design of a Pebble Bed Reactor (PBR), especially when considering the safety case during accident conditions. At higher temperatures the contribution of the radiation heat transfer component to the overall heat transfer in a PBR increases significantly. The wall effect present in the near-wall region of a packed pebble bed affects the heat transfer in this region.

Various correlations exist to predict the effective thermal conductivity through a packed pebble bed, but not all of the correlations consider the contribution of radiation and some are only applicable to the bulk region. Experimental research has been done on the heat transfer through a packed pebble bed. However, most of the results are case specific and cannot necessarily be used to validate models or simulations to predict the effective thermal conductivity of a pebble bed.

The objective of this study is to develop a methodology that uses experimental work together with Computational Fluid Dynamics (CFD) simulations to predict the effective thermal conductivity in the near-wall region of a randomly packed pebble bed, and to separate the conduction and radiation components of the effective thermal conductivity. The proposed methodology inter alia includes experimental tests and the calibration of a CFD model to obtain numerical results that correlate well with the experimental results.

To illustrate the proposed methodology the newly constructed Near-wall Effect Thermal Conductivity Test Facility (NWETCTF) was used to gather experimental results for the temperature and heat transfer distribution through a randomly packed pebble bed. Two identical but separate experimental tests were performed and the results of the two tests were in good agreement. From the experimental results the effective thermal conductivity was derived. The effect of the near-wall region on the heat transfer and the significance of radiation at higher temperatures are evident from the results. Recommendations were made for future experimental work with the NWETCTF from the findings of the investigation.

A numerically packed pebble bed that is representative of the experimental pebble bed was generated using the Discrete Element Method (DEM) and a CFD model was set up for the heat transfer through the pebble bed using STAR-CCM+.. The CFD results showed trends similar to that of the experimental results. However, some discrepancies were identified that must be addressed in future studies by calibrating the CFD model. The effective thermal conductivity for the numerical simulation was determined using the CFD results and the conduction and radiation components were separated.

Keywords: Effective thermal conductivity, Packed pebble bed, Near-wall region, Thermal radiation

Table of Contents

List of Tables

List of Figures

Nomenclature

Abbreviations

BEM	Boundary Element Method
CFD	Computational Fluid Dynamics
CPU	Central processing unit
CSUN	Cylindrical Spherical Unit Nodalisation
DEM	Discrete Element Method
DOM	Discrete Ordinates Method
EES	Engineering Equation Solver
ESS	Emergency Shutdown System
FVM	Finite Volume Method
GIF	Generation IV International Forum
HTGR	High Temperature Gas-cooled Reactor
HTO	High Temperature Oven
HTTU	High Temperature Test Unit
MRT	Multiple-Rays Tracing
MSUC	Multi Sphere Unit Cell
NWETCTF	Near-wall Effect Thermal Conductivity Test Facility
PBMR	Pebble Bed Modular Reactor
PBR	Pebble Bed gas-cooled Reactors
RDF	Radial Distribution Function
RTC	Radiative Transfer Coefficient
RTD	Resistance Thermometer Device
RTE	Radiative Transfer Equation
S2S	Surface-to-Surface
SC	Simple Cubic
SCADA	Supervisory Control and Data Acquisition
SIS	Safety Instrumented System
SUN	Spherical Unit Nodalisation
TRISO	Tristructural-isotropic
VBA	Visual Basic for Applications
VHTR	Very High Temperature gas-cooled Reactor
ZM	Zone Method

Symbols

A	Area [m^2]
a	Polynomial coefficient [-]
B	Mesh base size [*mm*]
$b(x)$	Slope of polynomial curve as a function of position [°C/m]
c	Polynomial coefficient of heat transfer function [-]
c_p	Specific heat capacity value of water [$J / kg \cdot K$]
d_p	Particle diameter [*m*]
dA	Elemental area [m^2]
dT/dy / dT/dr	Temperature gradient [°C/m]
E_b	Blackbody emissive power [*W*]
F	View factor [-]
F_E^*	Radiation exchange factor [-]
J	Radiosity [W / m^2]
k	Number of coefficients in polynomial [-]
k_{AL}	Thermal conductivity of AL-45 insulation material [$W / m \cdot K$]
k_{eff}	Effective thermal conductivity [$W / m \cdot K$]
$k_e^{\ c}$	Effective thermal conductivity due to conduction [$W / m \cdot K$]
$k_e^{g,c}$	Effective thermal conductivity through gas, contact point and contact area [$W / m \cdot K$]
k_e^r	Effective thermal conductivity due to radiation [$W / m \cdot K$]
$k_e^{\ r,L}$	Effective thermal conductivity due to long-range radiation [$W / m \cdot K$]
$k_e^{\ r,S}$	Effective thermal conductivity due to short-range radiation [$W / m \cdot K$]
k_{ins}	Thermal conductivity of insulation material [$W / m \cdot K$]
k_{SALI}	Thermal conductivity of SALI-2 insulation material [$W / m \cdot K$]
L	Height of NWETCTF test section [*m*]
L_{AL}	Thickness of AL-45 insulation layer [*m*]
L_{ins}	Thickness of insulation material [*m*]

L_{SALI}	Thickness of SALI-2 insulation layer [m]
m	Polynomial order [-]
$\dot{m}$	Water mass flow rate [kg/s]
N	Number of data points in a data set
q	Radiation heat transfer [W]
Q	Heat transfer [W]
Q_{bed}	Heat transfer through packed pebble bed [W]
$Q_{bed}(r)$	Heat transfer through packed pebble bed as a function of radial position [W]
$Q_{coolers}$	Heat removed via element coolers [W]
$Q_{heater,loss}$	Miscellaneous heat losses [W]
$Q_{i,loss}$	Heat loss through insulation material for ith increment [W]
Q_{in}	Heat entering pebble bed through inner reflector [W]
$Q_{ins,top/bottom/side}$	Heat loss through top, bottom or side insulation walls [W]
$Q_{totLoss}$	Total heat loss through insulation material [W]
Q_{wj} or Q_{out}	Heat extracted via water jacket [W]
$Q(r)$	Heat transfer as a function of radial position [W]
R / r	Radial distance / Radius [m]
SS	Relative minimum surface size [mm]
T	Temperature [°C or K]
$\overline{T}$	Average temperature [K]
T_{bed}	Temperature at top/bottom/side of pebble bed near insulation wall [°C]
T_{env}	Temperature near environment next to outside of insulation material [°C]
$T_{w,in}$	Water inlet temperature [°C]
$T_{w,out}$	Water outlet temperature [°C]
$T(x)$	Polynomial curve fitted to temperature data [°C]
u_{drift}	Drift uncertainty
u_i	Data point uncertainty
$u_{i,\frac{dT}{dy}}$	Uncertainty associated with temperature gradient [°C/m]
$u_{i,T(y)}$	Uncertainty associated with curve fit [°C]
$u_{instrument}$	Instrument uncertainty

$u_{measurement}$	Measurement uncertainty
$u_{scatter}$	Scatter uncertainty of curve fit
$u_{statistical}$	Statistical variance of a measurement
$u(dT/dy)$	Uncertainty of temperature gradient [°C/m]
$u(k_{eff})$	Uncertainty of effective thermal conductivity [$W/m \cdot K$]
$u(x)$	Pointwise uncertainty in curve fit
$u(Q_{bed})$	Uncertainty of heat transfer through pebble bed [*W*]
$u(Q_{wj})$	Uncertainty of heat removed via water jacket [*W*]
$u(Q_{totLoss})$	Uncertainty of total heat loss through insulation [*W*]
w	Width of one increment of NWETCTF test section [*m*]
x	Dimensionless distance / Coordinate in x-direction [-]
x_i	Measured experimental value
$\overline{x}$	Average of measured experimental value
y	Distance in y-direction [*m*]
z	Distance expressed in sphere diameters [-]
α	Absorptivity [-]
ε	Emissivity [-]
θ	Polar angle [*rad*]
ρ	Reflectivity [-]
σ	Stefan-Boltzmann constant [$W/m^2 \cdot K^4$]
$\sigma(b(x))$	Uncertainty in slope of polynomial curve fit [°C/m]
τ	Transmissivity [-]

1

Introduction

The search for a sustainable solution to the global energy demand crisis remains a highly discussed topic. Economic and population growth in developing countries, as well as growing levels of energy consumption in developed countries result in an annual increase in the worldwide energy demand. According to the U.S. Energy Information Administration (2013) there is an expected 56% increase in world energy consumption from 2010 to 2040. Currently energy poverty leaves 1.3 billion people without access to electricity (World Energy Council, 2013). Even with current energy management strategies and possible solutions in place, the continuation of existing energy consumption trends still results in energy shortage problems in the near future. In order to ensure a more sustainable global energy outlook more efficient and cleaner energy solutions are required. (International Energy Agency, 2012)

Nuclear power plants are considered as one of the energy solutions. In addition to the reliable and predictable supply of energy, the low carbon emissions associated with nuclear energy make it a feasible solution to the energy need (Echàvarri, 2013). However, there are certain factors that adversely affect the future of nuclear power, a major one being nuclear safety. The recent Fukushima nuclear accident in 2011 only increased the awareness of the safety risks involved with the use of nuclear energy, negatively affecting the social acceptance and support of nuclear power. Chu and Majumdar (2012) state that there have been mixed reactions to the Fukushima disaster. Some countries continue their use of nuclear energy with caution and show an increased interest in new nuclear programmes, whilst others have put their plans on hold or decided to phase-out their current nuclear plants.

Amano (2013) states that at the international ministerial conference on nuclear power in the 21st century, they recognised that “nuclear power remains an important option for many countries to improve energy security, reduce the impact of volatile fossil fuels prices and mitigate the effects of climate change, despite the accident at the Fukushima Daiichi Nuclear

Power Station." Nevertheless he also emphasizes that there is a responsibility to ensure that the most robust levels of nuclear safety are implemented at all nuclear programmes worldwide. This shows the importance of the development and construction of inherently safe reactor designs.

The Generation IV International Forum (GIF) is a research and development initiative that focuses on the design of future nuclear energy systems. Enhanced safety is one of the key design criteria for these Generation IV reactors. One of the technologies selected for further development by the GIF is the Very High Temperature gas-cooled Reactor (VHTR) (Kelly, 2014). The packed pebble bed is a specific VHTR design with a wider range of applications, higher power conversion efficiencies and important safety characteristics (Van Antwerpen, 2009). In the current study the focus is on Pebble Bed gas-cooled Reactors (PBR).

1.1 Background

The basic design of a PBR consists of a randomly packed bed of spherical fuel elements, referred to as pebbles, which make up the reactor core. Each pebble is made of graphite and contains thousands of TRISO-fuel particles. Heat is transferred from the reactor core to the power generation applications through the convection mechanism, using an inert gas such as helium. There are three contributing factors to the passive safety case of the PBR. Firstly the reactor has a very low power density and as a result natural heat transfer mechanisms such as conduction and radiation can remove any heat produced even if active cooling is absent. The pebble fuel design also contributes as the coated fuel particles prevent the release of fission products and the amount of fuel in each pebble is very small (Kadak, 2005). Thirdly the pebble fuel also has a negative reactivity coefficient.

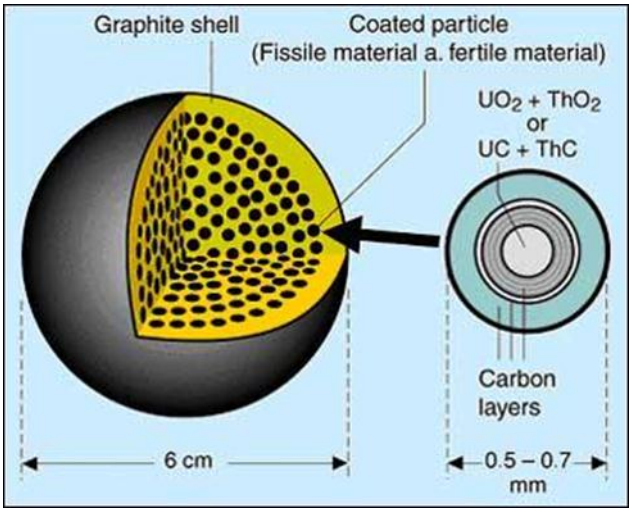

Figure 1.1: Illustration of pebble containing TRISO-fuel particles (Paul Scherrer Institut, 2012).

Effective thermal conductivity is a parameter that represents the overall heat transfer through a packed bed of spheres. Radiation and conduction are the two heat transfer mechanisms that specifically contribute to the overall heat transfer during upset conditions, when convective cooling is absent. It is important to predict the effective thermal conductivity in order to determine the inherent safety of a reactor design (Rousseau *et al.*, 2012a).

The reason for the importance of the above mentioned phenomena lies in the fact that it forms a part of the self-acting decay heat removal chain in a PBR. Decay heat is defined as the heat that is continuously produced in a PBR during upset conditions (Van Antwerpen, 2009). It is the natural heat transfer mechanisms described by the effective thermal conductivity that ensure the passive cooling and removal of decay heat in the PBR safety case. During upset conditions temperatures of up to 1600°C can be expected in a PBR (Breitbach & Barthels, 1980; Rousseau & Van Staden, 2008).

At higher temperatures, above approximately 650°C, the contribution of the radiation component to the effective thermal conductivity of a packed bed of spheres becomes significant (Breitbach & Barthels, 1980; Zhou *et al.*, 2007; Cheng & Yu, 2013; Talukdar *et al.*, 2013). For temperatures of about 800°C and higher radiation becomes the dominant heat transfer mechanism in a packed pebble bed. Despite the significance of radiation heat transfer at higher temperatures some studies in current literature still neglect the effect of the radiation component when determining the effective thermal conductivity (Van Antwerpen *et al.*, 2010a).

Van Antwerpen *et al.* (2010a) reviewed various existing correlations that characterise the effective thermal conductivity in packed pebble beds. The results showed that most correlations were only applicable to the bulk region of a packed bed and did not take into account the changes in the packing structure found in the near-wall region. The near-wall region includes the pebble-to-reflector interface which forms part of the critical path for decay heat removal, thus an accurate prediction of the effective thermal conductivity in this region is important.

A new model, the Multi Sphere Unit Cell (MSUC) model, was developed by Van Antwerpen (2009) to provide more accurate predictions of the effective thermal conductivity in both the bulk and the near-wall regions. Experimental data from the High Temperature Test Unit (HTTU) was used to validate this model. However, the modelling of the long range radiation component included in the MSUC model was only a first approximation and left room for further investigations. Prediction of the radiation phenomena at very high temperatures by the model could not be validated as the HTTU experiment only provided data up to temperatures of 1200°C. A detailed investigation of the heat transfer in the near-wall region was also not included in the HTTU experiments.

Further studies were done to improve on the shortcomings of the MSUC model and develop models that can be used in unison with the existing model. Pitso (2011) developed the Spherical Unit Nodalisation (SUN) model which uses a fundamental approach to describe the radiation heat transfer in the bulk region of a packed bed more accurately. The Cylindrical Spherical Unit Nodalisation (CSUN) model was developed by Van der Meer (2011), which transformed the SUN model into cylindrical coordinates so that it can be applied to an annular reactor. Both studies concluded that no experimental data exists to verify these models at very high temperatures above 1200°C and the models are only applicable to the bulk region of a packed pebble bed.

1.2 Problem Statement

From the previous discussion it is clear that various correlations have been developed to predict the effective thermal conductivity through a packed pebble bed. However, not all of the correlations consider the critical near-wall region in the packed bed of spheres and some studies neglect the contribution of radiation heat transfer. This is problematic when considering the PBR safety case as very high temperatures are present during upset conditions and the near-wall region forms part of the critical path of decay heat removal.

A need also exists for experimental data with associated uncertainties of the heat transfer at very high temperatures through the near-wall region of a packed bed of spheres, which can be used to validate new or existing effective thermal conductivity models. It is also important that the contribution of the radiation component to the overall heat transfer can be determined as the phenomenon becomes more significant at higher temperatures.

The problem to be solved for the current study is the development of a methodology that can be used to obtain experimental data for the heat transfer through the near-wall region of a packed bed of spheres at very high temperatures. The developed methodology must include the calculation of the effective thermal conductivity from the experimental data, together with a comprehensive uncertainty analysis in order to evaluate the accuracy of the experimental results. The methodology must also include the development of a numerical model with the use of Computational Fluid Dynamics (CFD), which can be used together with the experimental data to separate the contribution of conduction and radiation heat transfer, thus characterising the radiation component of the effective thermal conductivity in the near-wall region of a packed pebble bed.

1.3 Objectives

The primary objectives of the current study are:

- To develop a methodology with which experimental data of the temperature distribution and heat transfer in the near-wall region of a packed bed of spheres can be obtained, especially at higher temperatures.
- Provide a method to determine the effective thermal conductivity of the packed pebble bed from the measured experimental data together with associated uncertainties.
- Develop a CFD model similar to the experimental setup and a methodology to separate the conduction and radiation components of the experimental effective thermal conductivity of the packed pebble bed.

The enabling objectives of the study are:

- Commissioning and fault finding during first time operation of the newly constructed Near-wall Effect Thermal Conductivity Test Facility (NWETCTF).
- Get the NWETCTF (pronounced N-WET-C-T-F) test facility in good working condition so that future researchers do not have to spend time on the commissioning of the system.
- Obtain a first set of experimental data from the NWETCTF to develop the methodology as described in the primary objectives.

The following aspects are not included in the scope of this study:

- Obtaining a final set of experimental results that can be used to validate existing and new models for the effective thermal conductivity through a packed bed of spheres and specifically the radiation component of the effective thermal conductivity. Rather the focus of the current study is the development of the methodology that can be used to obtain such final results with associated uncertainties.
- Although the NWETCTF was designed to obtain experimental data at temperatures of up to 1600°C it was not necessary for the development of the methodology in the current study to perform experimental tests up to these temperatures. Experimental tests were performed up to temperatures of 800°C in the current study, due to the fact that the NWETCTF is a new system and the commissioning of the system formed a part of the current study. As a result certain practical problems arose that were solved and the time constraint associated with the project only allowed for a limited number of experimental tests to be done. However, future researchers can perform experimental tests up to these temperatures using the NWETCTF and obtain results using the developed methodology of the current study.

1.4 Methodology

The experimental data for the development of the methodology was obtained with the NWETCTF test facility. Methods similar to that used by Van Antwerpen (2009), Rousseau *et al.* (2012a) and Van Antwerpen *et al.* (2010b) were used for the experimental data and uncertainty analysis as well as the derivation of the effective thermal conductivity from the experimental results. Two separate but identical experimental tests were conducted for various temperature cases. The results of the two experimental tests were compared and combined to form a single set of experimental data used for the calculation of the effective thermal conductivity for the different temperature cases.

A numerical packed bed of spheres similar to the experimental setup was generated using the DEM model of STAR-CCM+ and a method similar to that used by Van der Merwe (2014). The CFD model for the heat transfer through the packed bed of spheres was developed using STAR-CCM+. The CFD results were compared with the experimental results for each of the temperature cases. Some discrepancies between the CFD and experimental results were identified and were attributed to the fact that no provision was made for contact resistances in the CFD model. Recommendations were made to resolve the problem and calibrate the CFD model in future studies. For the separation of the conduction and radiation heat transfer components the CFD model and an expression for the total effective thermal conductivity by Van Antwerpen *et al.* (2012) were used.

1.5 Overview of document

Following this introductory chapter stating the objectives of the current study the document provides the detail of the work done to achieve the objectives. Chapter 2 presents the literature review conducted on the heat transfer through a packed pebble bed and the derivation of the effective thermal conductivity. A definition of packed pebble beds is given together with a discussion on the packing structure and various regions found in a packed bed of spheres.

Focus is placed on the radiation heat transfer component, the parameters affecting the radiation heat transfer as well as the models used to predict the radiation in current literature. The generation of numerically packed pebble beds and the numerical heat transfer analysis with the use of CFD simulations are discussed. Experimental work done on the heat transfer through a packed bed of spheres and the experimental test facilities used are reviewed.

Chapter 3 summarises the fundamental principles for the calculation of radiation heat transfer as well as the theoretical principles used for the data and uncertainty analysis of the

experimental results for the heat transfer through a packed pebble bed. An overview of the proposed methodology with the detail of the methods used and developed during this study to obtain the necessary results is discussed in Chapter 4. The method used to obtain the experimental data and the operation of the experimental test facility is described. The steps followed for the data and uncertainty analyses as well as the derivation of the effective thermal conductivity from the experimental results are discussed. Chapter 4 also provides the detail of the setup for the Discrete Element Method (DEM) and CFD heat transfer simulations, together with the methods used for the processing of the results. The method proposed for the separation of the radiation and conduction components of the effective thermal conductivity results is discussed.

The results obtained with the use of the proposed methodology are given in Chapter 5. The measured temperature and heat transfer results obtained with the experimental test facility and the calculated effective thermal conductivity results of the experimental tests are presented. An analysis of the quality of the DEM generated pebble bed is also provided in this chapter together with the results of the CFD heat transfer simulations. The experimental results are compared with the results obtained with the CFD simulations. The results for the separation of the radiation and conduction components of the effective thermal conductivity are presented.

Finally Chapter 6 concludes the document with a summary of the work done and conclusions made from the results obtained. Recommendations for future work emanating from this study are also given.

2

Literature Review

The packing characteristics of a packed pebble bed together with the concept of effective thermal conductivity are discussed in this chapter. The significance of radiation heat transfer at high temperatures as well as parameters affecting the radiation heat transfer is discussed. A review of the various models that exist to predict the radiation heat transfer through a packed bed of spheres is also presented.

The reader is introduced to the methods used to numerically generate a packed pebble bed and complete the CFD modelling of the heat transfer present in the packed bed. Experimental work is used to validate the models that describe the heat transfer through a packed bed of spheres. Various experimental test facilities used for the investigation of the heat transfer through a packed bed of spheres as well as the methods used to perform the experimental work are discussed.

2.1 Packed pebble beds

Randomly packed beds of spherical particles are used in several thermal-fluid industrial applications. Most of these applications involve energy transfer processes; the PBR is a prime example of such a thermal-fluid system. For the design of a PBR it is essential to have a thorough understanding of the heat transfer, fluid flow and pressure drop phenomena through a packed pebble bed as well as its structural properties (Béttega *et al.*, 2013; Van Antwerpen *et al.*, 2010a; Van Antwerpen *et al.*, 2012).

Two primary directions of heat transfer exist in a PBR, heat transfer in the axial direction and heat transfer in the radial direction. According to Van Antwerpen (2009) the main contributing mechanism to axial heat transfer is forced convection as a result of fluid flow in the reactor core under normal operating conditions. A number of heat transfer mechanisms that occur

simultaneously contribute to the transverse heat transfer in a PBR under normal operating and accident conditions. The overall effect of the axial and transverse heat transfer is combined to form a single parameter defined as the bed effective thermal conductivity, which is representative of the overall heat transfer through a packed bed of spheres (Van Antwerpen *et al.*, 2012).

2.1.1 Packing structure

Effective thermal conductivity of a packed bed is a characterisation of the phenomena present in a solid-fluid medium rather than a thermo-physical property, which makes the prediction of the parameter difficult (Aichlmayr & Kulacki, 2006). A thorough understanding of the characteristics of the packing structure of a randomly packed bed is required to perform an analysis of the physical and thermal-fluid phenomena in the bed (Suikkanen *et al.*, 2014). For this reason the structure of a packed bed is described in the following section to gain sufficient knowledge on the subject before a study of the heat transfer mechanisms in the bed is done (Van Antwerpen *et al.*, 2010a).

The geometry of a randomly packed bed consists of two main regions namely the bulk region and the wall region. The porous structure of a packed bed changes significantly in the region near any wall as the packing geometry is disrupted in this area (Van Antwerpen *et al.*, 2010a; Van Antwerpen *et al.*, 2012). Du Toit (2008) determined the radial variation in porosity for experimentally and numerically packed pebble beds and compared the results, as can be seen in Figure 2.1. The sharp variation in the porosity values at the area next to the wall in Figure 2.1 is a clear indication of the changes in the porous structure of a packed pebble bed in the wall region. This variation in packing structure is known as the wall effect and consists of two separate components. The first is the wall effect in the radial direction due to the side wall and secondly the wall effect in the axial direction due to the top-bottom wall (Zou & Yu, 1995). In the current study the focus is on the wall effect in the radial direction.

To obtain a more accurate prediction of the effective thermal conductivity in the area next to the wall Van Antwerpen (2009) subdivided this area into two regions namely the wall region and the near-wall region. He defined the wall region as $0 \le z \le 0.5$ and the near-wall region as $0.5 \le z \le 5$, with z the distance expressed in multiples of sphere diameters.

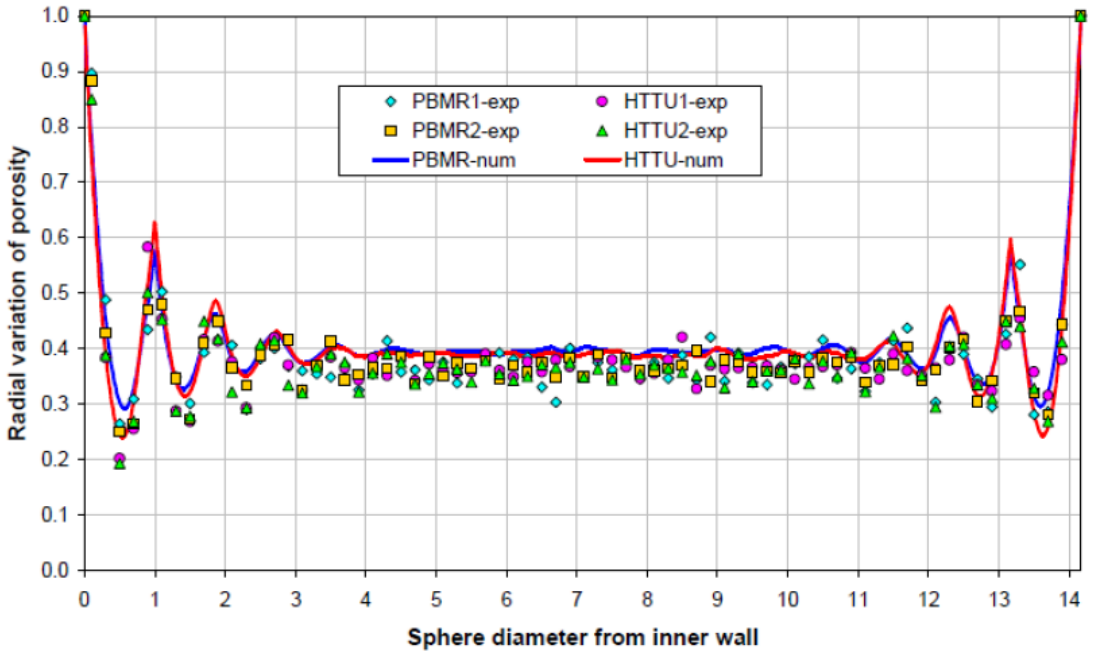

Figure 2.1: Radial variation in porosity for experimental and numerical annular packed pebble beds (Du Toit, 2008).

In general the porous structure of a packed bed is characterised by the bulk porosity or the variation in the axial and radial porosity of the bed (Van Antwerpen *et al.*, 2012). Porosity is defined as the ratio of the pore volume to the total volume of the packed bed. It shows the fraction of the packed bed volume that make up the voids between the spheres (Rouquerol *et al.*, 1994; Van der Meer, 2011). Van Antwerpen (2009) concluded that characterising the porous structure only using porosity is not always sufficient in effective thermal conductivity calculations. The reason is that most existing correlations for the effective thermal conductivity are only valid within specified porosity bounds. These porosity bounds coincide with a random packing that has a constant average porosity which is found in the bulk region of a packed bed where the wall effect is not present.

For this reason Du Toit *et al*. (2009) concluded that it is insufficient to define the porous structure of the wall area only using porosity and showed that the porous structure is better defined in terms of the variation in porosity, coordination number and contact angles between neighbouring spheres. According to Van Antwerpen *et al.* (2012) the coordination number is defined as the number of spheres in contact with the sphere under consideration and the contact angle as the angle between the line that connects the centre points of two spheres in contact and the line perpendicular to the direction of the heat flux.

Van Antwerpen (2009) applied this definition of the porous structure in his development of the MSUC model. He also considered the effect of discretisation intervals in the near-wall region

and developed a corrected porosity correlation with the use of a radial distribution function (RDF). The RDF was used to calculate the porous structure parameters at points in the radial direction where the probability of finding sphere centres were the highest. This definition of the porous structure improved the prediction of the effective thermal conductivity in the wall and near-wall regions and resulted in a more accurate prediction of the temperatures at the reflector interface of the packed bed (Van Antwerpen *et al.*, 2012).

The porosity correction factor developed by Van Antwerpen (2009) was valid for $0.5 \leq z \leq 3.8$ which further simplified the definition of the near-wall region. This definition of the near-wall region is used in the present study. An illustration of the definition of the three regions in the packing structure as defined by Van Antwerpen (2009) is shown in Figure 2.2.

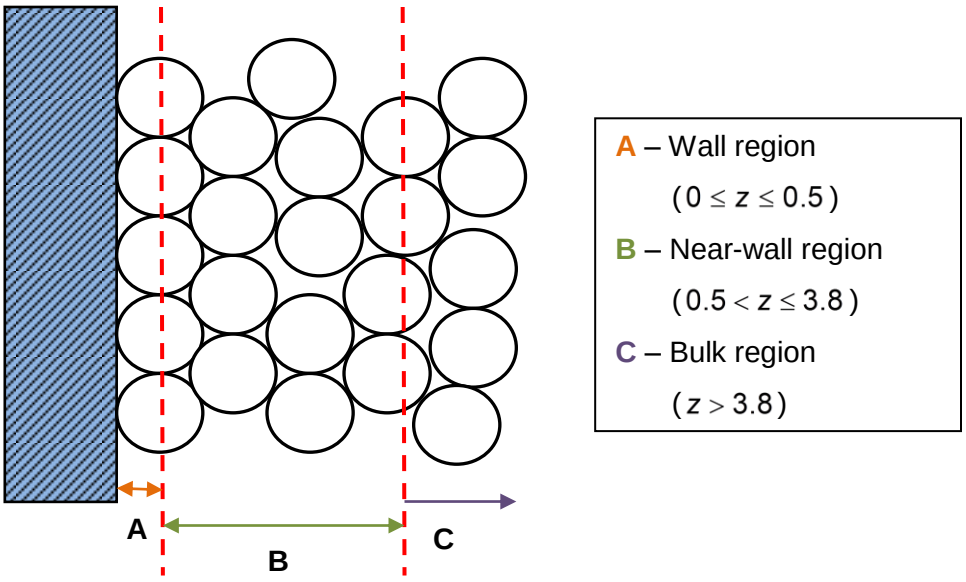

Figure 2.2: Definition of packing structure regions in packed bed.

2.1.2 Effective thermal conductivity

A proper understanding of the thermal properties of a packed pebble bed, particularly the effective thermal conductivity, is also important to achieve the correct design of a PBR (Zhou *et al.*, 2007). According to Rousseau *et al.* (2012a) the calculation of the effective thermal conductivity is based on a simple Fourier conduction rate equation in the radial direction of a packed pebble bed. This is shown in Equation (2.1)

$$Q(r) = -k_{eff} A \frac{dT}{dr} \tag{2.1}$$

where $Q(r)$ is the heat transfer rate as a function of the radial position and the combined effects of the heat transfer mechanisms are converted into an effective thermal conductivity, k_{eff}, similar to that of a solid. The area in the pebble bed through which the heat transfer takes place, A, is perpendicular to the temperature gradient, dT/dr, through the packed bed.

Bauer (cited by Van Antwerpen, 2009) stated that one can identify three components that contribute to the overall effective thermal conductivity of a packed bed. The first component is the effective thermal conductivity representing a combination of four heat transfer mechanisms that include: (1) conduction through solid phases; (2) conduction through contact points of neighbouring spheres; (3) conduction through the stationary gas phase present in the packed bed and (4) thermal radiation between solid surfaces. Figure 2.3 shows an illustration of these heat transfer mechanisms in a packed pebble bed.

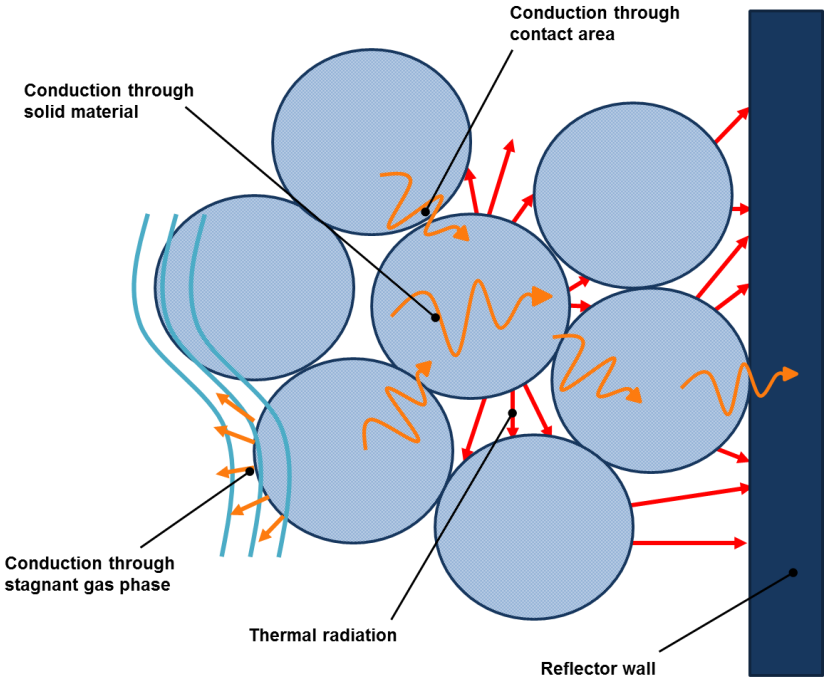

Figure 2.3: Heat transfer mechanisms in a packed pebble bed (Van Antwerpen, 2009).

The second component is the fluid effective conductivity as a result of the turbulent mixing of the gas as it flows through the irregular flow paths created by the voids between the spheres while the spheres remain stationary. A disturbance in the packing of the bed results in the movement of both the solid and gas phases bringing about additional heat transfer in the bed. This additional heat transfer make up the third component of the bed effective thermal conductivity. However, it is important to note that this case made use of a local thermal equilibrium approach in which a single energy equation was used for both the fluid and the

solids, thus assuming the fluid and solid temperatures to be the same. A more representative approach would be a local thermal non-equilibrium approach that makes use of separate energy equations for the fluid and the solids, allowing the temperatures of the fluid and solids to be different.

Safety assessments of a PBR are not only concerned with possible design basis accidents, but also focus on detailed studies of very unlikely accident conditions which contribute very little to the safety risk involved (Breitbach & Barthels, 1980). The effective thermal conductivity parameter is used to determine the heat transfer through a packed bed during normal operating and severe upset conditions (Van Antwerpen *et al.*, 2010a). Severe upset conditions refer to the scenario where all methods of active cooling are lost during operation of a PBR and very high temperatures are reached in the packed bed.

According to Breitbach and Barthels (1980) during a hypothetical accident condition, in which all emergency cooling systems fail, the decay heat in the reactor after shutdown will cause an extreme increase in temperatures of the reactor core. Temperatures between 2000°C and 3000°C are expected. However, during upset conditions all cooling systems in a PBR will not fail as the design and safety case include passive cooling of the reactor core. Natural heat transfer mechanisms can remove any decay heat from the reactor core even if active cooling methods are absent, as described in section 1.1.

As a result, temperatures in the reactor core will be lower than the hypothetical accident condition described by Breitbach and Barthels. They completed experimental work in which they determined the effective thermal conductivity in pebble beds at temperatures up to a 1500°C (Breitbach & Barthels, 1980). The HTTU test facility was developed to provide experimental data of the heat transfer phenomena through a packed bed that could be used during the design process of the Pebble Bed Modular Reactor (PBMR). The expected temperatures in the PBMR reactor during normal operation were between 300°C and 1130°C. However, in order to account for upset conditions in the design of the PBMR the HTTU test facility was designed to achieve temperatures up to 1600°C (Rousseau & Van Staden, 2008).

During upset conditions the spheres in the packed bed remains motionless and the forced convective heat transfer mechanism is absent. Breitbach and Barthels (1980) stated that at such high temperatures the effect of the stationary gas on the heat transfer inside the packed bed can be neglected. Thus the overall heat transfer in the packed bed occurs as a result of radiation in the voids between the pebbles and conduction through the solid spheres, with radiation the dominant contributing mechanism to the overall heat transfer in the packed bed (Breitbach & Barthels, 1980; Talukdar *et al.*, 2013).

For this reason the present study focuses particularly on the radiation heat transfer during upset conditions in a packed bed of spheres. Under these conditions the bed effective thermal conductivity only consists of the first component as described by Bauer (Van Antwerpen *et al.*, 2010a) with focus on: (1) thermal radiation between solid surfaces, (2) conduction through the pebble material itself and (3) conduction through physical contact points on the surfaces of the solid materials. Equation (2.2) shows an expression for the effective thermal conductivity as used by Van Antwerpen *et al.* (2012).

$$k_{eff} = k_e^{g,c} + k_e^{r} \tag{2.2}$$

The first component, $k_e^{g,c}$, includes the conduction through the solid and stagnant gas phase as well as the conduction through the contact area between neighbouring spheres. The second component, k_e^{r}, describes the radiation heat transfer between solid surfaces.

Van Antwerpen *et al.* (2012) divided the effective thermal conductivity due to radiation heat transfer into two components as shown in Equation (2.3):

$$k_e^{r} = k_e^{r,S} + k_e^{r,L} \tag{2.3}$$

The first component is the effective thermal conductivity due to short-range radiation, $k_e^{r,S}$, and the second component is the effective thermal conductivity due to long-range radiation, $k_e^{r,L}$. Short-range radiation is defined as the radiation heat transfer between spheres in direct contact with one another. Long-range radiation is the radiation heat transfer through the voids in the pebble bed, to or from spheres that are not in contact with the sphere under consideration (Van Antwerpen *et al.*, 2012).

Various publications on the simulation of the packing structure and the effective thermal conductivity of a randomly packed pebble bed are available. A review and comparison between the different existing models based on the packing structure and the heat transfer including gas conduction, solid conduction, contact area, surface roughness and thermal radiation was done by Van Antwerpen *et al.* (2010a). A review of the work done by Van Antwerpen *et al.* is discussed in the following section. Existing models that predict the radiation heat transfer in a packed bed is also considered.

2.2 Radiation heat transfer

The significance of radiation heat transfer at high temperatures as noted in literature is described in the following section. A short summary of the effects of various parameters on the radiation heat transfer in a packed pebble bed is presented. Existing models to predict the radiation component of the effective thermal conductivity in a packed bed are discussed and current methods to model the radiation heat transfer are considered.

2.2.1 Radiation at high temperatures

The study done by Van Antwerpen *et al.* (2010a) presented a review of the different methodologies in current literature to predict the effective thermal conductivity in a packed bed. A number of correlations identified in this study neglected the effect of thermal radiation. This assumption is problematic when a packed bed of spheres at high temperatures is considered.

As mentioned previously a number of studies concluded that the effect of thermal radiation in a packed bed of spheres becomes noteworthy at high temperatures (Breitbach & Barthels, 1980; Zhou *et al.*, 2007; Cheng & Yu, 2013; Talukdar *et al.*, 2013).

Balakrishnan and Pei (1979) stated that at temperatures above 125°C (400K) radiation contributes substantially to the overall heat transfer in a packed pebble bed. In their study they also found that at temperatures of about 675°C (950K) the contribution of conduction and radiation to the overall heat transfer were almost equal. At higher temperatures the radiation contribution increased significantly. Therefore it is important to include a detailed analysis of the effects of thermal radiation when considering the heat transfer through a packed pebble bed at temperatures above 225°C (500K).

An investigation to determine the contribution of radiation to the overall heat transfer in packed beds was done by Chen and Churchill (1963). According to their findings radiation became important relative to conduction heat transfer at temperatures above approximately 870°C (1600°F). Chen and Churchill stated that Schotte found the radiation contribution to the overall heat transfer to be as high as 80% in certain cases. Feng and Han (2012) also noted that at temperatures of about 800°C and above radiation is the dominant heat transfer mechanism in a PBR.

2.2.2 Parameters affecting radiation heat transfer

An investigation to determine the effects of mean temperature, particle size and surface emissivity on the effective thermal conductivity was included in the study done by Zhou *et al.*

(2007). Cheng and Yu (2013) also used their proposed method to understand the effect of these variables on the calculation of the effective thermal conductivity as well as radiation heat transfer in a packed bed of spheres.

Radiation heat transfer is directly influenced by the mean temperature in the packed bed as well as the size of the spherical particles. Results showed that an increase in mean temperature and particle size causes an increase in the effective thermal conductivity. Asakuma *et al.* (2014) noted that for larger particles radiation becomes the dominant heat transfer mechanism and the effective thermal conductivity becomes dependent on the emissivity. The radiation heat transfer component only becomes negligible for particle diameters smaller than 0.001m.

Thus the contribution of the radiation heat transfer mechanism becomes more important at higher temperatures and in instances where larger particles are used. The effective thermal conductivity also increases with an increase in the solid surface emissivity. These conclusions are in agreement with the findings of Chen and Churchill (1963) and Talukdar *et al.* (2013).

2.2.3 Current radiation models

Radiation models in general are used to predict the radiation heat transfer in a wide variety of applications for example furnaces, combustion chambers and nuclear reactors. Various approaches exist that can be used for the modelling of radiation heat transfer. In general the different types of radiation models include the Discrete Ordinates Method (DOM), the Zone Method (ZM), the Finite Volume Method (FVM), Flux models and the Monte Carlo method (Caliot, 2010; Tucker, 2004). Each of the radiation models has different advantages and disadvantages depending on the application for which the radiation heat transfer must be determined. This section provides a review of the current radiation models used to predict the radiation heat transfer through a packed pebble bed.

Van Antwerpen *et al.* (2010a) performed a review of different radiation models noted in literature that are applicable to packed pebble beds. A part of the study done by Van Antwerpen *et al.* (2010a) focused specifically on the effective thermal conductivity due to thermal radiation. As the focus of the present study is mainly on the radiation heat transfer component emphasis is placed on this component in the revision of the work done by Van Antwerpen *et al.* (2010a). According to Lee *et al.* (2001) the various existing methods to simulate the radiation heat transfer in a packed sphere bed can be grouped into three different approaches.

The first approach is the Radiative Transfer Equation (RTE) approach, which is a radiative energy balance equation for the emitting, absorbing and scattering medium. Optical properties of the packing structure are required to solve the intensity distribution through the packing. The

optical properties are unique to each packed bed of spheres and can be determined experimentally or numerically. As stated by Van Antwerpen *et al.* (2010a) researchers that used the RTE approach in their studies include Argento and Bouvard (1996), Modest (1993) and Kamiuto *et al.* (1993)

The unit cell method is considered as the second approach. Van Antwerpen *et al.* (2010a) reviewed the work done by Chen and Churchill (1963), Cheng *et al.* (2002), Vortmeyer (1978), Robold (1982) and Breitbach and Barthels (1980) who all used this approach in their studies. In this approach the pebble bed was represented by an arrangement of unit cells of which the optical properties were known (Breitbach & Barthels, 1980; Van Antwerpen *et al.*, 2010a). A set of simple algebraic equations described the energy distribution for the system. For a unit cell in a packed bed of spheres the general form of the radiative conductivity was given as $k_e^r = 4F_E^* \sigma d_p \overline{T}^3$ where F_E^* is the radiation exchange factor, σ is the Stefan-Boltzmann constant and d_p the particle diameter (Van Antwerpen *et al.*, 2010a).

A limitation of the approach, as noted by Strieder (1997), is that the thermal radiative conductivity was only valid if it was assumed that the steady state temperature drop over the local average bed dimension was much smaller than the average bed temperature, thus $\Delta T / \overline{T} << 1$. According to Van Antwerpen *et al.* (2010a) another limitation of the unit cell approach is that the value of the radiation exchange factor was difficult to calculate and this has led researchers to view this approach as inaccurate.

The third approach is the method that uses the Radiative Transfer Coefficient (RTC) developed by Lee *et al.* (2001). The RTC is a function of the microstructure and radiative properties of the packed bed of spheres and was calculated using a Monte Carlo ray-tracing method. It is an iterative numerical method that used a set of algebraic equations to determine the energy in each sphere of the packed bed. The temperature distribution in each sphere could then be calculated.

The Monte Carlo method refers to a collection of probabilistic methods that can be used to predict the overall behaviour of a system. A typical application of a Monte Carlo method is modelling the radiative heat transfer within a packed bed of spheres. One specific method that can be used is the Monte Carlo ray-tracing method which injects a ray of energy into the bed at random and then traces the ray until it has been completely absorbed or escaped from the bed. A random generator was used to model the interaction between the rays and the surfaces and the process was repeated until the necessary convergence was obtained (Wu & Lee, 2000).

Although the Monte Carlo method has provided accurate results for various applications it has a high computational cost and can pose difficulties when applied for complex surface interactions. Therefore Wu and Lee (2000) developed a non-probabilistic based ray tracing scheme known as the Multiple-Rays Tracing (MRT) scheme to shorten the computational time required and to allow for more complex surface interactions in the modelling. However, a drawback of the scheme was the large number of rays that the computer had to keep track of, but for certain problems this could be addressed by applying the proposed scheme repeatedly.

In order to decrease the computational resources required an acceleration scheme was used during the search procedure in ray tracing where interacting spheres were identified. The probability that the next interacting sphere will be the immediate neighbouring sphere was used to reduce the search time in the process.

Various sub-studies were done to validate the newly proposed non-probabilistic method and compare its performance to that of the general probabilistic based Monte Carlo method. The results showed a comparable accuracy for the two schemes, but the MRT scheme was easier to implement for more complex surfaces. The MRT scheme was also computationally faster for certain configurations.

A boundary element method (BEM) was developed by Zhou *et al.* (2007) to predict the effective thermal conductivity in a two-dimensional packed bed. The BEM can be used to predict the conduction-radiation heat transfer through the packed pebble bed. Conduction differential equations with a continuous temperature and heat flux boundary condition for the solid and gas phases can be solved to obtain the temperature distribution in the packed bed. From the temperature field the effective thermal conductivity could be calculated. The BEM converted the partial differential equation into a boundary integral equation that was solved with an iterative procedure to reduce the computational resources needed.

Zhou *et al.* (2007) combined a net radiation method with the BEM to determine the radiation heat exchange between solid surfaces. In the calculation of the radiation it was assumed that the solid phase was opaque with diffuse and gray surfaces and a non-participating medium was present in the voids of the pebble bed. The method was applied to a square array and hexagonal array ordered packing configuration. Thus the voids in the packed bed were enclosed by the boundaries of the solid surfaces surrounding it, as can be seen in Figure 2.4. As a result the radiation was solved for a closed cavity.

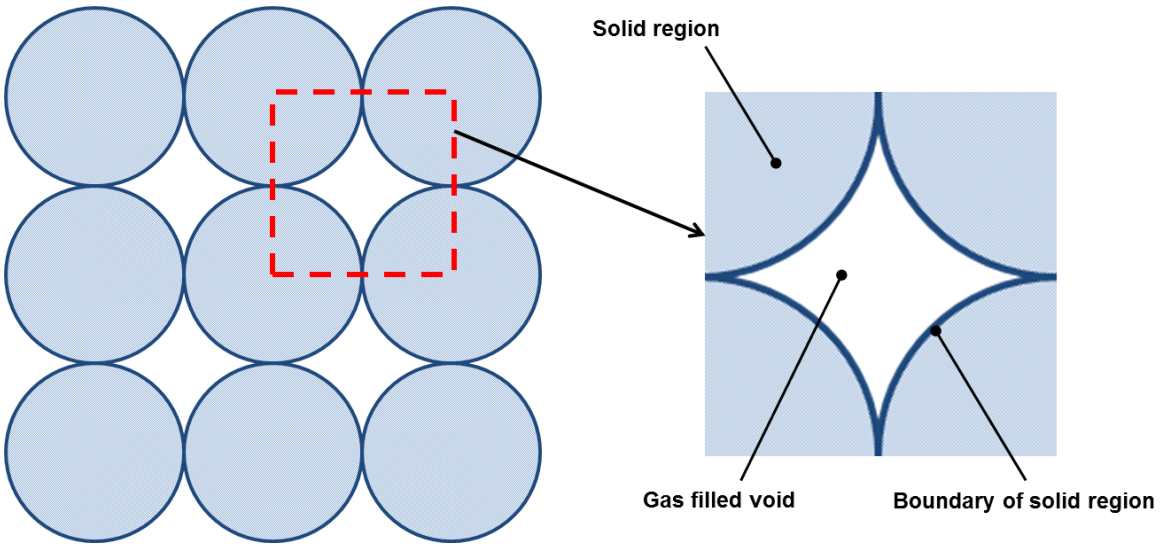

Figure 2.4: Illustration of square array packing structure and gas filled void between adjacent spheres.

For a random packing of spherical particles the radiation problem becomes more complex as radiation rays can travel to other voids in the packed bed of spheres. Although the method produced good results for square and hexagonal packing structures further studies were required to make the current method applicable to a random packed pebble bed.

According to Feng and Han (2012) most of the current models for heat transfer are continuum based methodologies that assume the packed bed is a continuous porous medium and make use of empirical correlations. To support the reactor safety case a more fundamental approach was required in the modelling of the heat transfer mechanisms. In a randomly packed bed the view between two spheres of one another can be partially blocked by other spheres in the packed bed. For instances where such a blockage occurs conventional numerical integration methods could be used to determine the view factors between the two spheres under consideration, however it was done at a high computational cost.

The evaluation of view factors between spheres in a large scale random packing with complex blockages continues to be computationally challenging. A numerical method to accurately predict the geometric view factors between spheres of equal size in a randomly packed bed was developed by Feng and Han (2012). The determined view factors were used to model the thermal radiation in the packed bed. It was assumed that all sphere surfaces were diffuse and gray with a zero reflectivity. The proposed numerical approach was a combination of three techniques that included the Tanaka integral expression for the view factor between two unit spheres, the Fibonacci integration scheme for integrals on spheres and the use of a specific non-uniform scaling function.

Results showed that the suggested method was accurate for small packed beds, but for larger packed beds such as a PBR the CPU time cost could be high. An advantage for the analysis of a large packed bed was that the view factors for the entire packing only had to be calculated once. The result could then be stored and used multiple times in the analysis of the thermal radiation for different boundary conditions. The results of the radiation heat transfer could be characterized as a discrete network system that could be combined with a conduction network system developed by the authors in previous studies. Thus the current approach can be used to model the combined radiation and conduction heat transfer in a packed bed.

Talukdar *et al.* (2013) proposed a new method to solve a heat transfer problem in a complex porous structure. A three dimensional numerical model that considered combined conduction and radiation heat transfer with the finite volume method integrated with a blocked-off region approach was used. The solid surfaces under consideration were assumed to be gray and diffuse.

The suggested approach simplified the solution of problems involving porous structures as it eliminated the complexity of grid generation generally involved with conventional methods. Representative porous structures considered in the study were the cubic cell and honeycomb structures. The accuracy of the proposed method was determined by simulation of simple test cases with different optical parameters. Results were obtained for cases with pure radiation and combined conduction-radiation heat transfer problems. It was observed that the results were in reasonably good agreement with existing literature and CFD simulations.

One of the main features of the blocked-off region approach was the use of voxel-based uniform Cartesian grid information. The method could be extended for non-uniform meshes on generalized curvilinear coordinates and non-uniform thermo-physical properties for both solid and fluid phases. As a result the method was recommended for the evaluation of the effective thermal conductivity of real-life porous media, especially at high temperatures where radiation heat transfer could not be neglected.

According to Cheng and Yu (2013) in general two approaches exist for the evaluation of effective thermal conductivity through a packed bed due to radiation heat transfer. The first is a microscopic approach based on the fundamental principles of radiation and details of the geometry under consideration, whereas the macroscopic approach is based on simplifying assumptions for the radiation and the packing structure of the bed.

The RTE and RTC approaches as well as the MRT scheme described previously can be classified as microscopic approaches. Although the microscopic approach is more favourable it

is difficult to implement and computationally challenging. The unit cell method and the BEM mentioned earlier are considered as macroscopic approaches.

A new numerical macroscopic approach to calculate the radiation heat transfer in a packed bed of uniform spheres was proposed by Cheng and Yu (2013). The difference between the proposed approach and existing studies was that the packing structure was used directly in the calculation of the effective thermal conductivity. This was done by using a Voronoi network model and resulted in a particle scale approach for the calculation of the effective thermal conductivity.

The radiation heat transfer between two neighbouring Voronoi elements was described using the network method. It was assumed that the solid spheres were opaque with gray and diffuse surfaces. The value of $\Delta T/\overline{T}$ was also much smaller than unity across a sphere layer in the packed bed. For the study the model only accounted for the short range component of the radiation heat transfer in a packed pebble bed. A numerical method proposed by Jones (as quoted by Cheng and Yu (2013)) was used to determine the view factors between surfaces required for their calculations. In the proposed approach the heat flow rates between particles were limited to particles inside the packed bed assuming adiabatic conditions at the boundaries.

The results obtained for the effective thermal conductivity using the proposed approach were in good agreement with the results of existing publications. Although the structural approach of the proposed method was general the model and results were applicable to coupled conductive and radiative heat transfer in a packed bed of uniform spheres with high thermal conductivity and a porosity of 0.36. For the development of a more comprehensive model that predict the effective thermal conductivity of a packed bed further study was required. Focus for further studies should be placed on the radiation and conduction heat transfer through the pores in a packed bed as well as the effects of porosity and different packing structures.

The importance of radiation heat transfer at very high temperatures was also considered by Asakuma *et al.* (2014). They presented a homogenisation method that can be used to perform a thermal analysis of a packed pebble bed. The advantage of the proposed method was that it evaluated exact changes in microstructure and temperature by using a three-dimensional finite element method. Asakuma *et al.* used the homogenisation method to add thermal radiation to an existing model for a packed bed. The effective thermal conductivity was then calculated to study the heat transfer in the packed pebble bed at very high temperatures.

For the completed study the homogenisation method was only applied to simple packed and body centred cubic packing structures of a pebble bed. These geometries are too simple when

compared to a real packed bed of spheres, but it is still a useful method as it evaluates complex microstructures. Results for the proposed model were compared with results generated with an empirical conventional model. The conventional method showed appropriate results for the effect of temperature on the effective thermal conductivity for body centred cubic geometries, but did not provide good results for a simple packed bed.

From the results it was concluded that the proposed method can be used to model the heat transfer in complex systems such as packed beds. Combining the proposed method and conventional models can be useful to reduce computational costs when performing large scale analyses of complex geometries.

2.2.4 Radiation models for the near-wall region

One of the conclusions made by Van Antwerpen *et al.* (2010a), in their review of the correlations for the effective thermal conductivity, was that most of the correlations developed were specifically applicable to the bulk region of a packed pebble bed. However, these correlations were also applied to regions where large porosity variations occur in the packing structure, particularly the near-wall region.

Van Antwerpen *et al.* (2010a) reported the findings of a study done by Thurgood *et al.* (2004) to determine the applicability of these effective thermal conductivity correlations when it was applied to the near-wall region. The results of the study showed that the correlations were not valid at high temperatures in the near-wall region, resulting in inaccurate predictions of the heat transfer. This was due to the presence of the wall effect in the near-wall region causing a more ordered packing structure in the area next to the wall. If radiation was neglected the only method of heat transfer was conduction through the contact point between the wall and each pebble, as a result there was a reduction in the overall heat transfer. These results proved that ignoring the effect of radiation heat transfer at high temperatures in the near-wall region is a poor assumption, especially if upset conditions in a PBR are the focus of the study.

As most of the existing models were incapable of accurately predicting the effective thermal conductivity in the near-wall region Van Antwerpen (2009) developed a new model, namely the Multi-sphere Unit Cell (MSUC) model, which can be used for both the bulk and the near-wall regions. The new model included a characterisation of the porous structure, conduction heat transfer as well as a component that specifically addressed radiation heat transfer in the packed pebble bed (Van Antwerpen *et al.*, 2012).

The effective thermal conductivity due to radiation in the MSUC model consisted of two components: a short-range and a long-range radiation component. Short-range radiation was

defined as the radiation exchange between two neighbouring spheres that are in contact. The long-range radiation component referred to the radiation exchange through the voids in the packed bed from spheres not in contact with the sphere under consideration (Van Antwerpen, 2009).

The long-range radiation is a complex phenomenon to model because of the difficulty characterising the porous structure. The MSUC model made use of an average long-range diffuse view factor to address the long-range radiation. Pitso (2011) studied the distribution of the long-range diffuse view factor in the bulk region of a numerically packed bed with the use of a CFD package's built-in ray tracing view factor calculator. Figure 2.5 shows the distribution of the calculated view factors in the bulk region of a randomly packed bed. It is clear that the long-range view factor decreases to zero at a distance of approximately 2.25 sphere diameters from the sphere under consideration. Thus a sphere in the bulk region of a randomly packed bed does not have a view of spheres with centre points 2.25 sphere diameters or more away from the sphere under consideration.

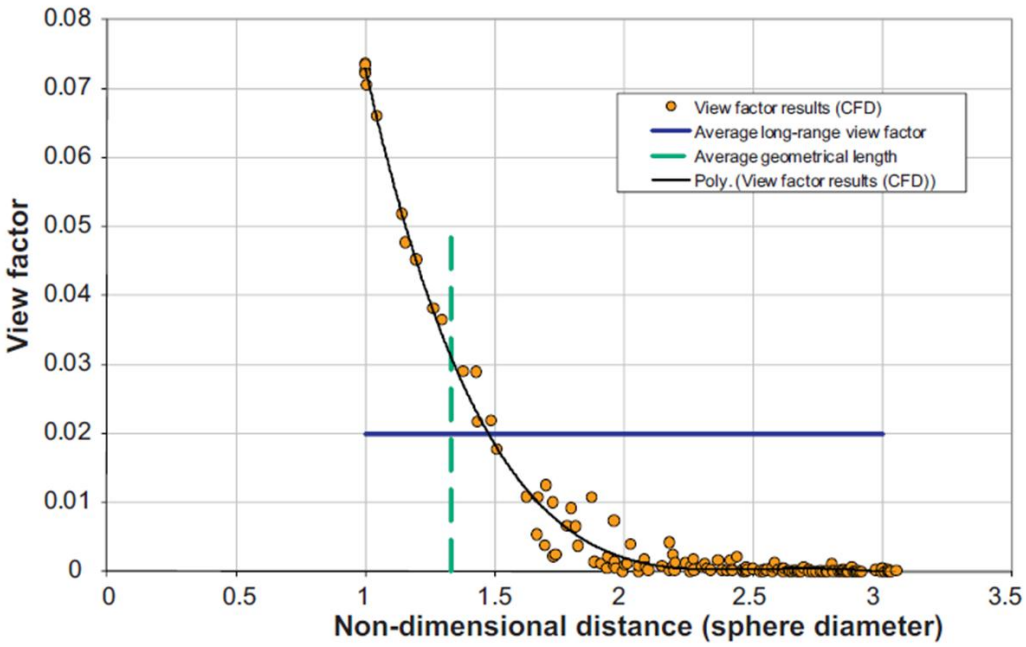

Figure 2.5: Long-range diffuse view factor in the bulk region of a packed bed (Van Antwerpen *et al.*, 2012).

Van Antwerpen (2009) used Pitso's results, that have been published since the completion of Van Antwerpen's study, to determine an unweighted average long-range diffuse view factor as a first approximation in his model of the long-range radiation component of the radiative conductivity (Van Antwerpen *et al.*, 2012). However, Van Antwerpen focused on the bulk region in his characterisation, due to the complex nature of the characterisation of the long-range

diffuse view factor in the near-wall region of a packed bed. As a result Van Antwerpen assumed the long-range radiation component of the effective thermal conductivity is the same in both the bulk and the near-wall regions (Van Antwerpen *et al.*, 2012).

Van Antwerpen (2009) concluded that as the model for the long-range radiation was only a first approximation, further study in this area should be done to refine the current model. Specifically the average long-range diffuse view factor should be defined as a function of radial position in a randomly packed bed to account for the wall effect in the near-wall region. The average long-range view factor must also be weighted to include radiation from the number of spheres that explicitly contribute to the long-range radiation.

The MSUC model was verified and validated using experimental data from various test facilities including the High Temperature Test Unit (HTTU), the High Temperature Oven (HTO) and the SANA-I experimental test facility. Results showed that the temperature and effective thermal conductivity values predicted using the MSUC model were in good agreement with the experimental results for temperatures below 1200°C, however some uncertainty existed for temperatures above 1200°C (Van Antwerpen, 2009). Therefore Van Antwerpen (2009) concluded that thermal radiation tests should be conducted at temperatures above 1200°C for the various regions in a packed pebble bed. A detailed investigation of the near-wall region is necessary to better characterise the radiation in this area.

A follow-up study on Van Antwerpen's work was done by Pitso (2011) to improve on the first approximation of the radiation component of the MSUC model. Pitso developed the SUN model based on a fundamental thermal radiation network approach using conventional CFD methods to characterise the thermal radiation (Rousseau *et al.*, 2012b). The approach of the SUN model was similar to the net radiation method used in the BEM developed by Zhou *et al.* (2007) as well as the method used by Feng and Han (2012) as discussed in section 2.2.3.

The assumption that the radiation heat transfer between the surface of a specific sphere under consideration and the surfaces of the spheres around it can be modelled as a conventional interconnected network of radiating surfaces was used as the base for the development of the SUN model (Rousseau *et al.*, 2012b). In order to simplify the model the spheres surrounding the central sphere could be grouped together to form concentric spherical shells around the central sphere at various characteristic lengths. For each of these shells an effective total view factor was defined that was representative of all the sphere surfaces included in the shell.

The applicability of the SUN model was verified by using CFD simulations and the results obtained were found to be sufficiently accurate. The SUN model can be used as a basis to

provide a more fundamental definition of the radiation component of effective thermal conductivity which can be incorporated into the MSUC model. However, currently the SUN model can be used for a spherical unit cell in the bulk region of a randomly packed bed whereas for a typical PBR design a cylindrical coordinate system is required. The present model also did not account for the wall and near-wall regions in a packed pebble bed. Rousseau *et al.* (2012b) also concluded that experimental data at temperatures above 1200°C will be useful to evaluate the current results of the SUN model.

Van der Meer (2011) went on to propose a discretisation methodology that transformed the SUN model into cylindrical coordinates. The new model, named the CSUN model, can be used to model the long-range radiation heat transfer in a packed pebble bed with a cylindrical reference frame. The CSUN model only accounted for temperature gradients in the radial direction. Van der Meer used the CSUN model to replace the existing long-range radiation component of the MSUC model. Results obtained by the study were compared with experimental data from the HTTU test facility and were found to be in good agreement for temperatures up to 1000°C.

It was concluded that future studies should be done to expand the current CSUN model to also account for temperature gradients in the axial direction. The present model does not take the wall effects into account and the model should be expanded to the near-wall region. Experimental steady-state tests should be conducted at temperatures higher than 1000°C in order to provide accurate experimental data that can be used to validate the model at higher temperatures (Van der Meer, 2011).

2.3 Analysis of a randomly packed pebble bed

Methods using purely empirical correlations to predict the heat transfer through a packed bed of spheres are becoming less popular and the focus is shifting to the analysis of numerically simulated packed beds (Van Antwerpen *et al.*, 2010a). A combined Discrete Element Method (DEM) and CFD approach has become popular in the analysis of heat transfer mechanisms through a packed bed (Tsory *et al.*, 2013). The DEM-CFD approach is used to determine the effective thermal conductivity of a packed bed of spheres and includes the evaluation of heat transfer mechanisms at a particle scale level (Zhou *et al.*, 2010). Previously high computational cost was a disadvantage of this approach, however recent improvements in computational power has made it a feasible option (Eppinger *et al.*, 2011).

A three dimensional structure of a packed bed is required before a fluid flow and heat transfer analysis can be done using CFD methods. The DEM is used to generate the structure of a

randomly packed bed of spheres using Newton's second law to simulate the motion and interaction of the discrete particles (Eppinger *et al.*, 2011; Tsory *et al.*, 2013). A mesh must be developed for the generated packed bed where the geometry of the three dimensional structure is subdivided into small control volumes (Eppinger *et al.*, 2011). For CFD simulations of a packed pebble bed the particle-to-particle and particle-to-wall contact points often create problems during the development of a mesh (Dixon *et al.*, 2013). Various methods exist to address these problems associated with contact points.

The following section focuses on the methodologies used in current literature for the generation, meshing and simulation of randomly packed beds of spherical particles. A review of the discrete element methods used in current literature is given. The different methods used to address the problems with contact points in mesh development are discussed. Various approaches for the CFD modelling of the heat transfer through a packed bed of spheres are presented.

2.3.1 Discrete element methods

The discrete element method is a popular approach for the analysis of granular materials such as the fuel pebbles in a PBR. In DEM simulations of granular materials the trajectories of individual particles are determined for consecutive time steps by calculating the acceleration of each particle due to the net forces applied to the specific particle (Suikkanen *et al.*, 2014).

Although DEM is a highly accurate method it can also imply high computational cost in the generation of dense packed beds. According to Suikkanen *et al.* (2014) other approaches using simpler algorithms based on geometrical parameters and simplified physical models have been used in literature as a faster way to generate packed beds. However, the packing characteristic of a packed bed of spheres generated by non-physical packing algorithms may not be completely realistic and therefore these approaches should be used selectively.

Suikkanen *et al.* (2014) stated that Du Toit (2008; 2002) conducted various studies to gain a better understanding of the packing characteristics of numerically generated pebble beds. Methods for the analysis of the variation of the porosity in the axial and radial directions through an annular pebble bed were presented in these studies. A comparison was done between the packing characteristics of a physically and a numerically packed pebble bed and it was concluded that numerically packed beds are adequate representations of real packed beds. Thus DEM is an acceptable approach for the generation of randomly packed pebble beds.

General purpose DEM codes were used by most researchers, but some studies included the development of a customised DEM code. A specialised DEM code can be adapted to fit the requirements for a specific application thus resulting in better results. Suikkanen *et al.* (2014)

developed a DEM code specifically for the analysis of pebble beds. Initially a random number generator algorithm was used to create a dilute packing inside the annular cylinder including all the pebbles required for the DEM simulation. The generated pebbles are then collapsed during the DEM simulation due to gravity and the Hertzian contact theory was used to describe the interactions between particles. To ensure stable calculations a suitable time step based on pebble mass and stiffness had to be used in the DEM simulation.

The results obtained with the developed DEM code was compared with available experimental data from literature and the results showed acceptable accuracy, thus realistically packed beds were formed using the DEM code. The method used in the proposed DEM code was not a perfect reproduction of the manner in which the packing of a real reactor is formed. If the method was to include the injection of each of the individual particles from specific feed locations the computational resources required would be too large. Therefore it was an acceptable compromise between realistic methods and computational cost.

Ookawara *et al.* (2007) and Nel *et al.* (2012) used general purpose DEM codes to generate packed beds of spherical particles. The DEM models of both studies were also based on the principle of gravity being exerted on individual particles. The results of the random packed beds produced in both cases were in good agreement with existing literature.

Eppinger *et al.* (2011) and Van der Merwe (2014) focused on simulations of reactors with a small tube to particle diameter ratio for which wall effects were significant. The DEM model of the CFD tool Star-CCM+, developed by CD-adapco (2013), was used for the generation of randomly packed beds in both studies. For this specific DEM model spherical particles were generated at either random locations or a specific point in the tubular fluid domain and fell to the bottom of the tube as a result of gravity.

A force balance was calculated for each of the individual particles and included the effect of gravity, interactions between the particles and the particles and the wall of the tube. Once the velocity of each particle was considered to be virtually zero the DEM simulation was converged. The porosity of the generated packing was dependent on the surface roughness, the tube to particle diameter ratio as well as the packing method.

In order to validate the proposed DEM simulations Eppinger *et al.* (2011) compared the global bed porosity and the radial porosity distribution of the generated bed with results from existing literature and the results were found to be in good agreement. Van der Merwe (2014) compared the bulk porosities as well as the porosity variations in the axial direction of the generated beds with correlations in literature and experimental measurements. He concluded that the results

were in good agreement and the generated DEM beds were of high quality. For the current study Star-CCM+ will also be used for the generation of a numerical randomly packed pebble bed.

2.3.2 Mesh development: Contact point treatment methods

Mesh development for CFD simulations of heat transfer through packed beds of spherical particles often pose problems. One of these problems is the cell quality of the generated mesh at the contact points between neighbouring particles and particles and the wall of the bed (Lee *et al.*, 2007; Eppinger *et al.*, 2011). The cells in these areas of the mesh are often highly skewed leading to convergence problems during calculation. As a result a very fine mesh is generated in this area resolving the convergence issues, but increasing the computational resources required to obtain a solution.

Numerous methods exist in literature to address these problems associated with contact points. In the study done by Dixon *et al.* (2013) a comparison between four methods that address the treatment of contact points was presented. These methods included the global and local reduction and enlargement of the geometry of the spherical particles. The various approaches were referred to as the Gaps, Overlaps, Bridges and Caps methods respectively. Figure 2.6 shows a representation of the different contact point treatment methods.

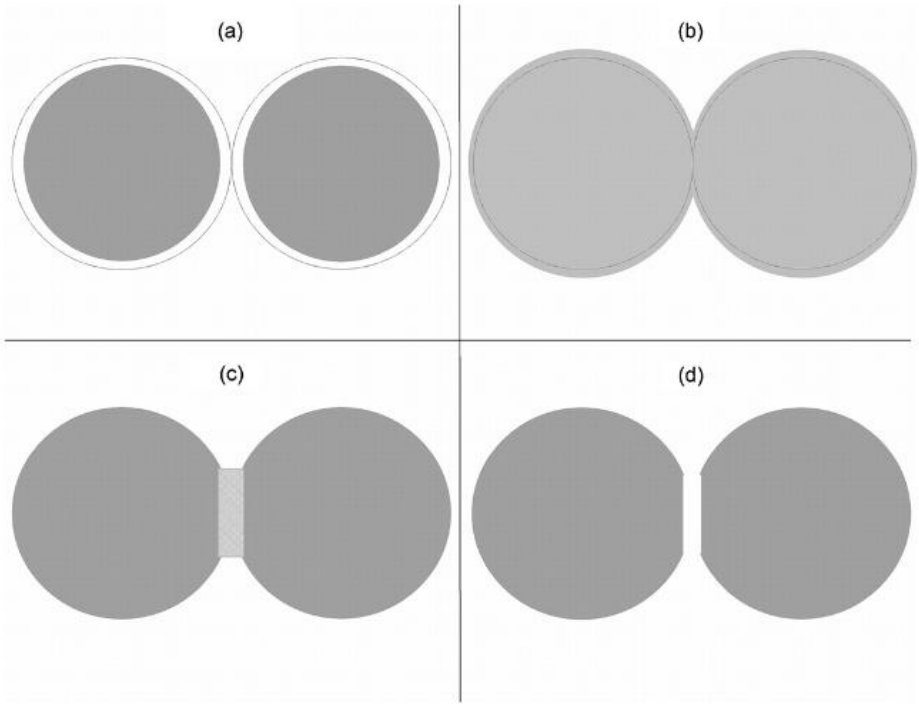

Figure 2.6: Schematic representation of the four contact point treatment methods: (a) Gaps, (b) Overlaps, (c) Bridges and (d) Caps (Dixon *et al.*, 2013).

Illustrations (a) and (b) in Figure 2.6 show the two global methods where the light and dark circles represent the original particle sizes before modification for case (a) and (b) respectively. The Gaps method was the simplest solution to the problem by shrinking the entire size of the spherical particles thus eliminating the contact points in the packed bed. Another approach will be to increase the size of the spherical particles by a specific percentage resulting in a small overlap between spheres at the contact points. These two methods both resulted in bed void fraction errors which might lead to significant errors in pressure drop calculations.

To eliminate changes to the bed void fractions local modifications to the model geometry have been considered where changes were only made to the contact point and its immediate surroundings. The Bridges method, shown in Figure 2.6 (c) involved the placement of a cylinder at the contact point between two spheres. This method eliminated contact points, decreased the required mesh size and limited changes to the bed void fraction. As opposed to this approach the Caps method, shown in Figure 2.6 (d), involved the local flattening of particles at the contact points which is equivalent to the removal of spherical caps at the contact points.

The effects of the use of the different contact point treatment methods were investigated by Dixon *et al.* (2013). Estimations of the errors introduced with the use of the various contact point modifications in simulations involving the flow and heat transfer through a packed bed of spheres were presented. The results could be divided into shell studies, where only the fluid domain was meshed, and particle studies, where the particles as well as the fluid were meshed.

Particle studies can be used specifically for work on heat transfer, intraparticle diffusion and heterogeneous reaction within the packed bed. The results showed that global modification methods such as the reduction or expansion of sphere sizes resulted in unacceptable high errors in the particle to particle heat transfer, unless the geometric modification was extremely small. However, even with small geometric modifications the meshing problem at the contact points will not be resolved unless prohibitively fine meshes were used.

For work involving heat transfer any fluid gap will lead to unrealistic temperature profiles and large errors in the heat flow, whilst overlapping particles result in a too high heat transfer rate. From the results the Bridges method, with an appropriate effective thermal conductivity for the bridge material, was recommended as the most suitable for work involving heat transfer.

Various other researchers also conducted studies to determine the effects associated with the use of different contact point treatments in the modelling of packed pebble beds. Lee *et al.* (2007) performed a sensitivity analysis to determine the effect of different contact point treatments in the CFD modelling of a PBR core. At first focus was placed on the methodology

and a qualitative assessment of contact point methods, thus the contact point between only two spherical pebbles with a 60 mm diameter was analysed.

Four cases were investigated during the sensitivity analysis. For the first two cases the contact point region between the spheres was approximated by a gap of 2 mm and 1 mm respectively. A direct contact in the form of a point contact and an area contact was applied between the two spheres in cases three and four. Figure 2.7 shows the results of the pebble surface temperatures for the four cases obtained in the study. It is clear from these results how the treatment of the contact region affects the temperature distribution on the pebble surface.

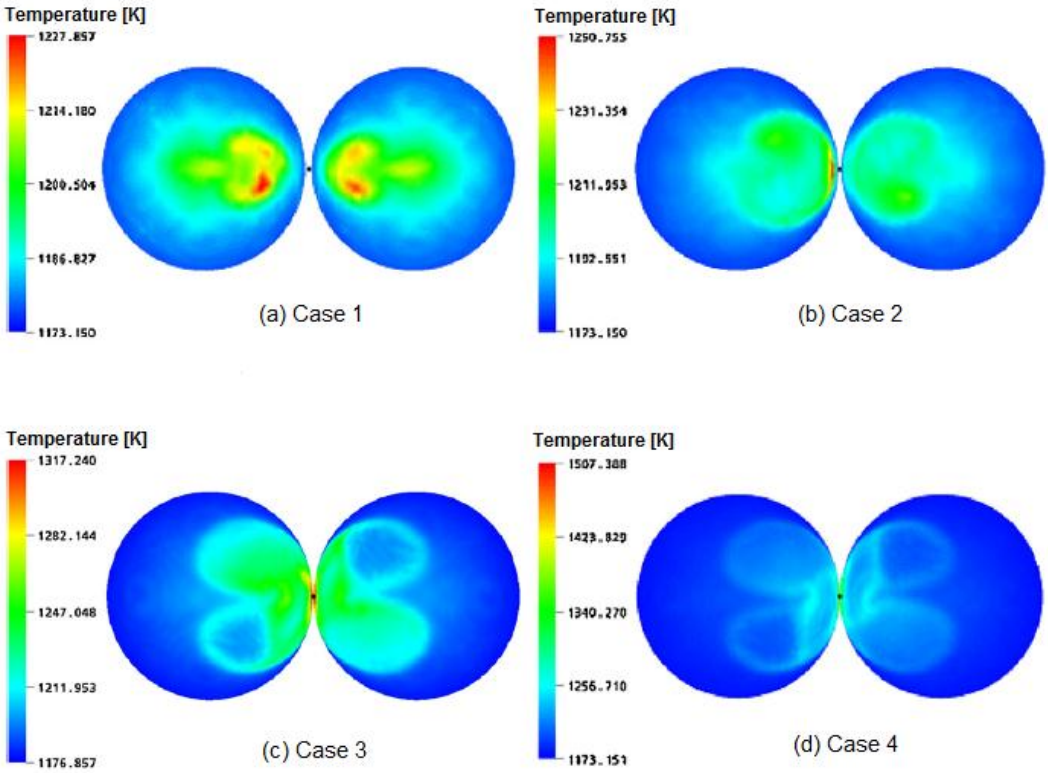

Figure 2.7: Temperature distribution on the sphere surfaces for the four different contact point modification methods (Lee *et al.*, 2007).

From the results of the sensitivity analysis, cases two and four were selected and the two contact treatment methods were applied to the simulation of a PBR core. The results of the study showed that although the gap representation of the contact region resolved the problems associated with mesh generation it provided inaccurate results. Therefore a direct contact treatment method provided more accurate and realistic results for the fluid flow and heat transfer phenomena in a PBR.

Eppinger *et al.* (2011) presented a study on the porosity and pressure drop in a packed bed of spheres with a small tube to particle diameter ratio. A method similar to the Caps method was

applied to the geometry where the particles were flattened locally at the contact points to avoid meshing problems. The results obtained with this method provided results of good accuracy.

The Bridges method described previously was used in the study by Ookawara *et al.* (2007) to reduce the presence of fine and skewed mesh cells at the contact points in a packed bed of spheres. Results showed that the Bridges method did not affect the macroscopic flow properties in the packed bed and provided accurate results for the heat transfer as well. Ookawara *et al.* (2007) concluded that the method produced good results for the contact point treatment in packed pebble beds.

To investigate the effect of the Bridges method on the global porosity of a packed bed Louw *et al.* (2012) used this method to address the contact points in four different packing structures. Particles with a diameter of 30 mm were used to generate three packed beds with structured packings of simple cubic, body centred cubic and face centred cubic respectively. One packed bed with a random packing structure consisting of 400 spherical particles was also included in the study.

Overall the Bridges method presented a decrease in the global porosity, which was expected as solid material was added at the contact points between particles. From the results obtained through the study it was evident that the porosity error introduced with the Bridges method increased considerably for a cylinder diameter greater than 30% of the spherical particle diameter. Therefore to avoid significant porosity errors and still minimise the generation of fine cells at the contact points Louw *et al.* (2012) recommended that a cylinder diameter between 20% and 30% of the particle diameter be used with the Bridges method.

Van der Merwe (2014) also presented a study on the porosity and pressure drop in a packed bed of spheres with a small cylinder to particle diameter ratio. He used a similar approach to that of the Bridges method by inserting a fillet with a specified radius at the particle-particle and particle-cylinder contact points. Figure 2.8 shows the particle-wall contact point in the top illustration and the particle-particle contact point in the bottom illustration with and without the fillet contact treatment. The results of the study showed that a fillet radius of 0.1 mm, which is equal to 0.2% of the particle diameter, had the smallest influence on the fluid flow and pressure drop through the packed bed of spheres while limiting the generation of low quality cells. The influence of the fillet size and the contact area between particles on the heat transfer through the packed bed were not investigated in the study.

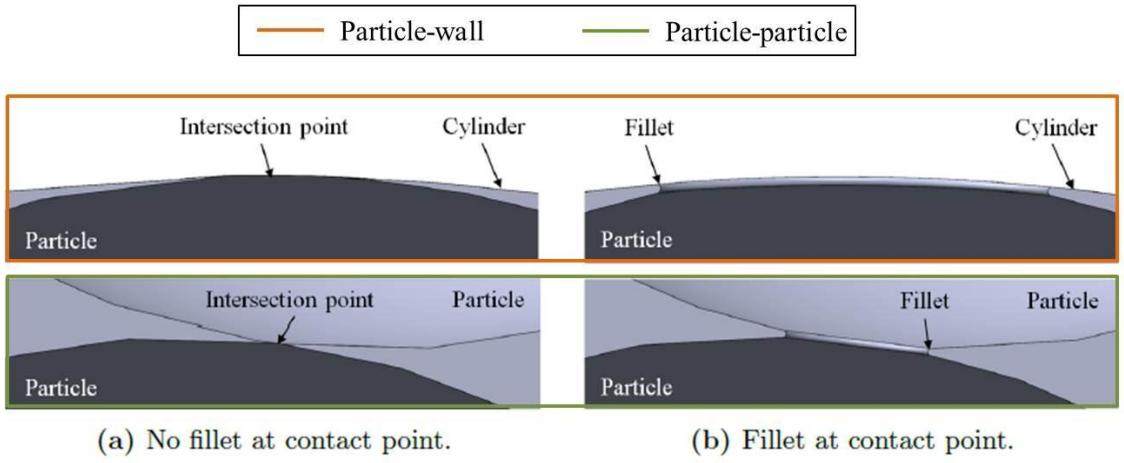

Figure 2.8: Illustrations of particle-wall (top) and particle-particle (bottom) contact points without and with fillet contact treatment (Van der Merwe, 2014).

In the present study the focus is on particle studies of a packed pebble bed, in particular the heat transfer between adjacent particles and the particles and the wall. It is evident from the conclusions made in the above mentioned studies that the Bridges method and the fillet contact treatment are the most suitable approaches to address contact point regions for this application.

2.3.3 CFD modelling of heat transfer in packed pebble beds

Various general purpose CFD codes exist which can be used to simulate the fluid flow and heat transfer phenomena in a packed pebble bed. CFD simulation results provide a good approximation for experimental data in comparison with the results from theoretical modelling (Béttega *et al.*, 2013). The methodologies followed by two researchers for conduction and radiation heat transfer CFD simulations are presented in the following section.

The commercial CFD code FLUENT together with a custom DEM code was used by Tsory *et al.* (2013) to simulate the heat transfer between neighbouring particles and the particles and the wall in a packed pebble bed. Steel spherical particles with a diameter of 1 mm with a constant density were used in the simulations. The effects of convection and radiation heat transfer mechanisms were neglected in the simulations. With the use of the DEM code a randomly packed bed was formed in a cylindrical tube. The initial temperatures of the spheres were specified as 300K and two boundary conditions were defined in the setup of the simulation, a constant heat rate of 2 W at the top wall and a constant temperature of 300 K at the bottom wall.

Pitso (2011) used the CFD code STAR-CCM+ to develop a model that specifically addressed the radiation heat transfer through a spherical section of a randomly packed pebble bed.

Pebbles with a diameter of 60 mm were used in the model and a thin spherical cover layer surrounded the pebble bed to form a closed system. A Gaps method was used to eliminate conduction between spheres by shrinking the particle diameter with 1 mm. The surface to surface radiation model that does not require a participating medium between surfaces, specific to the CFD code, was used to eliminate convection heat transfer. As boundary conditions a temperature of 1189°C was specified on the surface of the central sphere of the section and a negative heat rate of 1946.8 W at the outer surface of the cover layer (Rousseau *et al.*, 2012b).

For the present study the CFD code STAR-CCM+ will also be used for the modelling of the heat transfer in a packed pebble bed. Focus will be placed on the radiation and conduction heat transfer mechanisms as convection heat transfer can be present in accident conditions but only once buoyancy driven flow has developed.

2.4 Experimental test facilities

Models and simulations describing the effective thermal conductivity and specifically the radiation heat transfer through a packed pebble bed must be validated with experimental data. Therefore a need for experimental data describing the heat transfer through a packed pebble bed at higher temperatures exists, as was concluded from section 2.2. Experimental test facilities used to determine the effective thermal conductivity through a packed bed of spheres noted in current literature are mostly case specific (Van Antwerpen, 2009). Thus care should be taken when comparing the experimental results with the results of developed simulations and models.

Van Antwerpen (2009) concluded that far more experimental research was done at low temperatures with small diameter spheres than at high temperatures with larger spheres. In the present study focus is placed on accident conditions in a PBR, thus experimental research at very high temperatures with larger spheres becomes important. The following section describes existing experimental test facilities for experimental work at low and high temperatures with varying pebble sizes.

2.4.1 Experimental work at low temperatures and small particle sizes

Experimental tests were done by Widenfield *et al.* (2003) to predict the effective thermal conductivity under steady state conditions when a packed pebble bed was placed under axial compression stresses. Steel spheres with a diameter of 0.5 and 1 mm respectively were used and the cylindrical particulate bed was placed between two stainless steel bars. An electrical heater was used to produce a constant heat rate to the upper bar while a brass pipe around the

bottom bar cooled it down by means of circulating water. The side walls of the cylinder were insulated to ensure only axial heat conduction was present through the packed bed. Fourier's law together with the heat transfer rate and the temperature distribution across the packed bed allowed for the calculation of the effective thermal conductivity.

Mandal *et al.* (2012) considered a packed lithium-titanate pebble bed for the blanket of a fusion reactor. Thermal energy that is produced as a result of breeding and radiation from the reactor core must be removed. In order to ensure the adequate design of the blanket, experimental data on the effective thermal conductivity of the packed pebble bed was required.

An experimental setup was designed to obtain the required experimental data in which the lithium-titanate pebbles varied in sizes from 1 to 10 mm. A cylindrical stainless steel test section with an internal diameter of 162.74 mm and a height of 650 mm was used. For the various tests the test section was filled with pebbles up to a height of 330 mm. Two electrical resistance heating wires both with a heating capacity of 3 kW were used to heat up the test section.

Tests were conducted for a bed wall temperature of up to 600°C and the radiation heat transfer within the packed bed was neglected. Gas convection was included in the effective thermal conductivity term. Temperature measurements of the bed and the wall were taken, in both the radial and axial directions, at different positions in the test section over a period of time. The results presented the measured effective thermal conductivity for various pebble sizes, air flow rates and wall temperatures.

Experimental tests were performed by Béttega *et al.* (2013) to determine the heat transfer in a packed bed of glass spheres with a diameter of 1.9 mm. The vessel of the packed bed consisted of a cylinder with a diameter of 50 mm and a length of 800 mm with a heat source located on the wall. Air was used to induce flow through the packed bed of spheres and tests were conducted at two different bed heights and gas flow rates. Thermocouples were placed at various positions in the packed bed to obtain temperature profiles. The experimental tests were performed at very low temperatures up to approximately 320 K.

2.4.2 High Temperature Oven

Breitbach and Barthels (1980) conducted experimental work using the High Temperature Oven (HTO) test facility. The test facility consisted of a cylindrical graphite vessel in which the packed bed with a diameter of 500 mm and a height of 700 mm was placed. Heat was added to the system by means of an induction heating coil surrounding the cylindrical vessel. The graphite vessel was insulated at the top and bottom surfaces in order to minimise the heat loss in the

axial direction and to obtain a symmetrical radial temperature distribution through the packed bed of spheres. Figure 2.9 shows an illustration of the HTO experimental setup.

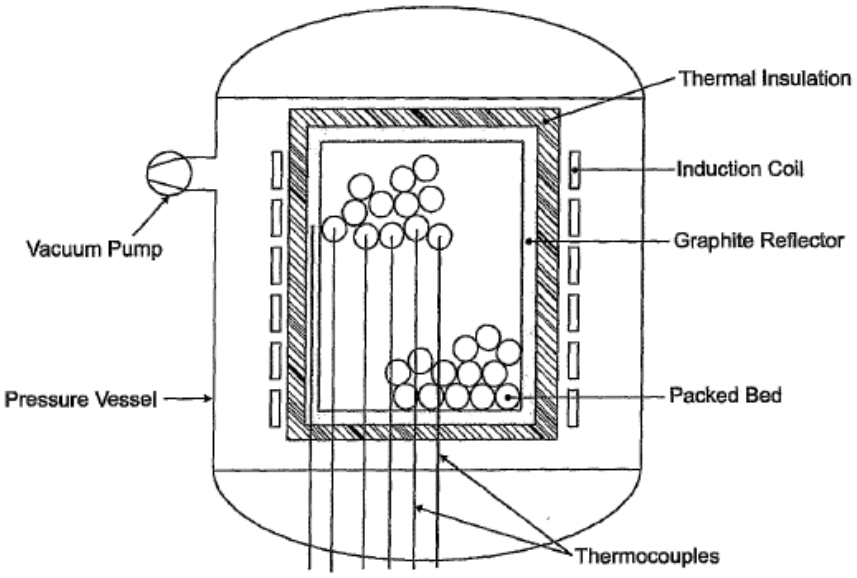

Figure 2.9: Illustration of the High Temperature Oven experimental test facility (Breitbach & Barthels, 1980).

Experimental tests were conducted with zirconium-oxide pebbles with a diameter of 45 mm and graphite pebbles with a diameter of 40 mm. The heating of the system was made in steps of 200°C for temperatures up to 1500°C. Thermocouples were placed at various radial positions in the packed bed and temperature measurements were taken for short time intervals throughout the experiment.

A least-squares regression function was fitted to the temperature distribution to obtain a smooth temperature function. The authors used a transient method to determine the effective thermal conductivity from the temperature distribution.

2.4.3 SANA-I Experimental Test Facility

Experimental tests were conducted by Stöcker and Niessen (1997) using the SANA-I test facility to investigate the heat transfer phenomena inside a High Temperature Gas-cooled Reactor (HTGR) core. The test facility consisted of a cylindrical vessel with an outer diameter of 1500 mm and a heater element at the centre with a diameter of 130 mm. A randomly packed pebble bed with a height of 1000 mm was placed inside the cylindrical vessel and was insulated at the top and bottom in the axial direction. Figure 2.10 shows an illustration of the SANA-I test facility.

Graphite pebbles with diameters of 60 mm and 30 mm were used for the packed pebble bed. Two steady state experimental tests were conducted for a heater power input of 10 kW and 35

kW respectively. Both experimental tests were performed with a helium environment at atmospheric pressure inside the vessel. Temperature measurements along the radial direction of the packed bed were taken for three different axial levels to obtain temperature distributions throughout the packed bed of spheres. The effective thermal conductivity for the packed pebble bed was calculated using the heat transfer and temperature measurements of the experimental results.

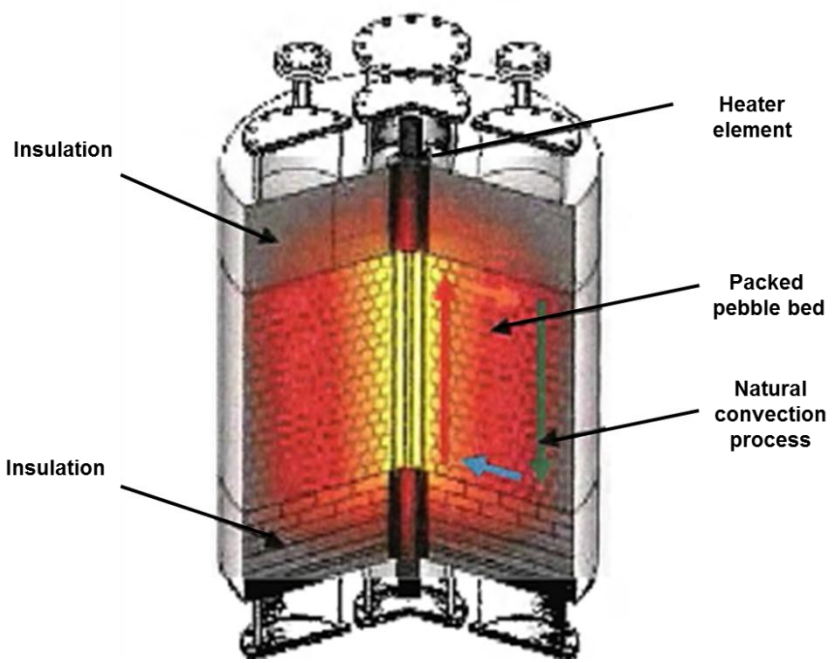

Figure 2.10: Illustration of SANA-I experimental test facility (Stöcker & Niessen, 1997).

2.4.4 High Temperature Test Unit test facility

Existing correlations and data to describe the thermal-fluid phenomena through a PBR reactor were insufficient to use in the design of the PBMR. The reasons were that not all of the available experimental data were obtained from experiments that were conducted under the necessary quality assurance certification and not all experiments provided detailed information with specified uncertainties (Rousseau *et al.*, 2012a). As a result the non-nuclear High Temperature Test Unit (HTTU) test facility was developed to conduct tests to more accurately describe the thermal fluid phenomena through an annular PBR.

Rousseau *et al.* (2012a) provided a description of the HTTU test facility and the experimental tests that were conducted to determine the effective thermal conductivity. Graphite spheres with a diameter of 60 mm containing no nuclear fuel were packed randomly between an inner and outer graphite reflector to form the test section. Approximately 25 000 graphite spheres were packed in the test section. A set of heater elements was included in the inner reflector whilst the

outer reflector was enclosed by a water-cooled jacket. This was done in order to obtain a temperature gradient in the radial direction through the pebble bed and the heat transfer rate was measured to determine an energy balance over the packed bed. The top and bottom surface of the test section were insulated in order to limit the heat transfer in the axial direction of the packed bed. Figure 2.11 shows a vertical cut through the HTTU test section.

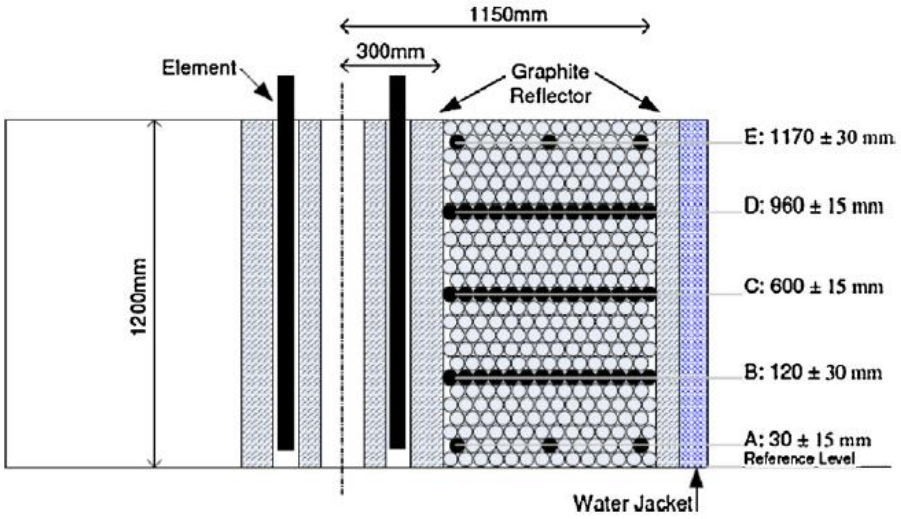

Figure 2.11: Representation of a vertical cut through the HTTU test section (Rousseau *et al.*, 2012a).

The temperature distributions through the bed at various positions were measured using thermocouples that were inserted in different spheres. The dark coloured spheres shown in Figure 2.11 represent the spheres fitted with thermocouples at the different levels in the test section. At levels B, C and D fourteen thermocouples were placed along the radial direction of the bed and two thermocouples in each of the reflectors. Each level consisted of three sets of thermocouples spaced around the circumference of the HTTU test section at 120° intervals as can be seen in Figure 2.12.

The test section containing the packed bed of spheres was enclosed in a vessel. The experimental tests were conducted at near-vacuum conditions with the vessel filled with nitrogen gas at an absolute pressure of 10 kPa. At this pressure the effect of natural convection heat transfer was negligible. Two experimental tests were conducted. For the first test the inner reflector surface temperature was set to roughly 1200°C and the inlet and outlet water temperatures of the water-cooled jacket were set to 25°C and 35°C respectively. The inner reflector surface temperature was maintained at about 600°C for the second test. To determine the repeatability of the results obtained two identical tests at different times were performed for both of the test cases.

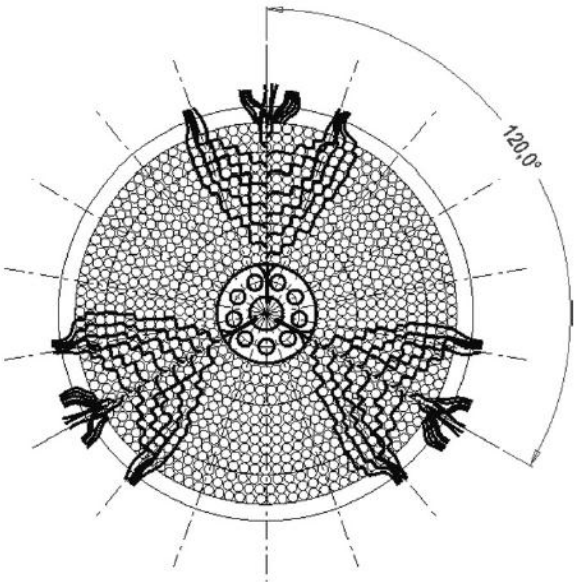

Figure 2.12: Illustration of a horizontal cut through the HTTU test section (Rousseau & Van Staden, 2008).

The effective thermal conductivity was determined by using a simple Fourier conduction rate equation for the radial direction in the packed bed together with the measured temperatures and estimated heat loss values throughout the packed bed. The temperature distributions for the various tests were combined to form one large set of data points and average values for the heat losses were used, because of the good correlation between the results for the two test cases. Radiation heat transfer between spheres, conduction heat transfer between spheres in contact and conduction through the pebble bed material were included in the values of the effective thermal conductivity. The thermal radiation component between the spheres had a large influence on the effective thermal conductivity.

From the results it was clear the effective thermal conductivity increased with an increase in temperature which was expected as the effect of thermal radiation is higher at higher temperatures. The effective thermal conductivity decreased in the near-wall region of the packed bed due to the altered packing structure of the graphite spheres in that region. It was also concluded that the effective thermal conductivity at a certain position in the bed was not only a function of temperature, but also of the macro temperature gradient at that position. This effect could be as a result of the long-range thermal radiation between non-adjacent pebbles.

An uncertainty analysis was included in the test results and made provision for the effects of statistical variances, instrument uncertainty and drift uncertainty. The total standard uncertainty for the measured temperatures at the various positions throughout the packed bed and the estimated heat losses proved to be small and the results obtained could be deemed accurate.

Thus the values obtained for the effective thermal conductivity can be used to validate existing models or for the development of new models.

2.5 Summary

The literature review was conducted to gain an understanding of the packing structures in a packed bed of spheres, the importance of the radiation heat transfer phenomena and the methods used for the experimental and numerical analyses of the heat transfer in a packed pebble bed.

The packing structure of a packed pebble bed can be divided into three regions namely the bulk, the wall and the near-wall regions. Near any wall in the packed pebble bed the porous structure of the packing is affected by the presence of the wall. The wall effect at the wall and the near-wall regions have a significant effect on the heat transfer phenomena in these regions and thus it also affects the prediction of the effective thermal conductivity.

Effective thermal conductivity is a parameter that describes the overall heat transfer in a pebble bed and it can be determined with the use of a simple Fourier conduction rate equation. During the design of a PBR, accident conditions must be considered in which all forms of active cooling are lost and the natural conduction and radiation mechanisms are used for the removal of decay heat. The expected temperatures in a PBR during upset conditions are extremely high.

Various studies proved that the effect of radiation heat transfer in a PBR becomes more significant at higher temperatures, to the extent that it becomes the main contributing heat transfer mechanism. Therefore a study of the heat transfer in a packed pebble bed should definitely include the effects of thermal radiation.

Different models exist in current literature with a wide range of approaches for the modelling of the radiation heat transfer in a packed pebble bed. However most of these models are only applicable to the bulk region of the packed pebble bed. Even though the correlations were developed for the bulk region some studies also applied these correlations to predict the effective thermal conductivity in the near-wall region, resulting in inaccurate results. In a study to specifically address the near-wall region a new model, the MSUC model, was developed.

The long-range radiation component of the MSUC model was only a first approximation leading to further studies in this area to more fundamentally address the long-range radiation component. A number of studies concluded that no experimental data at temperatures above 1200°C existed for the heat transfer and specifically the radiation heat transfer in a packed bed

of spheres. The models proposed for a more detailed definition of the long-range radiation component were also only applicable to the bulk region of a packed pebble bed.

A DEM-CFD approach for the investigation of the heat transfer mechanisms in a packed pebble bed has become popular. Various DEM methods exist for the generation of a numerically packed bed of spheres delivering accurate representations of real packed beds. One specific method includes the use of the DEM model of STAR-CCM+. The problems associated with the mesh development at the contact points for the DEM generated pebble beds can be addressed using various approaches. The Bridges approach and the fillet contact treatment were found to be the most suitable approaches resulting in accurate results and limiting the changes to the bed void fraction.

Various approaches for the CFD modelling of the heat transfer through a packed bed of spheres were presented. STAR-CCM+ was found to be a sufficient CFD code for the modelling of the heat transfer in a packed pebble bed.

A number of experimental test facilities used for the investigation of the heat transfer in packed pebble beds with small and large particle sizes as well as at low and high temperatures were discussed. None of the test facilities focused specifically on the heat transfer in the near-wall region of a packed pebble bed. Not all of the experimental data reported in current literature provide associated uncertainties, thus limiting the use of the data to validate new models.

In particular the experimental work done with the HTTU test facility led to the construction and design of the new Near-wall Effect Thermal Conductivity Test Facility (NWETCTF). The NWETCTF was used for the experimental work performed in the current investigation and methods similar to that used for the data and uncertainty analyses of the HTTU experimental results was used in the current study.

The following chapter provides an overview of the fundamental principles for the calculation of radiation heat transfer as well as the background of the theory on which the methods that will be used for the data and uncertainty analyses is based.

3

Background Theory

An overview of the fundamental principles of thermal radiation heat transfer is given in this chapter. The theoretical background of the methodologies used by researchers to perform data and uncertainty analyses of experimental results are discussed.

3.1 Fundamentals of thermal radiation

Thermal radiation is a very important heat transfer mechanism in a packed pebble bed, especially at high temperatures (Zhou *et al.*, 2007; Cheng & Yu, 2013), as concluded from Chapter 2. Therefore it is necessary to have a good understanding of the fundamental principles of radiation heat transfer. The following section addresses the most important principles associated with radiation heat transfer.

3.1.1 Radiative properties and behaviour

Thermal radiation is the energy emitted by a solid body when its temperature is above absolute zero Kelvin (Cengel & Ghajar, 2011). Radiation heat transfer occurs when two solid bodies at different temperatures interact with one another through this emitted energy. Unlike convection and conduction heat transfer mechanisms that require the presence of a temperature gradient in a medium to occur, radiation heat transfer requires no medium and can therefore take place under vacuum conditions (Incorpera *et al.*, 2007).

The amount of radiation energy emitted by a surface depends on a number of variables and as a result different bodies may emit different amounts of energy even if the surfaces are at the same temperature. Therefore it is important to firstly understand the radiation properties of an idealized body, namely a blackbody, to which the properties of real surfaces can be compared

(Cengel & Ghajar, 2011). According to Cengel and Ghajar (2011) a blackbody can be defined as a perfect emitter or absorber of radiation.

For a specified temperature and wavelength no surface can emit more energy than a blackbody. Irrespective of wavelength and direction of radiation a blackbody will absorb all incident radiation. A blackbody is a diffuse emitter, which means although the radiation emitted is a function of wavelength and temperature it is independent of direction. (Incorpera *et al.*, 2007; Cengel & Ghajar, 2011) Figure 3.1 illustrates the difference between the diffuse emission of a blackbody and the non-uniform emission by a real surface.

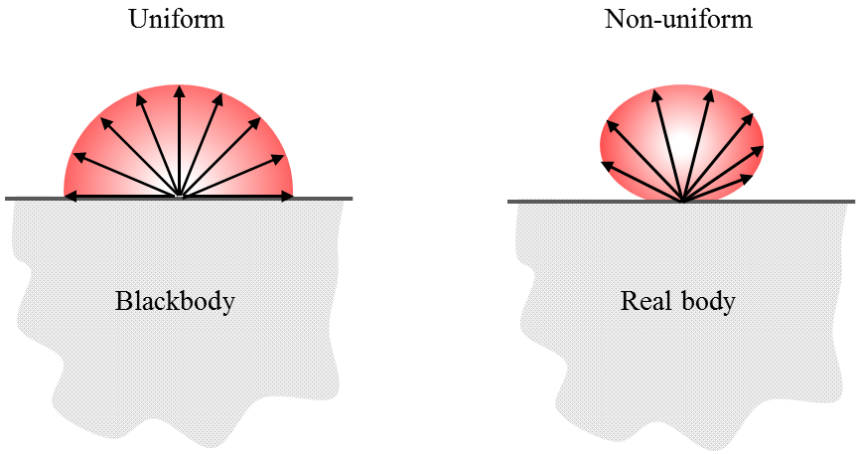

Figure 3.1: Diffuse emission of a blackbody compared to emission by a real surface (Cengel & Ghajar, 2011).

The amount of radiation energy emitted by a blackbody is determined by means of the Stefan-Boltzmann law, shown in Equation (3.1):

$$E_b = \sigma T^4 \tag{3.1}$$

where E_b is the blackbody emissive power, σ the Stefan-Boltzmann constant and T the absolute surface temperature measured in Kelvin.

However, no real surface has exactly the same properties as that of a blackbody. Some surfaces closely approximate a blackbody, but no actual surface can emit more radiation than a blackbody at the same temperature. In practice certain assumptions and approximations are made to simplify the radiation analysis of real surfaces. Firstly the radiation emitted by the interior regions of an opaque or non-transparent solid can never reach the surface of the solid and therefore any incident radiation is absorbed within a few microns from the surface (Cengel & Ghajar, 2011). Consequently radiation is considered to be a surface phenomenon for opaque solids as shown in Figure 3.2.

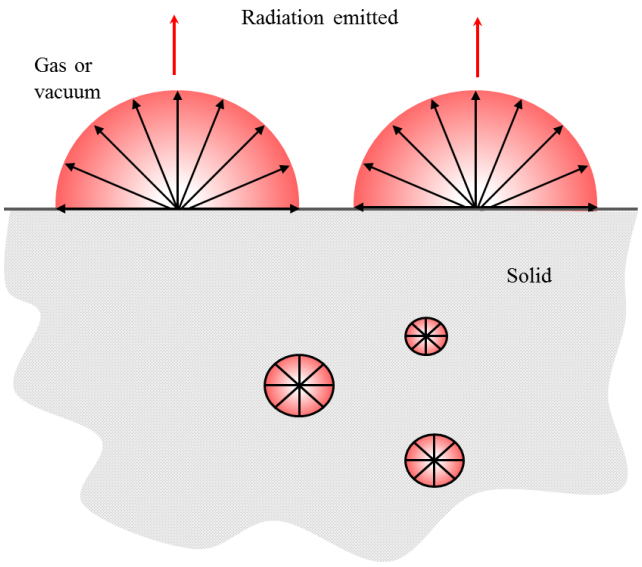

Figure 3.2: Radiation is a surface phenomenon for opaque solids (Cengel & Ghajar, 2011).

The second approximation is the diffuse approximation; although real surfaces do not emit radiation in a perfectly diffuse manner as blackbodies do, they often come close to this behavior. Therefore it is common practice to assume the surfaces to be diffuse emitters when performing a radiation analysis on real surfaces (Cengel & Ghajar, 2011). Thirdly real surfaces are often assumed to be gray during radiation analysis; this means the radiation properties of the surface are independent of wavelength (Incorpera *et al.*, 2007).

As most materials used in practice are opaque materials the radiative properties for surfaces of opaque materials are considered including emissivity, absorptivity, reflectivity and transmissivity. According to Incorpera *et al.* (2007) the emissivity, ε, of a surface is the ratio of the radiation emitted by the surface to the radiation emitted by a blackbody at the same temperature. Thus it is a measure of how closely a real surface approximates a blackbody (Cengel & Ghajar, 2011).

The emissivity of a real surface varies with surface temperature, wavelength and direction of the emitted radiation and is not a constant value. Thus in practice it is more suitable to work with hemispherical properties which are radiation properties averaged over all directions (Cengel & Ghajar, 2011). If a surface is assumed to be diffuse and gray the emissivity of the surface is equal to the average emissivity of the surface.

Figure 3.3 shows that the radiation incident on a surface is partly absorbed, partly reflected and the remaining part is transmitted. Cengel and Ghajar (2011) provide definitions for the radiation properties of a surface; the absorptivity, α, is the fraction of irradiation absorbed by the surface, reflectivity, ρ, is the fraction of irradiation reflected by the surface and lastly transmissivity, τ, is the fraction of irradiation transmitted by the surface. According to the first law of

thermodynamics the sum of the absorbed, reflected and transmitted radiation must be equal to the incident radiation as described in Equation (3.2).

$$\alpha + \rho + \tau = 1 \tag{3.2}$$

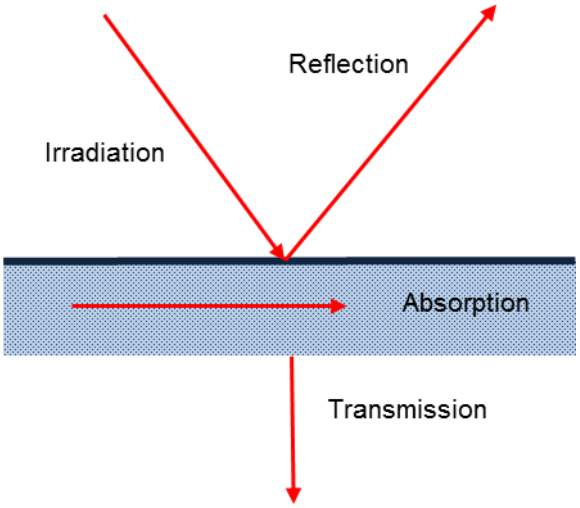

Figure 3.3: Absorption, reflection and transmission of irradiation.

When opaque surfaces are considered the transmissivity value is zero, $\tau = 0$. Kirchhoff's law states that the total average emissivity of a surface at a specific temperature is equal to its total average absorptivity for radiation coming from a blackbody at the same temperature (Cengel & Ghajar, 2011). The use of Kirchhoff's law in radiation analysis makes it possible to determine all three properties of an opaque surface from the knowledge of only one property. In practice this gives acceptable results for most cases; however one should take care when applying this law to cases where there is a significant difference between the surface temperature and the temperature of the source of the incident radiation.

3.1.2 View factors

Radiation heat transfer between surfaces does not only depend on the radiation properties and temperatures of the surfaces, but also depends on the orientation of the surfaces relative to each other. The view factor is a parameter that accounts for the effects of orientation on radiation heat transfer between two surfaces. It is independent of the surface properties and temperature and is purely a geometric quantity (Cengel & Ghajar, 2011).

Incorpera *et al.* (2007) define the view factor, F_{ij}, as the fraction of the radiation leaving surface i that strikes surface j directly. The arbitrarily oriented surfaces A_i and A_j shown in Figure 3.4 is used to develop a general expression for the view factor,

$$F_{ij} = \frac{1}{A_i}\int_{A_i}\int_{A_j}\frac{\cos\theta_i \cos\theta_j}{\pi R^2} dA_i dA_j \tag{3.3}$$

where dA_i and dA_j are elemental areas on these surfaces that are connected by a line of length R. The polar angles θ_i and θ_j are the angles formed between the normal on each surface and the line connecting the centres of the surfaces.

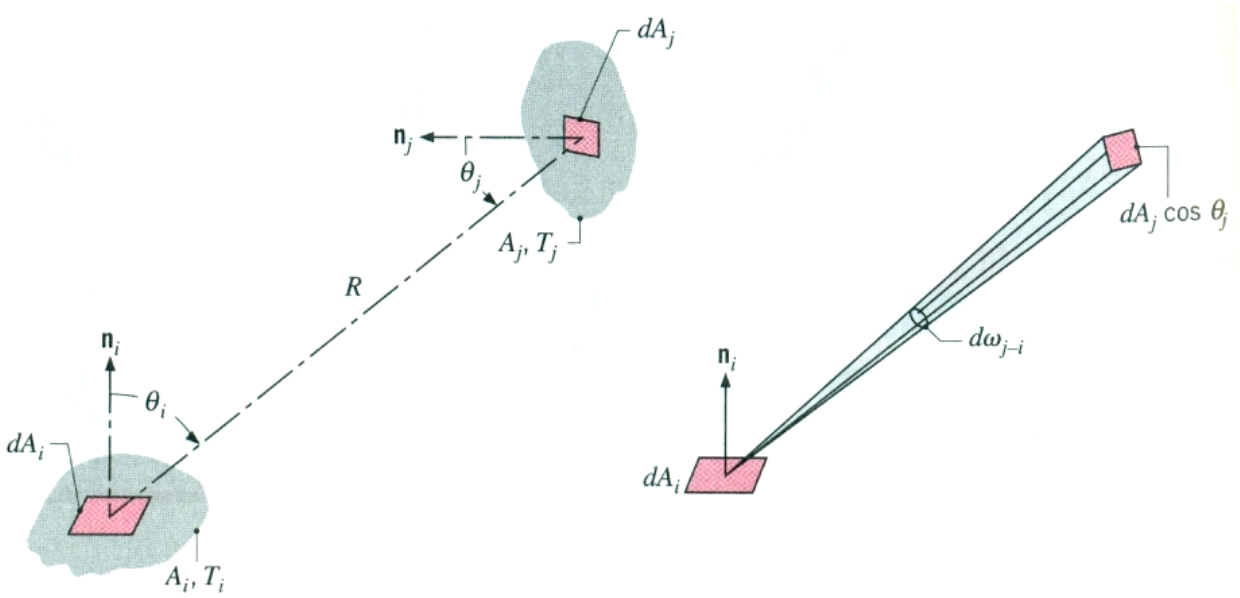

Figure 3.4: Geometry used for the definition of view factors between surfaces (Incorpera *et al.*, 2007).

View factors are very useful in radiation analyses as one can express the fraction of radiation leaving a surface that strikes another surface in terms of the orientation of these two surfaces with respect to one another. However, it is assumed that the surfaces involved in the radiation exchange are isothermal, diffuse emitters and reflectors and are separated by a non-participating medium, which does not absorb, emit or scatter radiation (Cengel & Ghajar, 2011).

In order to simplify the evaluation of view factors between surfaces during radiation analyses fundamental view factor relations can be used. As a result all of the view factors do not have to be evaluated directly and with a sufficient number of view factors known the remaining view factors can be determined using these relations. The first is the reciprocity relation given in Equation (3.4) which can be used to determine one view factor from the knowledge of another and the areas of the two surfaces under consideration (Incorpera *et al.*, 2007).

$$A_i F_{ij} = A_j F_{ji} \tag{3.4}$$

The second relation to consider is the summation rule. According to Cengel and Ghajar (2011) the summation rule states that the sum of the view factors from surface i of an enclosure to all surfaces of the enclosure must be equal to one. Equation (3.5) shows the mathematical expression of the summation rule:

$$\sum_{j=1}^{N} F_{ij} = 1 \tag{3.5}$$

where *N* is the number of surfaces of the enclosure. The superposition rule is the third relation and according to Cengel and Ghajar (2011) states that the view factor from a surface i to a surface j, which is divided into components, is equal to the sum of the view factors from surface i to the components of surface j.

3.1.3 Radiation exchange between surfaces

In the calculation of the radiation heat transfer between surfaces the total radiation energy flowing from a surface must be considered. A new parameter to quantify the total radiation energy leaving a surface is introduced namely the radiosity. Radiosity, J , is defined as the rate at which radiation leaves a surface as a result of emission and reflection in all directions per unit area of the surface (Incorpera *et al.*, 2007). Figure 3.5 shows an illustration of surface radiosity.

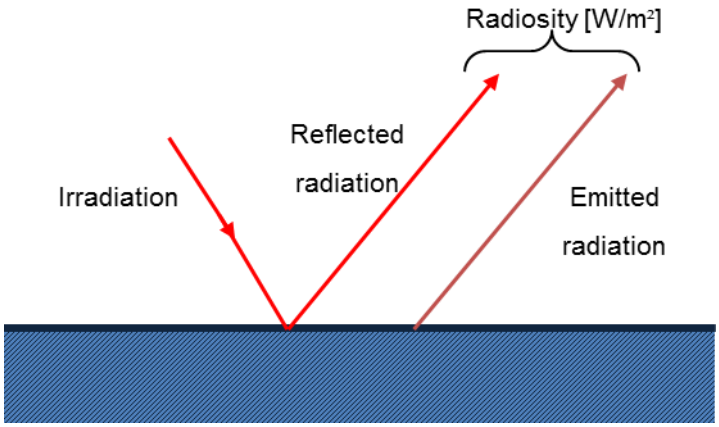

Figure 3.5: Illustration of surface radiosity.

Assumptions are made to simplify the radiation analysis between surfaces of an enclosure. Each of the surfaces of the enclosure is assumed to be isothermal with opaque, diffuse and gray surface behaviour and is characterized by a uniform irradiation and radiosity. The medium inside the enclosure is assumed to be non-participating (Incorpera *et al.*, 2007). Equation (3.6) expresses the net rate of radiation, q_i , that leaves a single surface i in the enclosure,

$$q_i = \frac{E_{bi} - J_i}{\frac{1-\varepsilon_i}{\varepsilon_i A_i}} \tag{3.6}$$

with E_{bi} the blackbody emissive power, J_i the radiosity, ε_i the emissivity and A_i the area of the surface i (Incorpera *et al.*, 2007).

The total rate at which radiation from surface i reaches all the surfaces in the enclosure is given in Equation (3.7):

$$q_i = \sum_{j=1}^{N} \frac{J_i - J_j}{(A_i F_{ij})^{-1}} \tag{3.7}$$

where *N* is the number of surfaces in the enclosure under consideration (Incorpera *et al.*, 2007). According to the law of conservation of energy the net heat transfer from a surface i in an enclosure must be equal to the sum of the net heat transfer from the surface i to each of the *N* surfaces in the enclosure (Cengel & Ghajar, 2011). The value of $(J_i - J_j)$ is the potential difference or the radiation heat transfer between two surfaces and $(A_i F_{ij})^{-1}$ is the space or geometrical resistance to the radiation exchange.

3.2 Experimental data and uncertainty analyses

The errors and uncertainties associated with the results of experimental work must be minimised by improving the experimental techniques used and proving the repeatability of the results. However, a certain margin of error remains when experimental work is done and must be estimated in order to evaluate the validity of the results (Bevington & Robinson, 2003). Experimental results can contain errors due to various sources such as inaccuracies of instrumentation, measurement techniques, limitations of experimental test facilities and the influence of the environment on the system (Uhia *et al.*, 2013). Uncertainty refers to the degree of goodness of the experimental result and the most accurate approximation of the experimental error.

The methodologies proposed by Van Antwerpen (2009) and Van Antwerpen *et al.* (2010b) for the data and uncertainty analysis of the HTTU experimental results are presented in the next section. A function describing the radial heat flux distribution through the packed pebble bed was derived and a temperature gradient was determined from the set of temperature measurements through the packed pebble bed. The heat flux function and the temperature gradient were required to determine the effective thermal conductivity results with its associated uncertainties. It is important to note that the HTTU test section contained an annular packed

bed, thus a function for the heat flux distribution in the radial direction was determined. The NWETCTF test section used for the experimental work in the current study is not cylindrical or annular and therefore the axial heat flux distribution function must be considered.

3.2.1 Radial heat flux distribution function

For the HTTU test facility the radial heat flux distribution through the packed pebble bed was derived as a function of radial position due to the axial heat losses through the top and bottom insulation of the test section (Van Antwerpen, 2009). Van Antwerpen (2009) predicted the values of the axial heat losses by discretising the top and bottom insulation into forty equally spaced radial increments. An approximate heat loss value for each of the increments was then calculated using Equation (3.8),

$$Q_{i,loss} = \frac{k_{ins} A_i}{L_{ins}} (T_{bed} - T_{env}) \tag{3.8}$$

with k_{ins} the thermal conductivity of the insulation material, A_i the conduction area for each increment, L_{ins} the thickness of the insulation material, T_{bed} the bed temperature at the top and bottom level of the test section and T_{env} the environmental temperature.

In order to obtain the bed temperatures at the top and bottom level of the HTTU test section Van Antwerpen (2009) fitted a curve through the measured temperature values for level A and E as shown in Figure 2.11. The bed temperature at the middle of each increment could then be obtained using the function of the fitted curve and the corresponding radial position.

The radial heat flux at a specific radial position in the packed pebble bed was estimated using Equation (3.9).

$$Q_{bed}(r_j) = Q_{wj} + Q_{totLoss} - (\sum_{i=1}^{j-1} Q_{i,loss}(r_i) + Q_{i,loss}(r_j)) \tag{3.9}$$

At a specific radial position r_j the radial heat flux Q_{bed} is the sum of the heat extracted via the water jacket, Q_{wj}, and the total heat loss, $Q_{totLoss}$, minus the heat losses for the increments up to the radial position under consideration.

The uncertainty associated with the radial heat flux is dependent on the uncertainty of the heat extracted through the water jacket and the uncertainty of the total heat loss through the top and bottom insulation as shown in Equation (3.10):

$$u(Q_{bed}) = \sqrt{u(Q_{wj})^2 + u(Q_{totLoss})^2} \tag{3.10}$$

3.2.2 Derivation of temperature gradient function

A method was required to determine the local temperature gradient of the HTTU experimental temperature distribution, without the local temperature variations resulting in large uncertainties in the temperature gradient. Van Antwerpen *et al.* (2010b) proposed the least-squares fitting of a polynomial to the set of temperature data and by differentiating the polynomial the temperature gradient was determined.

A short description of the derivation of the polynomial curve fit is given in the following section. For a more detailed derivation consult Van Antwerpen *et al.* (2010b). The power-series polynomial, $T(x)$, shown in Equation (3.11) is fitted to a set of experimental data, (x_i, T_i)

$$\begin{aligned} T(x) &= a_0 x^0 + a_1 x^1 + a_2 x^2 + \ldots + a_m x^m \\ \therefore T(x) &= \sum_{k=0}^{m} a_k x^k \end{aligned} \tag{3.11}$$

where a_0 to a_m are the coefficients of the polynomial and *m* is the order of the polynomial.

Define the function $f_k(x)$ as $f_k(x) = x^k$ and rewrite Equation (3.11) as:

$$T(x) = \sum_{k=0}^{m} a_k f_k(x) \tag{3.12}$$

The coefficients of the polynomial are determined from the solution of the system of equations shown in Equation (3.13).

$$\bar{\beta} = \alpha \bar{a} \tag{3.13}$$

For a data set with *N* data points $\bar{\beta}$ and α are defined as

$$\beta_k = \sum_i^N T_i x_i^k \tag{3.14}$$

and

$$\alpha_{lk} = \sum_i^N x_i^l x_i^k \tag{3.15}$$

Let ε be the inverse matrix of α then for the polynomial the fitted function is given in Equation (3.16).

$$\mathrm{T}(x) = \bar{\beta}^T \varepsilon^T \bar{f}$$

$$\therefore T(x) = \left[\beta_0, \beta_1, \beta_2, \cdots, \beta_m\right] \begin{pmatrix} \varepsilon_{00} \cdots \varepsilon_{0m} \\ \vdots \\ \varepsilon_{m0} \cdots \varepsilon_{mm} \end{pmatrix} \begin{bmatrix} x^0 \\ x^1 \\ x^2 \\ \vdots \\ x^m \end{bmatrix} \tag{3.16}$$

The slope of the regression function is determined by differentiating Equation (3.16).

$$b(x) = \frac{dT(x)}{dx} = \left[\beta_0, \beta_1, \beta_2, \cdots, \beta_m\right] \begin{pmatrix} \varepsilon_{00} \cdots \varepsilon_{0m} \\ \vdots \\ \varepsilon_{m0} \cdots \varepsilon_{mm} \end{pmatrix} \begin{bmatrix} 0 \\ 1 \\ 2x \\ 3x^2 \\ \vdots \\ mx^{m-1} \end{bmatrix} \tag{3.17}$$

3.2.3 Uncertainty of temperature gradient function

The uncertainty of the regression function must be calculated. The pointwise variance in the fit at a point *x*, is described by the function $u^2(x)$ shown in Equation (3.18).

$$u^2(x) = \left(\frac{\partial T(x)}{\partial T_1}\right)^2 u_1^2 + \left(\frac{\partial T(x)}{\partial T_2}\right)^2 u_2^2 + \cdots + \left(\frac{\partial T(x)}{\partial T_N}\right)^2 u_N^2$$

$$u^2(x) = \sum_{i=1}^{N} \left(\frac{\partial T(x)}{\partial T_i}\right)^2 u_i^2 \tag{3.18}$$

Equation (3.14) is substituted into Equation (3.16) in order to determine the derivative shown in Equation (3.19).

$$\frac{\partial T(x)}{\partial T_i} = \left[1, x_i, \mathrm{x}_i^2, \cdots, x_i^m\right] \begin{pmatrix} \varepsilon_{00} \cdots \varepsilon_{0m} \\ \vdots \\ \varepsilon_{m0} \cdots \varepsilon_{mm} \end{pmatrix} \begin{bmatrix} x^0 \\ x \\ x^2 \\ \vdots \\ x^m \end{bmatrix} \tag{3.19}$$

$$\therefore \frac{\partial T(x)}{\partial T_i} = \sum_{k=0}^{m} (x_i^k \sum_{j=0}^{m} \varepsilon_{kj} x^j)$$

Substitute Equation (3.19) into Equation (3.18):

$$u^2(x) = \sum_{i=1}^{N}\left(\sum_{k=0}^{m}\left(x_i^k \sum_{j=0}^{m}\varepsilon_{kj}x^j\right)\right)^2 u_i^2 \tag{3.20}$$

The data point uncertainty, u_i^2, is the sum of the measurement uncertainty and the scatter uncertainty.

$$u_i^2 = u_{measurement,i}^2 + u_{scatter,i}^2 \tag{3.21}$$

The measurement uncertainty includes the statistical variance and the instrument and drift uncertainty.

$$u_{measurement,i}^2 = u_{instrument,i}^2 + \frac{\sum_{i=1}^{N}(T_i - \overline{T})^2}{N-1} + u_{drift,i}^2 \tag{3.22}$$

Initially Van Antwerpen *et al.* (2010b) considered determining the uncertainty in the calculated temperature gradient using a perturbation analysis, but it would have required a significant programming effort with a large margin for error. Therefore analytical methods for the uncertainty calculation were found to be easier and more practical to implement. A detailed derivation of an uncertainty equation for the slope of the polynomial is given by Van Antwerpen *et al.* (2010b). The uncertainty in the slope of the regression function, $b(x)$, is given in Equation (3.23).

$$\sigma^2(b(x)) = \sum_{i=1}^{N}\left(\frac{\partial b(x)}{\partial T_i}\right)^2 \sigma_i^2 \tag{3.23}$$

The derivative shown in Equation (3.23) was calculated as:

$$\frac{\partial \mathrm{b}(x)}{\partial T_i} = \left[1, \mathrm{x}_i, \mathrm{x}_i^2, \cdots, \mathrm{x}_i^m\right]\begin{pmatrix}\varepsilon_{00}\cdots\varepsilon_{0m}\\ \vdots \\ \varepsilon_{m0}\cdots\varepsilon_{mm}\end{pmatrix}\begin{bmatrix}0\\1\\2x\\3x^2\\\vdots\\mx^{m-1}\end{bmatrix} \tag{3.24}$$

$$\therefore \frac{\partial b(x)}{\partial T_i} = \sum_{k=0}^{m}\left(x_i^k \sum_{j=0}^{m}\varepsilon_{kj} j x^{j-1}\right)$$

Substitute Equation (3.24) into Equation (3.23) to obtain the uncertainty in the slope of the fitted curve:

$$\sigma^2(b(x)) = \sum_{i=1}^{N}\left(\sum_{k=0}^{m}\left(x_i^k \sum_{j=0}^{m}\varepsilon_{kj} j x^{j-1}\right)\right)^2 \sigma_i^2 \tag{3.25}$$

Other methods for the calculation of the temperature gradient were also considered by Van Antwerpen *et al.* (2010b). The point-by-point finite difference method did not work due to the combination of varying space between measurement points and measurement uncertainty. Piecewise least-squares fitting of straight lines to the data presented better results than that obtained by the point-by-point difference method as it has a better capability of handling scattered data. However, the uncertainty results were still much bigger than that given by the polynomial method.

3.2.4 Uncertainty of effective thermal conductivity

Van Antwerpen (2009) used Equation (3.26) to determine the effective thermal conductivity values once the heat flux distribution and temperature gradient were known as functions of the radial position in the packed pebble bed.

$$k_{eff} = -\frac{Q_{bed}}{A\,dT/dr} \tag{3.26}$$

The uncertainty associated with the effective thermal conductivity values was calculated using Equation (3.27):

$$u(k_{eff}) = \sqrt{\left[\frac{\partial(k_{eff})}{\partial Q_{bed}} \cdot u(Q_{bed})\right]^2 + \left[\frac{\partial(k_{eff})}{\partial(dT/dr)} \cdot u(dT/dr)\right]^2} \tag{3.27}$$

with the partial derivatives shown in Equations (3.28) and (3.29) respectively.

$$\frac{\partial(k_{eff})}{\partial Q_{bed}} = \frac{-1}{A\,dT/dr} \tag{3.28}$$

$$\frac{\partial(k_{eff})}{\partial(dT/dr)} = \frac{Q_{bed}}{A(dT/dr)^2} \tag{3.29}$$

A detailed description of the method used to obtain the uncertainty associated with the effective thermal conductivity values is provided by Van Antwerpen (2009).

3.3 Summary

This chapter provided the basic principles required for a thorough understanding of the radiation heat transfer mechanism. The reader was introduced to the concept of view factors and the role of view factors in the calculation of radiation heat transfer between surfaces.

The theoretical background of the methods used for the calculation of the heat transfer distribution as well as the temperature distribution and temperature gradient functions for the experimental results of the HTTU test facility, with its associated uncertainties, was discussed. The derivation of the effective thermal conductivity and its uncertainty with the use of the heat transfer distribution and temperature gradient function was presented.

The next chapter uses the principles and methods described in this chapter to develop the methodology used for the work done in the current investigation.

4

Methodology

In this chapter the reader is introduced to the proposed methodology of the study for the calculation of the effective thermal conductivity in the near-wall region of a packed pebble bed using experimental and numerical methods. Firstly an initial outline of the proposed methodology and its main steps are given, followed by detailed descriptions of the methods used for each step to obtain the results and reach the objectives of the current study.

A description of the NWETCTF test facility and the procedures followed during the preparation of the experimental setup and operation of the test facility are discussed. The calculation of the effective thermal conductivity from the NWETCTF experimental results is given and the methods used for the data and uncertainty analyses are described.

The steps taken during the setup of the DEM simulation for the generation of the numerically packed pebble bed as well as the preparation of the solid model with contact point treatment for the CFD simulations are discussed. The detail of the CFD simulation setup and the processing of the numerical results are provided, including the method used for the separation of the conduction and radiation components of the effective thermal conductivity results.

4.1 Outline of methodology

An initial outline of the main steps of the proposed methodology is shown in Figure 4.1. This initial outline was used as a starting point for the development of the proposed methodology. The methodology entails the use of experimental as well as numerical methods.

Firstly experimental data had to be gathered for the heat transfer through a packed pebble bed by using the NWETCTF test facility. From the experimental results the effective thermal conductivity for the packed pebble bed had to be determined. A suitable CFD model had to be

set up to simulate the NWETCTF test conditions and the heat transfer through the packed pebble bed. In the fourth step the results obtained with the CFD model had to be compared with the experimental results and the CFD model had to be calibrated. The effective thermal conductivity of the packed pebble bed for the CFD simulations had to be determined.

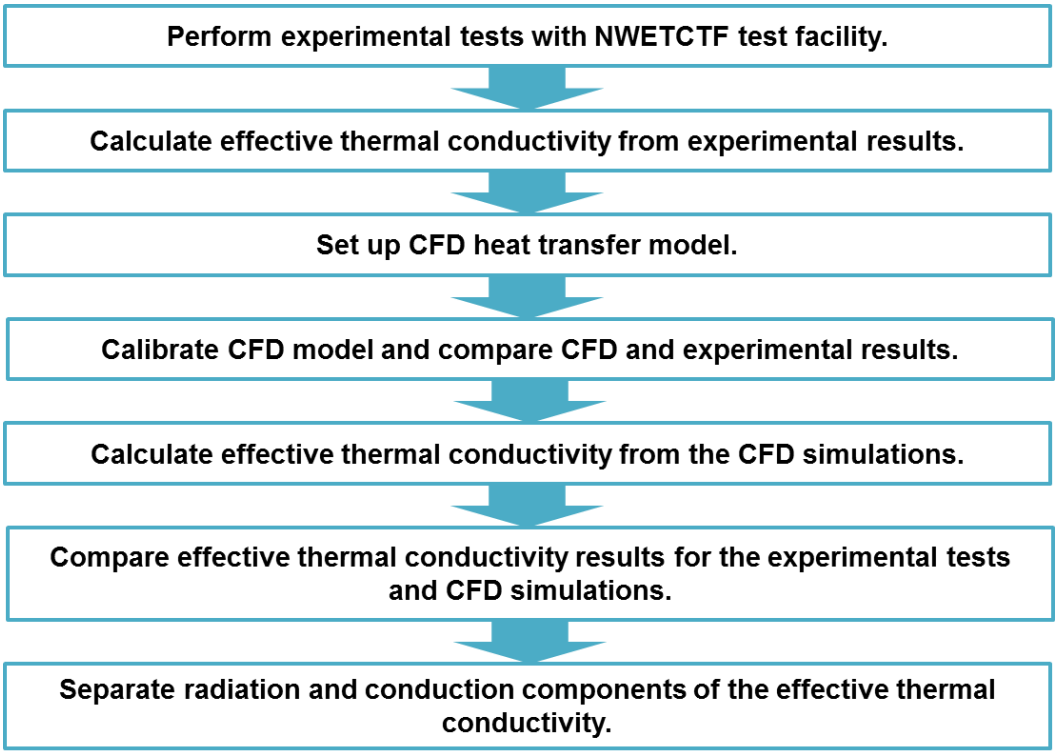

Figure 4.1: Initial outline of the proposed methodology and its main steps.

Finally the effective thermal conductivity of the numerical simulations had to be compared with the experimental effective thermal conductivity and the separation of the radiation and conduction components had to be completed. The detail of the methods used for the development of the final methodology and the detail of each of the steps of the methodology are described in the next sections of this chapter.

4.2 Experimental work

Experimental data describing the effective thermal conductivity and specifically the radiation heat transfer through a packed bed of spheres is important for the validation and verification of new and existing effective thermal conductivity models. From the literature review conducted in Chapter 2 it was concluded that detailed experimental investigations of the heat transfer through a packed bed of spheres are required.

In order to contribute towards investigations for the PBR safety case focus must be placed on the heat transfer at very high temperatures in the near-wall regions of a packed pebble bed, specifically the radiation heat transfer component. The reasons being that (1) the thermal radiation's contribution to the overall heat transfer increases significantly at higher temperatures, as discussed in section 2.2.1, and (2) the near-wall region forms part of the critical path for decay heat removal during upset conditions in a PBR, as stated in section 1.1.

As mentioned in section 2.4 most of the experimental work reported in the available literature to determine the effective thermal conductivity through a packed bed of spheres are case specific and the results cannot necessarily be compared with simulation models. A large number of existing studies focus specifically on the heat transfer at lower temperatures using smaller sphere sizes. None of the experimental test facilities discussed provide a detailed investigation of the heat transfer in the near-wall region of a packed pebble bed.

The experimental work conducted during this study forms an integral part of the investigation. The newly constructed Near-wall Effect Thermal Conductivity Test Facility (NWETCTF) at the North-West University was used to conduct all the experimental tests necessary for this study. The following section provides a description of the NWETCTF, the role of the student in the commissioning process of the system as well as a description of the experimental tests performed to gather experimental data.

4.2.1 NWETCTF test section layout

The tests conducted with the use of the HTTU test facility described in section 2.4.4 were focused on gathering experimental data that described the heat transfer phenomena through a large scale representative section of a PBR. However, it did not allow for detailed investigations of specific phenomena in the near-wall region of the packed pebbled bed. This led to the development of the smaller scale Near-wall Effect Thermal Conductivity Test Facility.

The purpose of the NWETCTF is to perform detailed investigations of the conduction and radiation heat transfer phenomena in the near-wall region of a packed pebble bed at temperatures of up to 1600°C. The experimental results obtained from the NWETCTF can be used to validate models for the effective thermal conductivity in the near-wall region of a packed bed of spheres by comparing the results of the models to the experimental data.

A schematic representation of a vertical cut through the NWETCTF test section is shown in Figure 4.2. The test section has a cubical configuration with a side length of 0.42 m which is equivalent to seven sphere diameters. From the definition of the near-wall region in section 2.1.1, this particular size was chosen in the design of the test section to ensure the inclusion of

the wall effects in the packing structure of the packed bed. For the two test cases considered in the study the test section consisted of 332 and 334 machined graphite spheres, with a diameter of 60 mm, respectively. The spheres were randomly packed inside the cubical configuration of the test section between the inner graphite radiator and the outer graphite reflector. The structured packing of the spheres shown in Figure 4.2 is only for illustration purposes. The method used for the packing of the pebble bed is described in more detail in section 4.2.3.

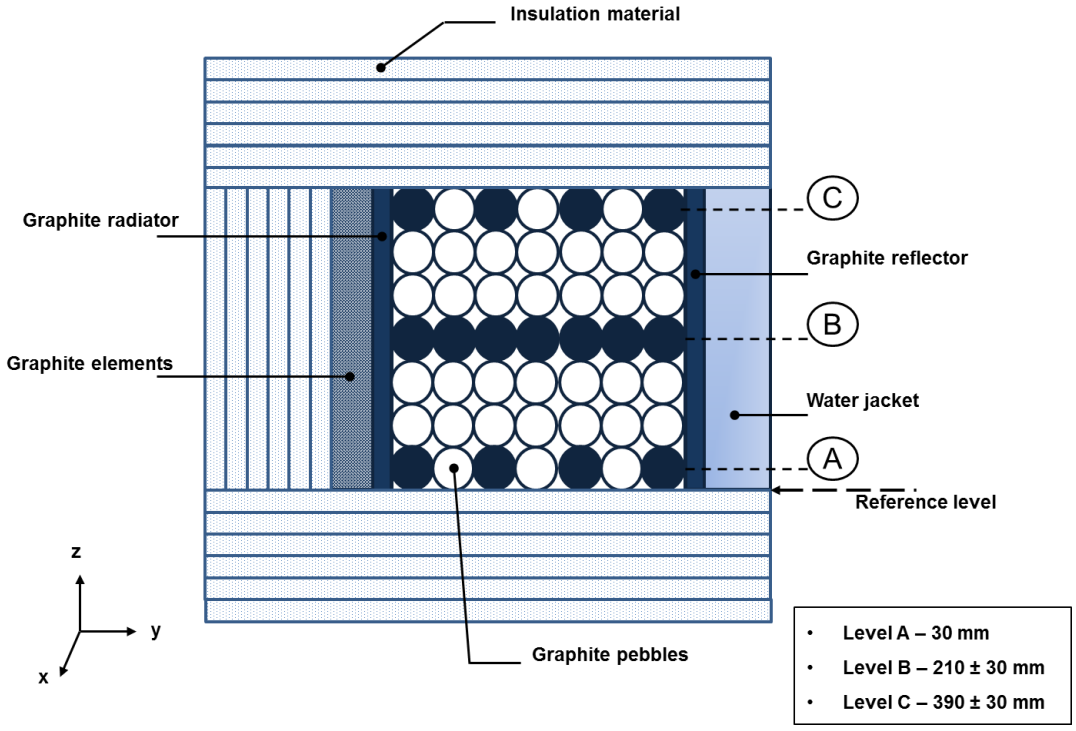

Figure 4.2: Schematic representation of a vertical cut through the NWETCTF test section.

Figure 4.3 shows an exploded view of a solid model of the NWETCTF test section with its various components. As can be seen in Figure 4.3 it consists of the packed bed area, the two graphite reflectors, the graphite heater elements, the water jacket, the element coolers and the surrounding insulation material.

Both the inner and outer reflector has a thickness of 0.02 m and a side length of 0.43 m. A set of graphite heater elements situated next to the inner reflector is used to heat it up and it is referred to as the heated wall. The water jacket situated next to the outer reflector extracts heat from the system thus cooling down the outer wall. As a result a temperature gradient in the y-direction is induced through the packed bed of spheres between the heated and cooled wall. The design of the heater elements and the water jacket heat exchanger ensures that a near-uniform temperature is obtained at the inner and outer walls.

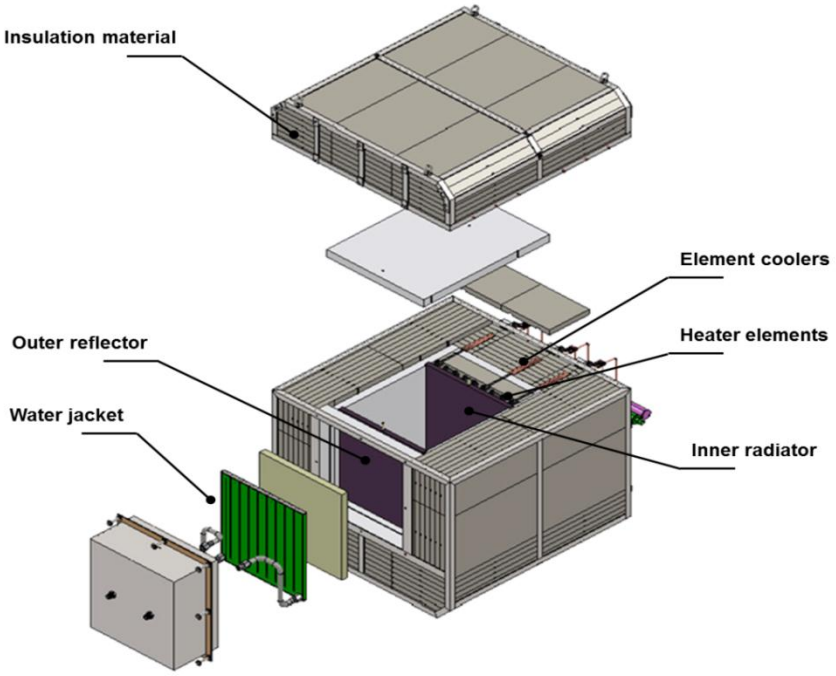

Figure 4.3: An exploded view of a solid model of the NWETCTF test section.

Insulation material covers the entire test section in an effort to minimize the heat losses in the x- and z-directions. One layer of Zircar type SALI-2 followed by five layers of Zircar type AL-45 insulation material are used with a single layer thickness of 0.038 m. The two different types of insulation material are used to decrease the costs of the materials. With minimal heat losses one can assume that a one-dimensional heat flow is imposed through the packed bed. The insulation material also lowers the temperatures near the vessel wall to a value below its maximum allowable temperature to ensure the integrity of the steel is not compromised.

The element coolers are small copper heat exchangers situated around the heater elements. During operation and testing of the system the element coolers ensures that desirable temperatures are maintained at the electrical connections of the elements for the various power inputs. A photograph of a top view of the test section is shown in Figure 4.4 with a close-up of the element coolers.

Thermocouples were placed at three different axial levels inside the randomly packed bed. The dark coloured spheres shown in Figure 4.2 indicate the three levels of instrumented spheres. For levels A and C there were two graphite spheres with thermocouples placed at the centre of each sphere. As level B represents the area of primary interest for the heat transfer through the packed bed, 12 spheres instrumented with thermocouples were spaced throughout the bed at this level. Two thermocouples are embedded in the inner graphite radiator and one in the outer

graphite reflector. The tolerance for the position of the spheres at each level was specified to compensate for the randomness of the packed bed.

Figure 4.4: Photograph of a top view of the NWETCTF test section and the element coolers.

In order to determine the amount of heat extracted through the water jacket the water inlet and outlet temperatures are measured with PT100 Resistance Thermometer Devices (RTD) with instrument uncertainties of ±0.2°C. The water flow rate through the water jacket as well as the element coolers is measured with magnetic-inductive flow meters with instrument uncertainties of ±0.5 l/min. The method used for the calculation of the heat transfer through the packed bed is discussed in detail in section 4.3.3.

4.2.2 NWETCTF test facility

A schematic representation of the NWETCTF plant layout is shown in Figure 4.5. The test section as well as all the internals is enclosed inside the NWETCTF pressure vessel. Connections for the process pipes of the various auxiliary systems are positioned on the vessel. The vessel has a removable side dome which provides access into the vessel. Figure 4.6 shows a solid model of the NWETCTF vessel and its test section. Inside the vessel the test section rests on a steel rail and a steel support bench is used to slide the test section out of the vessel in order to gain access to the packed bed during maintenance. The solid model in Figure 4.6

displays the two representations where the test section is positioned inside the vessel and the case where the test section is removed from the vessel and is resting on the support bench.

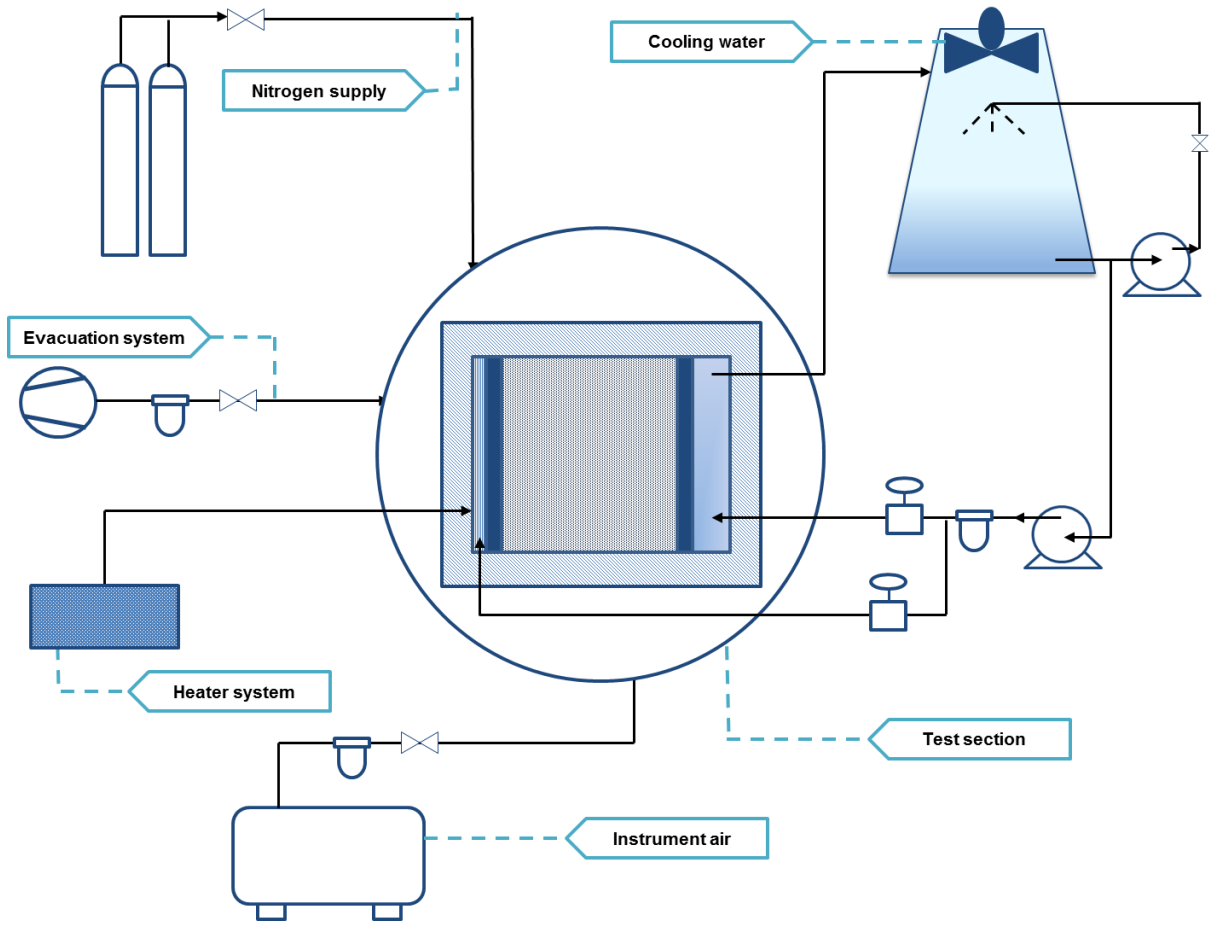

Figure 4.5: Schematic representation of the NWETCTF plant layout.

The Nitrogen supply system and the evacuation system are used to obtain a near-vacuum nitrogen environment inside the NWETCTF vessel during operation. The electrical power input provided by the heater system is controlled by three temperature measurements on the inner radiator to obtain a constant surface temperature as specified by the operator. Cooling water is supplied to both the water jacket heat exchanger and the element coolers from the cooling tower in order to remove heat from the pebble bed and maintain an acceptable temperature at the electrical connections of the elements. Dry air is supplied to the control valves of the NWETCTF via the instrument air system. Prinsloo (2014) provides a more detailed description of the various processes and their functions.

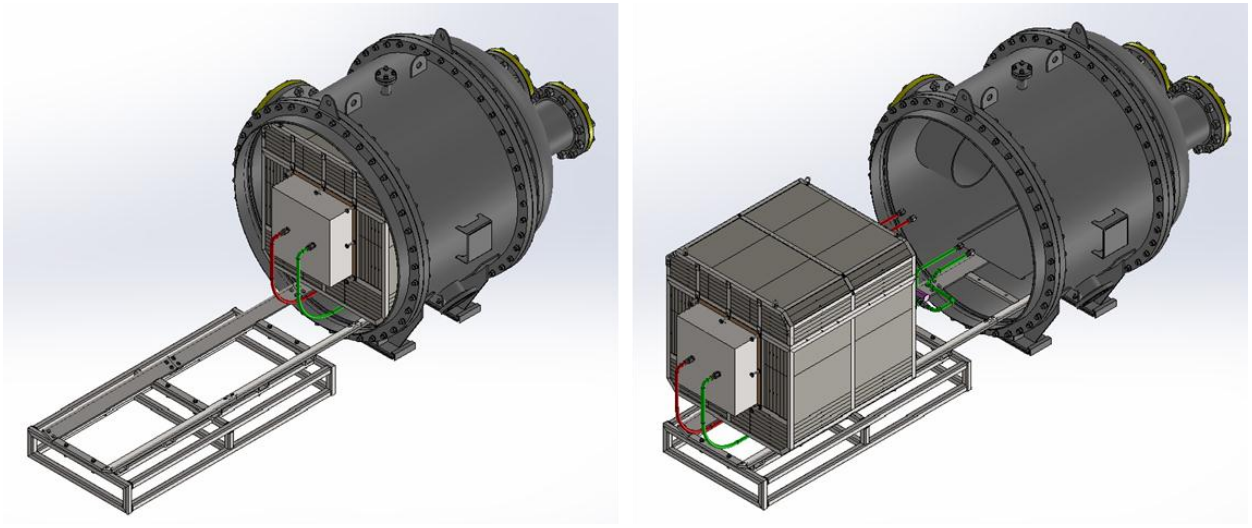

Figure 4.6: Solid model of the NWETCTF vessel and test section.

The existing auxiliary systems of the HTTU were utilized in the construction of the NWETCTF. Changes were made to the various systems to meet the requirements and the specifications of the NWETCTF. A number of the control and instrumentation hardware of the HTTU plant were also used in the construction of the NWETCTF. The graphite pebbles used for the NWETCTF were also used in the HTTU test facility. Photographs of the NWETCTF vessel and test section is shown in Figure 4.7.

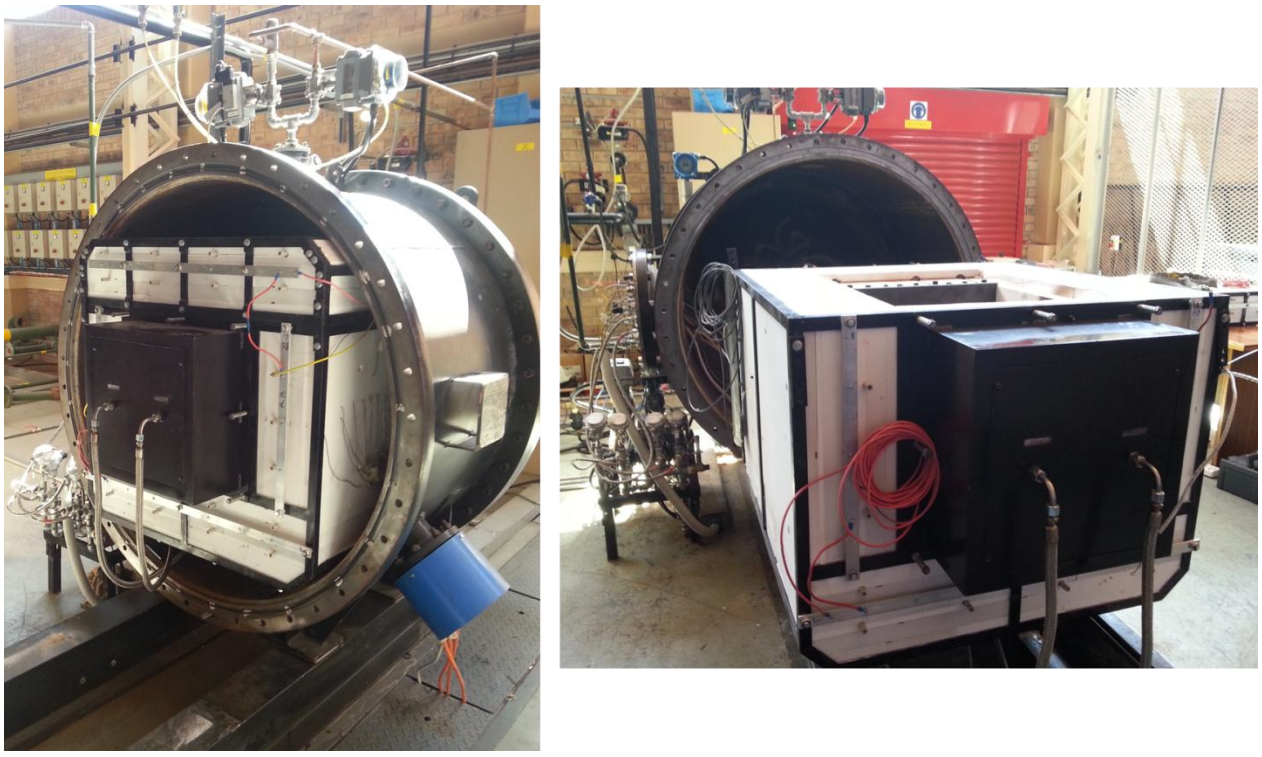

Figure 4.7: Photographs of the NWETCTF vessel and test section.

The control system of the NWETCTF includes a graphical user interface termed the SCADA (Supervisory Control and Data Acquisition) which provides the operator with a graphic process overview of the system. The SCADA makes use of a Piping and Instrumentation Diagram approach to mimic the system and provides the operator with information regarding the process control, variable trends, trips and alarms as well as the various operational modes of the NWETCTF (Prinsloo, 2014). Thus the SCADA provides the operator with the necessary information to ensure the safe and efficient operation of the system.

In order to ensure the safety of the operators as well as the protection of the system the NWETCTF had two safety systems that are separate from the main control system. The first was the Safety Instrumented System (SIS) that was designed to detect high-risk and possibly unsafe conditions during operation and act on these conditions by forcing the system into a failsafe mode. The second was the Emergency Shutdown System (ESS) that can be used by the operator to shut down the system in case of an emergency.

4.2.3 Packing of experimental bed

A photograph of a top view of the experimental packed bed of spheres can be seen in Figure 4.8 (a). The packing of the graphite spheres in the experimental test section was done by hand. In order to obtain a random packing structure approximately ten spheres were randomly thrown into the test section at a time. Once the spheres settled into position the process was repeated until the level at which the thermocouples must be placed was reached.

(a) (b)

Figure 4.8: Photographs of a top view of the experimental packed bed of spheres: (a) fully packed bed and (b) half packed bed with thermocouple wires.

Another approach to obtain a random packing would be to fill a container with spheres and drop the spheres from the smaller container into the test section. However, since the graphite material of the heater elements are extremely brittle any sort of impact on the inner radiator could result in the damage to the heater elements.

The thermocouple wires were threaded through the insulation side walls of the test section at the various levels. The thermocouple wires threaded to the middle of the packed bed at level B can be seen in Figure 4.8 (b). Two types of thermocouples were used for the temperature measurements in order to minimize the cost associated with the thermocouples. The packed bed was divided into two regions in the y-direction. The first region was the area nearest to the heated wall and the second region was the area nearest to the cooled wall. For the first region type B Platinum-Rhodium thermocouples were used with a maximum operating temperature of 1750°C and an instrument uncertainty of ±5°C. Type K Inconel thermocouples that can be operated up to temperatures of 1350°C with an instrument uncertainty of ±3°C were used for the second region.

A small hole with a depth of 0.03 m was drilled into the graphite spheres that were instrumented with the thermocouples. Figure 4.9 shows a photograph of a graphite sphere with the drilled hole. The diameter of the drilled holes is approximately 1 mm for both the type B and type K thermocouples to ensure a tight fit once the thermocouple wire was inserted into the sphere. The thermocouple wires were threaded through the packed bed and inserted into the various spheres taking care to minimize the disruption to the packing structure of the packed bed.

Figure 4.9: Graphite sphere with drilled hole for thermocouple wire insertion.

Approximate measurements for the positions of the instrumented spheres were taken. The coordinates for the positions of the instrumented spheres of the packed beds for the two

experimental tests can be found in Table A.1. After the position measurements were taken for the level of the packed bed it was filled with spheres up to the next level until the test section was fully packed with graphite spheres.

The method used for the packing of the experimental pebble bed was not ideal as it created a wall effect on all the sides of the test section, thus wall regions existed next to the heated and cooled wall as well as next to the insulation walls. Ideally a packed bed of spheres with only one wall and near-wall region would be more applicable for a study of the heat transfer in this region. To obtain such an ideally packed bed one would want to create an experimentally packed bed similar to a section cut out of a bigger packed bed as shown in Figure 4.10.

Realistically to create such a packed bed some of the graphite spheres would have to be cut into different sizes and inserted next to the cooled wall and the insulation walls to eliminate the wall effect in these areas. One approach would be to create a numerically packed pebble bed, take a section cut the size of the NWETCTF test section from the numerically packed bed and extract the coordinates of each of the spheres. An attempt can then be made to replicate the numerically packed bed during the packing of the test section.

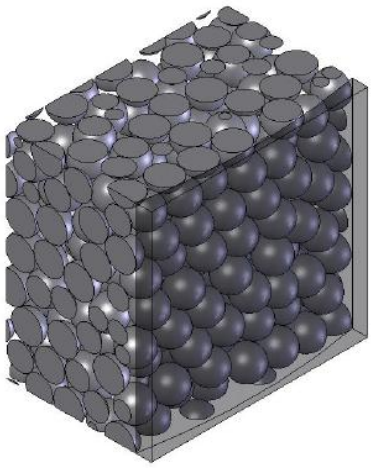

Figure 4.10: Section cut of packed pebble bed with a single near-wall region (Pitso, 2011).

Although this approach might seem simple the task of positioning the spheres at the exact positions as well as cutting the spheres into the different shapes and sizes might prove to be daunting. Another approach is to perform the experimental tests with a packed pebble bed that has more than one wall effect as was done in the current study. The CFD results can then be compared to the experimental results and the CFD model can be calibrated. Once the CFD model has been calibrated the heat transfer can easily be investigated for a packed pebble bed with only one wall region.

For the current study the main focus is the development of a methodology that can be used to obtain experimental data for the heat transfer in the near-wall region. The second approach for the packing of the experimental bed was used in the study. Although having more than one wall effect was not ideal it was sufficient for the development of the methodology and the objectives of the current study.

4.2.4 Commissioning of the NWETCTF

The NWETCTF is a newly constructed test facility and therefore various problems were bound to present itself during first time operation of the system. An important part of the current study was the commissioning of the experimental system after it was handed over by the contractors responsible for building it. This included the identification of all the "teething" problems and formulating and implementing the necessary solutions and/or design improvements. Thus future researchers will be able to spend their time more efficiently to conduct a large number of experimental tests whilst less time will be spent on fault tracing and the improvement of the system.

The process of ensuring the system was functioning properly was necessary to obtain the first set of experimental results and prove that the system can be used to investigate the heat transfer phenomena in the near-wall region of a packed pebble bed. Thus it forms an essential part of one of the objectives of this study which is to provide a method that can be used to obtain experimental data at high temperatures.

Given this, the candidate was responsible for getting the NWETCTF system up and running and for solving the different problems identified during operation. The first experimental tests also verified the applicability of the methodology used to obtain the experimental data showing that it can be applied in future studies to obtain experimental data at higher temperatures. The candidate was involved in the cold commissioning phase of the system in order to become familiar with the plant layout and the hardware of the system. The contractors also introduced the candidate to the NWETCTF control system and how to use the system during operation.

Another one of the candidate’s responsibilities was the training of other operators. The system was handed over for first time operation by the contractors in April 2014. Various problems were identified and solved before the system was in a good working condition and the first experimental test was conducted. A detailed description of the commissioning process and the problems experienced as well as the solutions implemented are given in Annexure A.2.

4.2.5 Description of experimental tests

Prior to conducting any experimental tests using the NWETCTF a bake-out cycle must first be completed. Insulation material similar to that used in the HTTU plant was used in the NWETCTF. As the insulation material is highly hygroscopic any moisture absorbed by the insulation from the atmosphere at lower temperatures will bake-out at higher temperatures (Rousseau, 2008). This will result in moisture being released into the vessel during testing.

The moisture subsequently reacts with the graphite components in the test section leading to two problems. Firstly the reaction will systematically degrade the graphite components and secondly both Hydrogen and Carbon Monoxide is formed during the reaction which are flammable gasses for certain concentration levels (Rousseau, 2008). In order to ensure the prolonged life of the test facility and its components as well as the safe operation of the plant the moisture must be removed beforehand until an acceptably low moisture concentration level is reached.

Therefore, before the start of each experimental test the insulation surrounding the packed bed was subjected to a bake-out sequence. During the bake-out sequence the insulation material was heated up uniformly to 300°C using three small electrical heater units with elements placed throughout the insulation material at evenly distributed positions. As the moisture was released over time it was removed from the vessel by maintaining a near-vacuum environment inside the vessel and continuously flushing the vessel with Nitrogen gas. Through the use of a bake-out model it was determined that a time period of five days was sufficient to complete the bake-out sequence and reach an acceptable moisture concentration level (Van der Walt, 2014). However, currently there is no Relative Humidity meter installed in the NWETCTF to measure the moisture content in the vessel during operation. For future tests conducted with the NWETCTF at higher temperatures it will be beneficial to install a Relative Humidity as it might become a critical instrument when operating at 1600°C.

The test schedule that was followed for the duration of one experimental test conducted with the NWETCTF is presented in the schematic shown in Figure 4.11. The duration of a single experimental test was approximately nine days including the five day time period required to complete the necessary bake-out sequence. In order to remove the excess air from the vessel before commencing with the bake-out sequence three Nitrogen purge cycles were completed at the beginning of each test. During a purge cycle the vessel was evacuated to a pressure of 10 kPa and pressurised with Nitrogen to 86 kPa, thus removing the air and replacing it with Nitrogen.

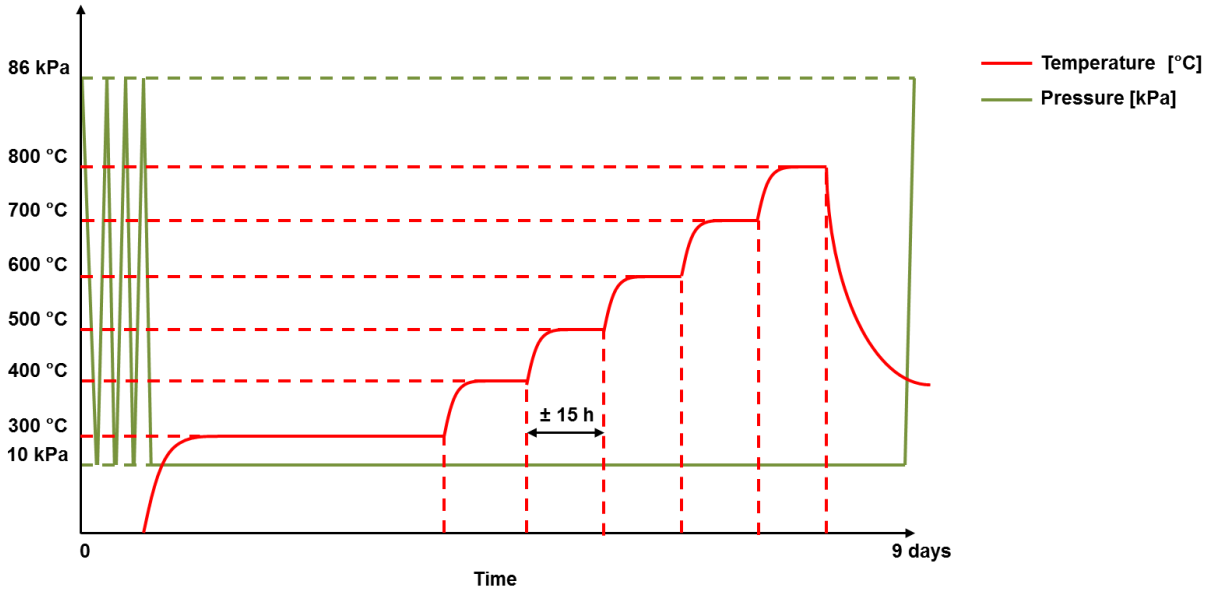

Figure 4.11: Experimental test schedule for the NWETCTF.

The current study focused on the heat transfer phenomena through a packed pebble bed during upset conditions. The effective thermal conductivity results should not include the effects of convection heat transfer through the gas that fills the voids between the pebbles, as it was assumed that buoyancy driven flow was not present in the pebble bed. Therefore the NWETCTF was designed to only include the following heat transfer mechanisms, as discussed in section 2.1.2: (1) thermal radiation between solid surfaces, (2) conduction through the pebble material itself and (3) conduction due to physical contact points on the surfaces of the solid materials.

A near-vacuum nitrogen environment at a constant system pressure of 10 kPa (absolute) was maintained inside the vessel during testing in order to ensure that the effects of convection heat transfer were negligible. As discussed in section 2.4.4 this specific pressure value was also used for the experimental tests performed using the HTTU test facility. According to Rousseau *et al.* (2012a) with the use of simulations it was determined that at this specific pressure the effects of natural convection are negligible.

For each experimental test the surface temperature of the inner radiator was maintained at an approximate value ranging from 400°C to 800°C in steps of a 100°C. The power input to the heater elements were adjusted to gradually heat up the inner radiator to the desired temperature. Once the desired surface temperature was reached the water inlet and outlet temperatures of the water jacket were kept constant at approximately 25°C and 30°C respectively until the system reached steady-state. The operators tracked the temperatures at the various positions throughout the packed pebble bed as well as the temperatures at the outer

reflector over an extended period of time, approximately 14 hours. Once the temperature values as well as the flow rates stabilized it was assumed that the system reached steady-state.

Experimental results for each of the steady-state cases at the various temperatures were extracted for a 10 minute time period with a 1 second interval between data points. After the steady-state data was obtained at a specific temperature the power input to the heater elements was increased to gradually heat up the inner radiator to the next required temperature level. The steady-state data obtained for the various temperatures will be referred to as the various temperature cases for each experimental test.

Two separate but identical experimental tests were conducted at different times for each of the temperature cases to determine the repeatability of the results. After the first test the plant was switched off and allowed to cool down completely. The vessel was opened and the pebble bed was unpacked to check for any signs of corrosion of the graphite pebbles as well as the condition of the electrical connections of the heater elements. The test section was packed with graphite spheres for a second time following the packing method described in section 4.2.3. At a much later time the plant was switched on again to conduct the second experimental test.

Unfortunately a malfunction with one of the thermocouples measuring the temperature on the inner radiator surface only allowed the extraction of experimental data up to a temperature of 700°C for Test 2. The vessel must be opened in order to replace the thermocouple before further tests can be conducted. The time constraint of the current study did not allow for the execution of another experimental test.

During operation of the NWETCTF system two operators must be on duty at in point in time. Four operators worked on the system for the duration of the experimental tests with two operators working an eight hour shift at a time. The responsibilities of the operators included monitoring of the system to ensure all sub-systems were functioning correctly, responding to any alarms or trips if a problem occurred during operation and the replacement of Nitrogen bottles if the supply bank pressure was low.

Although the NWETCTF was designed to operate at temperatures of up to a 1600°C tests were only conducted up to 800°C in the current study. The first reason for the limitation was that the NWETCTF is a new test facility, thus there was no knowledge on how the system would react during first time operation. Therefore not running the system at its maximum capacity for the first time ensured the safe operation of the plant protecting the system as well as the operators. Secondly the main objective of the current study is to provide a methodology which can be used

to obtain experimental data at higher temperatures. Therefore within the time constraint the experimental results up to 800°C were sufficient to prove the applicability of the methodology.

4.3 Experimental data and uncertainty analysis

The details of the methods used for the data and uncertainty analyses of the measured experimental results obtained with the NWETCTF are discussed in the following section.

4.3.1 Measured experimental data

The measured experimental data for the 10 minute time period for the different temperature cases were gathered for Test 1 and 2. For each of the measured experimental variables an average value was calculated which was used in further calculations to obtain the final results presented in Chapter 5.

The uncertainty associated with the average value of each of the measurements was calculated to determine the confidence interval associated with the measured experimental data. The total measurement uncertainty for the NWETCTF consisted of two types of uncertainties namely the instrument uncertainty and the statistical variance, similar to the methodology discussed in section 3.2.3. Accuracies of the instruments used in the NWETCTF as obtained from the manufacturers are listed in Table A.2. These accuracies were used to determine the instrument uncertainties associated with the various measurements.

The statistical variance was calculated using Equation (4.1):

$$u_{statistical,i} = \sqrt{\frac{\sum_{i=1}^{N}(x_i - \bar{x})^2}{N}} \tag{4.1}$$

where x_i is the measured experimental value and $\bar{x}$ is the average value of the N number of measured data points. The combination of the two uncertainties then provided the total measurement uncertainty associated with a specific measurement point as shown in Equation (4.2).

$$u_{measurement,i} = \sqrt{u_{instrument,i}^{\ 2} + u_{statistical,i}^{\ 2}} \tag{4.2}$$

The drift uncertainty was not considered in the calculation of the total measurement uncertainty as the experimental tests of the study were completed over a short period of time. However, the influence of the drift uncertainty must be considered in the application of the proposed

methodology in future studies when experimental tests are conducted over longer periods of time using the NWETCTF.

4.3.2 Derivation of effective thermal conductivity

The experimental data describing the temperature distribution through the packed bed of spheres can be used to determine the effective thermal conductivity through the pebble bed. As discussed in section 2.1.2 according to Rousseau *et al.* (2012a) the derivation of the effective thermal conductivity was based on a simple Fourier conduction rate equation. Figure 4.12 illustrates the calculation of the effective thermal conductivity for the y-component of the packed pebble bed.

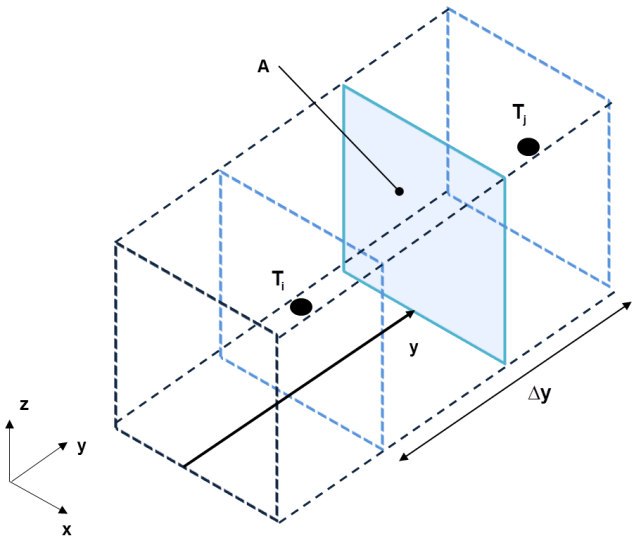

Figure 4.12: Illustration for the calculation of the effective thermal conductivity in the y-direction of the NWETCTF pebble bed.

Equation (2.1) was rewritten to describe the effective thermal conductivity as:

$$k_{eff} = -\frac{Q_{bed}(y)}{A\,dT/dy} \tag{4.3}$$

with $A = L^2$ and $L = 0.42m$ the height and width of the test section. The effective thermal conductivity, k_{eff}, the heat transfer rate, $Q_{bed}(y)$, and the temperature gradient, dT/dy, are all functions of the position in the y-direction of the pebble bed. Therefore in order to obtain values for the effective thermal conductivity it was first necessary to determine the functions describing the heat transfer rate as well as the temperature gradient through the packed bed as a function of position. The methods used to obtain these functions are described in the following sections.

Once the functions were known it could be combined with Equation (4.3) to calculate the effective thermal conductivity values.

The method used to determine the uncertainty of the calculated effective thermal conductivity values was similar to that used by Van Antwerpen (2009) as discussed in section 3.2.4. As can be seen from Equation (3.27) in order to obtain the uncertainty of the calculated effective thermal conductivity values, the uncertainty of the bed heat transfer $u(Q_{bed}(y))$ as well as the uncertainty of the temperature gradient function $u(dT/dy)$ had to be known.

4.3.3 Heat transfer distribution

The NWETCTF test section was insulated at the top and bottom as well as the sides, however some heat losses could still occur through the insulation material. As a result the effective heat transfer through the packed pebble bed was dependent on the position from the heated wall. In order to determine the heat transfer distribution through the packed bed of spheres a method similar to that used by Van Antwerpen (2009) as described in section 3.2.1 was used to determine a heat transfer function for each of the experimental temperature cases.

Figure 4.13 shows an illustration of a side or top view of the test section indicating the various heat flows through the test section. The heat that entered the packed pebble bed through the inner radiator, Q_{in}, was divided into various components. The component in the z-direction included the heat losses through the top and bottom insulation, $Q_{ins,top/bottom}$, whilst the x-component included the heat losses through the two side insulation walls, $Q_{ins,side}$. The third component was the heat transported through the packed pebble bed in the y-direction that was finally conducted through the outer reflector and extracted via the water jacket, Q_{out}.

The electrical power supplied by the heater system consisted of the heat that entered the packed pebble bed, the heat removed via the element coolers, $Q_{coolers}$, and several other heat losses, $Q_{heater,loss}$, that could not be measured directly. Due to the presence of the different heat losses throughout the packed pebble bed it could not be assumed that the heat transfer through the packed pebble bed was constant, but rather that it was a function of the position in the bed. Therefore an estimation of the heat losses was required to obtain a function describing the heat transfer distribution through the packed pebble bed.

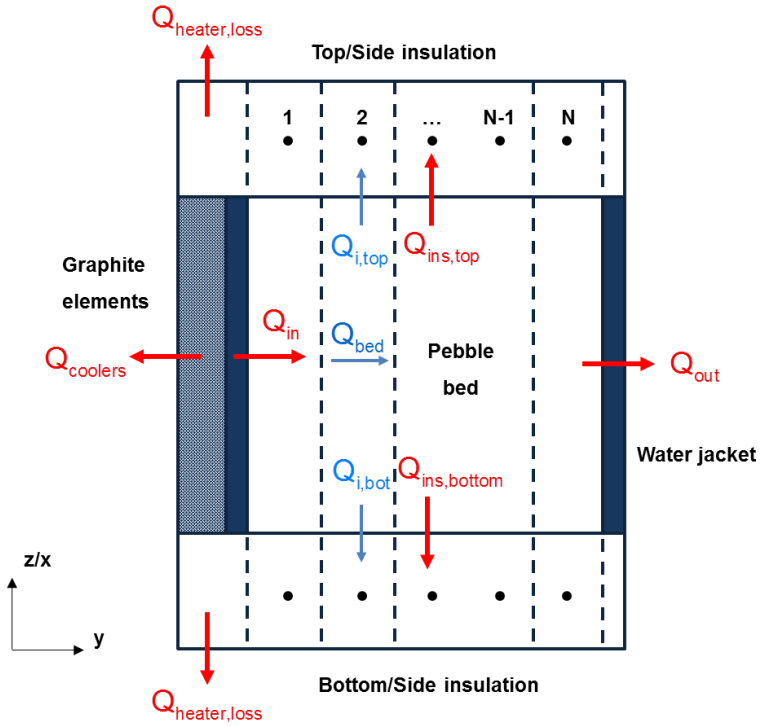

Figure 4.13: Schematic representation of a top/side view of the test section indicating the various heat flows through the test section.

Figure 4.13 also shows an illustration of the discretisation of the test section for the estimation of the heat losses through the top, bottom and side insulation material. The various insulation walls were discretised into 56 equally spaced increments along the y-axis. For each of the increments an estimated heat loss value was calculated for the various insulation walls using Equation (4.4) derived from Equation (3.8):

$$Q_{i,loss} = \left(\left(\frac{k_{SALI} A_i}{L_{SALI}} \right)^{-1} + \left(\frac{k_{AL} A_i}{L_{AL}} \right)^{-1} \right)^{-1} (T_{bed} - T_{env}) \tag{4.4}$$

where L_{SALI} and L_{AL} are the thickness of the layers of the two insulation materials and A_i is the area of one increment. The material thermal conductivity of the SALI-2, k_{SALI}, and the AL-45, k_{AL}, insulation material were specified for each of the temperature cases according to the values presented in Table A.3

A curve was fitted through the experimental temperature measurements for level A and C to obtain functions describing the bed temperatures at the bottom and top insulation material respectively. The bed temperature, T_{bed}, for each increment was calculated using the derived functions and the corresponding positions in the middle of each increment. No experimental

measurements were obtained for the bed temperatures next to the side insulation walls. The packing structure of the pebbles next to the side and the bottom insulation walls were similar as discussed in section 5.2 and therefore the function for the bed temperatures of the bottom insulation wall was also used for the side insulation walls.

During the experimental tests the temperatures of the outer layer of the insulation material at the top and side of the test section were measured. These temperatures for each case were used as the environmental temperature, T_{env}. The combined heat loss for each steady-state test case was calculated as the sum of all the incremental heat losses for all of the increments as shown in Equation (4.5):

$$Q_{totLoss} = \sum_{i=1}^{56} (Q_{i,loss,top} + Q_{i,loss,bottom} + 2Q_{i,loss,side}) \tag{4.5}$$

The local heat transfer rate at a specific position in the packed pebble bed was calculated using Equation (3.9). At a specific position y in the packed pebble bed the local bed heat transfer rate $Q_{bed}(y)$ was calculated as the sum of the heat extracted via the water jacket and the total heat loss through the insulation between position y and the outer reflector. The principle for the calculation of $Q_{bed}(y)$ is illustrated in Figure 4.14.

Assume the packed pebble bed is a single control volume discretised into *N* number of increments as shown in Figure 4.14 (a). Suppose position y, at which the local bed heat transfer rate must be determined, is situated at the ith increment of the control volume in Figure 4.14 (a). For the calculation of $Q_{bed}(y)$ only the increments following the ith increment are considered, thus a smaller control volume is used for the calculation comprising of only the applicable increments of the larger control volume. The red block, shown in Figure 4.14 (a), represents the smaller control volume considered for the calculation of the local bed heat transfer at position y or the ith increment.

Figure 4.14 (b) shows the heat fluxes flowing in and out of the smaller control volume identified in Figure 4.14 (a). For the calculation of the local bed heat transfer a heat balance is done over the smaller control volume, thus the heat flowing into the control volume $Q_{bed}(y)$ is equal to the sum of the heat flowing out of the control volume. The heat flowing out of the control volume consists of two components: (1) the heat extracted via the water jacket, Q_{out} and (2) the sum of the incremental heat losses through the top, bottom and side insulation walls, $Q_{i,loss,total}$.

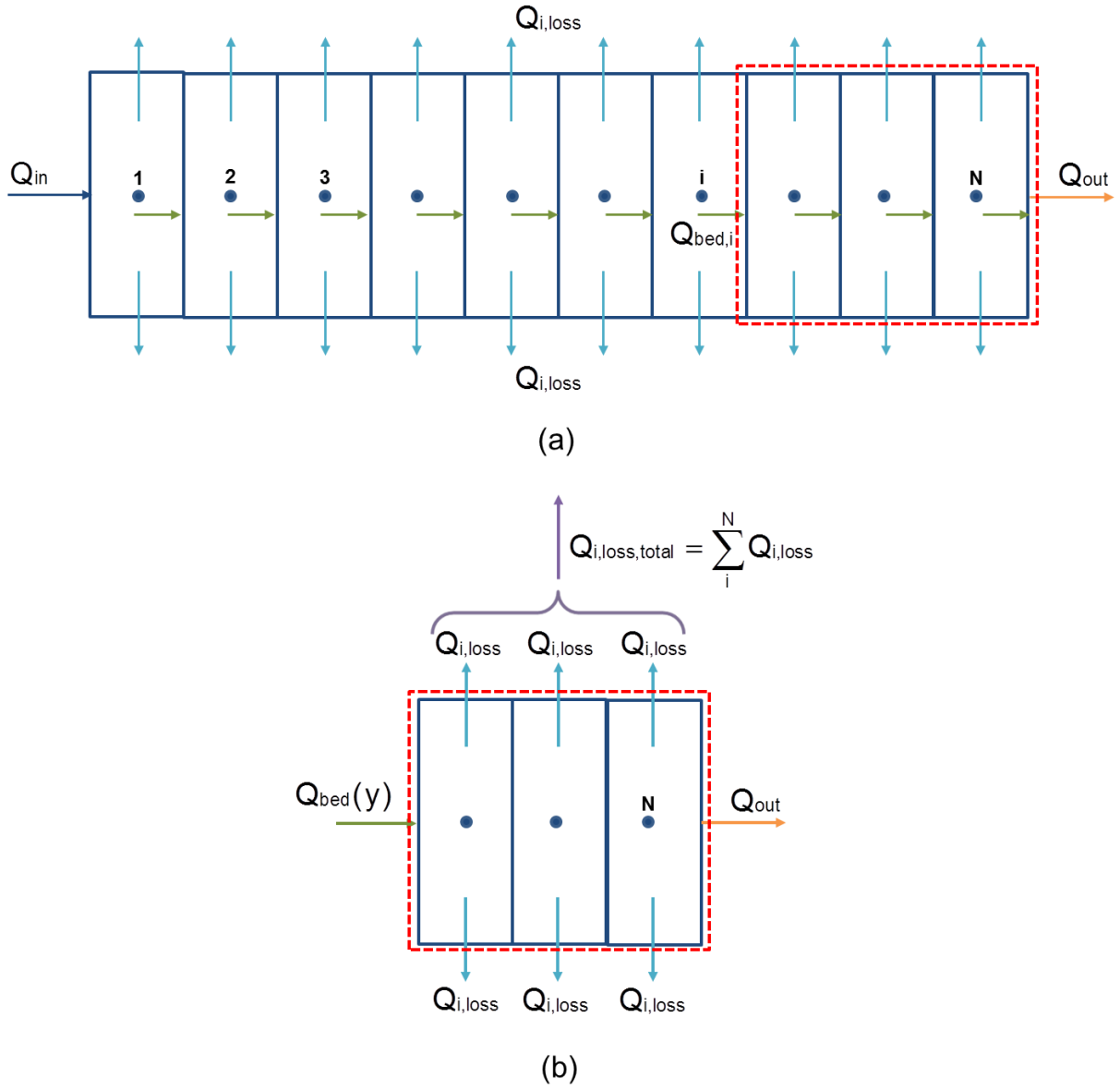

Figure 4.14: Illustration for the calculation of the local bed heat transfer rate at a specific position in the packed pebble bed.

The total heat removed through the water jacket was calculated using Equation (4.6):

$$Q_{out} = \dot{m} c_p (T_{w,out} - T_{w,in}) \tag{4.6}$$

where $\dot{m}$ is the measured water flow rate through the water jacket, c_p is the specific heat capacity value of water and $T_{w,out}$ and $T_{w,in}$ are the outlet and inlet water temperatures of the water jacket respectively.

A curve was fitted through the calculated bed heat transfer distribution values in order to obtain a function that can be used to estimate the heat transfer through the packed pebble bed at a

specific position. Equation (4.7) shows the standard function that was used for the various test cases:

$$Q_{bed}(y) = c_o y^3 + c_1 y^2 + c_2 y + c_3 \tag{4.7}$$

with $c_0 - c_3$ the polynomial coefficients specific to each test case.

The uncertainty associated with the heat transfer through the packed pebble bed $u(Q_{bed})$ was dependent on the uncertainty of the heat removed via the water jacket $u(Q_{out})$ as well as the uncertainty of the total heat loss through the insulation walls $u(Q_{totLoss})$ as described in Equation (4.8).

$$u(Q_{bed}) = \sqrt{u(Q_{out})^2 + u(Q_{totLoss})^2} \tag{4.8}$$

The software EES and Microsoft Excel were used for all of the heat transfer calculations. A detailed description of the calculation of the bed heat transfer functions as well as the uncertainty analysis of the heat transfer results are provided in Annexure B.2.

4.3.4 Temperature distribution function

As discussed in section 4.3.2 a temperature gradient function must be obtained in order to calculate the effective thermal conductivity through the packed bed of spheres. Before the temperature gradient function could be determined a temperature distribution function had to be derived first by fitting a smooth polynomial curve through the measured experimental temperature data for each of the test cases.

The method proposed by Van Antwerpen *et al.* (2010b) for the extraction of the temperature distribution and gradient from the results of the HTTU test facility, as discussed in section 3.2.2, was used. A function with the form as that shown in Equation (4.9) was fitted to the measured temperature data for each of the cases of the experimental tests

$$T(y) = a_0 y^0 + a_1 y^1 + a_2 y^2 + \ldots + a_m y^m \tag{4.9}$$

where $a_0 - a_m$ are the coefficients of the fitted polynomial for each case and *m* is the order of the polynomial. Van Antwerpen *et al.* (2010b) determined that a fifth order polynomial curve fit was the most applicable and delivered accurate results for the HTTU tests. Based on Van Antwerpen *et al.*'s (2010b) finding and a trial-and-error process a fifth order polynomial curve fit was also used in the current study.

The uncertainty associated with the curve fit as a function of position from the heated wall was calculated using Equation (4.10):

$$u_{i,T(y)}(y) = \sqrt{\sum_{i=1}^{N}\left(\frac{\partial}{\partial T_i}(T(y))\cdot u(T_i)\right)^2} \tag{4.10}$$

The data point uncertainty, $u(T_i)$, is the combination of the measurement uncertainty of the measured temperature data and the scatter uncertainty which indicates the error between the fitted polynomial result and the measured data point.

All of the calculations were done using the software program Microsoft Excel and its built-in functions. A standard program was written and a macro was created using Excel's Visual Basic for Applications (VBA).The macro calculates the polynomial fit and its uncertainty using a data set of any size as input values, thus the standard program was used for all of the experimental cases reducing the computational time. The measured temperature data and the measurement uncertainties together with the bed heat transfer function and its uncertainty were used as input values.

4.3.5 Temperature gradient function

After the temperature distribution function was determined for each of the experimental cases a polynomial had to be obtained for each case that represents the gradient of the temperature distribution as a function of position from the heated wall. As mentioned in section 4.3.4 the method used is that presented by Van Antwerpen *et al.* (2010b).

For each of the test cases a temperature gradient function was obtained, the general form of the polynomial is shown in Equation (4.11):

$$\frac{dT}{dy} = \frac{\partial}{\partial y}(T(y)) = c_1 + 2c_2 y + 3c_3 y^2 + \cdots + mc_m y^{m-1} \tag{4.11}$$

The temperature gradient function shown in Equation (4.11) is the derivative of the temperature distribution function shown in Equation (4.9).

The uncertainty of the temperature gradient as a function of position in the packed pebble bed was calculated using Equation (4.12).

$$u_{i,\frac{dT}{dy}}(y) = \sqrt{\sum_{i=1}^{N}\left(\frac{\partial}{\partial T_i}\left(\frac{dT}{dy}(y)\right)\cdot u(T_i)\right)^2} \tag{4.12}$$

The Excel VBA macro used to determine the temperature distribution function and its uncertainty was also used to determine the temperature gradient function with its uncertainty. The results of the polynomial fit were required to determine the gradient of the polynomial fit, therefore the calculations could easily be incorporated into the VBA program.

With the bed heat transfer and the temperature gradient function known the effective thermal conductivity was calculated for the packed pebble bed using the method discussed in section 4.3.2.

4.4 Generation of numerically packed pebble bed

One of the objectives of the current study was also to create a CFD model that simulate the NWETCTF test conditions that can be used to predict the heat transfer through the near-wall region of a packed bed of spheres. Therefore it was necessary to generate a numerically packed bed that could be used as the geometry model for the CFD simulation setup. A description of the methods used to obtain the numerically packed bed of spheres is provided in the next section.

4.4.1 DEM simulation setup

From the literature review conducted in Chapter 2 it was concluded that Eppinger *et al.* (2011) and Van der Merwe (2014) proved through their studies that STAR-CCM+ is a suitable CFD tool to use for the generation of randomly packed pebble beds with the use of a DEM model. Based on this conclusion STAR-CCM+ was used for the generation of a numerically packed pebble bed in the current study.

The method used for the generation of the numerical pebble bed is based on the method used by Van der Merwe (2014). The details of the setup of the DEM simulation according to the layout of STAR-CCM+ are discussed in the following section:

Geometry

Solidworks was used to create a simple cubical geometry with a side length of 0.42 m similar to the NWETCTF test section as described in section 4.2.1. The geometry file was imported into STAR-CCM+ as a surface mesh. A separate rectangular block with a width and length of 1 m and a height of 1.5 m was created in STAR-CCM+ using the built-in CAD functions.

The block was used as the injector region in which the DEM model randomly generated the particles used to form the packed bed and the cubical domain was set as the region in which the particles settled to form the packed bed. CD-adapco (2013) states that the injector region

should surround the volume of the main region, therefore the specific size of the rectangular block was chosen. The top, bottom and side surfaces of each of the geometries were set as wall boundaries for both of the regions.

Particle injector

For the generation of the spherical particles in the simulation the random injector was used. The random injector generated particles at a random point distribution in the injection region and then injected the particles into the main region during the simulation. According to CD-adapco (2013) the random injector is suitable for a less uniform and more arbitrary injection of particles into the main region, therefore this injector type was used to form the randomly packed pebble bed. The random injection of the particles was similar to the method used to create a randomly packed bed of spheres in the experimental setup as discussed in section 4.2.3.

The two regions had to be connected by using an internal interface that was set between the bottom boundaries of both regions. The number of seeds is the property that determines how many particles the injector tries to inject into the main region at the same time. It is recommended by CD-adapco (2013) that this value is set to a tenth of the total number of particles that can fill the volume of the injector region, the value was thus set to 30 particles.

The porosity limit defines the maximum packing limit of the injected particles (CD-adapco, 2013) and was set to 0.55 for the simulation. A particle diameter of 60mm was specified for the spheres which is the same as the graphite spheres used for the experimental tests. The spherical particles were set to fall from the top of the injector region to the bottom of the main region in the z-direction as a result of gravity with an acceleration of -9.81 m/s^2.

Mesh continua

The meshing models selected for the simulation setup was the Surface remesher and the Polyhedral mesher as used by Van der Merwe (2014). CD-adapco (2013) states that for DEM simulations coarser meshes are more preferable than finer meshes that are normally used for general CFD applications. A mesh that is too fine can cause high void fractions resulting in solver instability (CD-adapco, 2013). Van der Merwe (2014) used mesh base sizes equal to a quarter of the particle diameters, therefore a mesh base size of 0.015 m was specified for the DEM simulation.

Physics continua

The physics models used for the DEM simulation was the same as that used by Van der Merwe (2014) and are listed below:

- Implicit unsteady

- Coupled implicit solver
    - Coupled Flow
    - Coupled Energy
- Ideal gas (Air)
- Laminar
- Gravity
- Lagrangian multiphase: Discrete element model
    - DEM particles: Spherical particles
    - Solid: Graphite
    - Constant density
- Multiphase interaction
    - DEM phase interaction
    - Hertz-Mindlin no slip contact model

The implicit unsteady model was selected as DEM simulations are characteristically transient and the time step of the implicit unsteady model was set to 0.05 s with a DEM time scale of 0.05 for the DEM solver (Van der Merwe, 2014). CD-adapco (2013) recommends that for a DEM simulation the coupled solver with an incompressible ideal gas should be used. It was necessary to select these models, however the coupled implicit solver was frozen as the effects of the flow through the packed bed of spheres was not of interest to the current study. With the solver frozen the working fluid and the flow did not have an effect on the DEM results obtained.

As mentioned previously the gravity model was selected to include the effect of the gravity force acting on the particles causing the particles to fall into the main region and settle into position. The Discrete Element Model is an extension of the Lagrangian multiphase model that includes the inter-particle contact forces in the calculation of the equations of motion (CD-adapco, 2013). The solid spherical particles were defined as a phase under the Lagrangian DEM model with the STAR-CCM+ default values for graphite material set as the material properties for all of the regions.

The Multiphase interaction model was used to define the interaction between the particles and the boundary walls during collision. Two Multiphase interactions were defined: (1) particle-particle interaction and (2) particle-wall interaction. The Hertz-Mindlin contact model was selected for each of the multiphase interactions.

For more information and detailed descriptions of the various models consult CD-adapco (2013). The STAR-CCM+ parameters that were not addressed in this section were specified as the default values of STAR-CCM+.

Stopping Criteria

Maximum physical time and the porosity limit of the random injector were used to determine if the simulation was converged. The physical time for the simulation was set to 150 s and monitors for the magnitude of the particle velocity as well as the particle count in the packed pebble bed were created. The results of the DEM simulation were evaluated at various time intervals throughout the simulation. It was accepted that the particles were settled into their final positions once the maximum particle velocity was below $1x10^{-7}$ m/s. The particle count in the packed pebble bed was also monitored to determine whether any particles were still being generated by the injector. Once the particle count stayed constant over an extended period of time it was accepted that no more particles were generated by the injector and the porosity limit was reached.

4.4.2 DEM solid geometry

Data describing the coordinates of the position of each sphere centroid in the numerically packed bed of spheres was extracted and exported from STAR-CCM+. The data was used in Solidworks to create a solid body for each of the DEM particles forming the packed pebble bed geometry that was used for the CFD heat transfer simulations, described in section 4.5.1. Figure 4.15 shows a solid model of the DEM generated packed bed of spheres.

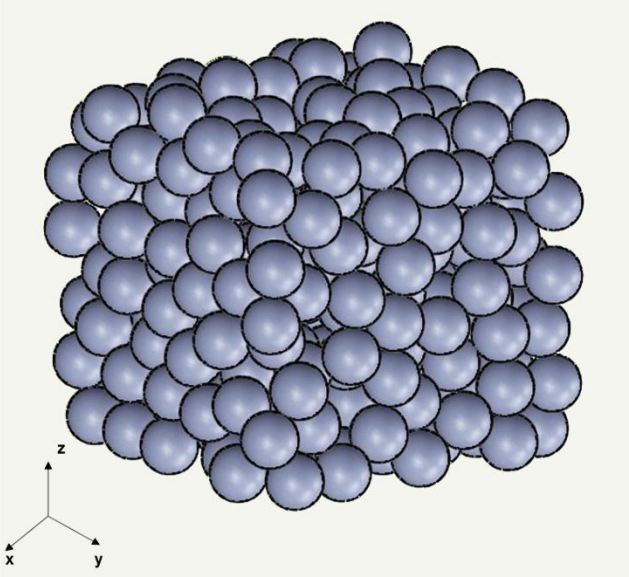

Figure 4.15: Solid model of the DEM generated pebble bed.

Solidworks was also used for the contact treatment of the contact points between the various neighbouring particles and the particles and the walls of the test section. Following the discussion on contact point treatment methods in section 2.3.2 it was decided to use a method similar to Van der Merwe (2014) for the contact treatment. No changes were made to the

particle geometries and a fillet was inserted at all the contact points between the particles and the particles and the walls. The radius of the fillet was specified as 0.2% of the particle diameter as specified by Van der Merwe (2014) in his study, thus a fillet radius of 0.12 mm was used. An illustration of the fillet inserted at the contact points is shown in Figure 4.16.

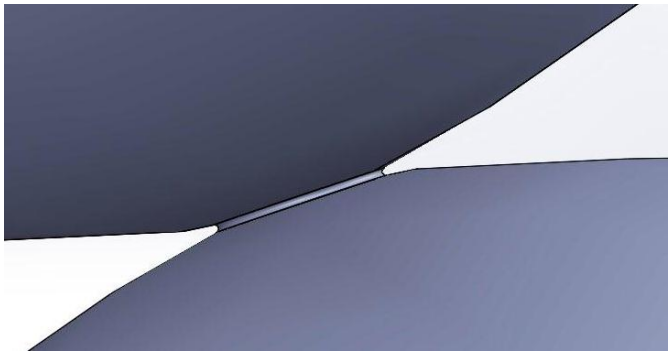

Figure 4.16: Example of fillet contact treatment inserted at contact points in the DEM generated pebble bed.

Van der Merwe (2014) investigated the effect of the contact area associated with the specified fillet on the fluid flow through the packed bed of spheres. His investigation did not include the effect of the contact area on the heat transfer between the particles. Although the focus of the current study is on the heat transfer through the packed pebble bed the scope of the study did not include the investigation of the effects of the fillet radius and contact area on the heat transfer between the particles. Therefore it was assumed that the fillet radius used by Van der Merwe (2014) would provide adequate results for the purpose of this study. It is recommended that a more detailed study of the effect of the contact area on the results of the heat transfer simulation of the packed pebble be done in future studies.

4.5 CFD heat transfer model

Following the discussion in section 4.2.3 it was necessary to develop a CFD model that is representative of the experimental test conditions and the results obtained with the CFD model could be compared to the experimental results. An important function of the CFD model was that it could be used to separate the effects of the conduction and radiation components of the heat transfer through the packed pebble bed. The separation of the phenomena is physically impossible in the experimental setup. Results for the radiation component of the effective thermal conductivity of the packed pebble bed can provide useful insights to the significance of the radiation contribution to the overall heat transfer in the near-wall region of a packed bed of spheres at various temperatures.

Based on the discussion in section 2.3.3 it was concluded from the work done by Pitso (2011) that STAR-CCM+ is sufficient to use for the modelling of radiation heat transfer in a packed pebble bed. A standard CFD model was developed using STAR-CCM+ and a simulation was performed for each of the experimental cases of Test 1 at the various temperatures. For the development of the method to separate the heat transfer phenomena only the 800°C case was considered.

The detail of the CFD simulation setup used to create the CFD model is discussed in this section. The results of the mesh independence study to determine the appropriate mesh for the CFD simulation is presented. The method used to determine the effective thermal conductivity of the packed bed for the numerical simulations as well as the separation of the conduction and radiation heat transfer phenomena is discussed.

4.5.1 CFD simulation setup

The following section provides a detailed description of the CFD simulation setup that was used to model the heat transfer through the packed bed of spheres. For all of the parameters that are not addressed specifically the default values of STAR-CCM+ were used.

Geometry

The geometry used for the CFD simulation consisted of the solid models of the DEM generated pebble bed, the inner and outer reflectors and the layers of insulation material that surrounded the entire packed bed of spheres. All of the geometry solid models were created in Solidworks and imported into STAR-CCM+ as surface meshes. The contact treatment as discussed in section 4.4.2 was applied to all of the contact points between neighbouring particles and particles and the reflector as well as insulation walls. Figure 4.17 shows an assembly of the solid models used as the geometry for the CFD simulation setup.

The side length of both the reflectors was specified as 0.42 m with a thickness of 0.02 m. The thickness of the SALI-2 and AL-45 insulation layers was specified as 0.038 m and 0.19 m respectively. All of the sizes of the solid models of the geometry were specified according the sizes of the NWETCTF test section as discussed in paragraph 4.2.1.

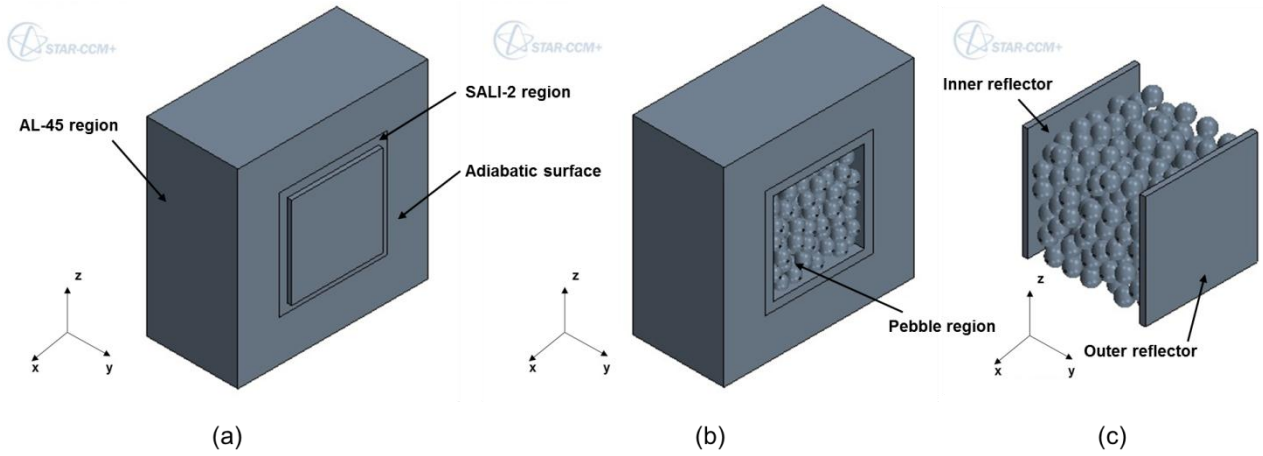

Figure 4.17: (a) Complete assembly of solid models, (b) solid models of pebbles and insulation layers and (c) solid models of reflectors and pebbles.

Regions and boundaries

Five regions were created from the imported geometry in STAR-CCM+; a region for the pebbles with the applied contact treatment, a region for each of the graphite reflectors and a region for each of the SALI-2 and AL-45 insulation layers. Each of the regions was split into various boundaries with a wall type boundary condition.

The measured values obtained from Test 1 of the NWETCTF experimental data was used as the boundary conditions for the simulation of each of the experimental cases. For the inner reflector or heated wall region as well as the outer reflector or cooled wall region surface temperatures were specified as boundary conditions. A temperature was specified for the top, bottom and side boundaries of the outer AL-45 insulation region. A list of the values for each of the boundary conditions is given in Table 4.1.

Table 4.1: Boundary conditions used for the CFD simulations.

Case	Boundary Temperature [°C]			
	Inner reflector	Outer reflector	AL-45 Top	AL-45 Bottom/Side
800°C	800	163.00	51.45	58.39
700°C	700	130.30	48.86	54.17
600°C	600	103.43	41.02	46.05
500°C	500	74.65	34.07	35.26
400°C	400	59.39	33.86	35.29

The side boundaries of the insulation regions in the y-direction were set to adiabatic to eliminate heat losses through the insulation in the y-direction. This approach was used for the simulation

setup in order to match the setup used for the experimental heat transfer calculations as described in section 4.3.3, with the only difference being that the side walls in the y-direction were specified as adiabatic with a zero emissivity.

The surface emissivity of the insulation boundaries with an adiabatic thermal specification was set to zero to ensure no heat loss to the environment as a result of radiation. The surface emissivity of the rest of the boundaries was set to 0.68 for the insulation walls and 0.8 for the graphite reflectors and pebbles. The initial temperature of the insulation regions was set to 20°C for all of the simulations. For the reflectors and pebble regions the initial temperature for each of the cases was set to a value that is 20°C less than the temperature of the outer reflector. The specific values were chosen as it was not too far from the expected final result, thus minimising possible convergence errors and decreasing the computational time of the simulations.

Interfaces

Interfaces were used to provide a connection between the boundaries of two regions and to allow energy transfer from one region to another (CD-adapco, 2013). When an interface is created between two boundaries of separate regions the defined interface combines and replaces the two boundaries in the simulation setup as shown in Figure 4.18.

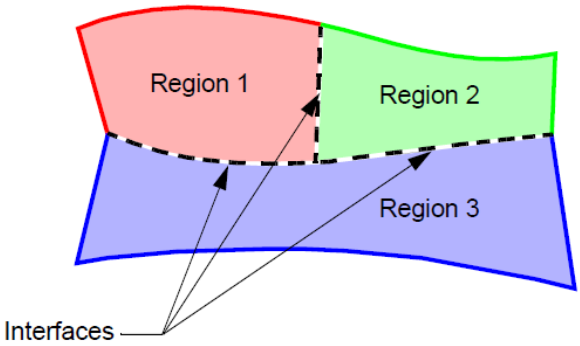

Figure 4.18: Illustration of an interface created from coincident boundaries of different regions (CD-adapco, 2013).

In-place contact interfaces were inserted between the pebbles and the heated wall, the pebbles and the cooled wall, the pebbles and the SALI-2 insulation walls as well as the SALI-2 insulation layer and the AL-45 insulation layer. The intersection tolerance was set to 0.025 for all of the interfaces to improve the cell matching of the interface between the two regions.

Mesh Continua

Two different mesh continua were specified for the CFD simulations; a coarser and a finer mesh. The coarser mesh was assigned to the insulation regions whilst the finer mesh was

assigned to the reflectors and pebble regions. The reflectors and pebble regions were the main area of interest for the heat transfer through the packed bed of spheres; therefore a finer mesh was used for these regions. For the insulation regions a coarser mesh was used to decrease the computational resources required to solve the simulation as a coarser mesh resulted in a lower cell count for the volume mesh of these regions.

The Surface remesher and the Polyhedral volume mesher models were selected for the CFD simulations. Van der Merwe (2014) also used these meshing models in his investigation together with a Prism layer mesher. According to CD-adapco (2013) the Prism layer mesher is mainly used to resolve flow boundary layers and is not generally required within solid regions. In the current study there was no flow simulated through the packed pebble bed as the experimental tests were performed under near-vacuum conditions to eliminate the effect of convection. Therefore only the solid regions were modelled and it was not necessary to select the Prism layer mesher.

The specifications for the mesh continua were selected based on the results of the mesh independence study discussed in section 4.5.2. A mesh base size of 5 mm and 3 mm were used for the coarser and the finer mesh respectively. The minimum surface size of both of the meshes was set to 25% of the mesh base size. For the pebbles region a custom minimum surface size was specified as 16% of the mesh base size.

Physics Continua

The following physics models were selected for the CFD simulations based on the recommendations for conduction and radiation heat transfer simulations between solid regions by CD-adapco (2013):

- Steady
- Solid
- Segregated Solid Energy
- Surface-to-Surface (S2S) Radiation
    - View Factors Calculator
    - Gray Thermal Radiation

The Segregated Solid Energy and S2S Radiation models were also used in the CFD simulation setup of the study done by Pitso (2011). The thermal conductivity values of the insulation materials listed in Table A.3 were used in the CFD simulations. A curve was fitted through the data in Table A.4 to obtain the thermal conductivity of the graphite as a function of temperature

in degrees Celsius. The function, shown in Equation (4.13), was used for the graphite thermal conductivity in the CFD simulations.

$$k_C = 1.5950\times10^{-14}T^5 - 5.0771\times10^{-11}T^4 - 1.7142\times10^{-9}T^3 + 0.0002T^2 - 0.2320T + 159.5961 \quad (4.13)$$

The S2S radiation model assumed all surfaces to be gray, diffuse and opaque for the radiation analysis in the pebble bed. The S2S orientation of the radiation model was set to outward for all the regions thus no internal radiation was simulated. The boundaries of the various regions were discretized into patches to form the elemental areas required to calculate the view factors. The patch/face proportion was set to 50% for the insulation regions and 25% for the reflectors and pebble regions as a finer mesh was used for these regions. Thus each patch consisted of two mesh cells for the insulation regions and 4 mesh cells for the reflectors and pebble regions. The View Factors Calculator uses a deterministic approach as opposed to the statistical approach of the Monte Carlo method, discussed in section 2.2.3, to determine the view factors between the boundaries of the regions.

Stopping Criteria

The maximum number of steps for the simulation was set to 10 000 and was specified as the stopping criterion for the simulation. It was accepted that the simulations were converged when the residual value was smaller than 10^{-6}, which is equivalent to a residual value magnitude drop of 5 orders.

Solvers and solution

The Segregated Energy solver solid under-relaxation factor was set to 0.99 to improve the convergence time of the simulations. The reciprocity tolerance of the View Factors solver was set to 0.001 with a maximum number of reciprocity iterations of 200. For the separation of the conduction and radiation heat transfer, discussed in section 4.5.4, the S2S solver was frozen and the simulation was only solved for conduction heat transfer excluding the effects of radiation.

Monitors and reports

To obtain the temperature distribution through the numerically packed pebble bed probe points were inserted at the centre of spheres in the pebble region. The positions of the probe points were similar to the positions of the instrumented spheres for Test 1 of the NWETCTF experimental setup, given in Table A.1. Table C.1 lists the positions of the probe points used in the simulation setup.

A maximum temperature report was created for each of the probe points and the temperature distribution data was extracted from STAR-CCM+. Surface average heat transfer reports were used to determine the heat flux over the boundary walls of the insulation regions and outer surface of the cooled wall. The values for the heat extracted through the cooled wall and the total heat loss through the insulation material were extracted from STAR-CCM+ for each of the simulations.

4.5.2 Mesh independence study

The development of a good quality mesh is important to ensure that accurate and stable solutions are obtained from the CFD simulations. Dense meshes generally provide more accurate solutions however it can be computationally costly. Therefore a mesh had to be developed that provided a good compromise between the accuracy of the solution obtained and the computational resources required.

The mesh density required at the contact points between neighbouring particles to obtain an accurate solution as well as the mesh density needed to obtain a mesh independent solution for the simulations were investigated. The methods used to evaluate the mesh quality are discussed in the following section.

Contact treatment

As discussed in section 4.4.2 a fillet with a radius of 0.12 mm was inserted at the contact points between adjacent particles and particles and the walls. The fillet was inserted as contact point treatment to avoid the generation of bad quality mesh cells at the contact points. The quality and density of the mesh at the contact point fillet between two neighbouring spheres had an influence on the results of the conduction heat transfer through the contact point. Therefore the minimum surface size of the cells required at the contact points to deliver a mesh independent solution had to be investigated.

A CFD simulation was set up with a solid model consisting of two half spheres with a fillet inserted at the contact point between the two half spheres. The solid model used for the CFD contact point simulation is shown in Figure 4.19. The CFD simulation setup was similar to the setup described in section 4.5.1. The effect of radiation heat transfer was not included in the simulation as only the conduction heat transfer through the solid material of the fillet from one half sphere to the other was of importance.

A hot and cold boundary were created for each of the flat surfaces of the two half spheres, the boundaries are indicated in Figure 4.19. As boundary conditions a temperature of 200°C and

170°C was specified on the hot and the cold boundary respectively. The boundary specification imposed a pure heat transfer from one sphere to the other through the half spheres region. Once the simulation was solved the heat flux extracted through the cold boundary could be determined.

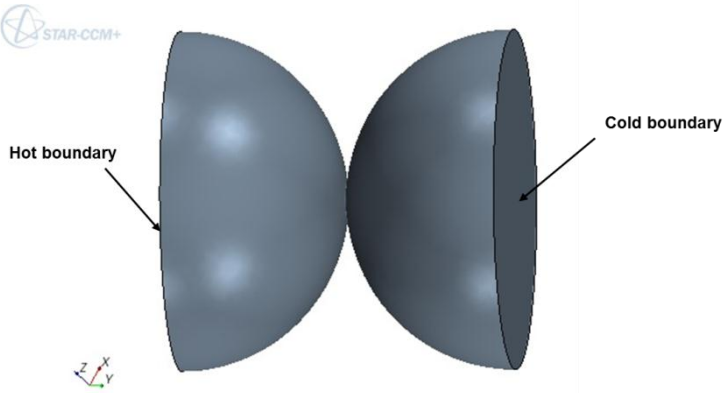

Figure 4.19: Solid model used for CFD simulation of contact point study.

The mesh base size, *B*, was specified as 3 mm and the relative minimum surface size, *SS*, was specified as a percentage of the base size. The influence of the mesh density on the conduction heat transfer through the contact point was analysed by solving the simulation for various cases. For each of the cases the minimum surface size was decreased, thus the cell count and the mesh density at the contact point was increased. Figure 4.20 shows the heat transfer results as a function of mesh density for the different cases.

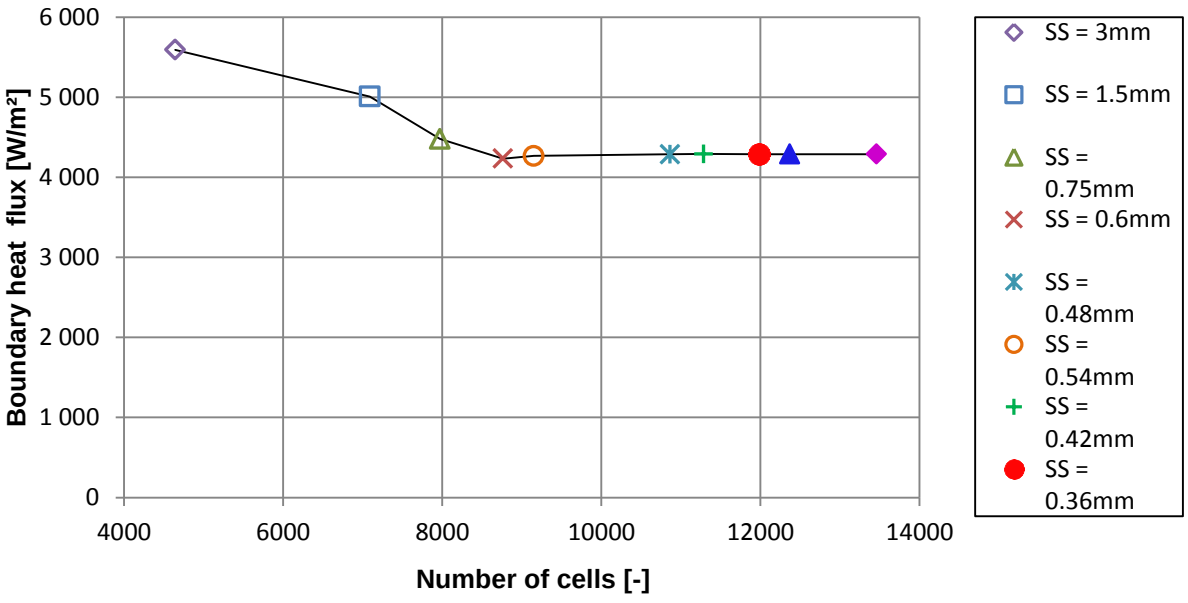

Figure 4.20: Heat flux extracted via the cold boundary as a function of mesh density.

From the results it is clear that the conduction heat transfer through the contact point between the two half spheres became mesh independent at approximately 10 800 cells with a minimum surface size of 0.48 mm. The minimum surface size of 0.48 mm was chosen for the pebble region of the CFD simulations discussed in section 4.5.1 as it showed mesh independency without an excessive cell count. The minimum surface size can also be expressed as 16% of the mesh base size. The structure of the mesh at the contact point is shown in Figure 4.21.

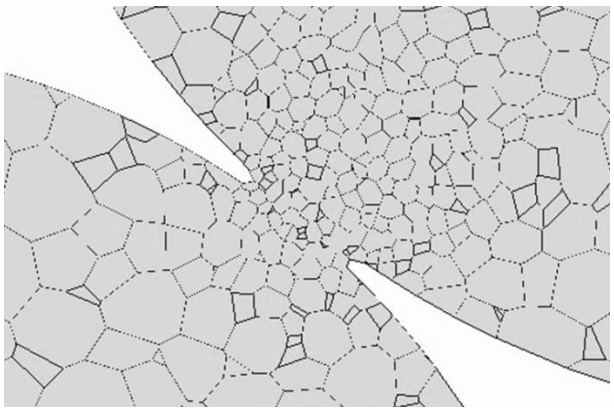

Figure 4.21: Structure of mesh at contact point.

Mesh density

The influence of the mesh density on the results of the CFD simulation for the entire test section was investigated by solving the simulation for various mesh base sizes. The mesh base size was decreased for each of the solutions obtained, thus increasing the cell count and the mesh density. Figure 4.22 shows the results for the investigation where the heat flux extracted at the cooled wall is shown as a function of mesh density.

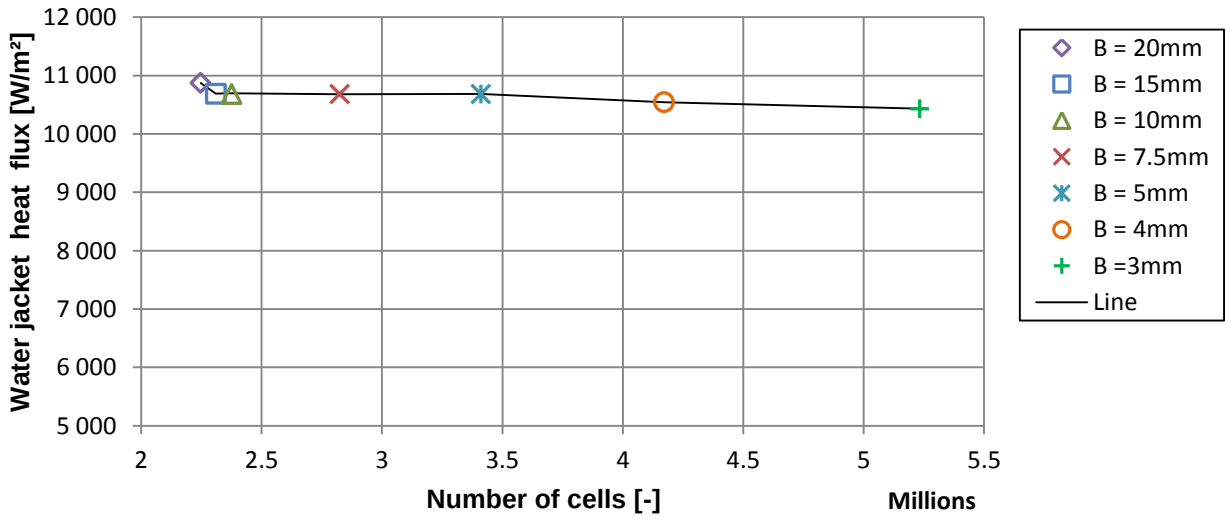

Figure 4.22: Heat flux extracted at the cooled wall as a function of mesh density.

For the cases with a base size of 4 mm and 3 mm the base size of the coarser mesh for the insulation regions were kept constant at 5 mm to provide results without an excessive cell count. The fillets at the contact points between the particles and the various walls were not included in the mesh density investigation; however the fillets for the contact points between the adjacent particles were included.

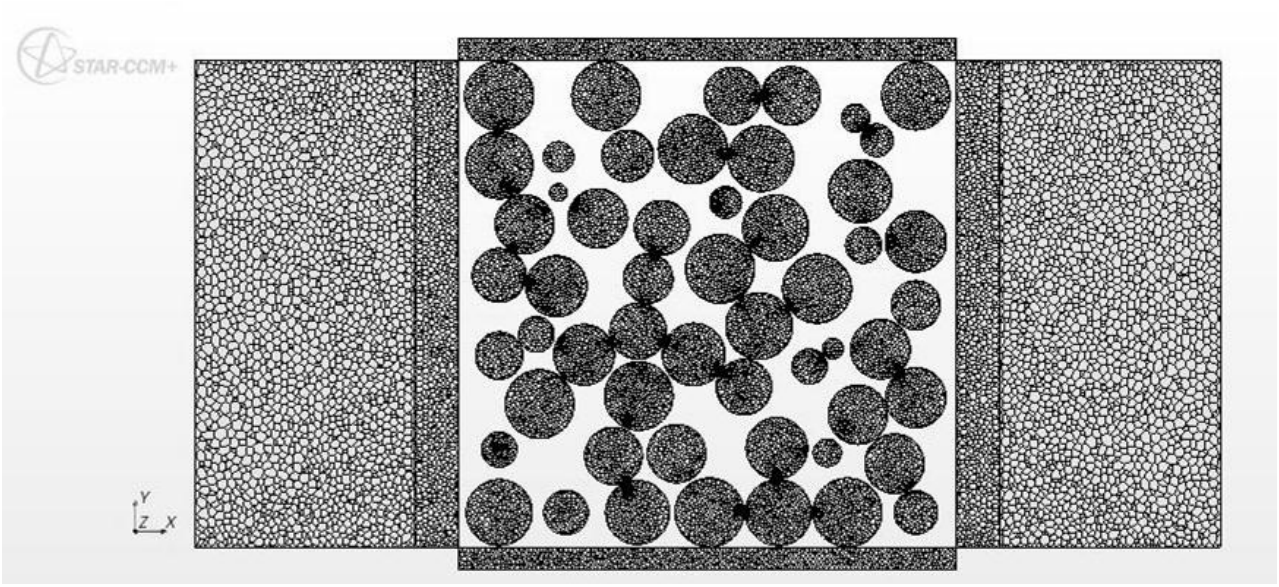

Figure 4.23: Section cut through the simulation regions displaying the mesh structure for a 3 mm base size.

The result for the heat flux for a base size of 4 mm is within 1.06% of the heat flux result for a base size of 3 mm. A mesh for a smaller base size than 3 mm could not be obtained for the simulation as the computational resources available only allowed for simulations with a cell count of approximately six million. Therefore it was decided that a base size of 3 mm delivers a solution that is mesh independent without an excessive cell count and the base size were used for all of the CFD simulations. Figure 4.23 shows the mesh structure with a base size of 3 mm for a section cut through the simulation regions

4.5.3 CFD heat transfer distribution

One approach to determine the heat transfer distribution through the packed bed of spheres would be to create plane section cuts throughout the packed bed at various positions from the heated wall. The average heat flux should then be obtained over the plane section to determine the heat flux through the pebble bed at various positions. Although this approach seemed quite simple it was found that STAR-CCM+ does not provide the ability to extract the heat flux over a surface other than the boundaries of the simulation.

Therefore a method similar to that used to obtain the heat transfer distribution through the packed bed of spheres for the experimental results was used to obtain the heat transfer distribution through the numerically packed bed of the CFD simulation. Following the discussion of the method in section 4.3.3 the heat transfer was determined by discretising the packed bed of spheres into a number of increments. The heat transfer at a certain position in the packed pebble bed was estimated as sum of the heat transfer removed via the water jacket and the total heat loss through the insulation walls for all of the increments between the position under consideration and the cooled wall, illustrated by Equation (3.9).

The discretisation of the packed pebble bed of the CFD simulation was done using thresholds. A threshold is a derived part that can be used to isolate a group of cells on a surface based on their relationship to specified scalar values (CD-adapco, 2013). The magnitude of the y-coordinate was used as the scalar value to divide the surface of the SALI-2 insulation layer into 21 increments with a width of 20 mm each. Figure 4.24 shows an illustration for the definition of a single threshold. The surface average of the boundary heat flux over the SALI-2 boundary was obtained for each of the defined thresholds with the surface area of a single threshold defined as $A_{threshold,i} = 4Lw$ where L is the height of the test section and w the width of one increment.

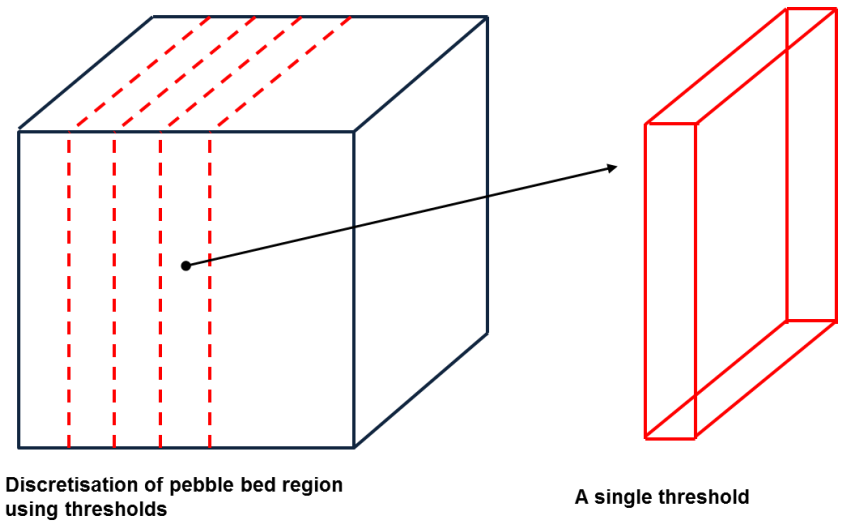

Figure 4.24: Illustration of discretisation of numerical pebble bed region using thresholds in STAR-CCM+.

The heat removed via the water jacket was determined by obtaining the surface average of the heat transfer over the cooled wall boundary. With the values of the heat removed via the water jacket as well as the incremental heat losses known the heat transfer through the numerically packed pebble bed was calculated.

4.5.4 Derivation of CFD effective thermal conductivity

To obtain the effective thermal conductivity through the packed bed of spheres for the CFD simulation the heat transfer distribution as well as the macro temperature gradient through the packed pebble bed was required. The macro temperature distribution through the packed pebble bed was obtained by inserting plane sections at various positions from the heated wall and obtaining the average surface temperature over each plane section. A total of 44 plane sections were used.

The numerical data for the heat transfer distribution as well as macro temperature distribution was extracted from STAR-CCM+. The same method and VBA program used for the experimental data and uncertainty analysis, discussed in section 4.3, were used for the numerical data and uncertainty analysis as well as the derivation of the effective thermal conductivity. As no measurement uncertainties were associated with the numerical data the uncertainty analysis only included the effect of the scatter uncertainty associated with the polynomial curve fit to the CFD results.

One of the objectives of the study includes the separation of the conduction and radiation components of the effective thermal conductivity to determine the contribution of radiation to the overall heat transfer in the near-wall region of the packed pebble bed. As mentioned in section 4.5.1, to determine the numerical results due to the effect of conduction heat transfer only, the S2S solver was frozen in the CFD simulation setup. This means that the effect of radiation was neglected and the heat transfer and temperature distribution obtained was solely due to the conduction component of the heat transfer.

The effective thermal conductivities for the numerical pebble bed was obtained for the combined effect of radiation and conduction heat transfer as well as the effect of the conduction component only. With the combined effective thermal conductivity and the conduction component known the radiation component of the effective thermal conductivity was calculated using Equation (4.14):

$$k_{eff} = k_e^{\,c} + k_e^{\,r} \tag{4.14}$$

where $k_e^{\,c}$ is the conduction component and $k_e^{\,r}$ is the radiation component of the effective thermal conductivity. The expression shown in Equation (4.14) is based on the expression used by Van Antwerpen *et al.* (2012) discussed in section 2.1.2, given in Equation (2.2).

The derivation of the radiation component of the effective thermal conductivity provided a characterisation of the radiation heat transfer in the near-wall region of the numerical pebble bed.

4.6 Summary

This chapter provided a description of the methods used for the experimental and numerical analyses of the heat transfer in the near-wall region of a packed pebble bed to obtain effective thermal conductivity results with associated uncertainties. A description of the new NWETCTF test facility and the commissioning of the system were given. The method used for the preparation and packing of the randomly packed pebble bed together with a description of the experimental tests performed during the study were discussed.

Once the measured experimental data was gathered the measured results had to be processed to obtain average values as well as the measurement uncertainties associated with each of the measured variables. The methods used for the calculation of the heat transfer distribution and temperature gradient functions through the packed pebble bed for each of the test cases were discussed. With these functions known the method described for the derivation of the effective thermal conductivity could be used to obtain the final experimental results.

Before numerical results could be calculated with the use of CFD simulations the solid geometry of a numerically packed pebble bed had to be created first. The steps taken during the setup of the DEM simulation in STAR-CCM+ were discussed. The contact point treatment applied to the DEM generated bed to ensure the development of a high quality mesh at the contact points for the CFD simulations was described in detail.

The procedure followed for the setup of the CFD heat transfer simulation was also described in this chapter followed by a discussion of the mesh independence study performed for the investigation. The mesh independence study proved that mesh independent solutions were achieved for the CFD simulations.

The methods proposed for the calculation of the heat transfer distribution through the numerically packed pebble bed, the macro temperature gradient and the derivation of the effective thermal conductivity for the numerical results were presented. The separation of the radiation and conduction heat transfer components of the numerical effective thermal conductivity is described in this chapter as well. The results obtained with all of the methods described in this chapter are presented and discussed in the following chapter.

5

Results

All of the results obtained with the methods described in Chapter 4 are given in this chapter. The measured temperature and heat transfer results of the NWETCTF experimental tests as well as the experimental effective thermal conductivity results are presented. The porosity variation and quality of the DEM generated pebble bed are analysed.

Numerical temperature and heat transfer results obtained with the CFD simulations are presented and compared with the experimental results of the NWETCTF. The results for the separation of the overall effective thermal conductivity into the conduction and radiation components are given. The radiative conductivity demonstrates the methodology used to characterise the radiation heat transfer in the near-wall region of the packed pebble bed.

5.1 Experimental results

The measured temperature and heat transfer results for the experimental tests are presented in the following section. The calculated temperature distribution function as well as the temperature gradient function is given for each of the experimental tests. Lastly the calculated experimental effective thermal conductivity results for the various test cases are discussed.

5.1.1 Temperature results

The results for the temperature measurements through the packed bed of spheres for the various temperature cases of both the experimental tests are presented in the following section. Detailed results of the average values of the experimental data together with their associated measurement uncertainties are given in Annexure B.1.

The measured temperatures for the 800°C case of Test 1 are shown in Figure 5.1. For the 800°C case the inner reflector surface temperature was maintained at 800.13°C resulting in a

surface temperature of 162.95°C at the cooled wall. The maximum measurement uncertainty for the results is 5.001°C. Although the error bars were plotted on the graph they are not really visible as the uncertainty values are very small.

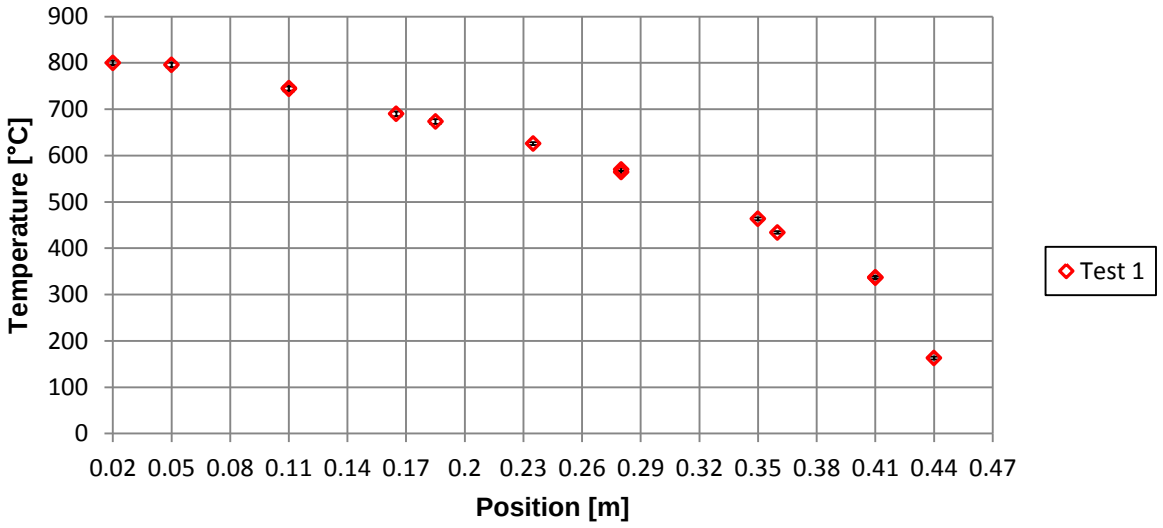

Figure 5.1: Measured temperatures for the 800°C case of the first experimental test.

Figure 5.2 to Figure 5.5 show the measured temperatures for the 700°C, 600°C, 500°C and 400°C cases for both Test 1 and Test 2. The error bars for the various cases were also plotted on the graphs, however the uncertainty values are very small as for the 800°C case and therefore the error bars are barely visible. For Test 1 and Test 2 of the 700°C case the surface temperature of the inner reflector was maintained at 699.96°C and 699.98°C respectively with a measured cooled wall temperature of 130.30°C and 131.11°C. The maximum measurement uncertainty for Test 1 and 2 is 5.001°C and 5.002°C.

The inner reflector surface temperature was kept constant at 600°C and 600.02°C for Test 1 and 2 of the 600°C case with a cooled wall temperature of 103.43°C and 106.24°C. The maximum measurement uncertainty for the first test is 5.002°C and 5.003°C for the second test. For both tests of the 500°C case the surface temperature of the inner reflector was maintained at 500°C with a measured cooled wall temperature of 74.65°C for Test 1 and 79.91°C for Test 2. The maximum measurement uncertainty for both experimental tests is 5.004°C.

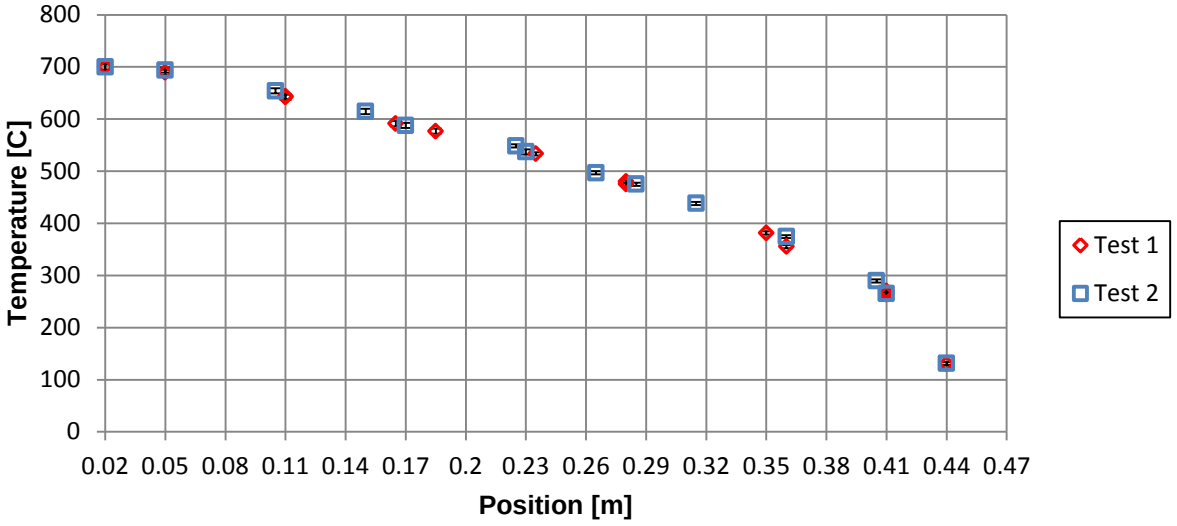

Figure 5.2: Measured temperatures for the 700°C case for both experimental tests.

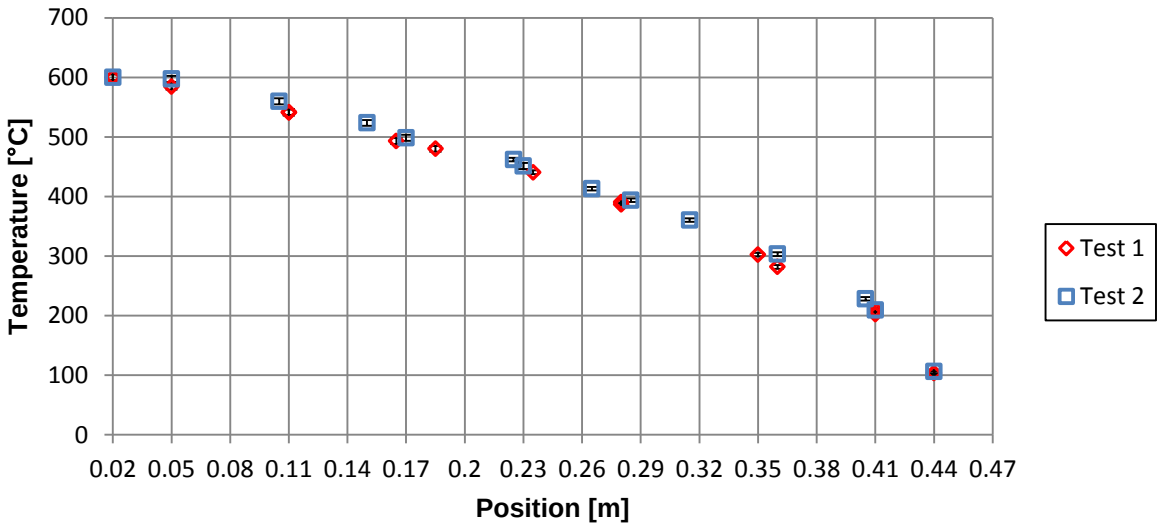

Figure 5.3: Measured temperatures for the 600°C case for both experimental tests.

For the 400°C case the surface temperature of the inner reflector was maintained at 400°C and 399.98°C with a cooled wall temperature of 59.39°C and 66.01°C for Test 1 and 2 respectively. The maximum measurement uncertainty for the first test is 5.006°C and 5.002°C for the second test. From the small measurement uncertainty values it is clear that good results were obtained for the various cases. As the thermocouples used for the temperature measurements were not calibrated between the two experimental tests a drift uncertainty component was not included in the uncertainty calculations. The repeatability of the results between Test 1 and Test 2 is good for all of the cases as can be seen from the results in Figure 5.2 through Figure 5.5.

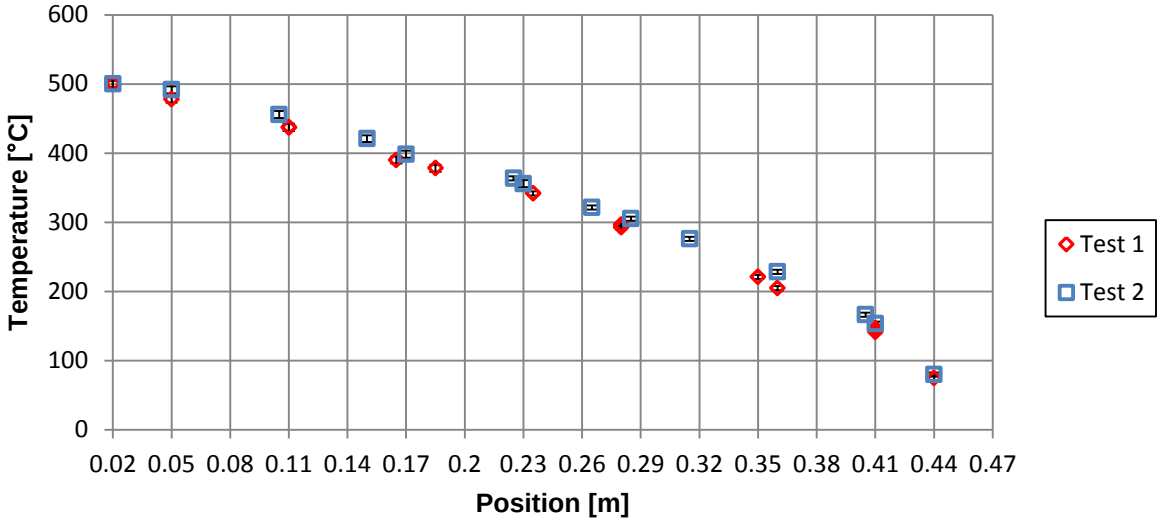

Figure 5.4: Measured temperatures for the 500°C case for both experimental tests.

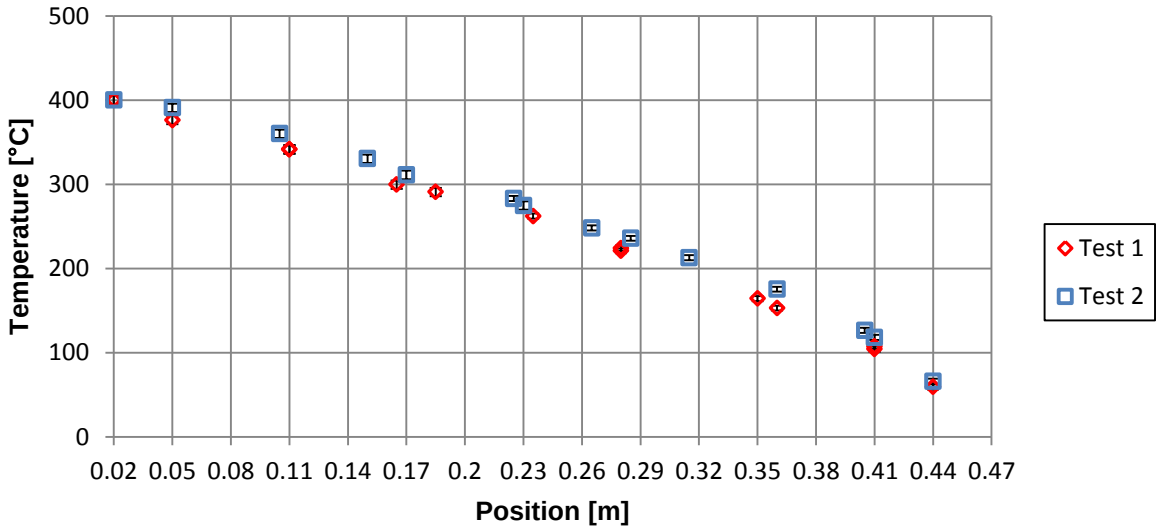

Figure 5.5: Measured temperatures for the 400°C case for both experimental tests.

It is also interesting to note that the temperature measurements in the wall region, as defined in section 2.1.1, are almost the same as the surface temperature of the heated wall for the 800°C, 700°C and 600°C cases. Whereas for the 500°C and 400°C cases a gradual decrease in the temperatures in the wall region is visible.

The first reason for this change in the temperature distribution at higher temperatures is that the contribution of the radiation component to the overall heat transfer is more significant at higher temperatures, as concluded from section 2.2.1. Secondly the average porosity of the packing structure in the region directly next to the wall is higher than the average porosity in the near-wall region of the packed pebble bed.

A higher porosity value indicates that more voids are present in the wall region. As a result the view factors from the heated wall to the spheres in the wall region will be larger than the view factors from the heated wall to the spheres in the near-wall region. Thus more radiative rays reach the pebbles in the wall region increasing the local radiation heat transfer rate and the measured temperatures. As the temperature of the heated wall decreases the significance of the radiation contribution to the overall heat transfer also decreases thus the temperatures in the wall region also decrease, as is evident in the 500°C and 400°C cases.

5.1.2 Heat transfer results

The results of the heat transfer through the packed bed of spheres for all of the cases of both experimental tests are presented in the following section. The method described in section 4.3.3 together with the measured experimental data was used to obtain the results.

For the 800°C case of Test 1 the heat transfer distribution through the packed pebble bed in the y-direction with its uncertainty is shown in Figure 5.6. The function shown in Equation (5.1) can be used to estimate heat transfer though the packed pebble bed at any position from the heated wall

$$Q_{bed,1,800C}(y) = 1409.152251y^3 + 139.038611y^2 - 1212.280141y + 2041.778480 \quad (5.1)$$

with a maximum uncertainty of 79.59 W. From the measured experimental data it was calculated that the heat extracted via the water jacket was 1657.60 ± 73.12 W, the total heat loss through the top, bottom and side insulation walls was 366.69 ± 31.44 W and the heat loss through the element coolers was 479.43 ± 13.27 W.

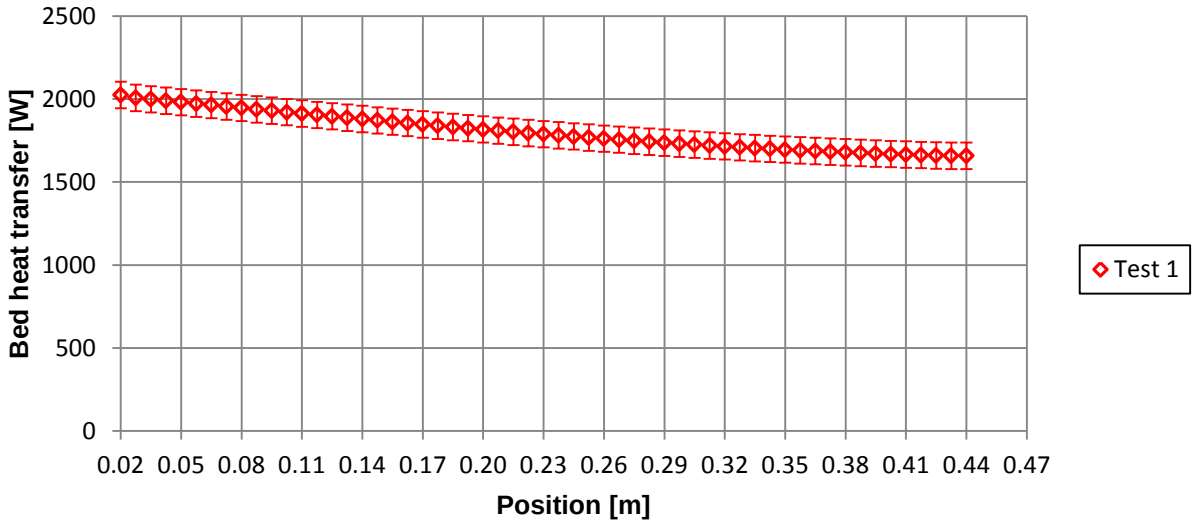

Figure 5.6: Measured heat transfer through pebble bed as a function of position for the 800°C case of Test 1.

The heat transfer distribution through the packed pebble bed for the 700°C case of Test 1 and Test 2 is shown in Figure 5.7. Equation (5.2) and (5.3) describe the heat transfer rate through the packed bed as a function of position for Test 1 and Test 2 respectively;

$$Q_{bed,1,700C}(y) = 1102.606437y^3 + 198.018960y^2 - 1007.338787y + 1463.887017 \quad (5.2)$$

$$Q_{bed,2,700C}(y) = 1290.139283y^3 + 111.022188y^2 - 1016.219944y + 1529.559067 \quad (5.3)$$

with a maximum uncertainty of 66.45 W for Test 1 and 65.42 W for Test 2.

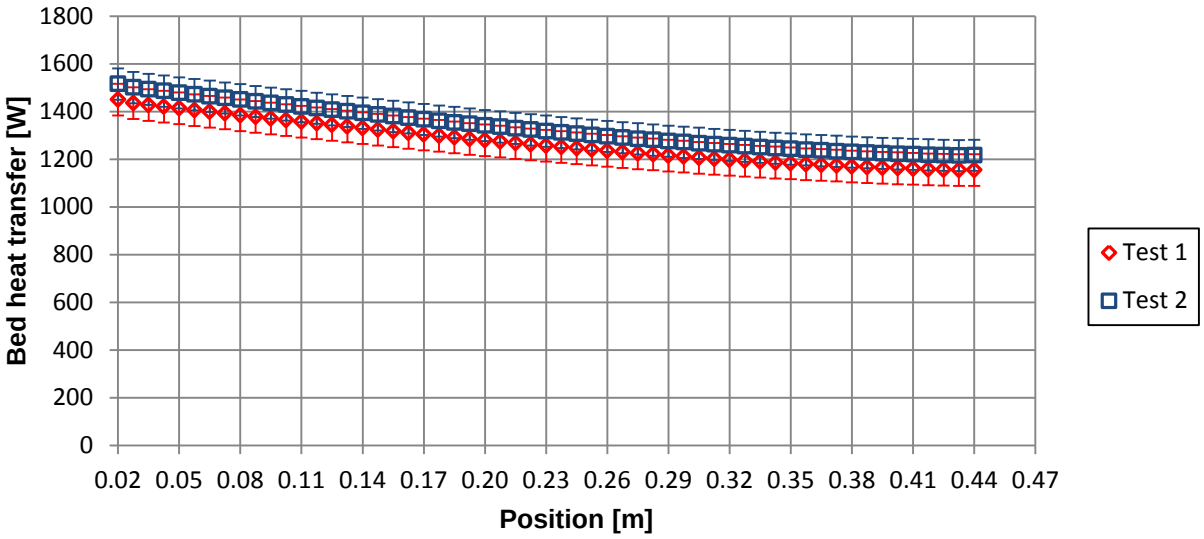

Figure 5.7: Measured heat transfer through pebble bed as a function of position for the 700°C case of both tests.

For Test 1 and Test 2 the measured heat extracted through the water jacket were 1155.32 ± 63.08 W and 1216.17 ± 64.04 W, the total heat loss through all the insulation walls 294.09 ± 20.88 W and 298.76 ± 13.39 W and the heat removed via the element coolers 405.95 ± 12.98 W and 521.07 ± 19.70 W. The heat transfer results for Test 1 and 2 for the 700°C case show good repeatability, as can be seen in Figure 5.7. The values of the heat transfer results are within 5% of each other.

Figure 5.8 shows the heat transfer distribution through the packed bed with its associated uncertainty for the 600°C case of both experimental tests. The functions describing the heat transfer rate at a certain position in the pebble bed are given in Equation (5.4) and (5.5) for Test 1 and Test 2 with a maximum uncertainty of 32.83 W and 37.72 W.

$$Q_{bed,1,600C}(y) = 755.375801y^3 + 266.899881y^2 - 811.929221y + 881.808960 \quad (5.4)$$

$$Q_{bed,2,600C}(y) = 945.399275y^3 + 163.569817y^2 - 815.629321y + 1008.546587 \quad (5.5)$$

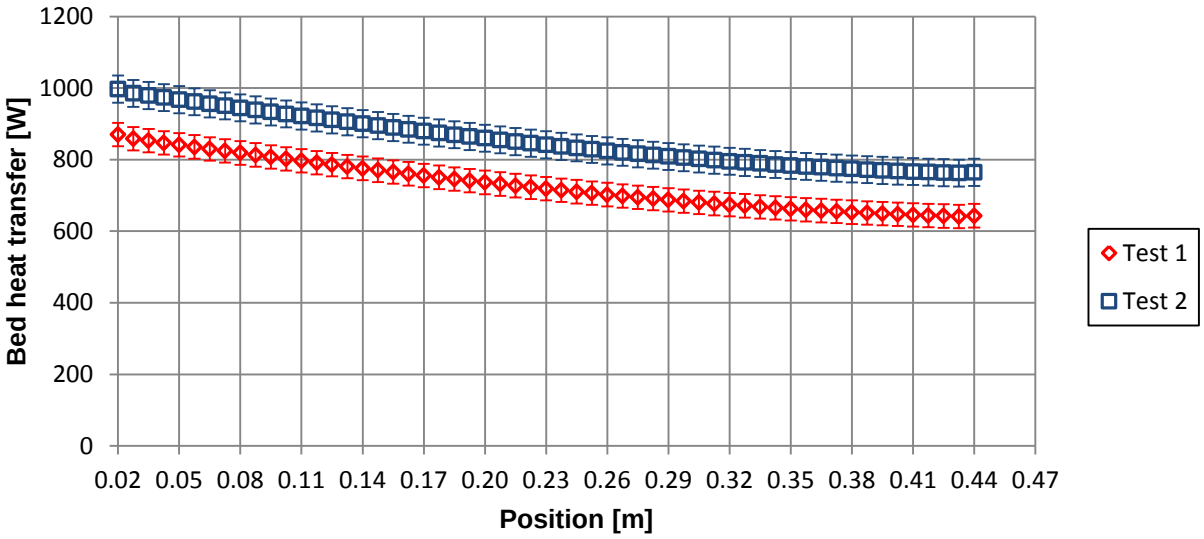

Figure 5.8: Measured heat transfer through pebble bed as a function of position for the 600°C case of both tests.

For the Test 1 and Test 2 the measured heat removed via the water jacket were 643.14 ± 30.68W and 764.14 ± 36.62W, the total heat loss through all the insulation walls 227.06 ± 11.68W and 232.45 ± 9.03W and the heat loss via the element coolers 283.88 ± 10.01 W and 466.83 ± 21.64 W. A larger amount of heat was lost via the element coolers for Test 2, because after Test 1 an inspection of the heater elements showed signs that the temperatures at the electrical connections of the heater elements were too high thus not enough heat was being extracted via the element coolers. To protect the system against damage the water mass flow rate through the element coolers was increased for Test 2.

The values of the heat transfer results for Test 1 and Test 2 are within 15.86% of each other. The repeatability between the heat transfer results for Test 1 and Test 2 of the 600°C case is not as good as the repeatability of the results for the 700°C case, as can be seen in Figure 5.8. The trend of the heat transfer distribution through the packed bed of spheres is similar for Test 1 and 2. The reason for the larger difference between the heat transfer results for the two tests is the design of the water jacket.

For Test 1 the temperature difference over the water jacket heat exchanger, ΔT_{wj}, was 6.34°C with an uncertainty of 0.30°C whilst the temperature difference for Test 2 was 7.67°C with an

uncertainty of 0.32°C. Thus the margin of error associated with ΔT_{wj} for Test 1 is 4.73% and 4.17% for Test 2. The water mass flow rate through the water jacket was measured as 0.0243 kg/s with an uncertainty of 0.0001 kg/s for Test 1 and 0.0238 kg/s with an uncertainty of 0.0006 kg/s for Test 2. Although the difference between the values for ΔT_{wj} of each of the tests does not seem significant, it creates a 15.86% difference between the amounts of heat extracted via the water jacket for each of the tests.

From Equation (B.9) it is clear that even though the error associated with ΔT_{wj} seems small it will increase the overall uncertainty of the heat extracted via the water jacket significantly. A relative small uncertainty associated with a smaller temperature difference results in a larger margin of error than a small uncertainty associated with a larger temperature difference. As a result the repeatability of the heat transfer results are adversely affected and a large margin of error exists between the heat transfer distributions for the two tests.

In order to reduce the effect of this problem and minimise the error associated with the temperature difference over the water jacket, the original design of the NWETCTF water jacket was done for a temperature difference of 10°C. For future experimental tests conducted with the NWETCTF care should be taken by the operators to maintain a temperature difference over the water jacket of at least 10°C. However, the temperature difference over the water jacket should not exceed 10°C as this will result in a non-uniform temperature distribution over the outer reflector of the test section.

As this study was focused on the development of a methodology to obtain experimental data as well as the commissioning of the NWETCTF facility, the scope of the project included the identification of such problems. Thus recommendations can be made for future studies to ensure accurate experimental results are obtained. Consequently the larger margin of error between the heat transfer results does not negatively affect the outcome of the project and the results are still useful and applicable for the development of the required methodology.

The heat transfer distribution through the packed pebble bed for the 500°C case of Test 1 and Test 2 is shown in Figure 5.9. Equation (5.6) and (5.7) describe the heat transfer rate through the packed bed as a function of position for Test 1 and Test 2 respectively;

$$Q_{bed,1,500C}(y) = 349.794020y^3 + 371.953573y^2 - 630.766251y + 585.965582 \quad (5.6)$$

$$Q_{bed,2,500C}(y) = 543.665708y^3 + 265.064365y^2 - 632.402228y + 706.588874 \quad (5.7)$$

with a maximum uncertainty of 30.08 W for Test 1 and 33.66 W for Test 2.

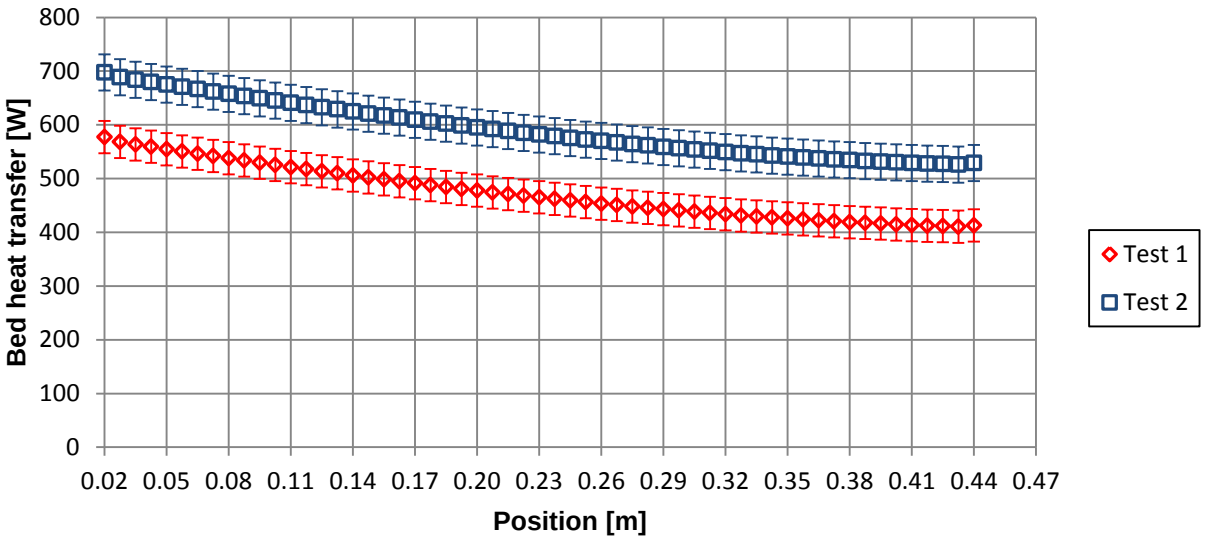

Figure 5.9: Measured heat transfer through pebble bed as a function of position for the 500°C case of both tests.

For the Test 1 and Test 2 the measured heat extracted through the water jacket were 412.96 ± 28.61W and 528.67 ± 33.14W, the total heat loss through all the insulation walls 164.06 ± 9.27W and 168.93 ± 5.93W and the heat removed via the element coolers 405.95 ± 14.13 W and 521.07 ± 23.97 W. The values of the heat transfer results are within 21.89% of each other.

Similar to the results for the 600°C case the repeatability between the heat transfer results for the 500°C case is not as good as the repeatability for the heat transfer results of the 700°C case. The reason for the large margin of error was discussed previously with the results of the 600°C case. For Test 1 the measured temperature difference over the water jacket was 4.73°C with an uncertainty of 0.32°C whereas for Test 2 it was 5.37°C with an uncertainty of 0.32°C. The water mass flow rate through the water jacket was measured as 0.0209 kg/s with an uncertainty of 0.0003 kg/s for Test 1 and 0.0235 kg/s with an uncertainty of 0.0005 kg/s for Test 2.

The 11.06% difference between the measured water mass flow rates for the two tests also had a significant contribution to the difference between the heat transfer results of the two tests. It is therefore also important that the operator maintain similar water mass flow rates when conducting separate tests at the same conditions. This too was a learning curve as it was the first time that the NWETCTF system was operated and used to obtain experimental data.

Figure 5.10 shows the heat transfer distribution through the packed bed with its associated uncertainty for the 400°C case of both experimental tests. The functions describing the heat transfer rate at a certain position in the pebble bed are given in Equation (5.8) and (5.9) for Test 1 and Test 2 with a maximum uncertainty of 16.13 W and 22.47 W.

$$Q_{bed,1,400C}(y) = 157.107970y^3 + 330.523211y^2 - 447.257528y + 403.921489 \quad (5.8)$$

$$Q_{bed,2,400C}(y) = 313.351808y^3 + 236.063324y^2 - 455.407671y + 349.169572 \quad (5.9)$$

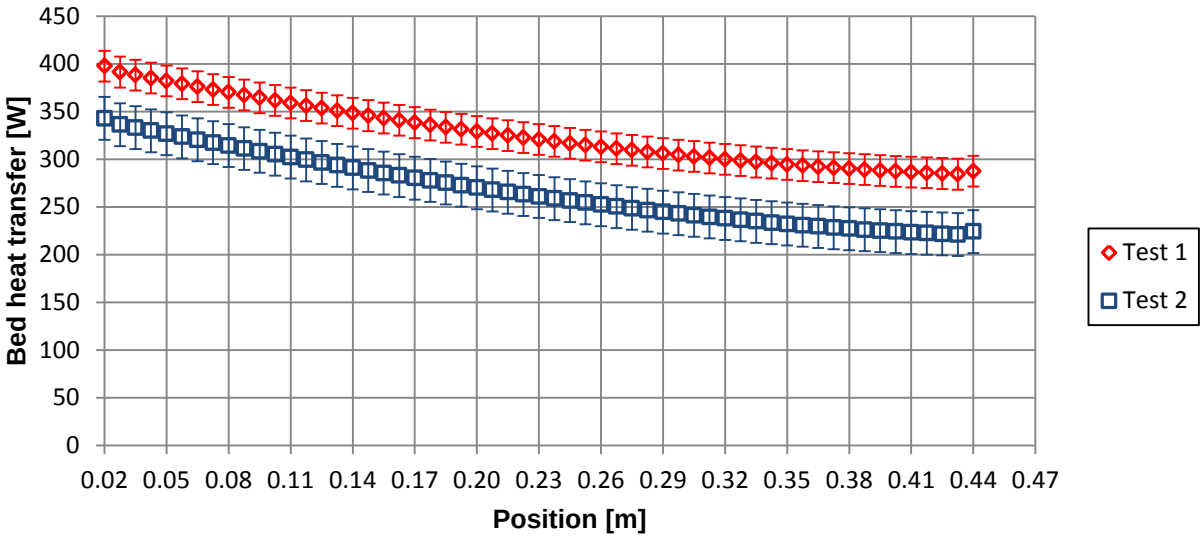

Figure 5.10: Measured heat transfer through pebble bed as a function of position for the 400°C case of both tests.

For the Test 1 and Test 2 the measured heat removed via the water jacket were 287.42 ± 15.12 W and 224.11 ± 21.93 W, the total heat loss through all the insulation walls 110.23 ± 5.59 W and 118.66 ± 4.87 W and the heat loss via the element coolers 258.18 ± 11.46 W and 193.41 ± 17.60 W. The values of the heat transfer results for Test 1 and Test 2 are within 22.03% of each other.

As for the 500°C and 600°C cases the repeatability of the heat transfer results for the 400°C case is not as good as the repeatability for the 700°C case. For Test 1 the measured temperature difference over the water jacket was 5.54°C with an uncertainty of 0.28°C whereas for Test 2 it was 5.18°C with an uncertainty of 0.35°C. The water mass flow rate through the water jacket was measured as 0.0124 kg/s with an uncertainty of 0.0001 kg/s for Test 1 and 0.0103 kg/s with an uncertainty of 0.0007 kg/s for Test 2.

As discussed previously, the small temperature difference over the water jacket as well as the 16.94% difference between the measured water mass flow rates for the two experimental tests caused the large difference between the heat transfer results for Test 1 and Test 2. It is important to note that for future experimental work done with the NWETCTF the temperature difference over the water jacket should be maintained as close to 10°C as possible and not less. This will ensure good repeatability is achieved between the measured heat transfer results of identical but separate tests.

5.1.3 Temperature distribution function results

The measured experimental temperature results obtained from the NWETCTF showed good repeatability between Test 1 and Test 2 for all the cases, as was discussed in section 5.1.1. Since good repeatability was obtained between Test 1 and Test 2 the measured temperature results were combined to form a single data set of measured temperatures that was used to calculate the temperature distribution function and temperature gradient for each of the cases.

The method described in section 4.3.4 with a fifth order polynomial was used to obtain the temperature distribution functions for each of the test cases. The temperature distribution function fitted to the measured experimental temperature data for the 800°C case is shown in Figure 5.11. The upper and lower uncertainty bounds of the function are also indicated on the graph although they are barely visible as the uncertainty values are very small.

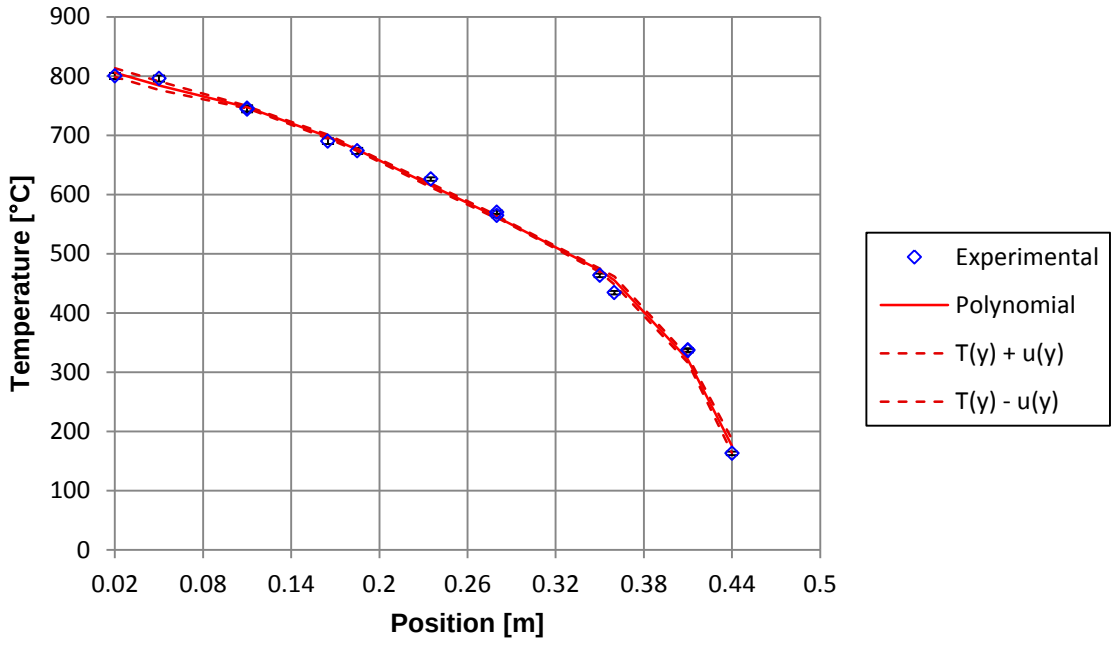

Figure 5.11: Measured temperatures with fifth order polynomial curve fit and uncertainties for the 800°C test case.

The temperature distribution function for the 800°C test case is given in Equation (5.10) showing the coefficients calculated for the curve fit:

$$T_{800C}(y) = 829 - 1433y + 15644y^2 - 119792y^3 + 353861y^4 - 370541y^5 \quad (5.10)$$

The temperature distribution function fitted to the measured experimental temperature data for the 700°C case is shown in Figure 5.12. The upper and lower uncertainty bounds of the function are also indicated on the graph although they are barely visible as the uncertainty values are very small. Equation (5.11) describes the temperature distribution function for the 700°C test case with its calculated coefficients.

$$T_{700C}(y) = 722 - 1058y + 9517y^2 - 78304y^3 + 238701y^4 - 256949y^5 \quad (5.11)$$

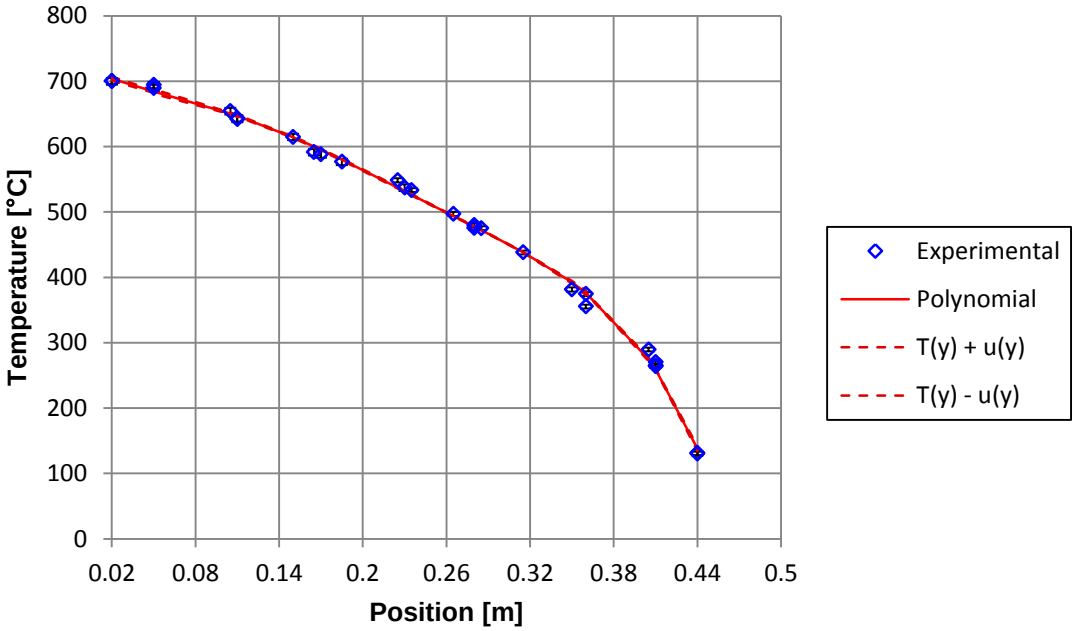

Figure 5.12: Measured temperatures with fifth order polynomial curve fit and uncertainties for the 700°C test case.

For the 600°C case the temperature distribution function fitted through the measured temperature results and its uncertainties are shown in Figure 5.13. The temperature distribution function with the calculated coefficients of the polynomial is given in Equation (5.12).

$$T_{600C}(y) = 618 - 836y + 5667y^2 - 49168y^3 + 150831y^4 - 163843y^5 \quad (5.12)$$

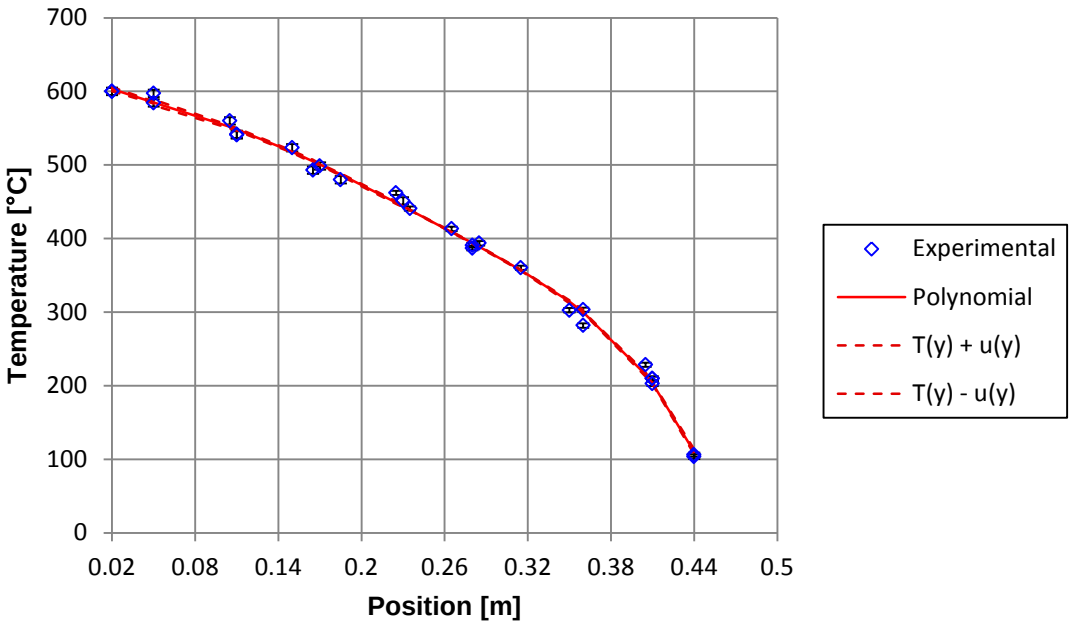

Figure 5.13: Measured temperatures with fifth order polynomial curve fit and uncertainties for the 600°C test case.

The temperature distribution function fitted to the measured experimental temperature data for the 500°C case with its associated uncertainty ranges is shown in Figure 5.14. Equation (5.13) describes the temperature distribution function for the 500°C test case with its calculated coefficients.

$$T_{500C}(y) = 517 - 816y + 3640y^2 - 29345y^3 + 86832y^4 - 93180y^5 \quad (5.13)$$

For the 400°C case the temperature distribution function fitted through the measured temperature results and its uncertainties are shown in Figure 5.15. The temperature distribution function with the calculated coefficients of the polynomial is given in Equation (5.14).

$$T_{400C}(y) = 414 - 720y + 2236y^2 - 15867y^3 + 44650y^4 - 47760y^5 \quad (5.14)$$

When comparing the results for the various test cases it is clear that the wall effect as well the effect of radiation can be seen for the cases of higher temperatures as noted in the discussion of the measured temperature results in section 5.1.1. For the 800°C, 700°C and 600°C cases the temperatures next to the heated wall are higher and almost equal to the temperatures measured at the wall and the temperature distribution decreases at a more consistent trend at approximately 1.5 sphere diameters from the wall. However, for the 500°C and 400°C cases the temperature distributions next to the wall decrease gradually almost with a more linear trend throughout the packed pebble bed.

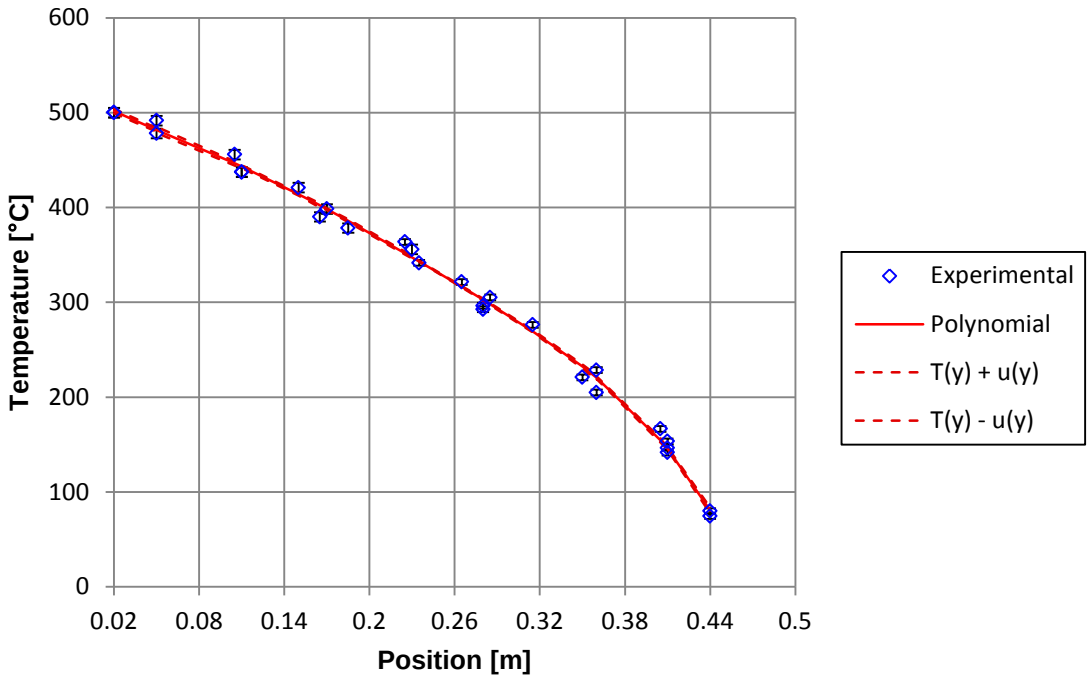

Figure 5.14: Measured temperatures with fifth order polynomial curve fit and uncertainties for the 500°C test case.

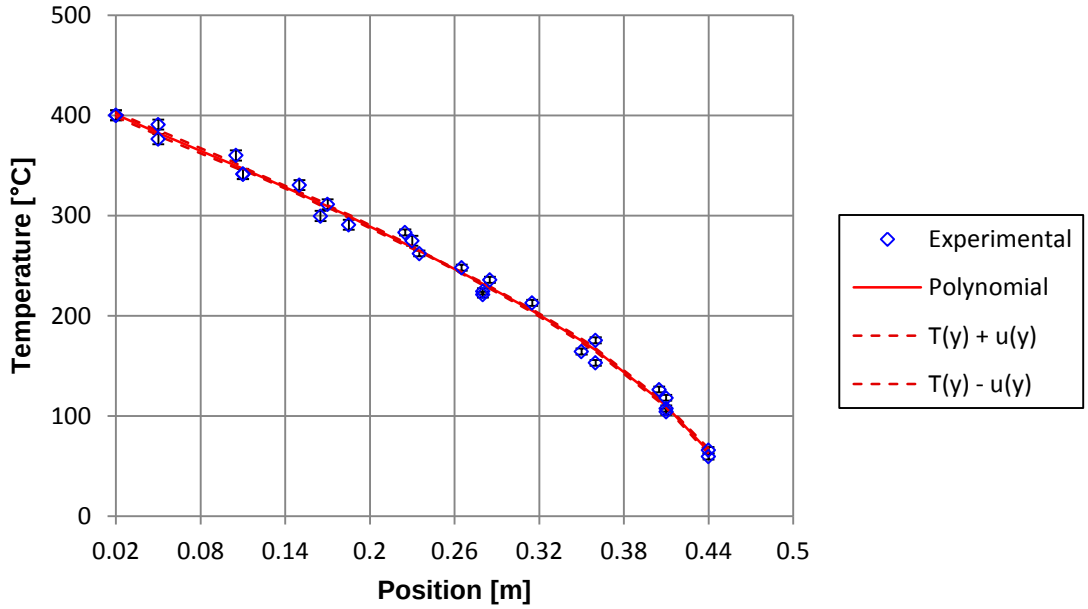

Figure 5.15: Measured temperatures with fifth order polynomial curve fit and uncertainties for the 400°C test case.

The difference between the gradient of the fitted polynomial curve for the temperature distribution next to the wall of the higher and lower temperature cases is due to the wall effect and the contribution of radiation to the overall heat transfer. As discussed in section 5.1.1 with

the wall effect present next to the heated wall the packing structure has a higher average porosity in the wall region than in the near-wall region, thus more voids are present in the wall region. With more voids present in the wall region the packing of spheres next to the wall is less dense and therefore less contact points exist through which conduction heat transfer can occur.

Following the discussion in section 2.2.1 it was concluded that the contribution of radiation and conduction heat transfer in a pebble bed becomes equal at approximately 675°C and the radiation component increases significantly at higher temperatures. From the higher temperature distributions in the wall region for the 800°C, 700°C and 600°C cases the increasing contribution of the radiation component is visible. One can also see how the contribution of the radiation component decreases for the 500°C and 400°C cases resulting in the almost linear temperature distributions.

The packed pebble bed for the experimental setup also included wall effects at the cooled wall and the insulation walls as discussed in section 4.2.3. Thus a wall region was also present next to the cooled wall for all of the cases. The effect of the variation in the packing structure next to the cooled wall is clearly visible for the results of all of the cases showing a steep decrease in the temperature distribution next to the cooled wall. As the temperatures next to the cooled wall are lower than about 400°C for all of the cases radiation does not play such a significant role in the variation of the temperature distribution. The temperature distribution next to the cooled wall is mainly affected by the variation in the packing structure, with less physical contact points resulting in less conduction heat transfer and lower temperatures.

5.1.4 Temperature gradient function results

The method described in section 4.3.5 was used to obtain the polynomial curve that best describes the temperature gradient of the temperature distribution functions presented in section 5.1.3. The upper and lower uncertainty bounds associated with the temperature gradient function was also determined for each of the test cases.

For the 800°C case the temperature gradient as a function of position from the heated wall is shown in Figure 5.16. The uncertainties are barely visible as the uncertainty values are small, except for the regions directly next to the walls. In the regions next to the walls the uncertainty values are larger; this could be as a result of the influence of the wall effect being more prominent in these areas. The temperatures measured at the reflector walls were also included in the calculation of the temperature gradient and can also result in the larger uncertainty values.

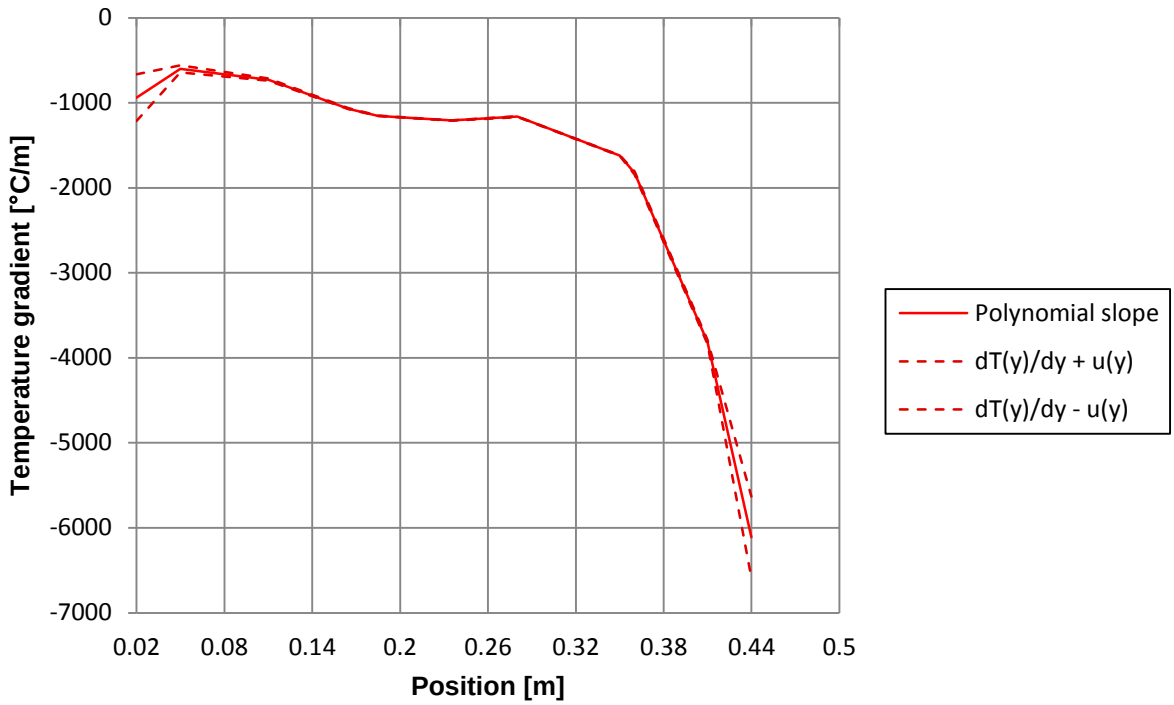

Figure 5.16: Temperature gradient function with uncertainties for the 800°C test case.

The temperature gradient function for the 700°C test case is shown in Figure 5.17 with its calculated uncertainties that are barely visible as the values are very small. The uncertainty values for the regions directly next to the walls are smaller than the uncertainty values for these regions for the 800°C case. The experimental data set used for the calculations of the 800°C case had less data points than for the other cases as only one experimental test was performed for the 800°C case. This could also contribute to the larger uncertainty values in the regions next to the walls.

For the 600°C case the temperature gradient as a function of position from the heated wall with its upper and lower uncertainty ranges is shown in Figure 5.18. As for the 800°C and 700°C cases the uncertainties for the regions next to the walls are larger than the uncertainties for the regions closer to the middle of the pebble bed. The temperature gradient function for the 500°C test case is shown in Figure 5.19 with the uncertainty values showing the same trend as that of the 800°C, 700°C and 600°C cases.

For the 400°C case the temperature gradient as a function of position from the heated wall with its upper and lower uncertainty ranges is shown in Figure 5.20. There is a significant difference in the magnitude of the temperature gradient results for the higher and lower temperature cases. This is expected as the heat flux through the packed bed of spheres is much higher for the 800°C case than for the 400°C case.

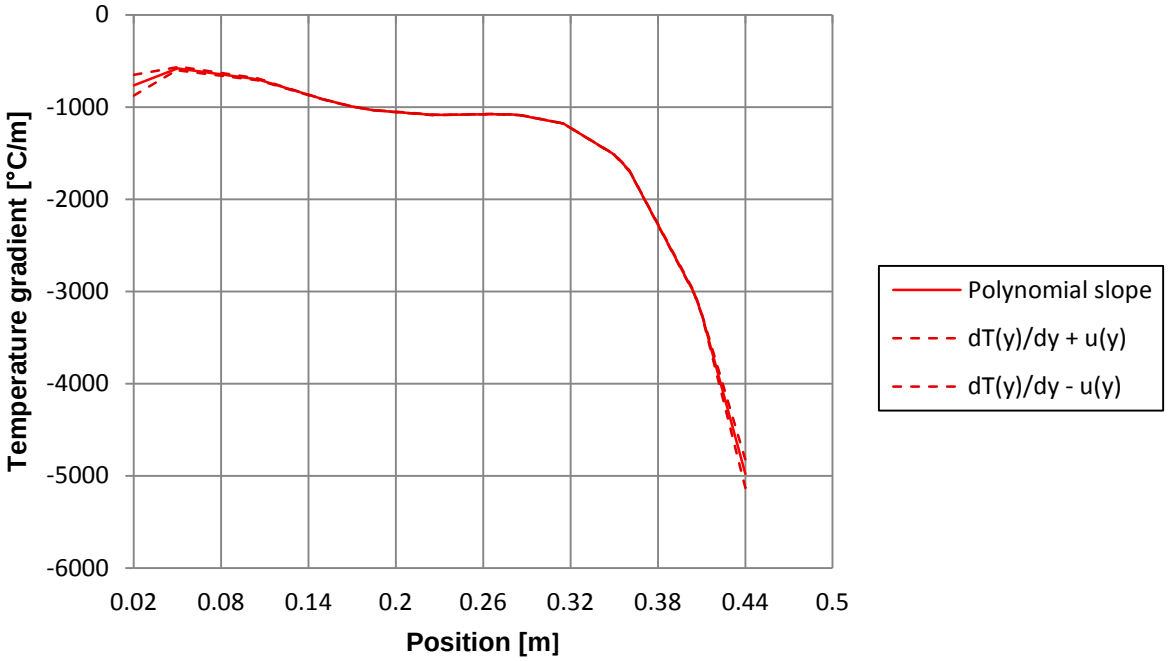

Figure 5.17: Temperature gradient function with uncertainties for the 700°C test case.

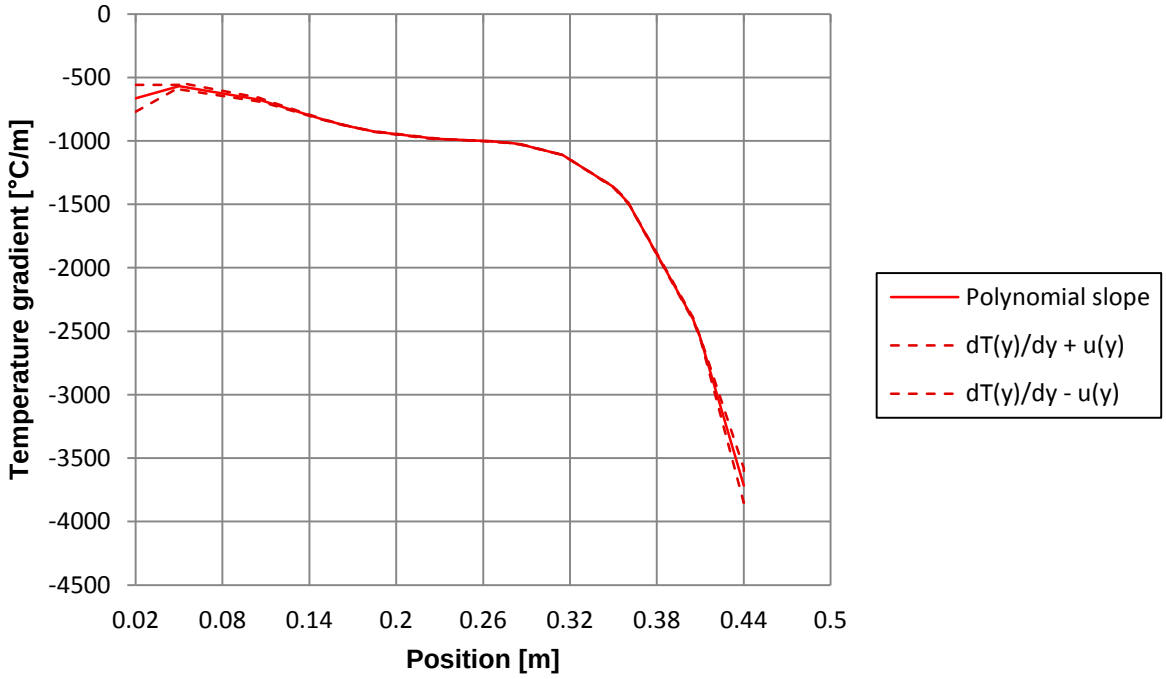

Figure 5.18: Temperature gradient function with uncertainties for the 600°C test case.

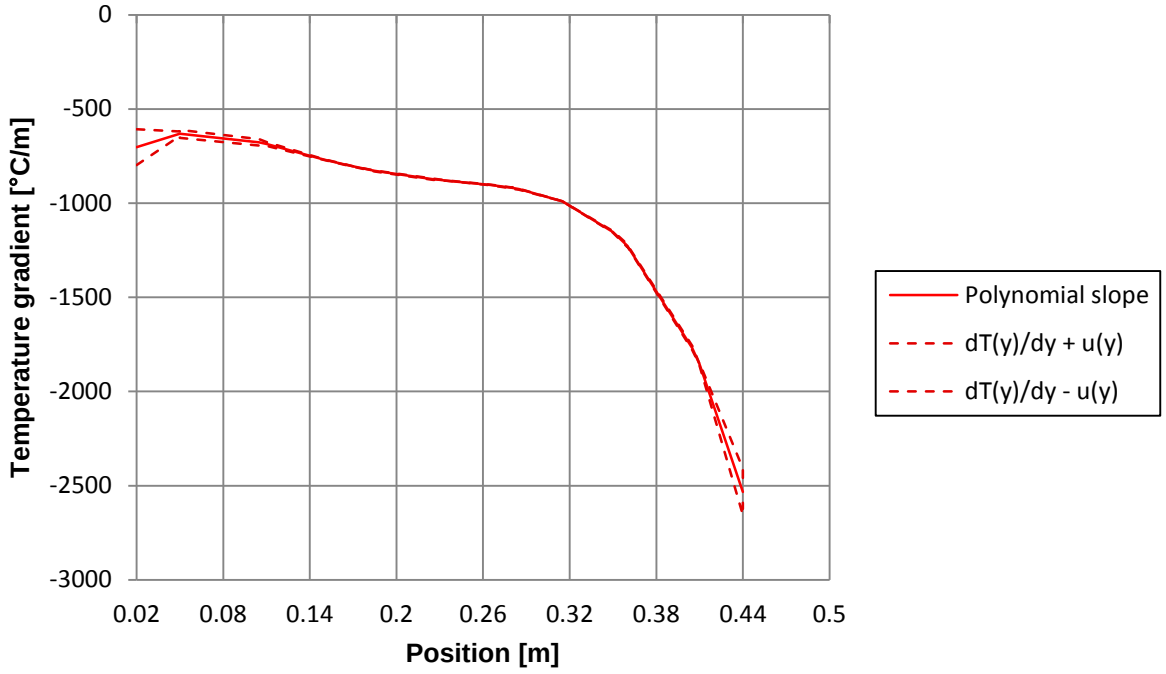

Figure 5.19: Temperature gradient function with uncertainties for the 500°C test case.

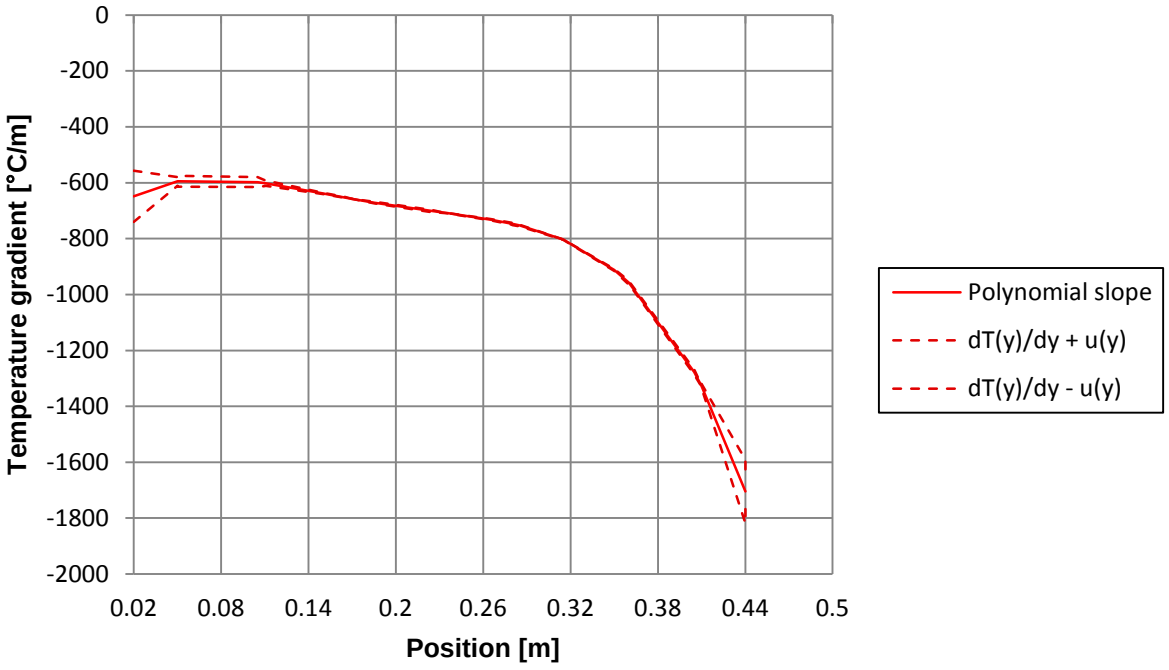

Figure 5.20: Temperature gradient function with uncertainties for the 400°C test case.

5.1.5 Effective thermal conductivity results

Following the discussion in section 4.3.2 it was established that the temperature gradient as well as the heat transfer distribution through the packed bed of spheres were required to calculate the effective thermal conductivity.

Even though the repeatability between the measured heat transfer results, presented in section 5.1.2, was not as good as the repeatability between the measured temperature results, the average heat transfer distribution of Test 1 and Test 2 was used for the effective thermal conductivity calculations. Thus a single data set of average heat transfer values for the two experimental tests was obtained.

The method described in section 4.3.2 was used for the calculation of the effective thermal conductivity for each of the test cases. Detailed results of the calculated effective thermal conductivity values together with their associated uncertainties for each of the test cases are given in Annexure B.3. The effective thermal conductivity calculated for the 800°C test case with its associated uncertainties as a function of position and as a function of temperature is shown in Figure 5.21 and Figure 5.22 respectively.

Figure 5.23 and Figure 5.24 show the effective thermal conductivity calculated for the 700°C test case with its associated uncertainties as a function of position and as a function of temperature. The effective thermal conductivity calculated for the 600°C test case with its associated uncertainties as a function of position and as a function of temperature is shown in Figure 5.25 and Figure 5.26 respectively.

Figure 5.27 and Figure 5.28 show the effective thermal conductivity calculated for the 500°C test case with its associated uncertainties as a function of position and as a function of temperature. The effective thermal conductivity calculated for the 400°C test case with its associated uncertainties as a function of position and as a function of temperature is shown in Figure 5.29 and Figure 5.30 respectively.

As discussed in section 4.2.3 and the analysis of the temperature distribution results the packing structure of the packed bed of spheres included wall effects next to both the heated and cooled walls. Thus a near-wall region existed next to the heated wall as well as the cooled wall during the experimental tests. This means that the values of the effective thermal conductivity presented were influenced by the packing structure in the near-wall region for all of the test cases.

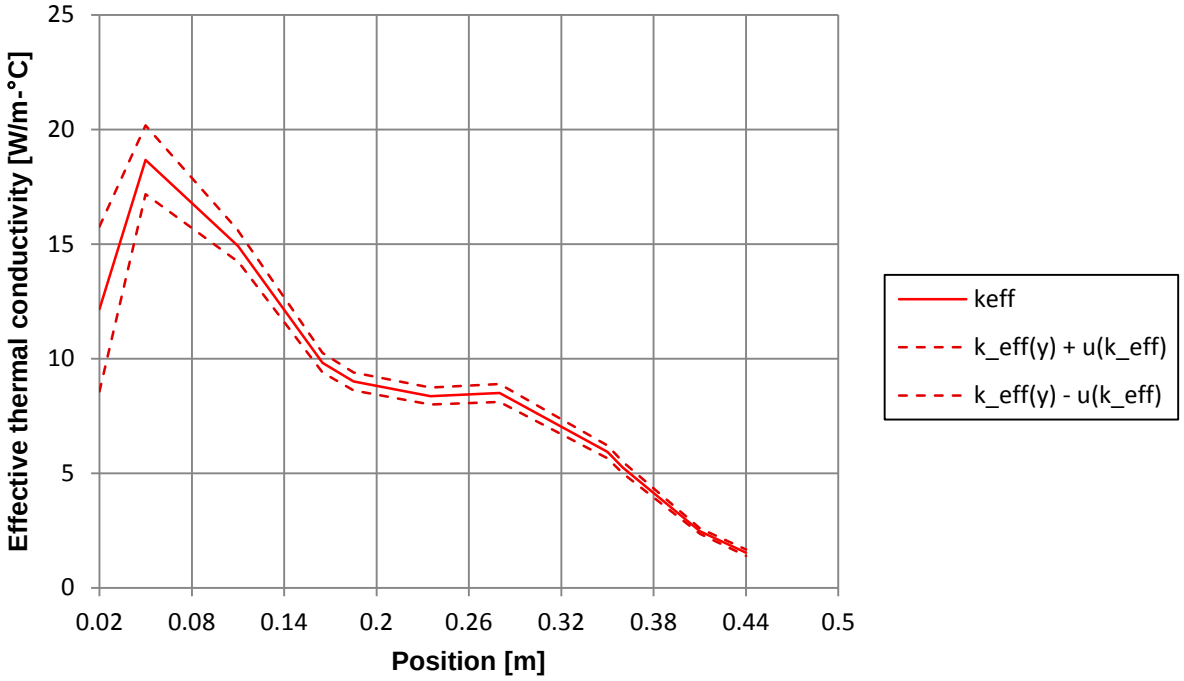

Figure 5.21: Effective thermal conductivity with uncertainties as a function of position from the heated wall for the 800°C test case.

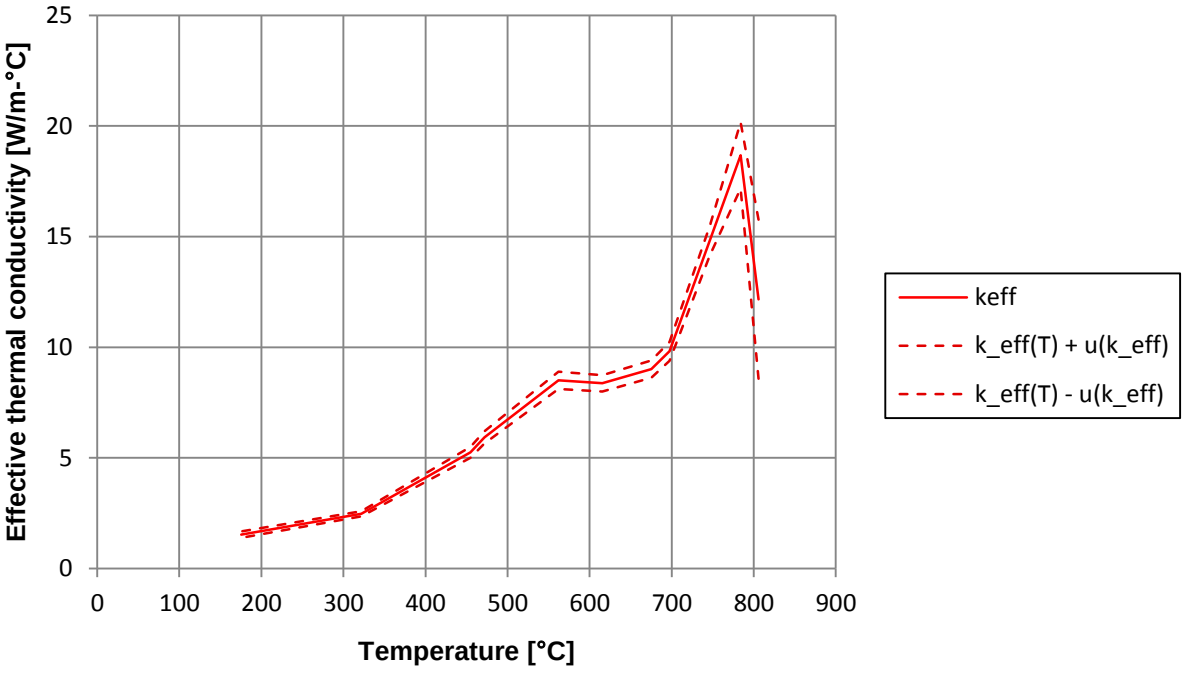

Figure 5.22: Effective thermal conductivity with uncertainties as a function of temperature for the 800°C test case.

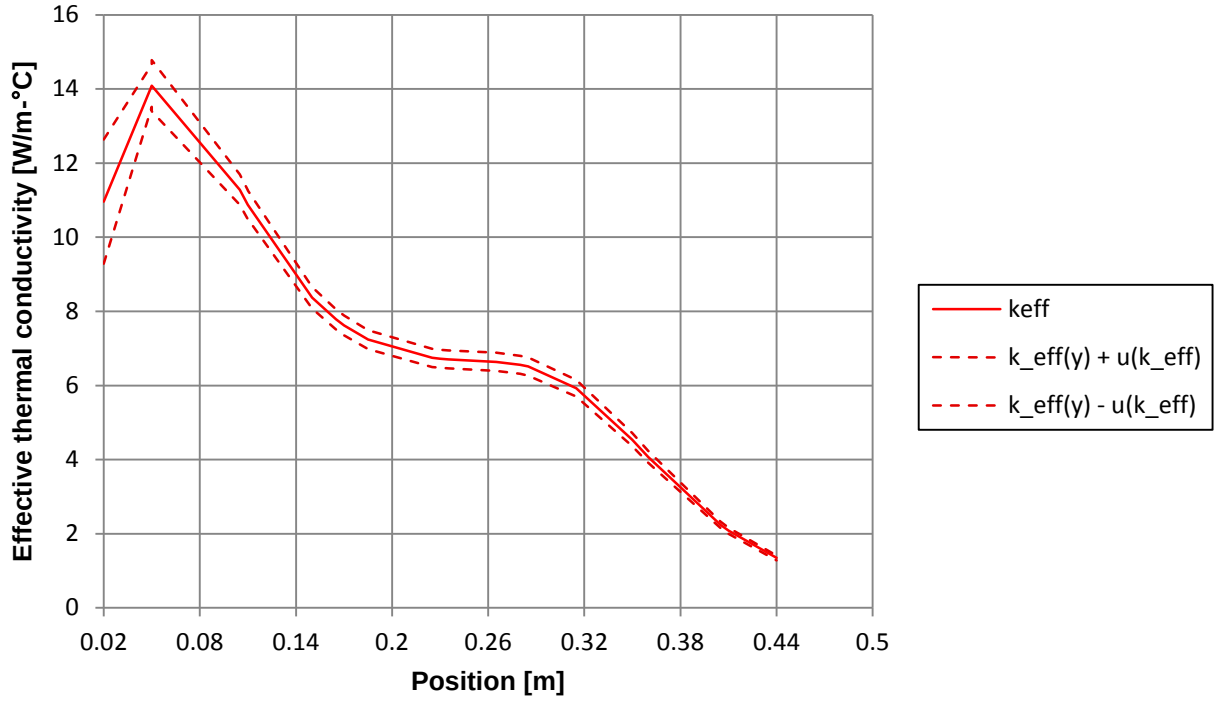

Figure 5.23: Effective thermal conductivity with uncertainties as a function of position from the heated wall for the 700°C test case.

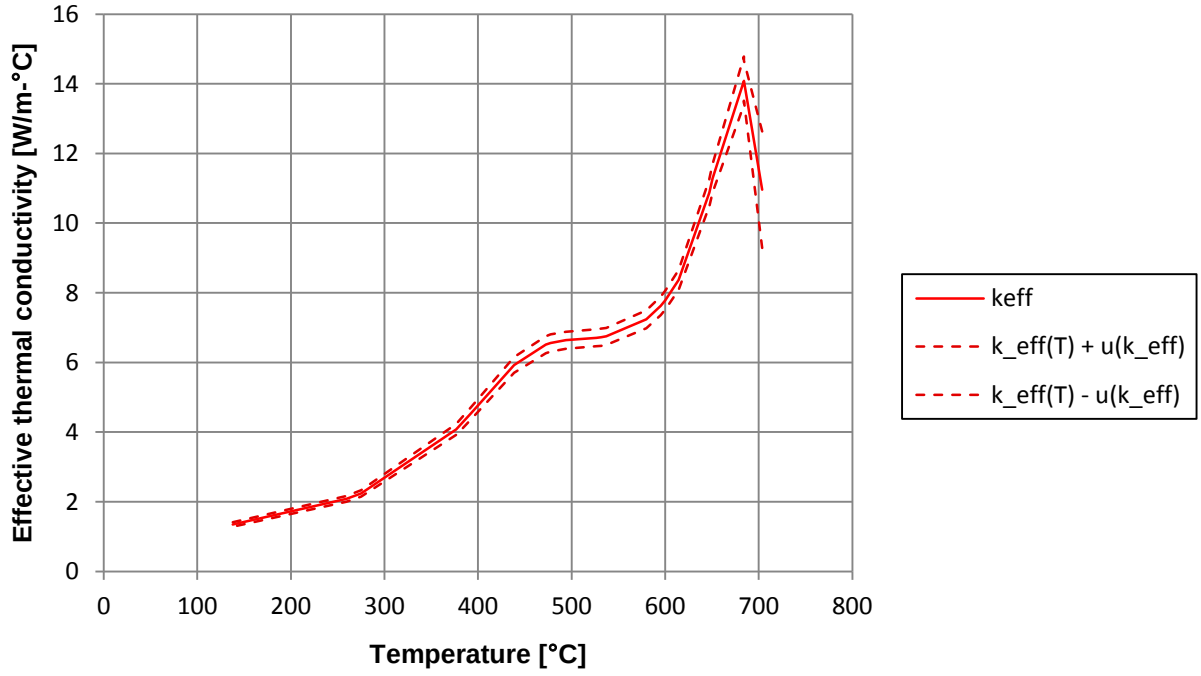

Figure 5.24: Effective thermal conductivity with uncertainties as a function of temperature for the 700°C test case.

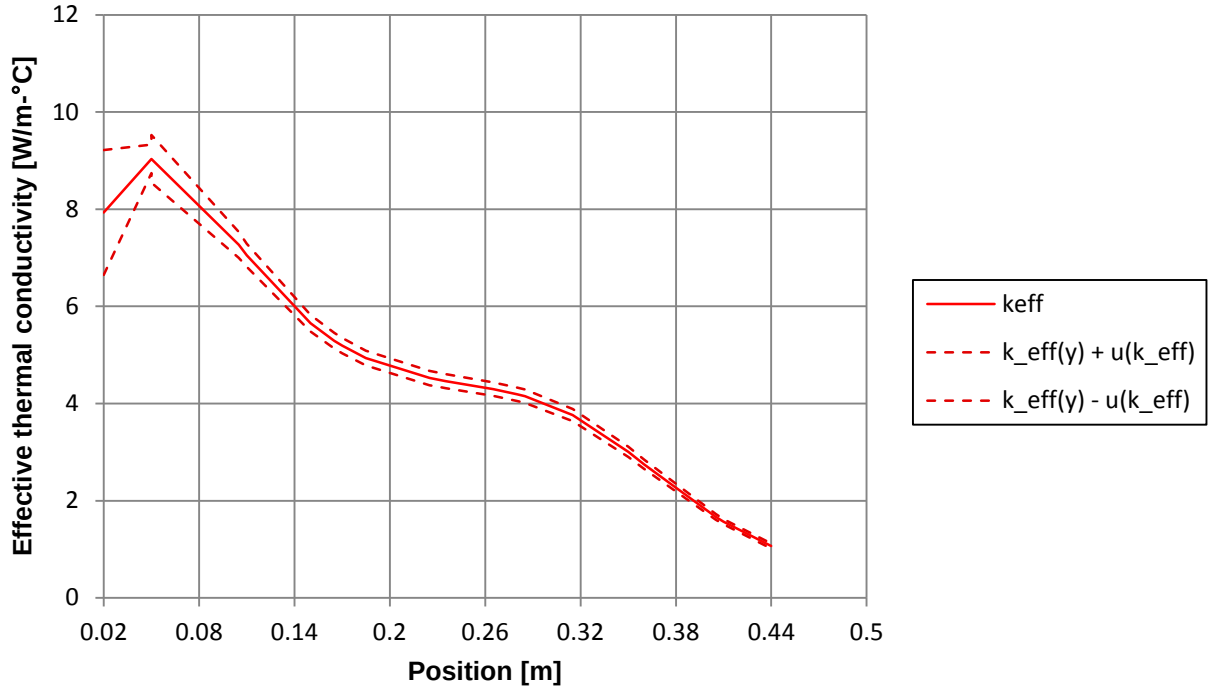

Figure 5.25: Effective thermal conductivity with uncertainties as a function of position from the heated wall for the 600°C test case.

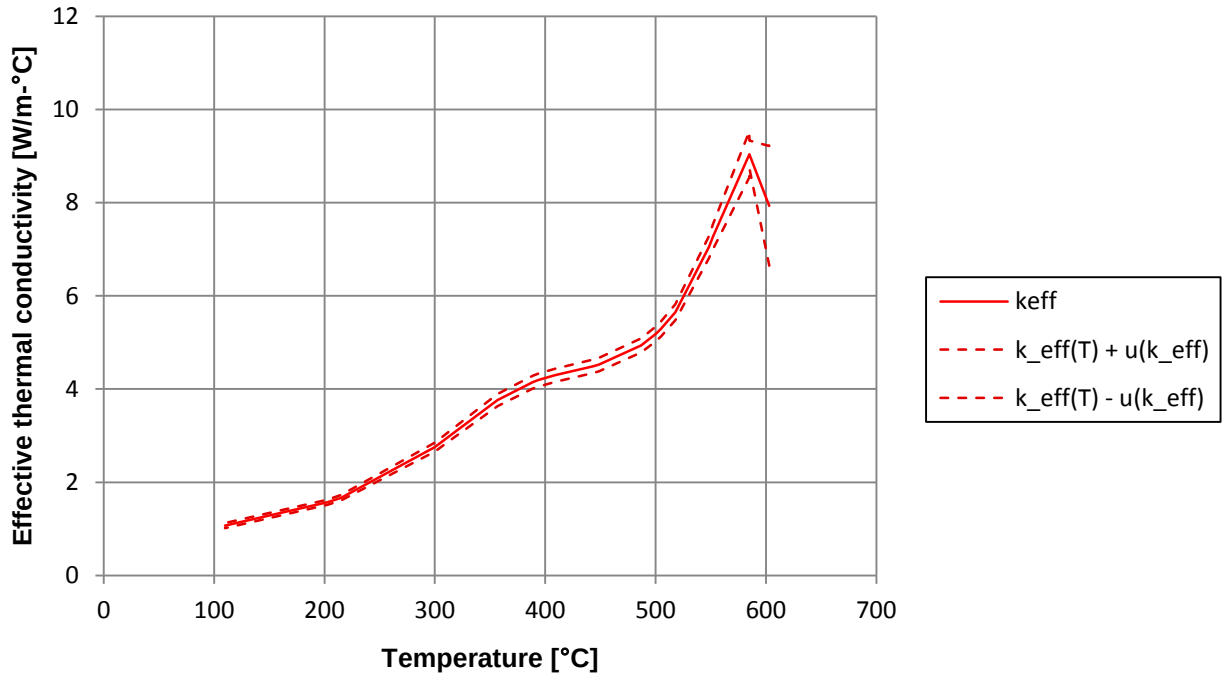

Figure 5.26: Effective thermal conductivity with uncertainties as a function of temperature for the 600°C test case.

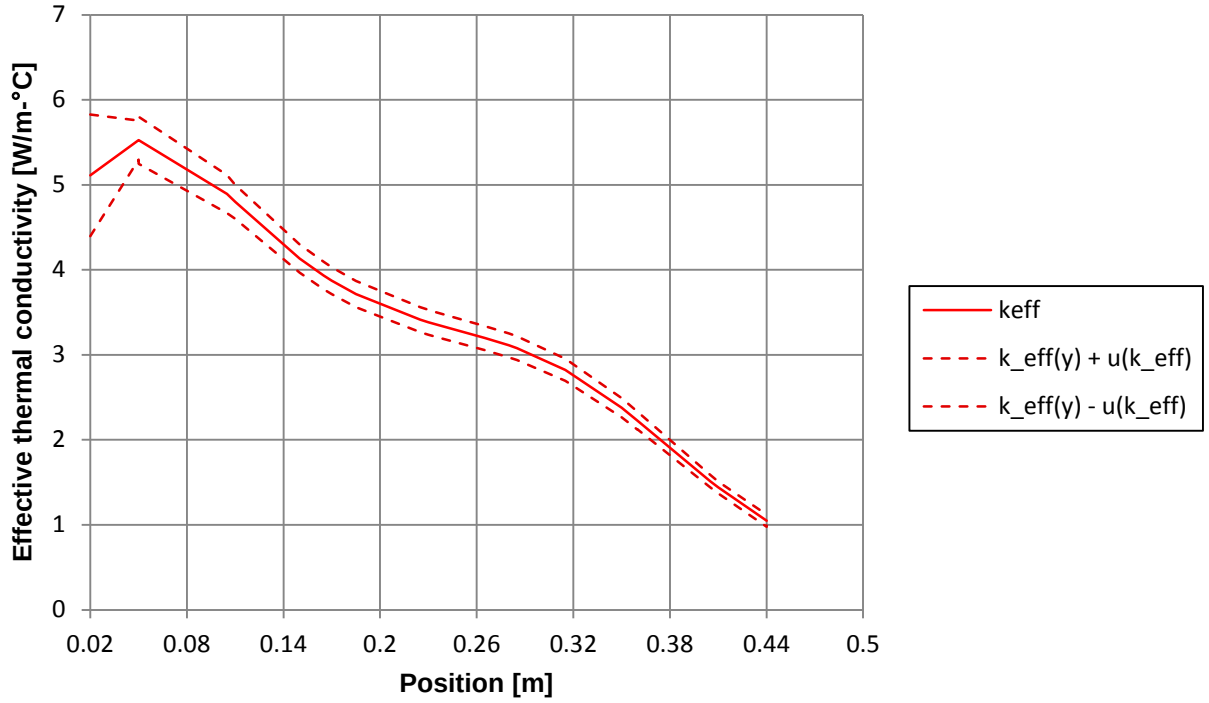

Figure 5.27: Effective thermal conductivity with uncertainties as a function of position from the heated wall for the 500°C test case.

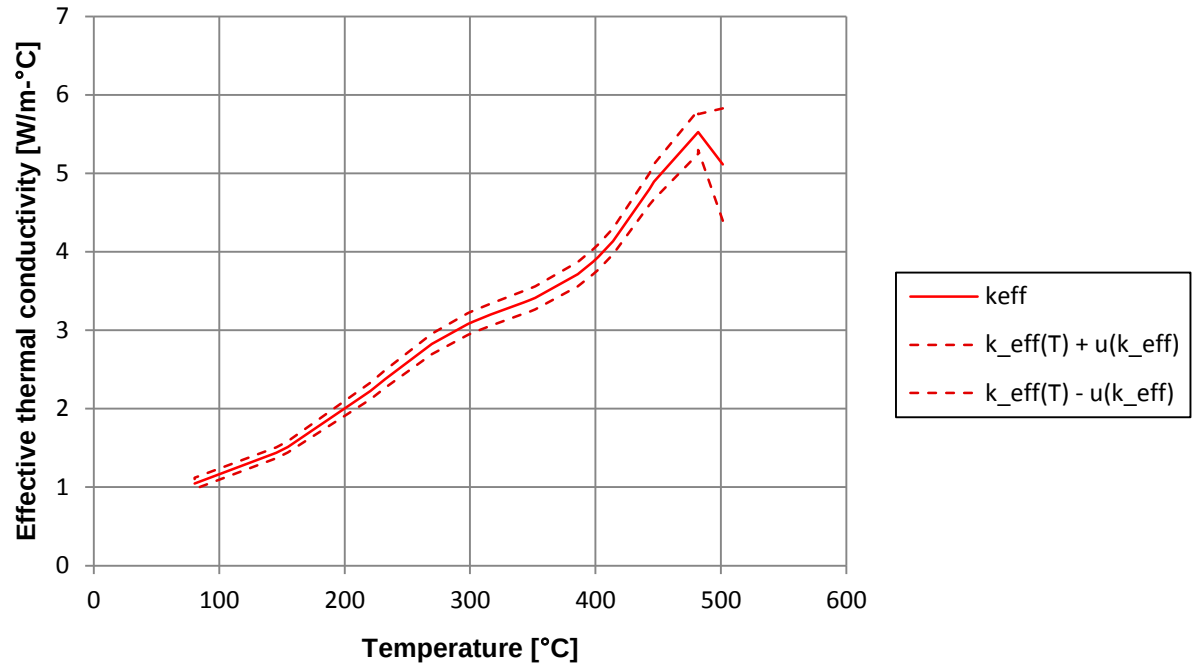

Figure 5.28: Effective thermal conductivity with uncertainties as a function of temperature for the 500°C test case.

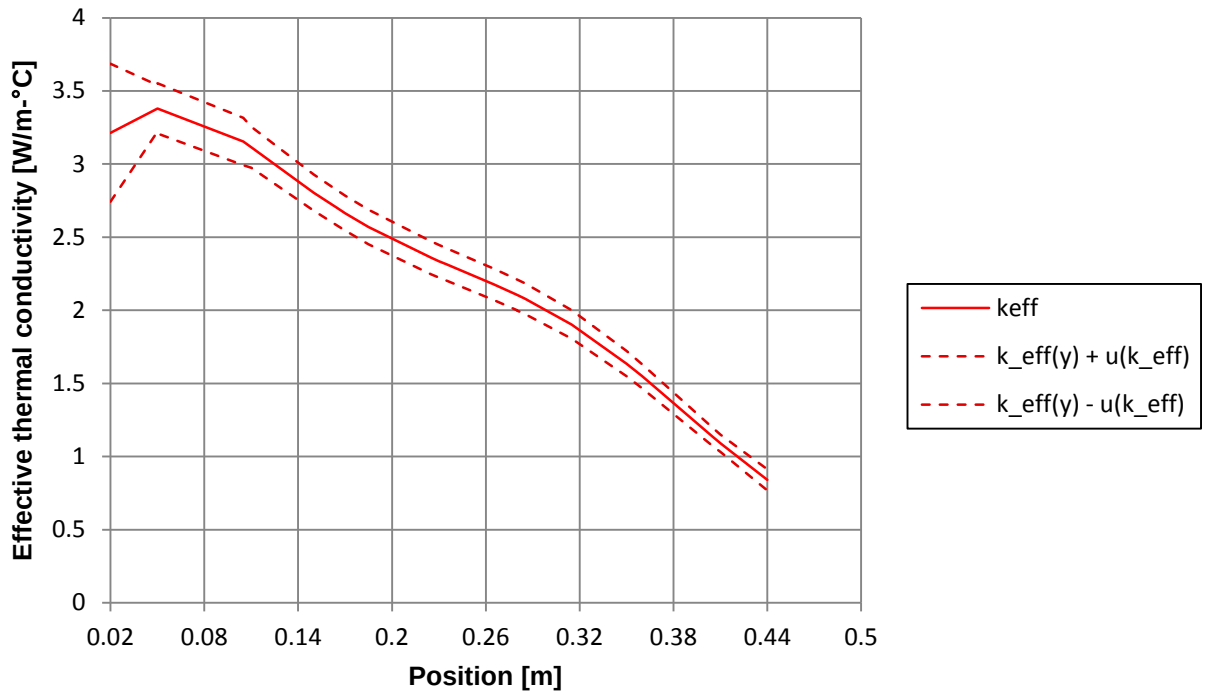

Figure 5.29: Effective thermal conductivity with uncertainties as a function of position from the heated wall for the 400°C test case.

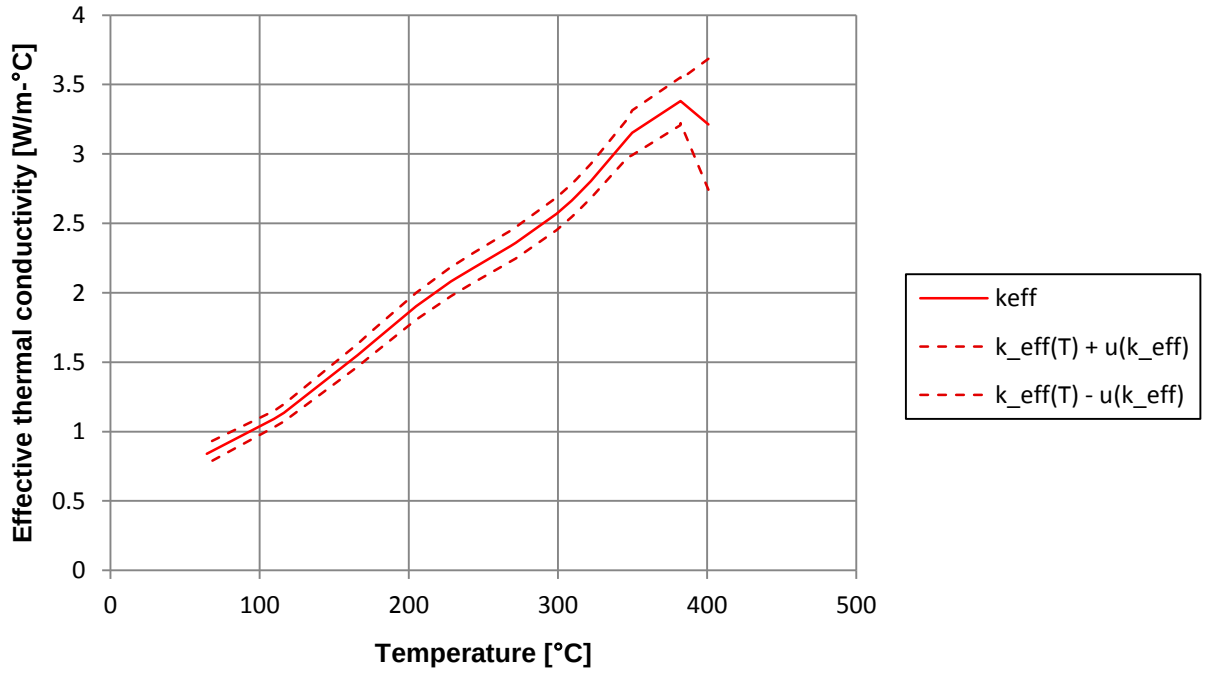

Figure 5.30: Effective thermal conductivity with uncertainties as a function of temperature for the 400°C test case.

Due to the effect of the variation in packing structure in the near-wall region a sharp peak can be seen for the effective thermal conductivity values next to the heated wall for all of the test cases. The surface temperatures measured at the heated and cooled walls were also included in the calculation of the effective thermal conductivity which can also contribute to the sharp peak in the calculated values. For all of the graphs of the effective thermal conductivity as a function of position a sharp increase can be seen in the effective thermal conductivity values up to roughly 0.5 sphere diameters from the heated wall after which the values decreases significantly.

The peak in the effective thermal conductivity results is much more prominent for the higher temperature cases, shown in Figure 5.21 and Figure 5.23, and the size of the peak gradually decreases for the lower temperature cases, shown in Figure 5.25, Figure 5.27 and Figure 5.29. The reason for this is that for the higher temperature cases the temperatures next to the heated wall is much higher than for the lower temperature cases and thus radiation contributes more significantly to the overall heat transfer than for the lower temperature cases.

The effect of the altered packing structure on the effective thermal conductivity values in the near-wall region next to the cooled wall is not as distinct as the effect due to the near-wall region next to the heated wall. However, a change in the gradient of the effective thermal conductivity curve can be noted for all of the test cases. The change in the gradient is less prominent for the lower temperature cases owing to the lower temperatures for these cases. The fact that the effect of the altered packing structure is more prominent for the near-wall region next to the heated wall than for near-wall region next to the cooled wall can be attributed to the lower temperatures at the cooled wall. As a result conduction heat transfer is dominant at the cooled wall and the radiation contribution is less significant.

A comparison of the effective thermal conductivity results for all of the test cases is shown in Figure 5.31. In this graph the effect of radiation and the presence of the wall are distinctly visible for the higher temperature cases. At lower temperatures the results for the effective thermal conductivity of the different cases are in good agreement. The effect of radiation and the packing structure is less prominent at lower temperatures as can be seen for the region next to the cooled wall.

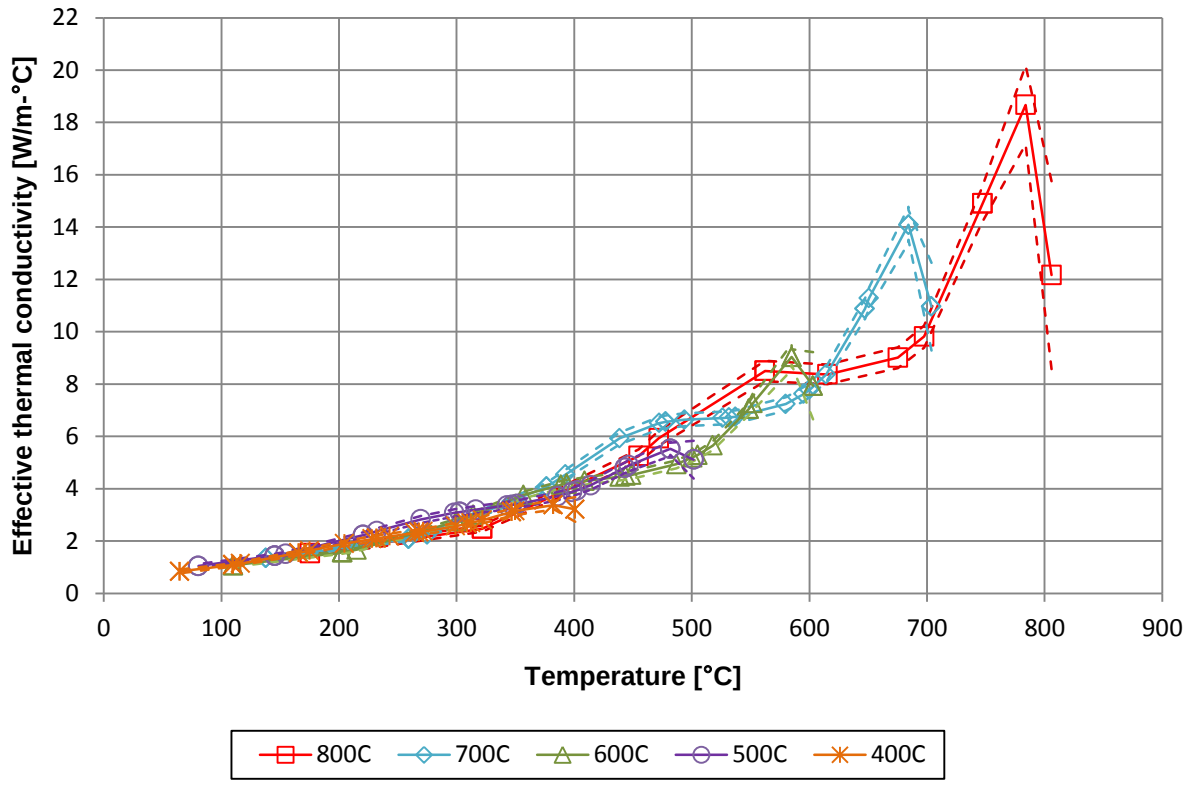

Figure 5.31: Comparison of effective thermal conductivities with uncertainties as a function of temperature for all the test cases.

For all of the test cases it is clear that the effective thermal conductivity is not a linear function of temperature, as can be seen in Figure 5.22, Figure 5.24, Figure 5.26, Figure 5.28, Figure 5.30 and Figure 5.31. The gradient of the effective thermal conductivity increases gradually with an increase in temperature. As temperature increases the effect of radiation becomes more significant, thus it causes the observed increase in the effective thermal conductivity values as can be seen in Figure 5.31.

Figure 5.31 also shows that even though the temperatures are the same at certain positions from the walls the value of the effective thermal conductivity is not necessarily the same for the different test cases. The differences between the effective thermal conductivity results cannot be attributed to the effect of the graphite thermal conductivity. The reason is that even though the thermal conductivity of the graphite material is a function of temperature, the temperatures are the same at the points where the differences in the effective thermal conductivity results are observed.

A comparison of the temperature gradient results for all of the test cases are shown in Figure 5.32. It is evident from Figure 5.32 that there is a difference in the macro temperature gradient at various positions in the pebble bed. This also contributes to the differences between the

effective thermal conductivity results for the different test cases. Thus the effective thermal conductivity is not only a function of temperature, but also of the macro temperature gradient at a specific position in the packed pebble bed.

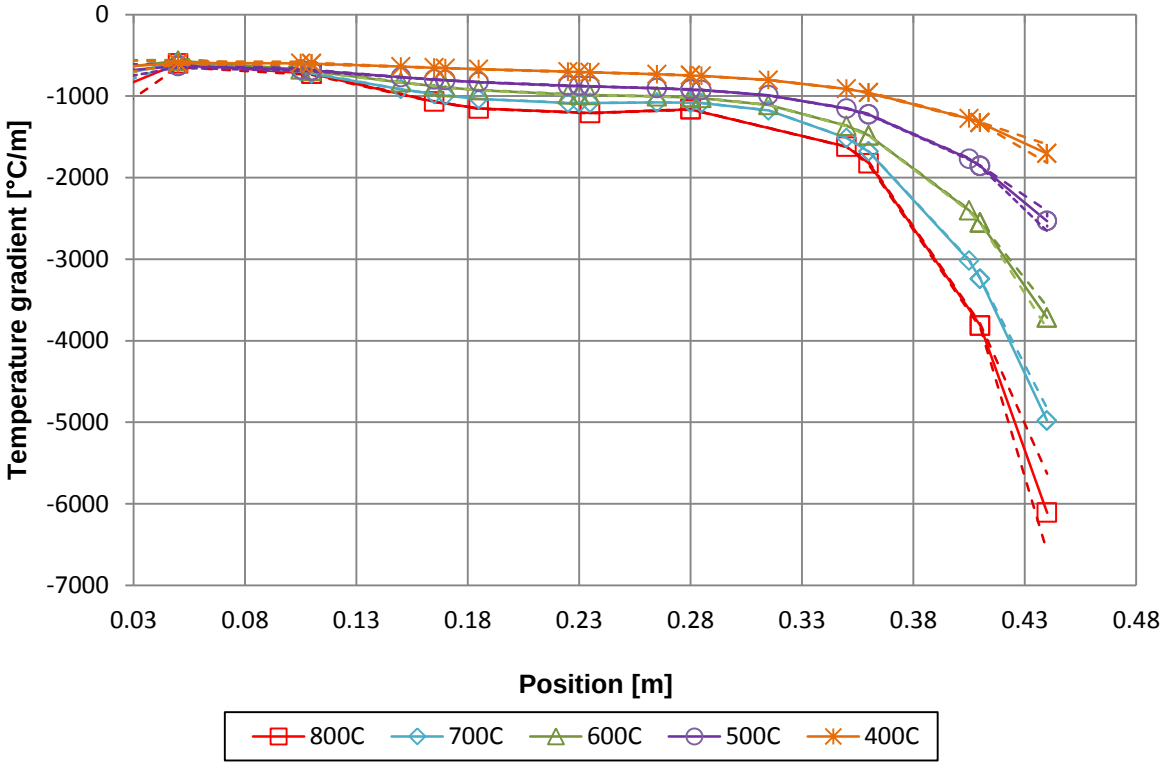

Figure 5.32: Comparison of the temperature gradient functions for all of the test cases.

The packing structure in the experimental pebble bed also did not include just a single near-wall region, as discussed in section 4.2.3. A wall effect was present next to each of the reflector walls as well as the insulation walls, thus no definite bulk region existed in the packed pebble bed. The variations in the packing structure that were present as a result of the wall effects may also have had an influence on the differences in the effective thermal conductivity results. Thus the effective thermal conductivity is also a function of the packing structure of the pebble bed.

5.2 Analysis of numerically packed pebble bed

The solved DEM simulation with the generated numerically packed bed of spheres is shown in Figure 5.33. The DEM generated bed consisted of 313 spherical particles in comparison to the 332 and 334 spheres used for the packing of the experimental pebble bed.

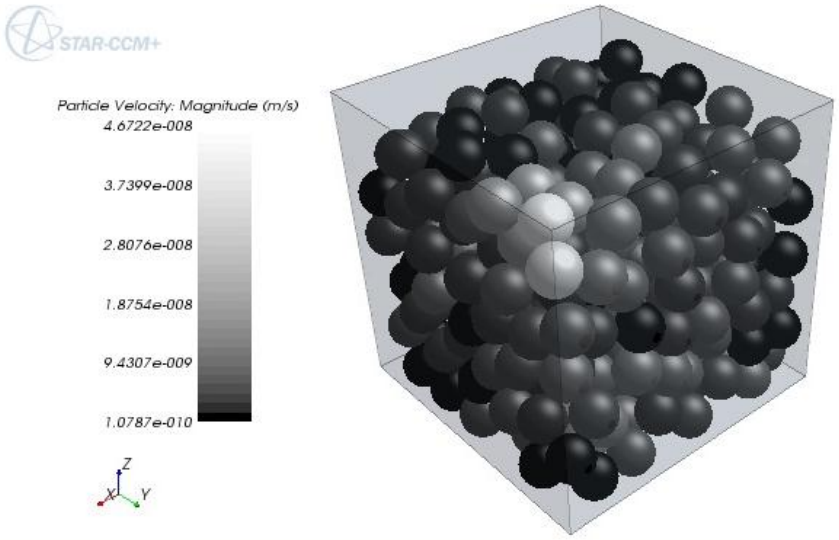

Figure 5.33: Example of the solved DEM simulation used to generate the numerically packed bed of spheres.

According to Du Toit (2002) and Van der Merwe (2014) the quality of the DEM generated bed can be assessed by determining the overlap between adjacent particles. For an ideal DEM generated bed no overlap should exist between particles. The percentage overlap between particles is the overlap between particles normalised with the particle diameter and expressed as a percentage. The maximum overlap for the numerically packed pebble bed is 0.053% and the average overlap is 0.011%.

The method proposed by Du Toit (2002) was used to determine the particle centre distribution as well as the porosity variations for the numerically packed pebble bed. The origin was placed in the centre of the bottom surface of the packed pebble bed for the analysis. Figure 5.34 shows a top view of the distribution of the centre coordinates of the spheres for the DEM generated bed. The more ordered packing structure next to the wall due to the wall effects is clearly visible in Figure 5.34, whilst the particle distribution becomes more disordered towards the centre of the packed pebble bed.

A side view of the numerically packed pebble bed with centre coordinate distribution of the particles is shown in Figure 5.35. The method used for the packing of the experimental bed as well as the numerical pebble bed left a gap between the top layer of spheres and the top cover of the experimental test section. This gap is clearly visible in Figure 5.35 whilst the more ordered packing structure next to the side and bottom insulation walls can also be seen. Therefore it is clear that the packing structures next to the side and bottom insulation walls are similar while the packing structure next to the top insulation wall differs, as assumed for the experimental heat transfer calculations in section 4.3.3.

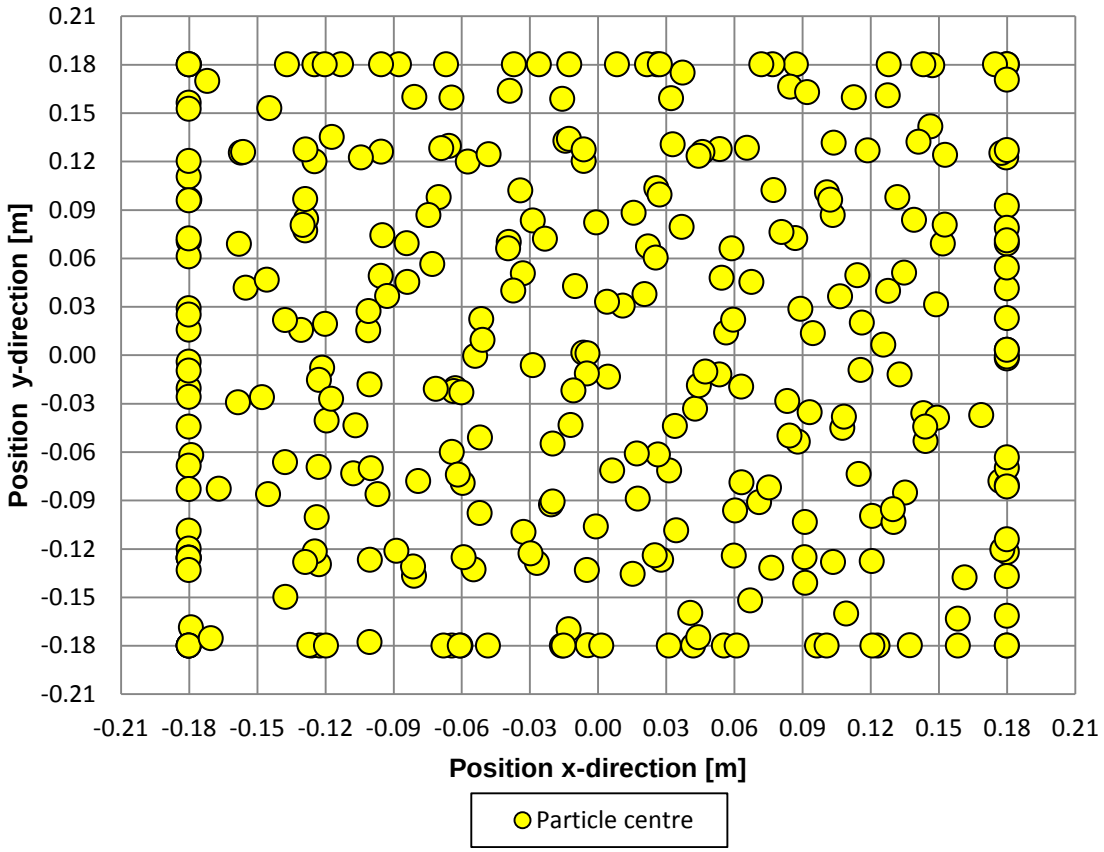

Figure 5.34: Top view of particle centre distribution for the DEM generated pebble bed.

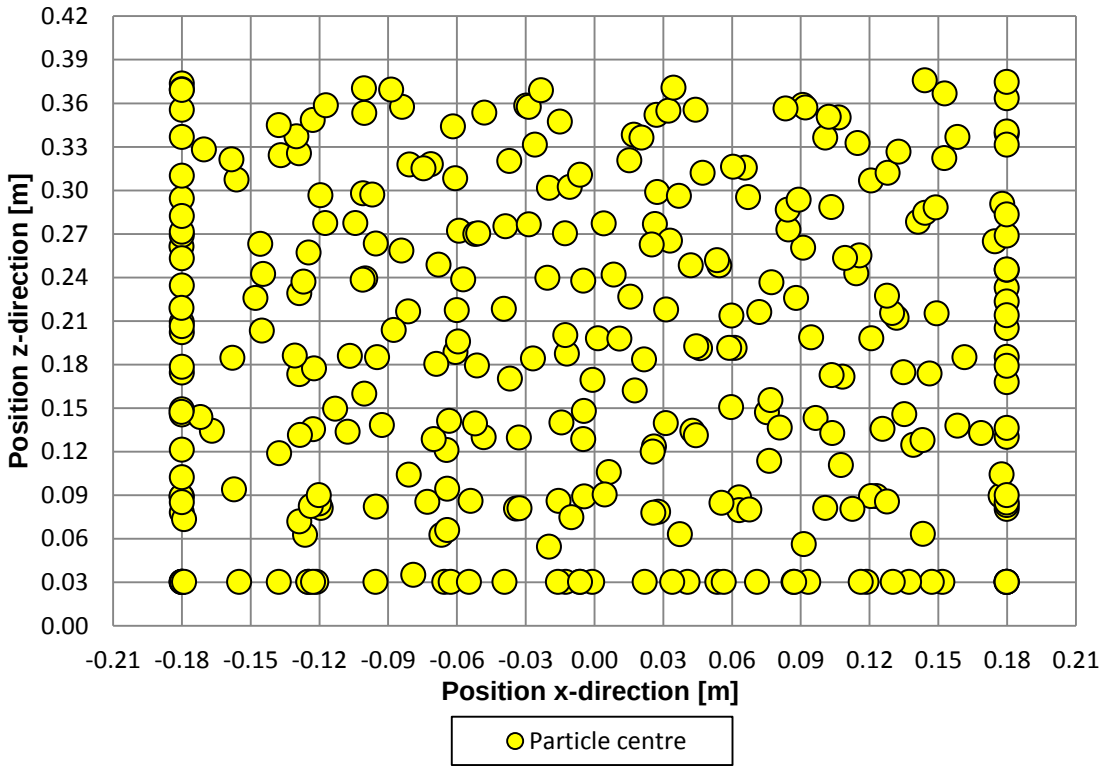

Figure 5.35: Side view of particle centre distribution for the DEM generated pebble bed.

The porosity variation for the randomly packed DEM pebble bed was analysed in the x-, y- and z-directions and was compared with the porosity variation of a packed bed of spheres with an ordered simple cubic packing structure. The results of the porosity variations are shown in Figure 5.36.

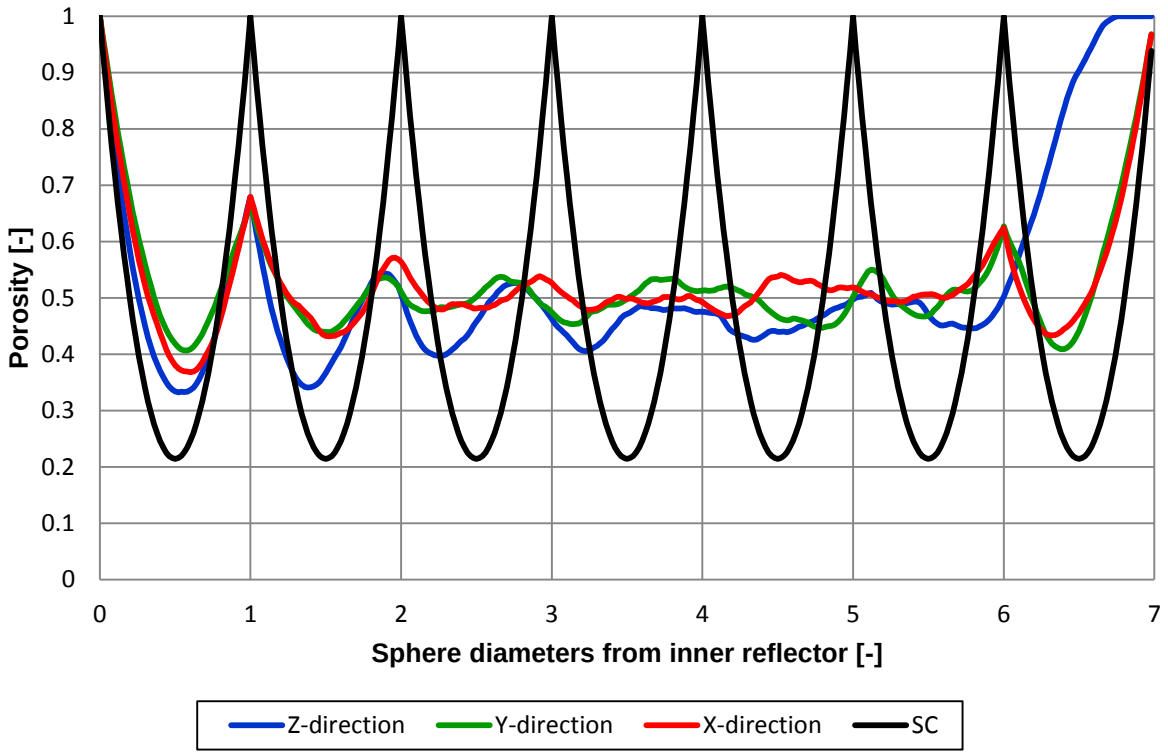

Figure 5.36: Variation in porosity for the numerically generated pebble bed compared to the variation in porosity for a numerical pebble bed with a structured packing.

The average porosity for the numerical pebble bed with a simple cubic packing structure is 0.477. Table 5.1 lists the average porosities for the wall regions, next to the inner and outer reflector, and the near-wall region for each of the directions in the DEM generated pebble bed. The wall and near-wall regions were defined according to the definition by Van Antwerpen (2009) as described in section 2.1.1. As wall effects were found on each side of the numerically packed pebble bed due to the packing method used no bulk region was present throughout the pebble bed.

When comparing the porosity variations of the randomly packed pebble bed to the ordered packed pebble bed it is clear that at the inner and outer wall the wall effects forces the packing structure to be more ordered. This is seen when comparing the trend of the porosity variations for the two cases at the inner and outer wall. As we move further away from the inner and outer wall the packing structure of the randomly packed pebble bed becomes more disordered

whereas the packing structure of the simple cubic packed pebble bed stays ordered as expected.

Table 5.1: Average porosities in the wall and near-wall regions of the DEM generated pebble bed.

Direction	Average porosity [-]		
	Inner wall region $0 \leq z \leq 0.5$	Near-wall region $0.5 < z < 6.5$	Outer wall region $6.5 \leq z \leq 7$
X	0.621	0.666	0.502
Y	0.626	0.683	0.499
Z	0.518	0.985	0.484

The effects of the side walls for the porosity variations in the x- and y-directions can be seen in Figure 5.36. For the porosity variation in the z-direction the effects of the bottom and top wall are also clear. The sharp increase in the porosity variation in the z-direction at approximately six sphere diameters is as a result of the gap left between the top layer of spheres and the top cover of the test section. The gap was formed due to the packing method used as well as the physical constraints of the geometry of the test section.

From the discussion in this section it can be concluded that a high quality numerically packed pebble bed was generated using the method discussed in section 4.4.1. Therefore the numerically packed bed of spheres can be considered as qualitatively similar to and an acceptable representation of the physically packed pebble bed used for the NWETCTF experimental tests. Thus the DEM generated bed can be used for the CFD simulations of the heat transfer through the packed bed of spheres.

5.3 CFD results

The results obtained with the CFD simulation, described in section 4.5.1, for all of the experimental test case conditions are presented in the following section. The numerical temperature and heat transfer results obtained with the CFD simulation are compared with the results of the various experimental cases for Test 1, as the measured experimental data of Test 1 was used as the boundary conditions for the CFD simulation setup.

The calculated numerical result for the effective thermal conductivity of the 800°C case with the use of the CFD simulation is given in this section. The results for the radiation and conduction components of the overall effective thermal conductivity are also presented to verify the method used for the characterisation of the radiation component.

5.3.1 CFD temperature results

A temperature distribution similar to the measured temperature results of the NWETCTF was obtained through the numerically packed bed by using the point probes and the method discussed in section 4.5.1. Figure 5.37 to Figure 5.41 show a comparison between the measured CFD temperature results and the measured experimental temperature results for the various test cases of Test 1.

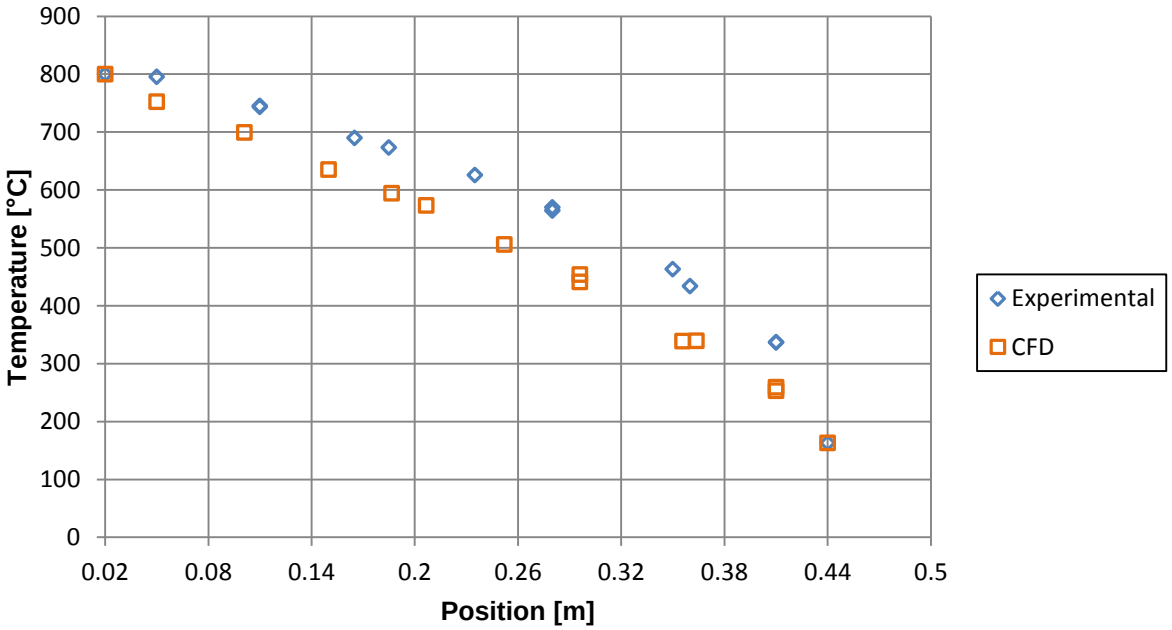

Figure 5.37: Comparison between measured CFD and experimental temperature results for the 800°C case of Test 1.

From the results it is clear that the temperatures through the packed bed of spheres are lower for the CFD results than the temperatures for the experimental tests. Although the individual temperatures for the CFD results are lower than the experimental results the overall trend line of the temperature distribution through the packed pebble bed has a similar shape for the CFD and experimental results.

The CFD simulation setup was modelled to match the experimental setup as closely as possible. The insulation side walls in the y-direction of the NWETCTF test section were modelled as adiabatic in the CFD simulation differing from the experimental setup. The fillets inserted at the particle-particle and particle-wall contact points were modelled as part of the pebble region and the thermal conductivity of the graphite material were also assigned to the fillet region. Thus the contact resistances that exist at the contact points in reality were not

modelled in the CFD simulation. The scope of the project did not include the modelling of the contact resistances at the contact points in the CFD simulations.

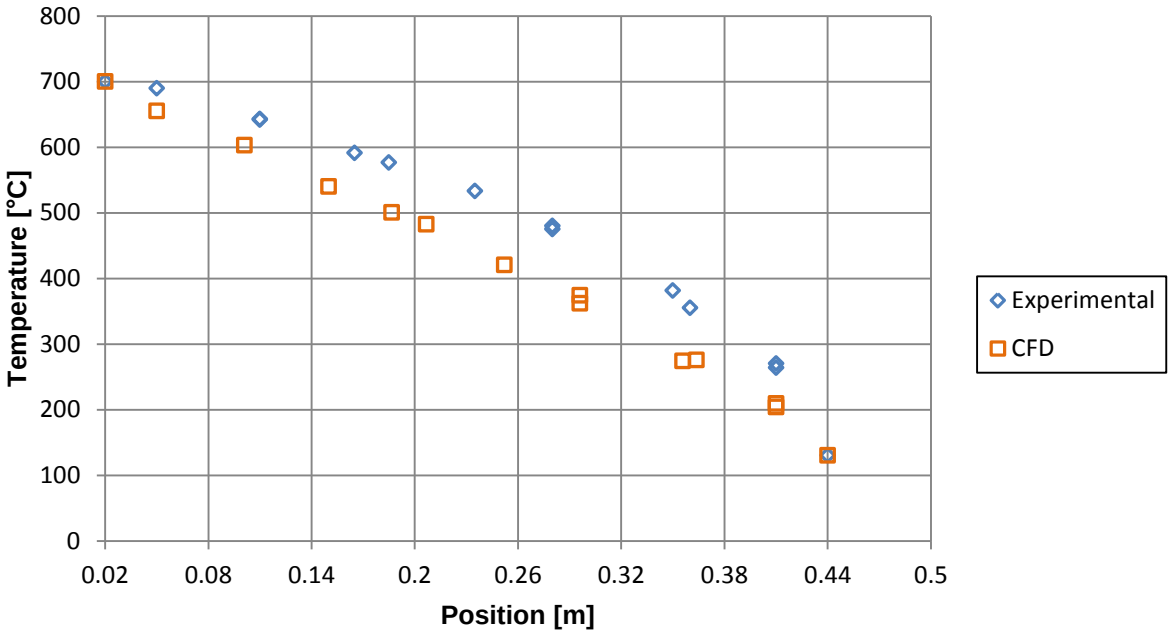

Figure 5.38: Comparison between measured CFD and experimental temperature results for the 700°C case of Test 1.

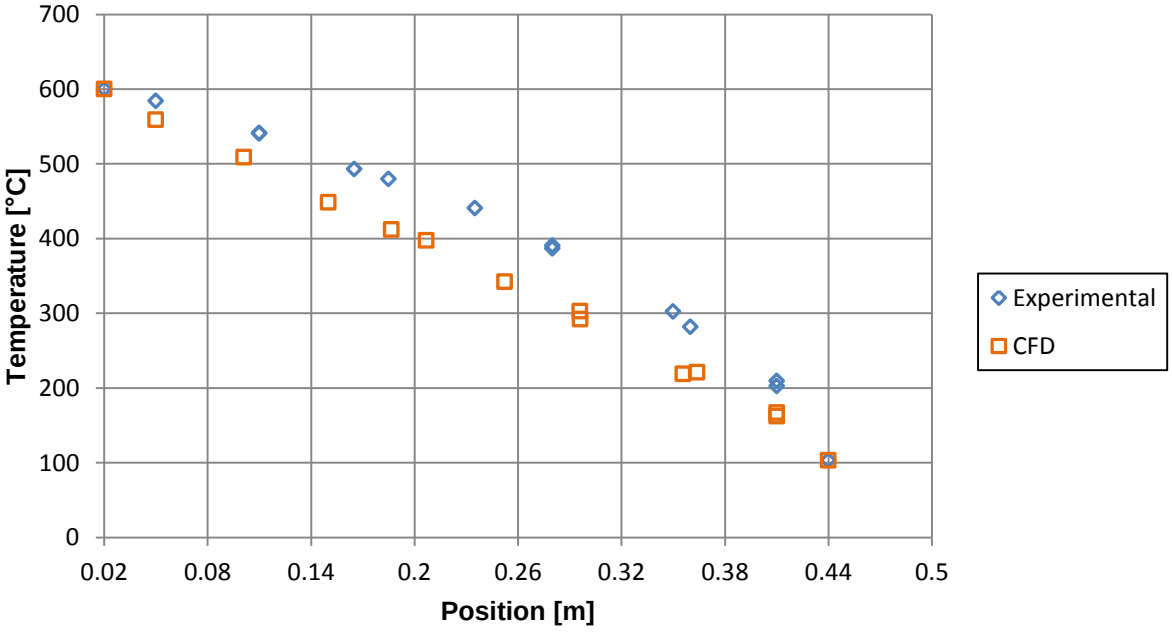

Figure 5.39: Comparison between measured CFD and experimental temperature results for the 600°C case of Test 1.

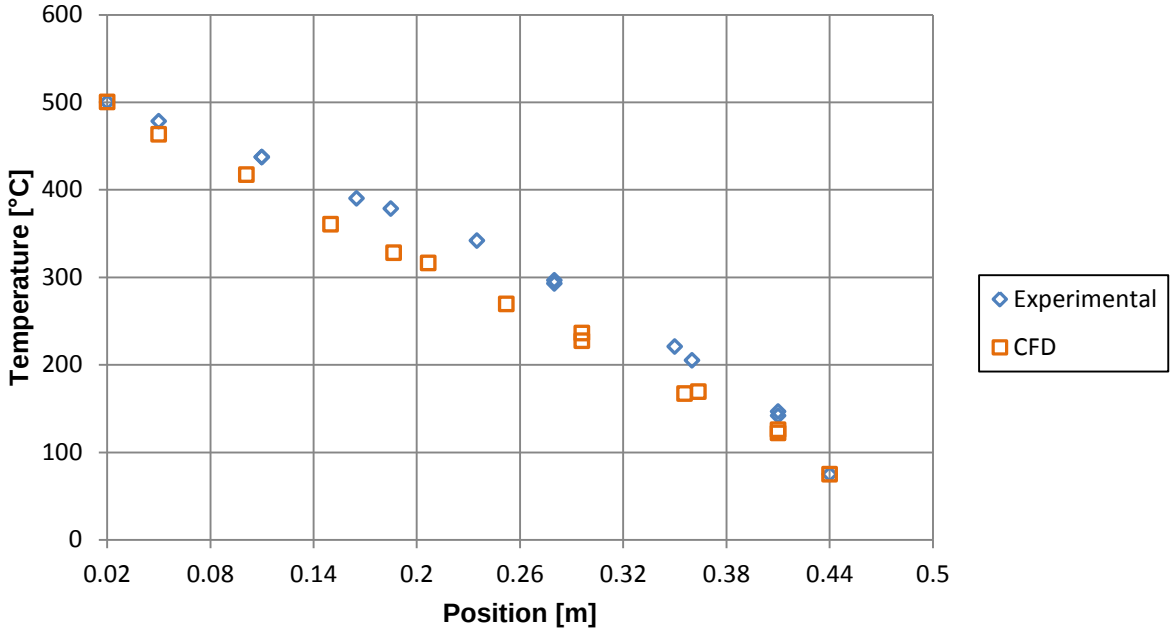

Figure 5.40: Comparison between measured CFD and experimental temperature results for the 500°C case of Test 1.

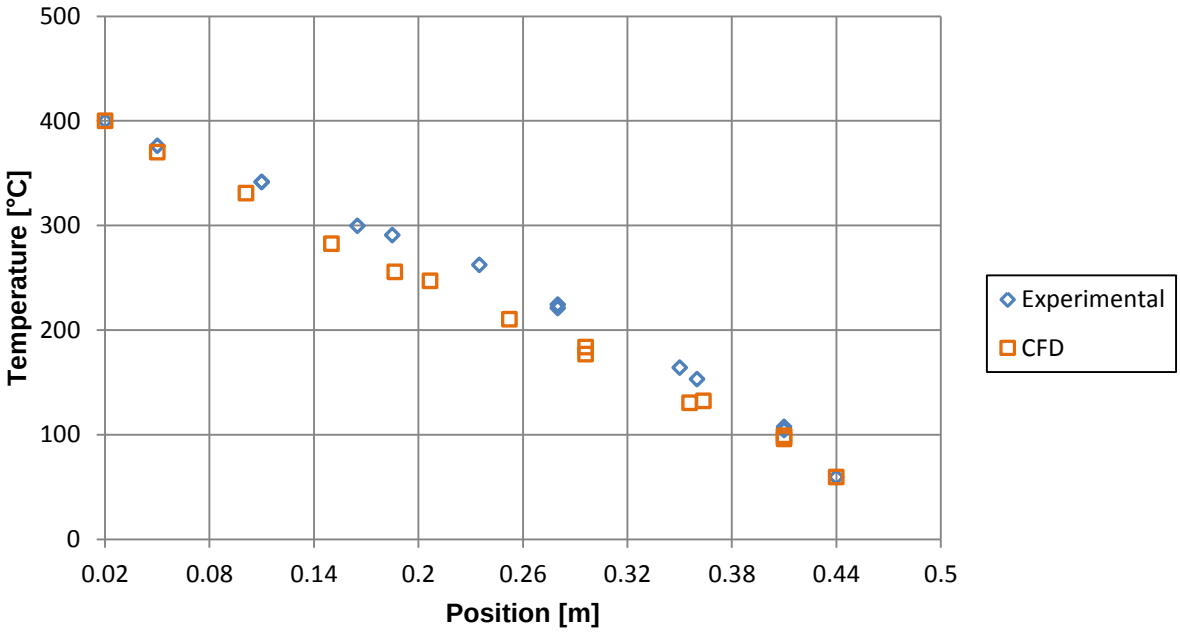

Figure 5.41: Comparison between measured CFD and experimental temperature results for the 400°C case of Test 1.

Without contact resistances at the contact points, heat can be conducted more effectively through the fillets than for a scenario with contact resistances that limit the amount of heat transfer conducted through the contact points between adjacent spheres. Consequently for a

scenario without contact resistances a larger amount of heat will be conducted through the packed bed of spheres resulting in a lower temperature distribution through the pebble bed. Thus the absence of contact resistances at the contact points may be the cause of the difference between the CFD and the experimental results.

For the experimental results, where contact resistances are present, less heat is conducted through the packed bed of spheres resulting in a higher temperature distribution throughout the packed pebble bed. In order to improve the accuracy of the results of the CFD simulation and obtain results closer to the NWETCTF experimental results, contact resistances should be added at the contact points in the CFD model with an applicable thermal conductivity value.

The surface emissivity value of the graphite material of the pebbles and the reflectors was kept constant in the CFD simulations as all surfaces were assumed to be diffuse and gray. This may also have an effect on the temperature distribution as the value of the emissivity is a function of temperature in reality.

5.3.2 CFD heat transfer results

The heat flux values over the boundaries of the outer reflector and the insulation walls obtained from the CFD simulations are compared with the values of the heat extracted via the water jacket and the total heat loss through the insulation material for the experimental tests. Table 5.2 shows the CFD and the experimental results as well as the percentage difference between the results.

Table 5.2: Comparison between CFD and experimental heat transfer results for Test 1.

Case	$Q_{water\ jacket}$ [W]			$Q_{total\ loss}$ [W]		
	Experimental	CFD	% Difference	Experimental	CFD	% Difference
800°C	1657.66	2020.43	17.95	367.22	347.06	5.49
700°C	1155.36	1661.04	30.44	294.77	275.67	6.48
600°C	643.16	1353.22	52.47	227.81	211.58	7.12
500°C	412.98	1119.13	63.10	164.06	155.27	5.36
400°C	287.44	874.97	67.15	110.24	104.68	5.04

The values for the total heat loss through the insulation walls for the CFD simulation and the experiment are in good agreement for all of the test cases. The heat loss values are within 5-7% of each other. However, there is a large difference between the CFD and experimental results

for the heat extracted via the water jacket. The difference between the results increases for the lower temperature cases. The result of the heat transfer rate through the pebble bed in the CFD model is higher than in the real-life experiment for the same overall temperature gradient. This implies that there is effectively less thermal resistance on average in the CFD model than in the real-life experiment. Therefore as discussed in section 5.3.1, the fact that the contact resistances at the particle-particle and particle-wall contact points were not modelled in the CFD simulation may be the reason for the difference in the heat transfer results.

The radiation contribution to the overall heat transfer becomes less significant as the temperatures decrease, thus conduction becomes the dominant heat transfer mechanism in the packed pebble bed. Contact resistances at the contact points has a direct impact on the conduction heat transfer through the packed pebble bed as it will limit the amount of heat conducted through the contact points. As discussed previously the fillets inserted at the contact points to solve mesh development problems were modelled as a part of the pebble region and the thermal conductivity of the pebble graphite material were also assigned to the fillet material. Thus heat could easily be transferred through the contact point between adjacent spheres without any resistance. This is not ideal as it does not realistically model the contact points and as can be seen from Table 5.2 it has a large influence on the results.

It is clear from the results that as the temperature decreases and conduction become more significant, the error associated with the modelling of the contact points also increases. This causes an increase in the difference between the CFD and experimental results for the heat extracted via the water jacket. For the 800°C case the effect of radiation is the most significant and the error associated with the modelling of the contact points is the smallest, thus the CFD and experimental results are in better agreement than for the other lower temperature cases.

Another factor contributing to the increase in the difference between the CFD and the experimental results is the thermal conductivity values of the pebble graphite material. Figure 5.42 shows the graphite thermal conductivity as a function of temperature. It can be seen in Figure 5.42 that the graphite thermal conductivity decreases significantly with an increase in temperature. Thus for the lower temperature cases where conduction is the main contributor to the heat transfer the graphite thermal conductivity values also increase.

For higher graphite thermal conductivity values more heat will be transferred through the fillets at the contact points and as a result a larger amount of heat will be extracted through the water jacket. This effect is evident from the results, especially for the 500°C and 400°C cases compared to the 800°C case.

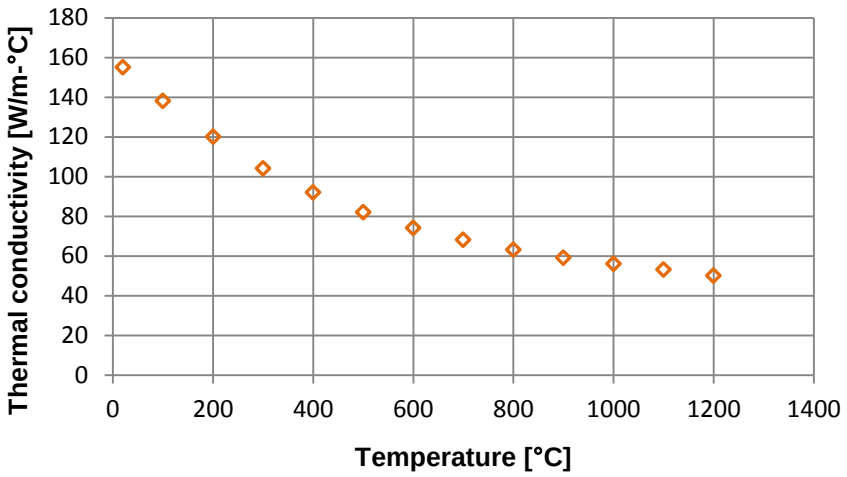

Figure 5.42: Graphite thermal conductivity as a function of temperature.

The temperature distribution and heat transfer results of the CFD simulations indicate the importance of the inclusion of contact resistances when modelling heat transfer through a packed bed of spheres, especially at lower temperatures where conduction is dominant. Further work must be done in the future to add the modelling of the contact resistances to the CFD simulations in an attempt to calibrate the CFD simulations to obtain results in better agreement with the experimental results. It is proposed that the thermal conductivity of the fillet material at the particle-particle and particle-wall contact points should be varied to emulate the contact resistances. This should be done in such a way that the best possible correlation between the temperature and heat transfer distribution results of the CFD model and the experimental tests is obtained.

Although the results obtained are not final and an exact representation of the experimental results the results show the expected trends. Therefore a methodology has been set in place that can be improved upon and finally can be used to model the heat transfer through the packed bed of spheres. This is sufficient for the scope of the current study as the objective was to develop a method that can be used rather than providing a set of accurate results.

5.3.3 CFD effective thermal conductivity results

Following the discussion in section 5.3.2 it was impractical to calculate the effective thermal conductivity for all of the cases of the CFD simulations, as the results obtained were not an accurate representation of the experimental results. However, one of the objectives of the study was to develop a method that can be used to separate the conduction and radiation components of the effective thermal conductivity results.

The results presented in the following section illustrate the method that can be used to determine the contribution of conduction and radiation to the effective thermal conductivity, discussed in section 4.5.4. Thus once the CFD simulation has been revised and the contact resistances have been added the method can be used to separate the effects of conduction and radiation, when the CFD results are in good agreement with the experimental results.

As the CFD results for the 800°C case were the most accurate representation of the experimental results from all of the cases, it was used to illustrate the effective thermal conductivity separation method. The macro temperature gradient and the heat transfer distribution through the numerically packed pebble bed were determined using the methods described in section 4.5.3 and 4.5.4. After the CFD simulation was solved for conduction and radiation effects the radiation model was switched off and results were obtained for the 800°C case when only conduction heat transfer was present in the pebble bed.

The temperature results as well as the polynomial curves fitted through the temperature distributions for the radiation-conduction and conduction cases are shown in Figure 5.43. From the results it is clear that radiation is significant at higher temperatures as the temperature distribution is higher for the radiation-conduction case than for the case with conduction heat transfer only. The influence of the wall effects on the temperature distributions can also be seen for both cases, as there is a slight change visible in the gradient of the polynomial curve fits in the regions next to the inner and outer walls.

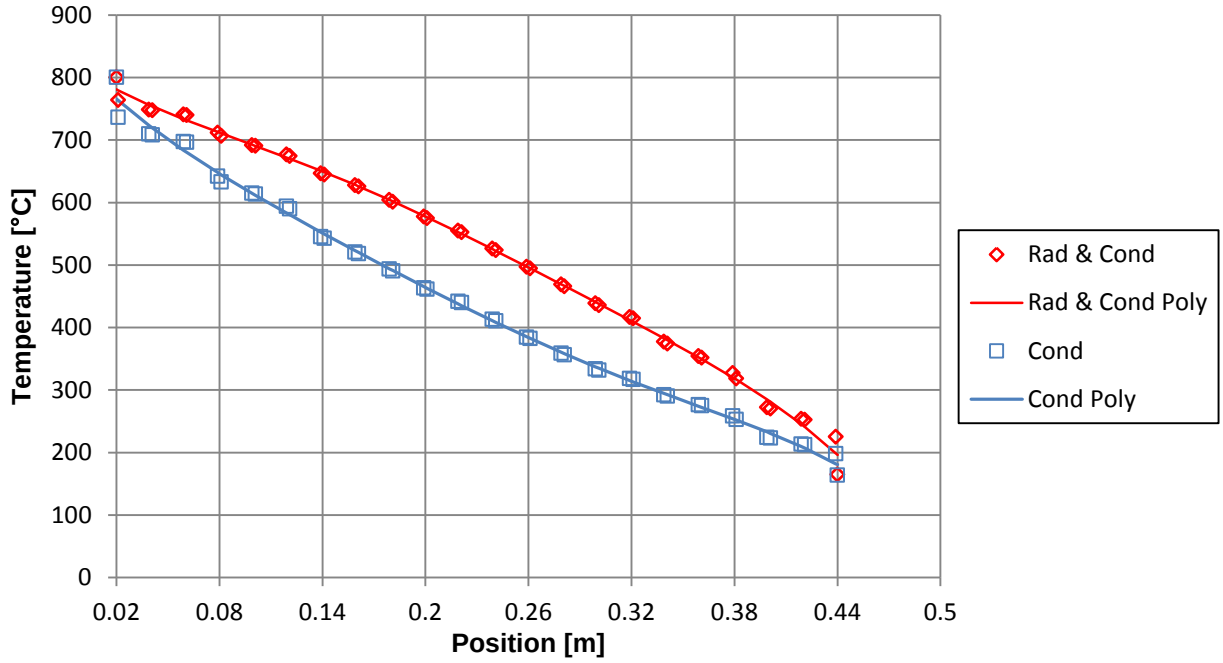

Figure 5.43: CFD temperatures with fifth order polynomial curve fit for the 800°C radiation-conduction and conduction cases.

Figure 5.44 shows the macro temperature gradients for the radiation-conduction case as well as the conduction only case. The macro temperature gradient for the case with conduction only is initially much lower than the radiation-conduction case with values of approximately -1400°C/m versus -2400°C/m. Thereafter the temperature gradient for the radiation-conduction slightly increases after which it gradually decreases. The temperature gradient for the conduction case however gradually increases and slightly decreases near the outer reflector wall.

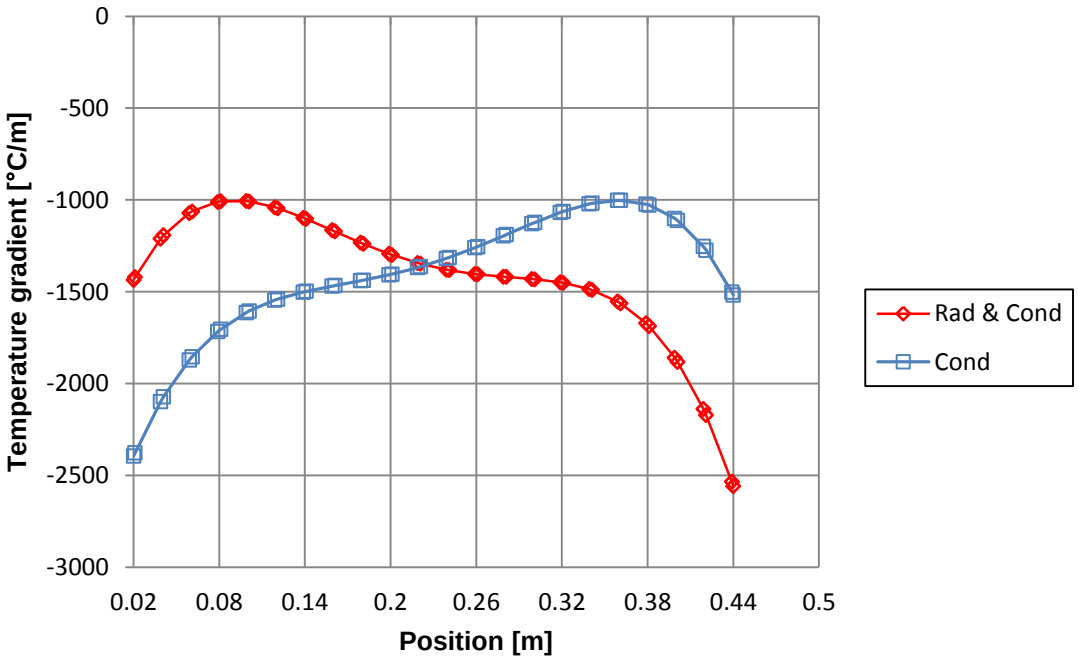

Figure 5.44: Temperature gradient functions for the 800°C radiation-conduction and conduction cases.

The decrease in the temperature gradient of the radiation-conduction case can be attributed to the fact that the effect of radiation becomes less significant at lower temperatures. The increase in the temperature gradient for the conduction case may be as a result of the graphite material's thermal conductivity increasing with a decrease in temperature, as shown in Figure 5.42. It is interesting to note that the temperature gradient is higher for the conduction case than for the case with radiation and conduction in the near-wall region next to the outer reflector. The wall effects are also clearly visible for the results of both cases.

The heat transfer distribution through the numerically packed pebble bed for the radiation-conduction case as well as the conduction case is shown in Figure 5.45. Equations (5.15) and (5.16) describe the heat transfer through the pebble bed as a function of position from the heated wall for the radiation-conduction and conduction case respectively.

$$Q_{bed,rad-cond}(y) = 678.033259y^3 + 941.464759y^2 - 1396.870526y + 2394.623950 \quad (5.15)$$

$$Q_{bed,cond}(y) = 1.381841y^3 + 1225.869676y^2 - 249.365701y + 1075.348033 \quad (5.16)$$

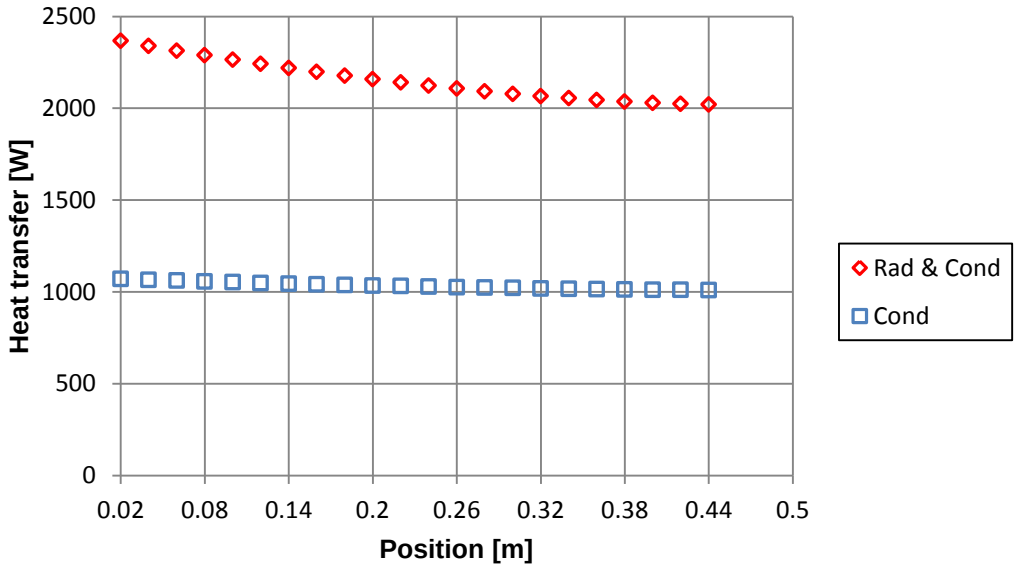

Figure 5.45: Heat transfer distribution through the numerically generated pebble bed for the 800°C radiation-conduction and conduction cases.

The heat transfer distribution for the conduction case is almost constant showing a slight decrease whereas the heat transfer distribution for the radiation-conduction case shows a distinct gradual decrease. The reason is that the heat loss value for the conduction case is much smaller than for the radiation-conduction case, 347.06W and 60.44W respectively.

This makes sense as for the radiation-conduction case the radiation heat transfer mechanism contributes significantly to the overall heat loss by radiating heat to the insulation walls. For the conduction case on the other hand conduction through the particle-wall contact points is the only method of heat loss in the packed pebble bed. The diameter of the fillet inserted at the contact point is very small, 0.12 mm, thus the contact area between the pebble and the insulation wall is also very small resulting in a small heat loss value.

The results for the effective thermal conductivity for the radiation-conduction case as well as the separate cases of conduction and radiation are shown in Figure 5.46. By comparing the results in Figure 5.21 and Figure 5.46 it is clear that the overall effective thermal conductivity through the pebble bed of the CFD model is lower than that of the NWETCTF experiment. It was explained in section 5.3.2 that there is effectively less thermal resistance in the CFD model than in the experiment. Therefore adding an additional contact resistance to the CFD model may

result in a higher overall effective thermal conductivity result for the CFD model that is in better correlation with the experimental results.

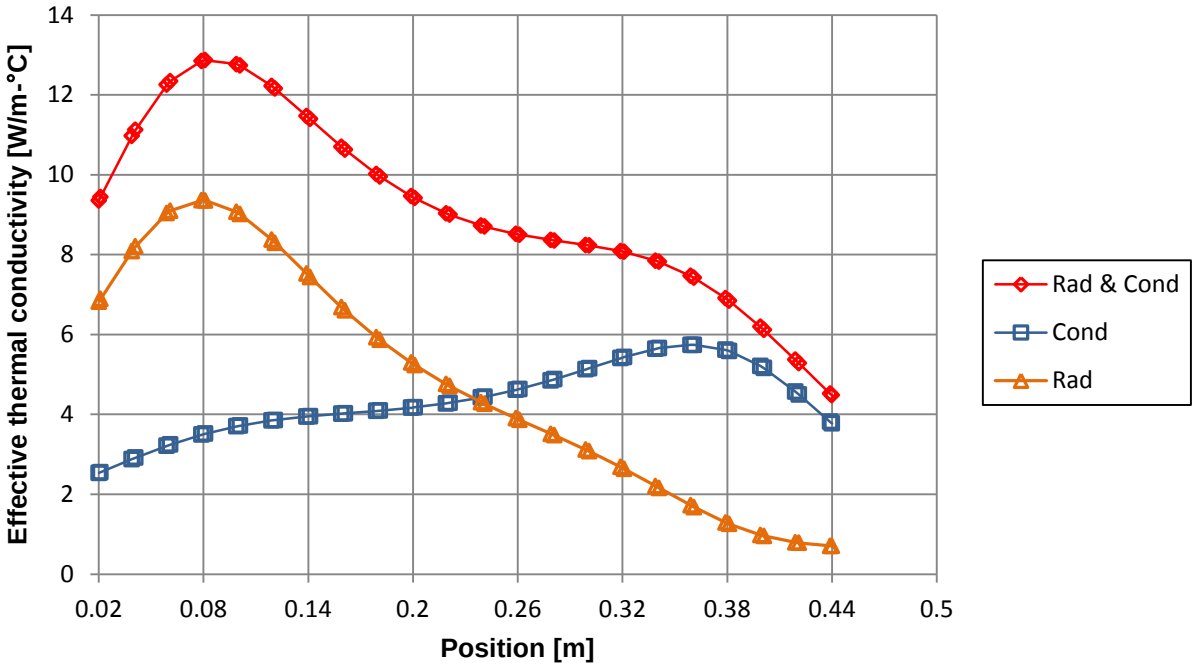

Figure 5.46: Effective thermal conductivity results for the combined and separate effects of radiation and conduction for the 800°C case.

From the results in Figure 5.46 it can be seen that for higher temperatures radiation is the main contributor to the overall effective thermal conductivity whilst for lower temperatures conduction becomes the main contributor. The increase in the effective thermal conductivity for the conduction case is due to the higher graphite thermal conductivity at lower temperatures. The wall effect is also visible for the results of the case where only conduction heat transfer was present in the pebble bed.

At the inner reflector the wall effect has a larger influence on the radiation effective thermal conductivity whereas at the outer reflector the wall effect has a more significant influence on the conduction effective thermal conductivity. The reason being that at the inner reflector the temperatures in the pebble bed are higher thus the effect of radiation is more significant, but at the outer reflector the temperatures are lower and the material thermal conductivity higher thus the effect of conduction is dominant.

This section proved that the method proposed for the separation of the radiation and conduction components of the effective thermal conductivity is viable and that it can be used to characterise the radiation heat transfer phenomena in a packed pebble bed.

5.4 Final proposed methodology

The final proposed methodology that uses experimental work together with a CFD model to predict the effective thermal conductivity in the near-wall region of a randomly packed pebble bed, and separate the conduction and radiation components of the effective thermal conductivity is presented in Figure 5.47. The conclusions drawn from the results presented in this chapter were used to develop the final revised methodology.

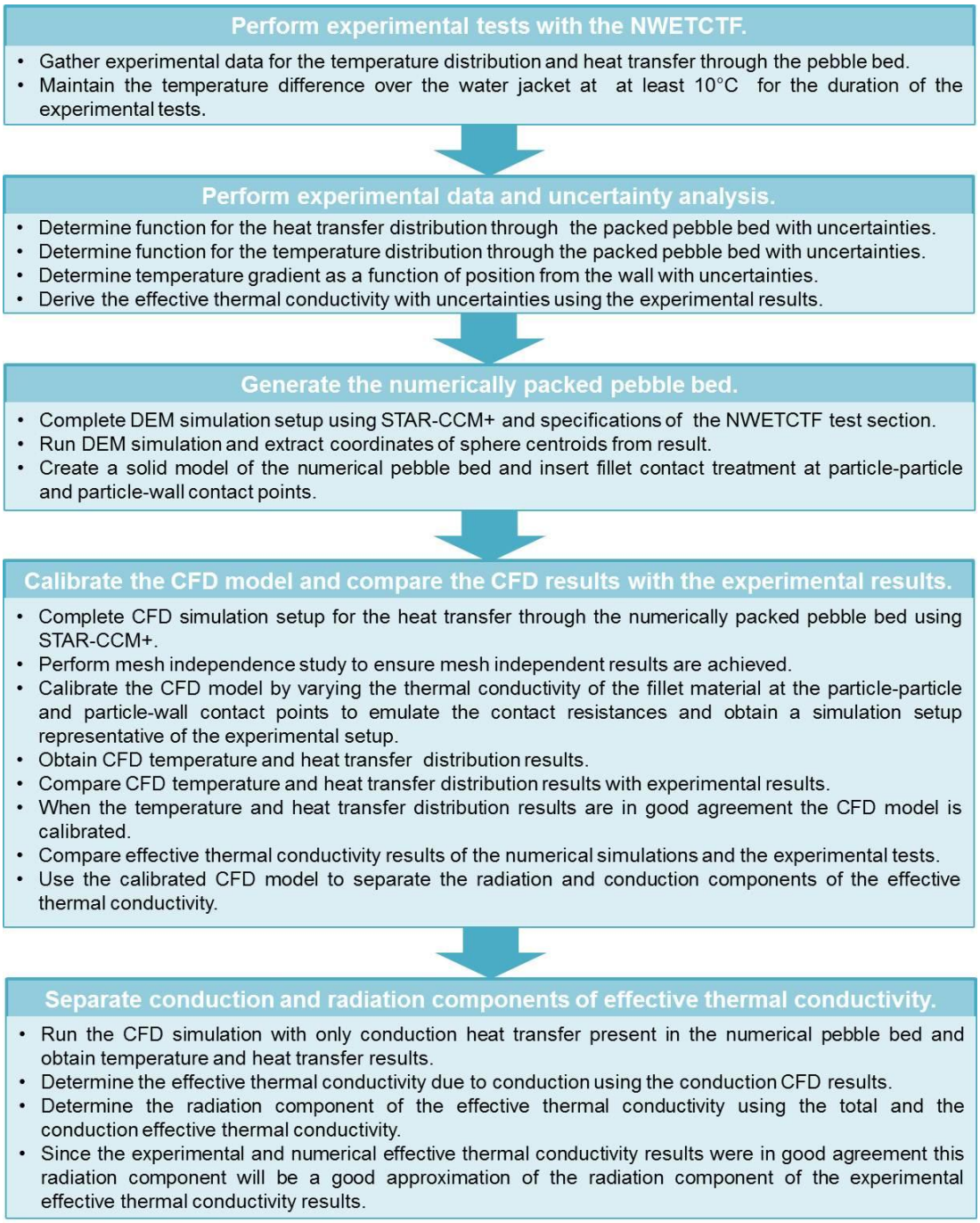

Figure 5.47: Final proposed methodology.

Experimental tests have to be conducted in order to determine the effective thermal conductivity for the randomly packed pebble bed from the experimental results. It is important to note that the temperature difference between the water inlet and outlet temperatures of the water jacket should be maintained at 10°C. The calibration of the CFD model must be done by adjusting the thermal conductivity of the fillet material at the particle-particle and particle-wall contact points in the packed pebble bed in order to emulate the contact resistances. The calibration of the CFD model should be done in such a manner that the best possible correlation between the CFD and experimental results is obtained. To determine if the CFD model is calibrated the results of the temperature distribution, heat transfer and effective thermal conductivity of the CFD simulations must be compared with the NWETCTF experimental results. Therefore it is important that the experimental tests are conducted.

Once the CFD model is calibrated the CFD model can be used to separate the radiation and conduction components of the effective thermal conductivity. This section showed that the objectives of the current study, as discussed in section 1.3, were achieved.

5.5 Summary

The experimental and numerical results of the study, determined with the application of the methods introduced in Chapter 4, were given in this chapter. Measured temperatures and heat transfer results for the various temperature cases obtained from the experimental tests, performed with the NWETCTF test facility, were presented. Good repeatability was shown between the temperature results for all of the test cases of Test 1 and Test 2. The uncertainties associated with the temperature results were also very small.

The repeatability between the heat transfer results of Test 1 and Test 2 proved to be not as good as the repeatability of the temperature results for the 600°C, 500°C and 400°C cases. The larger difference between the heat transfer results for these cases can be attributed to the temperature difference maintained over the water jacket for the two experimental tests and the measured water mass flow rates for each of the tests. These results showed that it is crucial that the temperature difference of the water between the inlet and outlet of the water jacket must be maintained at at least 10°C for all tests in order to minimise the uncertainty in the heat flux results.

Results of the temperature distribution functions as well as the temperature gradient functions derived from the experimental results for all of the experimental test cases were presented. The average values of the measured experimental temperatures and heat transfer results for Test 1 and Test 2 were used for the derivation of the functions. The calculated effective thermal

conductivity values as a function of position and temperature for each of the test cases were given. It was clear from the results that the wall effects influence the results as well as the effect of radiation heat transfer, especially for the higher temperature cases. A comparison between the effective thermal conductivity results for all of the test cases also proved that the macro temperature gradient, at a specific position in the pebble bed, has an influence on the effective thermal conductivity.

The particle centre distribution and the porosity variations in the DEM generated packed pebble bed were given. The wall effects in the numerical pebble bed were clearly visible causing a more ordered particle distribution near the walls and a large variation in porosity in the near-wall regions. From the results it was concluded that the DEM generated pebble bed was an accurate representation of the NWETCTF physically packed pebble bed used in the experimental tests. Therefore the numerical pebble bed could be used in the CFD simulations to obtain numerical results that could be compared to the NWETCTF experimental results.

From the CFD simulations temperature and heat transfer results were obtained that were compared with the experimental results of Test 1. The temperatures of the CFD results were lower than the temperatures of the experimental results, but the CFD temperature distribution showed the same trend as that of the experimental temperature distribution. It was also important to compare the heat transfer results of the CFD model with that of the experimental setup as the combination of the heat transfer rate and the temperature gradient will determine the effective thermal conductivity. The heat transfer results of the CFD simulations were much higher than the experimental heat transfer results for the same overall temperature gradient, with the difference between the results increasing for the lower temperature cases. This implies that there is effectively less thermal resistance on average in the CFD model than in the real-life experiment.

For the CFD simulations contact resistances were not inserted at the particle-particle and particle-wall contact points that can be expected to be present in the real-life experiment. This explained the difference between the CFD and experimental results as more heat was transferred through the packed pebble bed resulting in a lower temperature distribution. The difference between the CFD and experimental results were smaller for the 800°C case as the effect of radiation heat transfer was more dominant.

The effective thermal conductivity for the numerical simulation was only calculated for the CFD results of the 800°C case as the comparison between the CFD and experimental results proved to be the best for this particular case and the effect of radiation was the most significant for this case. The radiation and conduction components of the numerical effective thermal conductivity

result were determined. At higher temperatures the radiative conductivity was more significant whilst at lower temperatures the conduction conductivity became dominant.

The final proposed methodology with its detailed steps is presented at the end of the chapter. Experimental tests are performed using the NWETCTF and the effective thermal conductivity for the packed pebble bed is calculated from the experimental results. The CFD model must be calibrated by varying the thermal conductivity of the fillet material at the contact points in the packed pebble bed to emulate the contact resistances. The CFD model is calibrated when the temperature distribution, heat transfer and effective thermal conductivity results of the numerical simulations and the experimental tests are in good agreement. The calibrated CFD model can be used to separate the radiation and conduction components of the effective thermal conductivity for the packed pebble bed. The proposed methodology showed that the objectives of the current study were achieved.

6

Conclusion

The main objectives of the study were (1) to develop a methodology with which experimental data could be obtained for the heat transfer in the near-wall region of a packed pebble bed especially at higher temperatures; (2) provide a method to determine the effective thermal conductivity from the measured experimental data and (3) propose a method to separate the contribution of radiation and conduction heat transfer to the experimental effective thermal conductivity.

All of these objectives contribute towards determining the significance of radiation heat transfer at higher temperatures in the near-wall region of a packed pebble bed. Thus the proposed methodology would as a result characterise the radiation heat transfer in the near-wall region of a packed bed of spheres. Experimental as well as numerical methods were used to develop the required methodology. The conclusions drawn from the results obtained in this study, as discussed in Chapter 5, and the recommendations for future work emanating from this study are presented in this chapter.

6.1 Conclusions

The newly constructed NWETCTF test facility was used to conduct an experimental investigation at various temperatures of the heat transfer in the near-wall region of a packed pebble bed. As it was to be the first time operation of the NWETCTF, the system had to be commissioned before the first experimental tests could be conducted and a large part of the focus of the study was to get the system up and running.

Various problems were identified and consequently solved to get the system in a good working condition and a first set of experimental data was gathered. The first set of experimental data proved that the NWETCTF system and the operation procedure of the system could be used in

future studies to conduct experimental tests without having to spent time on the development and commissioning of the system. The procedures required for the maintenance and efficient operation of the system were also determined and can be used in future studies.

Experimental data was obtained for temperatures up to 800°C in the current study. As it was the first time operation of the system the first tests were not conducted at higher temperatures to ensure the safety of the operators and the system while getting the system in an operational condition. For the development of the methodology required to achieve the objectives of this study, experimental tests at temperatures higher than 800°C were not necessary. The NWETCTF was designed to operate at temperatures up to 1600°C; therefore future studies should be able to obtain experimental data at higher temperatures.

The measured temperature and heat transfer data obtained with the NWETCTF were presented with the associated uncertainties describing the accuracy of the data. The repeatability of the NWETCTF temperature and heat transfer results proved to be good, with some discrepancies for the heat transfer results of the 600°C, 500°C and 400°C cases. The sources of the discrepancies were identified and recommendations were made to limit and minimise these differences in future experimental tests.

Methods identified from literature were applied to the experimental data to obtain the experimental results for the temperature distribution, the temperature gradient and finally the effective thermal conductivity values together with the associated uncertainties. Thus the methodology to process and analyse the NWETCTF experimental data was developed and proved to deliver good results. From the experimental results it was concluded that the wall effects had a definite effect on the heat transfer in the near-wall regions of the pebble bed. The significance of the radiation contribution to the overall heat transfer at higher temperatures was also evident from the results.

The packed pebble bed of the NWETCTF did not include just one wall effect due to the method used for the packing of the pebble bed in the test section. Packing of the NWETCTF pebble bed to contain only one near-wall region proved to be difficult and impractical.

The separation of the contribution of conduction and radiation to the overall heat transfer and effective thermal conductivity of the experimental results could not be done experimentally as the natural heat transfer mechanisms could not be physically separated. Therefore a CFD simulation was developed similar to the experimental setup used in the NWETCTF. In future studies the developed CFD model can be calibrated by adding contact resistances to the current model, this should be done in such a way that the best possible correlation between the

CFD and the experimental results is obtained. The calibrated CFD model can then be used for the separation of the conduction and radiation components of the effective thermal conductivity. Although the CFD model was not calibrated in the current study it was used as is to determine the conduction and radiation components of the effective thermal conductivity in order to illustrate the proposed methodology.

A numerically random packed pebble bed similar to the experimental pebble bed was developed by using the DEM model of STAR-CCM+. An analysis of the particle distribution and the porosity variation of the numerical pebble bed proved it to be an accurate representation of the experimental pebble bed. Therefore it was used as the solid geometry model to develop the CFD heat transfer simulation. A fillet contact treatment was inserted at the contact points between adjacent spheres and spheres and the walls in order to ensure a good quality mesh was generated at the contact points.

The CFD simulation was developed using STAR-CCM+ and a setup similar to the NWETCTF with the measured experimental data specified as the boundary conditions for the simulation. Simulations were solved for each of the temperature cases of the experimental tests. The radiation component of the heat transfer could easily be eliminated in the CFD simulation as the radiation model in the simulation was simply switched off. Thus results could be obtained for combined conduction and radiation heat transfer as well as for conduction heat transfer only.

A mesh independence study was performed to determine the effect of mesh size at the contact points on the conduction heat transfer through the fillet regions. The influence of the mesh density on the solution of the simulation was also investigated. To ensure a mesh independent solution was obtained with the CFD simulation the mesh properties specified were based on the results of the mesh independence study.

The temperature results obtained with the CFD simulation was lower than temperatures for the experimental results. Although the temperatures were lower the trend of the temperature distribution through the numerically packed pebble bed was similar to the trend of the experimental temperature distribution. The difference between the CFD and experimental heat transfer results was large. The heat extracted via the water jacket was higher for the CFD results than for the experimental results. From the results it was clear that the difference between the numerical and experimental results increased for the lower temperature cases where conduction was the dominant heat transfer mechanism.

It was concluded that the only difference between the experimental setup and the CFD simulation setup was that the contact resistances at the particle-particle and particle-wall

contact points were not included in the numerical pebble bed. The fillets at the contact points were specified as a part of the pebble region and thus also had the graphite thermal conductivity value. This resulted in heat easily being conducted through the contact points in the pebble bed without any resistance. Consequently more heat was transferred through the pebble bed than for the experimental setup where contact resistances were present. A further study is required to add the modelling of the contact resistances to the current CFD simulation setup in order to obtain results more accurately describing the experimental results.

Although the CFD simulation results were not final and an exact representation of the experimental results it showed the expected trends. Therefore a methodology has been set in place that can be improved upon in future studies to obtain results more accurately describing the experimental results of the NWETCTF. The developed method was sufficient for the scope of the current study as the objective was to develop a method that can be used rather than providing a set of accurate results.

The 800°C CFD simulation case delivered the results in closest agreement with the experimental results. Thus the results for the 800°C case were used to develop the method for the separation of the conduction and radiation components of the effective thermal conductivity. The results for the effective thermal conductivity showed that radiation was the main contributor to the overall heat transfer at higher temperatures whereas conduction became the main contributing heat transfer mechanism at lower temperatures.

The experimental setup applied in this study is not fully representative of an actual packed bed reactor. However, it was shown that the proposed methodology may be used to characterise the radiation heat transfer in a packed bed, including the near-wall region. Therefore, the methodology may be applied in future to an appropriately packed test section in order characterise the near-wall region of a packed bed reactor.

6.2 Recommendations

This study proposed a methodology to predict and characterise the overall heat transfer as well as the separate conduction and radiation components of the heat transfer in the near-wall region of a packed pebble bed with the use of experimental and numerical work. Although the NWETCTF test facility is in a good working condition to obtain experimental results some improvements can be made to the system. Certain improvements to the CFD simulations are also required as mentioned previously to improve the accuracy of results obtained.

Recommendations for future investigations of the heat transfer in the near-wall region of a packed pebble bed using the NWETCTF and the proposed methodology are given in the following section:

- To minimise and limit the problem associated with the repeatability of the NWETCTF heat transfer results a temperature difference of at least 10°C between the inlet and outlet temperatures of the water jacket should be maintained during operation. The temperature difference over the water jacket should also not be much higher than 10°C as this will result in a non-uniform temperature distribution over the outer reflector. When conducting separate but identical tests to prove repeatability, similar water mass flow rate values should be maintained during operation of the NWETCTF as far as possible.
- Currently the flow meters for the water jacket and the element coolers of the NWETCTF use the same water supply line with a single pump. Thus the water supplied from the pump is divided between the flow to the water jacket and the flow to the element coolers. At some point a point of equilibrium is reached for the division of the water supply between the two lines making it difficult to accurately control the mass flow rates at a constant value. It is recommended that an extra pump be installed separating the water supply to the water jacket and the element coolers to solve this problem.
- As a large number of thermocouples were damaged during the commissioning of the NWETCTF a number of type B thermocouples must be replaced.
- Currently there is no Relative Humidity meter installed in the experimental test facility to measure the moisture content in the vessel during operation. For future experimental tests that will be conducted at temperatures up to 1600°C this might become a critical instrument. Thus the installation of a Relative Humidity meter in the NWETCTF should be considered before conducting tests at higher temperatures.
- The drift uncertainty was not included in the calculation of the measurement uncertainty for the experimental results. The instruments must be calibrated between experimental tests and the drift uncertainty must be included to provide a more complete set of results.
- The results presented in this study were sufficient for the development of the proposed methodology, however it included more than one near-wall region and improvements have to be made to the CFD simulations. More experimental tests must be done using the NWETCTF to provide a larger set of experimental data including cases at higher temperatures.
- The influence of the size of the fillet radius used for the contact treatment of the particle-particle and particle-wall contact points was not investigated during this study. A thorough

investigation of the influence of the fillet and contact area size on the conduction heat transfer between adjacent pebbles should be completed.

- Contact resistances should be modelled at the contact points in the CFD simulations by varying the thermal conductivity value of the fillet material at the contact points. The results for the CFD model with the contact resistances should be compared to the NWETCTF experimental results until the best possible correlation between the results is obtained. Once the CFD model has been calibrated it can be used to investigate the heat transfer through a section of a numerically packed pebble bed that includes only one near-wall region.

Bibliography

Aichlmayr, H.T. & Kulacki, F.A. 2006. The Effective Thermal Conductivity of Saturated Porous Media. *Advances in Heat Transfer*, 39:377-460.

Amano, Y. 2013. Interest in nuclear power steady despite Fukushima. *World Energy Insight 2013*:69-70.

Argento, C. & Bouvard, D. 1996. A ray tracing method for evaluating the radiative heat transfer in porous media. *International Journal of Heat and Mass Transfer*:3175-3180.

Asakuma, Y., Kanazawa, Y. & Yamamoto, T. 2014. Thermal radiation analysis of packed bed by a homogenization method. *International Journal of Heat and Mass Transfer*, 73(2014):97-102.

Balkrishnan, A.R. & Pei, D.C.T. 1979. Heat transfer in gas-solid packed bed systems. 2. The conduction mode. *Industrial & Engineering Chemistry Process Design & Development*, 18(1):40-46.

Béttega, R., Barrozo, M.A.S., Corrêa, R.G. & Freire, J.T. 2013. CFD simulation of heat transfer inside packed beds: Evaluation of effective thermal conductivity. *JP Journal of Heat and Mass Transfer*, 8(2):137-148.

Bevington, P.R. & Robinson, D.K. 2003. Data Reduction and Error Analysis for the Physical Sciences. (3rd ed. New York: McGraw-Hill.).

Breitbach, G. & Barthels, H. 1980. The radiant heat transfer in the high temperature reactor core after failure of the afterheat removal systems. *Nuclear Technology*, 49:392-399.

Caliot, C. 2010. Numerical methods in Radiative Transfer. Introduction to DOM, FVM and MCM. http://sfera.sollab.eu/downloads/Schools/Caliot_DOM_FVM_MCM.pdf Date of access: 11 November. 2014.

CD-adapco. 2013. STAR-CCM+ User Guide. 8th ed.

Cengel, Y.A. & Ghajar, A.J. 2011. (*In*: Heat and Mass Transfer. 4th ed. Singapore: McGraw-Hill.).

Chen, J.C. & Churchill, S.W. 1963. Radiation heat transfer in packed beds. *American Institute of Chemical Engineers*, 9(1):35-41.

Cheng, G.J. & Yu, A.B. 2013. Particle scale evaluation of the effective thermal conductivity from the structure of a packed bed: Radiation heat transfer. *Industrial & Engineering Chemistry Research*, 52(34):12202-12211.

Cheng, G.J., Yu, A.B., Zulli, P. & Xu, D.L. 2002. Radiation Heat Transfer in Random Packing of Mono-sized Spheres. (*In* Proceedings of the 4th World Congress on Particle Technology. Sydney.)

Chu, S. & Majumdar, A. 2012. Opportunities and challenges for a sustainable energy future. *Nature*, 488(7411):294-303. http://nwulib.nwu.ac.za/login?url=http://search.ebscohost.com/login.aspx?direct=true&db=aph&AN=78913286&site=eds-live.

Dixon, A.G., Nijemeisland, M. & Stitt, E.H. 2013. Systematic mesh development for 3D CFD simulation of fixed beds: Contact points study. *Computers and Chemical Engineering*, 48(2013):135-153.

Du Toit, C.G. 2002. The numerical determination of the variation in the porosity of the pebble-bed core. (*In* Proceedings of 1st International Topical Meeting on High Temperature Reactor Technology (HTR-2002). Petten, Netherlands.)

Du Toit, C.G. 2008. Radial variation in porosity in annular packed beds. *Nuclear Engineering and Design*, 238(2008):3073-3079.

Du Toit, C.G., Van Antwerpen, W. & Rousseau, P.G. 2009. Analysis of the porous structure of an annular pebble bed reactor. (*In* ICAPP. Tokyo. p. 1-10.)

Echàvarri, L. 2013. Nuclear power in the aftermath of Fukushima. (*In* World Energy Insight 2013. p. 62-63.)

Eppinger, T., Seidler, K. & Kraume, M. 2011. DEM-CFD simulations of fixed bed reactors with small tube to particle diameter ratios. *Chemical Engineering Journal*, 166(2011):324-331.

Feng, Y.T. & Han, K. 2012. An accurate evaluation of geometric view factors for modelling radiative heat transfer in randomly packed beds of equally sized spheres. *International Journal of Heat and Mass Transfer*, 55(2012):6374-6383.

Incorpera, F.P., Dewitt, D.P., Bergman, T.L. & Lavine, A.S. 2007. (*In*: Fundamentals of Heat and Mass Transfer. 6th ed. USA: John Wiley & Sons.).

International Energy Agency. 2012. World Energy Outlook 2012: Executive Summary. http://www.iea.org/publications/freepublications/publication/English.pdf Date of access: 19 March. 2014. [Date of access: 19 March 2014].

Kadak, A.C. 2005. A future for nuclear energy: pebble bed reactors. *International Journal of Critical Infrastructures*, 1(4):330-345.

Kamiuto, K., Iwamoto, M. & Nagumo, Y. 1993. Combined Conduction and Correlated-Radiation Heat Transfer in Packed Beds. *Journal of Thermophysics and Heat Transfer*, 7(3)

Kelly, J.E. 2014. Generation IV International Forum: A decade of progress through international cooperation. *Progress in Nuclear Energy*, 2014:1-7.

Lee, S.H.-K., Ip, S.C.-H. & Wu, A.K.C. 2001. Sphere-to-Sphere Radiative Transfer Coefficient for packed sphere system. (*In* Proceedings of 2001 ASME International Mechanical Engineering Congress and Exposition. New York. p. 105-110.)

Lee, J.J., Park, G.C., Kim, K.Y. & Lee, W.J. 2007. Numerical treatment of pebble contact in the flow and heat transfer analysis of a pebble bed reactor core. *Nuclear Engineering and Design*, 237(2007):2183-2196.

Louw, A.D.R., Nel, R.G. & Gauché, P. 2012. A DEM-CFD approach to predict the pressure drop through an air-rock bed thermal energy storage system: Part 2 of 2. Stellenbosch University. http://hdl.handle.net/10019.1/83968 Date of access: 15 January. 2014.

Mandal, D., Sathiyamoorthy, D. & Vinjamur, M. 2012. Experimental measurement of effective thermal conductivity of packed lithium-titanate pebble bed. *Fusion Engineering and Design*, 87(2012):67-76.

Markgraaff, J. 2012. NWETCTF-MEM-02 Mechanical Design Feasibility. (Technical memo).

Modest, M.F. 1993. Radiative Heat Transfer. New York: McGraw-Hill.

Nel, R.G., Louw, A.D.R. & Coetzee, C.J. 2012. A DEM-CFD approach to predict the pressure drop through an air-rock bed thermal storage system: Part 1. (*In* Southern African Solar Energy Conference.)

Ookawara, S., Kuroki, M., Street, D. & Ogawa, K. 2007. High-fidelity DEM-CFD modelling of packed bed reactors for process intensification. (*In* Proceedings of European Congress of Chemical Engineering (ECCE-6). Copenhagen.)

Paul Scherrer Institut. 2012. High Temperature Reactor Experimental Programme. http://proteus.web.psi.ch/HTR-PROTEUS/index.html Date of access: 5 April. 2014.

Pitso, M.L. 2011. Characterisation of long range radiation heat transfer in packed pebble beds. Potchefstroom: North West University. (M Dissertation).

Prinsloo, J. 2014. Near-wall Effect Thermal Conductivity Test Facility Process Functional Description. (NWETCTF Technical report NWETCTF01-0002 REV2).

Robold, K. 1982. Wärmetransport im Inneren und in der Randzone von Kugelschüttungen. (Dissertation Jül-1796).

Rouquerol, J., Avnir, D., Fairbridge, C.W., Everett, D.H., Haynes, J.H.. Pernicone, N., Ramsay, J.D.F. & Sing, K.S.W.. Unger, K.K. 1994. Recommendations for the characterization of porous solids. *Pure and Applied Chemistry*, 66(8):1739-1758.

Rousseau, P.G. 2008. High Temperature Test Unit Test Execution. (M-Tech Industrial Doc HTTU0002-MEM-0067 V3).

Rousseau, P.G., Du Toit, C.G. & Pitso, M.L. 2012b. The SUN model for radiation heat transfer in packed pebble bed gas cooled reactors. (*In* Proceedings of the HTR 2012: Paper HTR2012-6-020. Tokyo.)

Rousseau, P.G., Du Toit, C.G., Van Antwerpen, W. & Van Antwerpen, H.J. 2012a. Separate effects tests to determine the effective thermal conductivity in the PBMR HTTU test facility. (*In* HTR 2012. Tokyo.)

Rousseau, P.G. & Van Staden, M. 2008. Introduction to the PBMR heat transfer test facility. *Nuclear Engineering and Design*, 238(2008):3060-3072.

Stöcker, B. & Niessen, H.F. 1997. The SANA-I-experiments for self-acting removal of the afterheat from a pebble bed.

Strieder, W. 1997. Radiation heat transport in disordered media. *Advances in Water Resources*, 20(2-3):171-187.

Suikkanen, H., Ritvanen, J., Jalali, P. & Kyrki-Rajamäki, R. 2014. Discrete element modelling of pebble packing in pebble bed reactors. *Nuclear Engineering and Design*, 273(2014):24-32.

Talukdar, P., Mendes, M.A.A., Parida, R.K., Trimis, D. & Ray, S. 2013. Modelling of conduction-radiation in a porous medium with blocked-off region approach. *International Journal of Thermal Sciences*, 72(2013):102-114.

Thurgood, C.P., Amphlett, J.C., Mann, R.F. & Peppley, B.A. 2004. Radiative Heat Transfer in Packed-beds: the Near-wall Region. (*In* A.I.Ch.E. Spring National Meeting April 25 - 29. New Orleans.)

Tsory, T., Ben-Jacob, N., Brosh, T. & Levy, A. 2013. Thermal DEM-CFD modelling and simulation of heat transfer through packed bed. *Powder Technology*, 244(2013):52-60.

Tucker, R.J. 14 June. 2004. How do I predict radiative heat transfer in industrial furnaces? IFRF Online Combustion Handbook. www.handbook.ifrf.net Date of access: 11 November. 2014.

U.S. Energy Information Administration. 2013. World energy demand and economic outlook. (*In*: International Energy Outlook. p. 9-21).

Uhia, F.J., Campo, A. & Fernandez-seara, J. 2013. Uncertainty analysis for experimental heat transfer data obtained by the Wilson plot method. *Thermal Science*, 17(2):471-487.

Van Antwerpen, W. 2009. Modelling the effective thermal conductivity in the near-wall region of a packed pebble bed. Potchefstroom: NWU. (Thesis - Ph.D.).

Van Antwerpen, W., Du Toit, C.G. & Rousseau, P.G. 2010a. A review of correlations to model the packing structure and effective thermal conductivity in packed beds of mono-sized spherical particles. *Nuclear Engineering and Design*, 240(2010):1803-1818.

Van Antwerpen, H.J., Rousseau, P.G. & Du Toit, C.G. 2010b. The extraction of the temperature gradient from measured temperature profiles with uncertainty propagation as applied to the High Temperature Test Unit. (*In* Seventh South African Conference on Computational and Applied Mechanics. Pretoria.)

Van Antwerpen, W., Rousseau, P.G. & Du Toit, C.G. 2012. Multi-sphere Unit Cell model to calculate the effective thermal conductivity in packed pebble beds of mono-sized spheres. *Nuclear Engineering and Design.*, 247(2012):183-201.

Van der Meer, W.A. 2011. Modelling long-range radiation heat transfer in a pebble bed reactor. Potchefstroom: North West University. (M Dissertation).

Van der Merwe, W.J.S. 2014. Analysis of flow through cylindrical packed beds with small cylinder diameter to particle diameter ratios. Potchefstroom: NWU. (Dissertation - M).

Van der Walt, B. 2014. Investigation into radiation and conduction heat transfer of a packed bed. Potchefstroom: North West University. (Project Report).

Vortmeyer, D. 1978. Radiation in packed solids. (*In* Proceedings, 6th International Heat Transfer Conference. Toronto. p. 525-539.)

Widenfield, G., Weiss, Y. & Kalman, H. 2003. The effect of compression and preconsolidation on the effective thermal conductivity of particulate beds. *Powder Technology*, 133(2003):15-22.

World Energy Council. 2013. World Energy Insight 2013. http://www.worldenergy.org/publications/2013/world-energy-insight-2013 Date of access: 13 March. 2014.

Wu, A.K.C. & Lee, S.H.K. 2000. Multiple-rays tracing technique for radiative exchange within packed beds. *Numerical Heat Transfer, Part B: Fundamentals: An International Journal of Computation and Methodology*, 37(4):469-487.

Zhou, J., Yu, A. & Zhang, Y. 2007. A boundary element method for evaluation of the effective thermal conductivity of packed beds. *Journal of Heat Transfer*, 129:363-371.

Zhou, Z.Y., Yu, A.B. & Zulli, P. 2010. A new computational method for studying heat transfer in fluid bed reactors. *Powder Technology*, 197(2010):102-110.

Zou, R.P. & Yu, A.B. 1995. The packing of spheres in a cylindrical container: the thickness effect. *Chemical Engineering Science*, 50(9):1504-1507.

Annexures

A. NWETCTF test facility

This annexure provides detailed information on the positions of the instrumented spheres in the NWETCTF packed pebble bed, the measurement ranges and accuracies of the most important instruments and the properties of the insulation and graphite materials. A detailed description of the process followed during the commissioning of the system as well as the problem identification and solutions implemented by the researcher are given.

A.1 Position coordinates of instrumented spheres in experimental bed

The coordinates of the centroids of the instrumented spheres in the experimental packed pebble bed are given in Table A.1. The positions for level A, B and C in the packed pebble bed as well as the coordinate system correspond to the levels illustrated in Figure 4.2. For the measurement of the positions of the spheres the origin was placed in the centre of the bottom surface of the NWETCTF test section.

Table A.1: Coordinates of positions of instrumented spheres in experimental packed pebble bed.

Thermocouple tag	Coordinates [m]					
	x	y	z	x	y	z
Level A	**Test 1**			**Test 2**		
TT 311	-0.005	0.015	0.030	0.025	-0.010	0.030
TT 312	-0.005	0.180	0.030	-0.025	0.115	0.030
Level B	**Test 1**			**Test 2**		
TT 301	-0.040	-0.180	0.185	-0.040	-0.180	0.240
TT 302	0.010	-0.120	0.180	0.005	-0.060	0.230
TT 303	-0.045	-0.120	0.190	-0.005	-0.125	0.215
TT 304	0.005	-0.065	0.185	0.015	0.000	0.245
TT 305	-0.040	-0.045	0.220	-0.045	-0.080	0.220
TT 313	0.020	0.050	0.190	0.020	0.035	0.205
TT 314	-0.035	0.005	0.185	-0.040	-0.005	0.225
TT 315	0.015	0.120	0.190	0.035	0.085	0.240
TT 316	-0.030	0.050	0.220	-0.025	0.055	0.240
TT 317	0.015	0.180	0.205	0.015	0.175	0.215
TT 318	-0.040	0.130	0.190	-0.015	0.130	0.230
TT 320	-0.035	0.180	0.230	-0.045	0.180	0.230
Level C	**Test 1**			**Test 2**		
TT 319	0.010	0.020	0.360	0.025	-0.080	0.385
TT 321	-0.020	0.180	0.380	0.005	0.125	0.390

A.2 Commissioning of NWETCTF

An important part in the development of the methodology presented in this study was the commissioning of the NWETCTF and solving problems that were identified during first time operation. The process of ensuring the system was functioning properly was necessary to obtain the first set of experimental results and prove that the system can be used to investigate the heat transfer phenomena in the near-wall region of a packed pebble bed. A timeline of the commissioning process as well as a discussion of the problems experienced is provided in the following section.

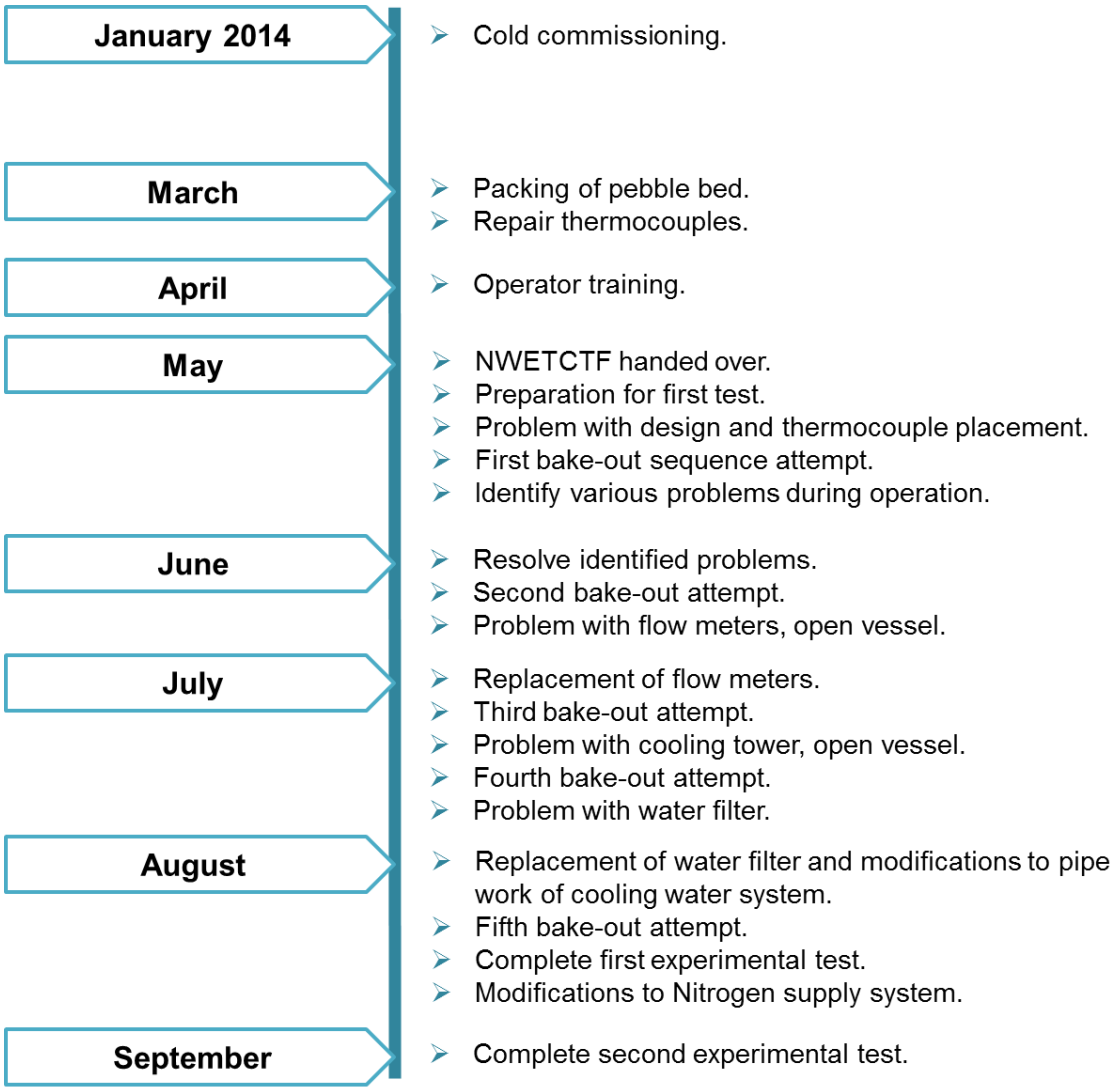

Figure A.1: Timeline of NWETCTF commissioning process.

The cold commissioning phase of the system was completed by the contractors at the end of April 2014. During this phase it was my responsibility to gain an understanding of the plant layout and the functions of the various components. I had to learn how to operate the system

and was informed of the possible high-risk scenarios during operation and how to address such scenarios.

The packing of the experimental bed was done for the first time during March 2014; however it was found that the plugs of the thermocouples inserted by the contractors were very sensitive to the slightest disruption. Once the test section was placed inside the NWETCTF vessel the sensitivity could cause some of the thermocouples to malfunction resulting in inaccurate readings or incomplete results. Another problem was that the type K thermocouples that were provided were too short to be inserted at the desired positions in the packed pebble bed. All of the thermocouples were removed from the test section in order to increase the cable length and the wiring in each of the thermocouple plugs were soldered to decrease the sensitivity

Once the modifications to the thermocouples were completed it was re-inserted into the test section and routed to the desired positions in the packed bed of spheres. The packing of the pebble bed was completed for a second time and the system was ready for the first experimental test by the middle of April. The training of the other operators was also completed during the month of April.

The system was handed over at the beginning of May by the contractors and the preparation for the first experimental test was started immediately. However, it was found that the design for the thermocouple cable placement at the bottom of the vessel was insufficient. As can be seen in Figure A.2 (a) before the test section is pushed into the vessel the cables of the thermocouples were placed at the bottom of the vessel and the test section had to be pushed in slowly. The problem was that the tolerance for the fit of the test section inside the vessel was very small and the thermocouples used were not ideal for the application, as a result thermocouples were damaged when the test section was pushed into the vessel. A photograph of a damaged thermocouple is shown in Figure A.2 (b).

The pebble bed was unpacked and the damaged thermocouples were removed from the test section. After the pebble bed was re-packed and the thermocouples were re-routed a new strategy was used to insert the test section into the vessel. Both sides of the vessel were removed in order to efficiently guide the thermocouples to the other side of the vessel whilst the test section was pushed into place. This method ensured that none of the thermocouples were damaged and the system was ready for operation by 13 May.

(a) (b)

Figure A.2: (a) Thermocouple cables placed at bottom of NWETCTF vessel and (b) a damaged thermocouple.

The first attempt at the completion of a bake-out sequence of the system was started immediately. As this was the first time that the system was operating for a long time period various problems were identified and addressed. A list of the identified problems together with the solutions implemented is provided:

- One of the small electrical heater units used for the bake-out sequence kept tripping the main power due to a short circuit. As a result the insulation material temperatures reached were too low to successfully complete the bake-out sequence. The heater unit was replaced.
- The heater system trips the entire system as soon as it is switched on and lets the system go into cool down mode. In case of an emergency if the heater system failed the safety system was designed to open the emergency drain valves to flush the system with cooling water. The signal that causes the valves to open was programmed incorrectly on the SIS and as a result as soon as the heater system was switched on the SIS tripped the system.
- The system's Nitrogen consumption was extremely high and a purge strategy had to be implemented for the bake-out sequence to improve the Nitrogen consumption.
- A lot of the components used for the NWETCTF were the same components that were used for the HTTU test facility, because of the wear and tear of these components maintenance problems were experienced. For example the relays of the vacuum pump and the ammeter of the cooling water pump controller unit had to be repaired.

- Problems with the control system were also experienced and various variables and limits had to be adjusted in the program.

Once all the identified problems were resolved the second attempt at the bake-out sequence was started on 23 June. During operation the heater system kept failing due to no flow to the water jacket and the element coolers. Oval gear flow meters, shown in Figure A.3 (a), were used to measure the flow rates of the cooling water. Impurities in the cooling water and the high lime content of the water caused wear on the gears of the flow meters and as a result the gears jammed blocking the flow of the water. It was decided that the flow meters had to be replaced with flow meters that do not have any mechanical moving parts which could cause the same problem, as the cooling system is a necessity for the safe operation of the NWETCTF especially at high temperatures.

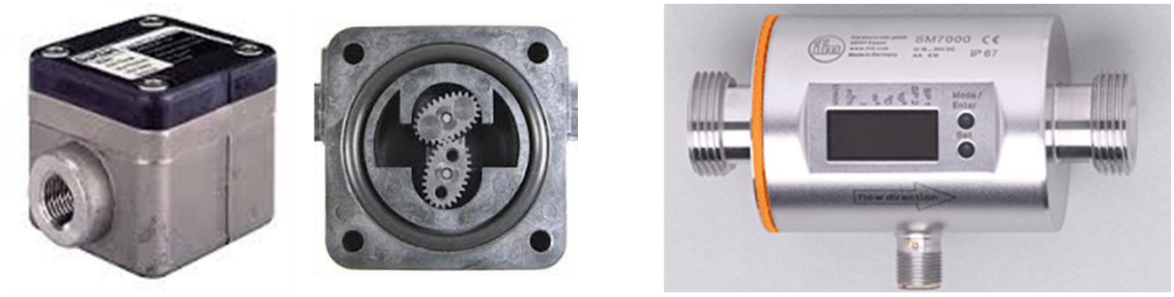

Figure A.3: (a) Oval gear flow meter and (b) magnetic-inductive flow meter.

Research was conducted on different flow meters that would be the most suitable for the application and it was decided to use magnetic-inductive flow meters, shown in Figure A.3 (b). The new flow meters were received on 7 July and during the following two weeks it was installed and changes were made to the control system to incorporate the new flow meters. The bleeding point to remove all the air from the water jacket system is situated on the water jacket and therefore the vessel had to be opened as air bubbles would result in the flow meters not functioning correctly. The third bake-out attempt was started on 21 July.

During the bake-out sequence the system again showed low flow problems to the water jacket and the element coolers. As the flow meters were replaced and had no mechanical moving parts the problem had to either be on the pipework or the in line filter before the flow meters. As can be seen in Figure A.4, the filter was opened and the sieves were cleaned with ethanol. It was found that that the pore size of the filter was extremely fine and thus the filter was easily blocked due to the impurities in the water. As a preventative measure the current filter had to be

opened and cleaned each time before a test was completed to prevent problems with water flow to the water jacket and element coolers.

Figure A.4: The sieves of the water filter before and after it was cleaned.

Unfortunately the cooling tower sump kept overflowing and at first it seemed that it might be the ball valve that was not functioning correctly. The ball valve was overhauled, but the problem still remained. After systematically looking for the possible cause it was found that one of the emergency valves was not fully closed during operation, thus water from the main water supply was bypassing the flow meters and entering the water jacket and the element coolers. As a result one could not know exactly what the water flow rates were at a specific moment. The emergency valve had to be overhauled and it was found that the valve was misaligned. Even if the valve indicator showed that the valve was closed it was in actual fact open. The vessel had to be opened once more to remove any air from the cooling water system and the fourth attempt at the bake-out sequence was started on 29 July.

Low flow problems to the water jacket and element coolers were experienced during the bake-out attempt. Unfortunately the filter had to be opened again as it was blocked and therefore the entire vessel had to be opened as there would be air in the pipelines. It was decided to replace the small filter with a bigger filter that has a larger pore size and additional inline bleeding points were installed after the new filter in order to ensure the vessel does not have to be opened each time to remove air bubbles from the cooling water system. The bake-out sequence was stopped and the modifications to the system were completed by 4 August. The fifth attempt at the bake-out sequence was started.

The system was functioning correctly and the bake-out sequence followed by the first experimental test was completed on 13 August. One last change was identified that would increase the safety of the system when operating at higher temperatures and would make it more convenient for operators working shifts. Initially the Nitrogen supply system of the

NWETCTF consisted of a bank of Nitrogen with six cylinders and a 200 bar capacity. During operation this Nitrogen supply would last for approximately 12 hours or less. As a result when the Nitrogen cylinders had to be replaced Nitrogen purging was stopped for about 30-60 minutes during operation and the vacuum was maintained inside the NWETCTF vessel. The replacement of the Nitrogen bottles could also be required at any time of the day as the system was operating for 24 hours per day, thus sometimes it had to be replaced at night time without proper lighting. To resolve this problem the Nitrogen supply line was modified to include another six cylinders with a switch valve, thus if the bank pressure was running low the operator could just switch to the second set of cylinders and the empty cylinders could be replaced during the day time.

Unfortunately there was a long waiting period for the components to arrive and the installation to be done along with the required safety tests, thus the modifications were completed by 19 September. During this time the vessel was opened and the pebble bed was re-packed. A bake-out sequence was completed and the second experimental test was finished by 23 September.

A.3 Instrument range and accuracy

Typically the instruments used in an experimental test facility can be grouped into different categories according to the importance of the results obtained from the instruments (Van Antwerpen, 2009). Type A instruments are of critical importance to ensure that accurate and useful results are obtained from the experimental test. Whereas type B instruments are important for the correct operation of the plant and type C instruments only provide indicators of certain variables, these instruments are only calibrated during the cold commissioning of the system (Van Antwerpen, 2009).

The ranges and accuracies of the NWETCTF instruments that can be categorized as Type A instruments are provided in Table A.2.

Table A.2: NWETCTF type A instrument ranges and accuracies.

Instrument	Range	Accuracy	Measured variable
Type B thermocouples	100 – 1600°C	± 5°C	Bed and inner reflector temperatures.
Type K thermocouples	0 – 1100°C	± 3°C	Bed, outer reflector and insulation temperatures.
PT100 RTD	0 - 60°C	± 0.2°C	Water jacket and element coolers inlet and outlet temperatures.
SM6100 magnetic-inductive flow meters	0.1 – 25 l/min	± 0.2%	Water flow rates.

A.4 Material properties

A summary of the material properties required for the calculation of the heat transfer and the effective thermal conductivity of the NWETCTF packed pebble bed is provided in the following section. Table A.3 lists the thermal conductivity values of the insulation materials used in the NWETCTF test section as specified by Markgraaff (2012). The thermal conductivity values of the pebble graphite at various temperatures are given in Table A.4. As the pebbles used for the NWETCTF is the same pebbles used for the HTTU test facility the values were obtained from Rousseau *et al.* (2012a).

Table A.3: Thermal conductivity of insulation materials (Markgraaff, 2012).

Temperature [°C]	Thermal Conductivity [W/m-K]	
	SALI-2	AL-45
250	0.15	0.16
525	0.20	0.20
800	0.25	0.23
1350	0.34	0.36
1650	0.39	0.43

Table A.4: Thermal conductivity of graphite pebbles (Rousseau *et al.*, 2012a).

Temperature [°C]	Thermal Conductivity [W/m-°C]
20	155
100	138
200	120
300	104
400	92
500	82
600	74
700	68
800	63
900	59
1000	56
1100	53
1200	50

B. NWETCTF data and uncertainty analysis

The following section provides a more detailed discussion of the methods used for the data and uncertainty analysis of the NWETCTF experimental results.

B.1 Temperature results

A summary of the experimental temperature results together with the associated measurement uncertainties are provided in this section. The average values of the measured temperatures for a specific position from the heated wall are listed in Table B.1 to Table B.5 for the various temperature cases and both experimental tests.

Table B.1: Measured temperatures for the 800°C steady-state test.

Test 1		
Position [m]	**Temperature [°C]**	**Uncertainty [±°C]**
Level A		
0.225	594.59	3.001066
0.390	324.80	3.002159
Level B		
0.030	795.71	5.000086
0.090	743.78	5.000851
0.090	745.40	5.000778
0.145	689.98	5.001059
0.165	673.50	5.001434
0.215	625.87	3.000759
0.260	569.98	3.000959
0.260	564.29	3.001010
0.330	463.27	3.001687
0.340	434.04	3.001457
0.390	337.33	3.001436
0.390	336.49	3.002035
Level C		
0.230	610.19	3.000671
0.390	366.31	3.001196

Table B.2: Measured temperatures for both the 700°C steady-state tests.

Test 1			Test 2		
Position [m]	**Temperature [°C]**	**Uncertainty [±°C]**	**Position [m]**	**Temperature [°C]**	**Uncertainty [±°C]**
Level A					
0.225	503.37	3.001229	0.200	543.22	3.001229
0.390	254.93	3.001367	0.325	372.94	3.005574
Level B					
0.030	689.56	5.001178	0.030	694.06	5.001186
0.090	642.05	5.001328	0.085	654.12	5.001376
0.090	643.18	5.000062	0.130	614.64	5.000727
0.145	591.31	5.000284	0.150	587.79	5.001535
0.165	576.66	5.001282	0.205	548.36	3.001457
0.215	533.36	3.000853	0.210	537.09	5.001845
0.260	480.06	3.001258	0.245	496.92	3.001710
0.260	475.28	3.001214	0.265	475.07	3.002709
0.330	381.48	3.001682	0.295	438.08	3.002221
0.340	355.37	3.001326	0.340	374.45	3.005089
0.390	270.14	3.001228	0.385	289.54	3.004428
0.390	264.17	3.001062	0.390	265.15	3.004275
Level C					
0.230	520.15	3.000786	0.130	618.13	3.000175
0.390	297.63	3.000872	0.335	399.82	3.002204

Table B.3: Measured temperatures for both the 600°C steady-state tests.

Test 1			Test 2		
Position [m]	**Temperature [°C]**	**Uncertainty [±°C]**	**Position [m]**	**Temperature [°C]**	**Uncertainty [±°C]**
Level A					
0.225	411.27	3.000643	0.200	454.64	3.002417
0.390	190.94	3.000408	0.325	302.20	3.005006
Level B					
0.030	584.30	5.000328	0.030	597.54	5.000161
0.090	540.86	5.000118	0.085	559.89	5.000730
0.090	541.69	5.000316	0.130	523.57	5.002391
0.145	493.00	5.000460	0.150	498.65	5.002289
0.165	480.02	5.001808	0.205	462.03	3.001892
0.215	440.77	3.000649	0.210	451.14	5.002794
0.260	390.77	3.000857	0.245	413.18	3.003356
0.260	386.89	3.000463	0.265	393.62	3.004009
0.330	302.62	3.000906	0.295	360.25	3.004286
0.340	281.75	3.000708	0.340	303.26	3.005436
0.390	209.68	3.000620	0.385	228.43	3.005588
0.390	202.67	3.000727	0.390	209.73	3.004311
Level C					
0.230	430.55	3.000440	0.130	529.11	3.000382
0.390	235.26	3.001042	0.335	326.91	3.004454

Table B.4: Measured temperatures for both the 500°C steady-state tests.

Test 1			Test 2		
Position [m]	**Temperature [°C]**	**Uncertainty [±°C]**	**Position [m]**	**Temperature [°C]**	**Uncertainty [±°C]**
Level A					
0.225	313.08	3.004921	0.200	356.87	3.004434
0.390	128.48	3.004455	0.325	225.96	3.006168
Level B					
0.030	478.04	5.000222	0.030	491.51	5.000510
0.090	437.24	5.002432	0.085	455.74	5.000220
0.090	437.31	5.002922	0.130	420.89	5.002778
0.145	390.05	5.002374	0.150	398.40	5.001242
0.165	378.25	5.003582	0.205	363.72	3.003416
0.215	341.66	3.003914	0.210	355.79	5.003285
0.260	296.33	3.005821	0.245	321.44	3.005100
0.260	292.62	3.005867	0.265	305.10	3.006353
0.330	220.89	3.007644	0.295	276.25	3.006266
0.340	204.98	3.005889	0.340	228.53	3.006593
0.390	146.49	3.005531	0.385	166.65	3.004993
0.390	141.62	3.005593	0.390	153.52	3.004559
Level C					
0.230	334.13	3.004232	0.130	430.04	3.000322
0.390	167.09	3.006614	0.335	249.34	3.004865

Table B.5: Measured temperatures for both the 400°C steady-state tests.

Test 1			Test 2		
Position [m]	**Temperature [°C]**	**Uncertainty [±°C]**	**Position [m]**	**Temperature [°C]**	**Uncertainty [±°C]**
Level A					
0.225	237.60	3.001433	0.200	277.30	3.000255
0.390	94.23	3.000149	0.325	174.11	3.000276
Level B					
0.030	376.24	5.001794	0.030	390.74	5.001808
0.090	341.42	5.003622	0.085	359.98	5.000223
0.090	341.49	5.002148	0.130	330.37	5.000375
0.145	299.56	5.005869	0.150	311.15	5.000950
0.165	290.80	5.002542	0.205	283.15	3.000129
0.215	262.19	3.001494	0.210	274.75	5.000536
0.260	224.23	3.001329	0.245	248.08	3.000171
0.260	221.00	3.001526	0.265	235.84	3.000354
0.330	164.20	3.000827	0.295	212.81	3.000206
0.340	152.99	3.000825	0.340	175.38	3.000123
0.390	107.44	3.000176	0.385	126.45	3.000190
0.390	104.26	3.000415	0.390	118.13	3.000081
Level C					
0.230	256.02	3.001213	0.130	341.08	3.000087
0.390	121.36	3.000326	0.335	191.49	3.000101

B.2 Heat transfer distribution and uncertainty analysis

A more detailed description of the methodology used to calculate the heat transfer through the packed pebble bed together with its associated uncertainties is provided in this section. The method used for the analysis is similar to the method used by Van Antwerpen (2009).

The heat transfer through the packed pebble is not constant but is a function of the position from the heated wall. As discussed in section 4.3.3, at a specific position in the packed pebble bed the local bed heat transfer rate can be calculated as the sum of the heat extracted via the water jacket and the total heat loss through the insulation between the position under consideration and the cooled wall.

In order to determine the heat losses through the top, bottom and side insulation walls of the test section the insulation walls were discretized into 56 equally spaced increments, as illustrated in Figure 4.13. For each of the increments the approximate heat loss was calculated for the various insulation walls using the measured bed and environmental temperatures as shown Equation (B.1):

$$Q_{i,loss} = \left(\left(\frac{k_{SALI} A_i}{L_{SALI}} \right)^{-1} + \left(\frac{k_{AL} A_i}{L_{AL}} \right)^{-1} \right)^{-1} (T_{bed} - T_{env}) \tag{B.1}$$

The material thermal conductivity of the SALI-2, k_{SALI}, and the AL-45, k_{AL}, insulation material is a function of temperature and was specified for each of the temperature cases. Table A.3 lists the thermal conductivity values that were used for the various temperatures. A single layer of insulation material has a thickness of 0.038 m thus L_{SALI} was specified as 0.038 m and L_{AL} as 0.19 m. The area of each increment was calculated as $A_i = L(y_{i+1} - y_i)$ with $L = 0.42m$ the width of the test section.

The environmental temperature, T_{env}, is the temperature measured on the outer layer of the insulation material of the various insulation walls. During the experimental tests temperature measurements were taken for the top and side insulation wall. As the packing structure next to the side insulation wall is similar to the packing structure next to the bottom insulation wall the temperature measurement for the side insulation was also used to calculate the heat losses through the bottom insulation. The insulation temperature measurements with the measurement uncertainties for the different cases of both experimental tests are given in Table B.6.

Table B.6: Measured temperatures of insulation material for both experimental tests.

Case	Test 1				Test 2			
	$T_{env,top}$ [°C]	$u(T_{env,top})$ [±°C]	$T_{env,side}$ [°C]	$u(T_{env,side})$ [±°C]	$T_{env,top}$ [°C]	$u(T_{env,top})$ [±°C]	$T_{env,side}$ [°C]	$u(T_{env,side})$ [±°C]
800°C	51.449	3.003	58.391	3.000	-	-	-	-
700°C	48.862	3.005	54.167	3.001	41.391	3.004	55.172	3.002
600°C	41.015	3.002	46.048	3.000	36.221	3.002	52.128	3.000
500°C	34.073	3.016	35.260	3.000	36.145	3.001	43.046	3.002
400°C	33.855	3.014	35.292	3.000	28.879	3.001	36.301	3.000

The measured bed temperatures for level A and C as listed in Table B.1 to Table B.5 were used to obtain the bed temperatures at the bottom and top insulation material respectively. As no temperature measurements were taken for the packed pebble bed next to the side insulation walls the bottom level bed temperatures were also used to estimate the heat losses through the side insulation walls. A curve was fitted through the experimental temperature measurements for level A and C of the various experimental cases to obtain functions describing the bed temperatures next to the bottom, side and top insulation walls.

Figure B.1 shows the fitted curve and functions for top and bottom level bed temperatures for the 800°C case. The bed temperature, T_{bed}, for each increment was calculated using the derived functions and the corresponding positions in the middle of each increment.

The total heat loss value for each of the steady-state test cases was calculated as the sum of all the incremental heat losses for the top, bottom and side insulation walls as shown in Equation (B.2):

$$Q_{totLoss} = \sum_{i=1}^{56} Q_{i,loss,top} + \sum_{i=1}^{56} Q_{i,loss,bottom} + \sum_{i=1}^{56} 2Q_{i,loss,side} \qquad \text{(B.2)}$$

The incremental heat losses through each of the insulation walls as well as the total incremental heat loss for the 800°C case are shown in Figure B.2:

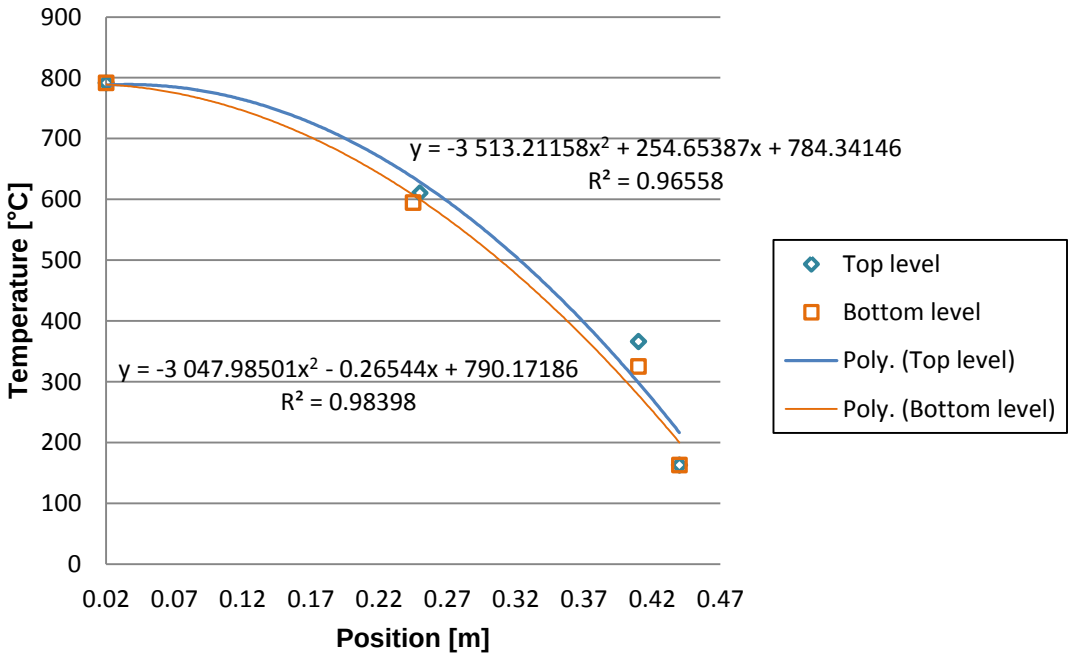

Figure B.1: Temperature curve fits for the bed temperatures at level A and C for the 800°C case of Test 1.

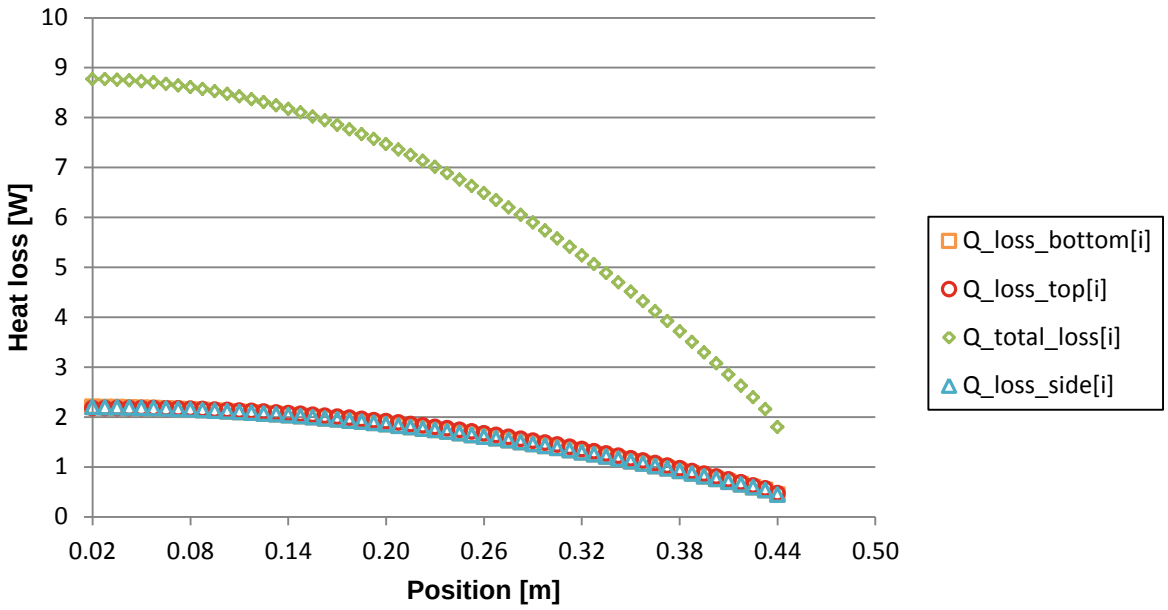

Figure B.2: Heat loss through insulation walls and total heat loss as a function of position from the heated wall for the 800°C case.

In order to determine the heat transfer through the packed pebble bed, the amount of heat extracted from the pebble bed via the water jacket must also be known. Equation (B.3) was used to calculate the heat removed through the water jacket:

$$Q_{out} = \dot{m} c_p (T_{w,out} - T_{w,in}) \tag{B.3}$$

with $\dot{m}$ the measured water flow rate through the water jacket, c_p the specific heat capacity value of water assumed to be constant at 4183J/kg-K and $T_{w,out}$ and $T_{w,in}$ the outlet and inlet water temperatures of the water jacket respectively. The measured experimental values together with measurement uncertainties of the water temperatures and flow rates as used in the calculations are given in Table B.7.

At a specific position in the packed pebble bed the heat transfer through the pebble bed was calculated as the difference between the total amount of heat entering the packed bed at the inner reflector and the total heat loss between the inner reflector and the position under consideration. Equation (B.4) was used for the calculation of the bed heat transfer:

$$Q_{bed}(r_j) = Q_{wj} + Q_{totLoss} - (\sum_{i=1}^{j-1} Q_{i,loss}(r_i) + Q_{i,loss}(r_j)) \tag{B.4}$$

where the total amount of heat entering the pebble bed is the sum of the heat extracted via the water jacket, Q_{wj} , and the total heat loss through the insulation walls, $Q_{totLoss}$.

Table B.7: Measured water temperatures and flow rates for both experimental tests.

Case	$T_{w,in}$ [°C]	$u(T_{w,in})$ [±°C]	$T_{w,out}$ [°C]	$u(T_{w,out})$ [±°C]	$\dot{m}$ [l/min]	$u(\dot{m})$ [±l/min]
Test 1						
800°C	25.06	0.21	31.83	0.22	3.511	0.009
700°C	24.93	0.20	30.36	0.22	3.051	0.009
600°C	24.28	0.21	30.62	0.21	1.456	0.007
500°C	23.77	0.22	28.50	0.23	1.253	0.016
400°C	20.53	0.19	26.07	0.21	0.744	0.009
Test 2						
700°C	25.10	0.20	31.87	0.24	2.580	0.066
600°C	24.86	0.21	32.53	0.24	1.431	0.034
500°C	25.08	0.22	30.45	0.23	1.413	0.027
400°C	25.20	0.24	30.38	0.25	0.620	0.044

An iterative method was used to calculate the bed heat transfer and the heat transfer rate at the heated and cooled walls was specified as the boundary values. The heat entering the packed pebble bed at the heated wall was specified as shown in Equation (B.5) whilst the heat removed at the cooled wall was specified as the heat removed via the water jacket, shown in Equation (B.6).

$$Q_{bed}(0.02m) = Q_{wj} + Q_{totLoss} \tag{B.5}$$

$$Q_{bed}(0.44m) = Q_{wj} \tag{B.6}$$

After the bed heat transfer was calculated a curve was fitted through the results for each of the cases of both Test 1 and Test 2 to obtain an expression for the bed heat transfer as a function of the y-position from the heated wall. The general form of the bed heat transfer function is shown in Equation (B.7) with $c_0 - c_3$ the coefficients of the fitted function for each test case.

$$Q_{bed}(y) = c_o y^3 + c_1 y^2 + c_2 y + c_3 \tag{B.7}$$

A summary of the coefficients for each of the cases of both experimental tests are provided in Table B.8.

Table B.8: Calculated coefficients of the bed heat transfer function for each test case.

Case	Test 1				Test 2			
	c_0	c_1	c_2	c_3	c_0	c_1	c_2	c_3
800°C	1409.152	139.039	-1212.280	2041.778	-	-	-	-
700°C	1102.606	198.019	-1007.339	1463.887	1290.139	111.022	-1016.220	1529.559
600°C	755.376	266.900	-811.929	881.809	945.399	163.570	-815.629	1008.547
500°C	349.794	371.954	-630.766	585.966	543.666	265.064	-632.402	706.589
400°C	157.108	330.52	-447.26	403.921	313.352	236.063	-455.408	349.170

The method used by Van Antwerpen (2009) for the uncertainty analysis of the heat transfer distribution through the packed pebble bed of the HTTU test facility was used to determine the uncertainties associated with the NWETCTF heat transfer results. Equation (B.8) was used to calculate the uncertainty associated with the heat transfer through the packed pebble bed, $u(Q_{bed})$, that is dependent on the uncertainty of the heat removed via the water jacket, $u(Q_{out})$, as well as the uncertainty of the total heat loss through the insulation walls, $u(Q_{totLoss})$.

$$u(Q_{bed}) = \sqrt{u(Q_{wj})^2 + u(Q_{totLoss})^2} \tag{B.8}$$

The uncertainty associated with the heat removed via the water jacket was calculated using Equation (B.9):

$$u(Q_{wj}) = \sqrt{\left[\frac{\partial Q_{wj}}{\partial \dot{m}} u(\dot{m})\right]^2 + \left[\frac{\partial Q_{wj}}{\partial \Delta T_{wj}} u(\Delta T_{wj})\right]^2} \tag{B.9}$$

where $u(\dot{m})$ is the measurement uncertainty of the measured water flow rate through the water jacket and $u(\Delta T_{wj})$ is the uncertainty of the temperature difference over the water jacket. The partial derivatives shown in Equation (B.9) were calculated with Equation (B.10) and (B.11) respectively.

$$\frac{\partial Q_{wj}}{\partial \dot{m}} = c_p \Delta T_{wj} \tag{B.10}$$

$$\frac{\partial Q_{wj}}{\partial \Delta T_{wj}} = \dot{m} c_p \tag{B.11}$$

Equation (B.12) shows the uncertainty of the temperature difference over the water jacket:

$$u(\Delta T_{wj}) = \sqrt{\left[\frac{\partial \Delta T_{wj}}{\partial T_{w,in}} u(T_{w,in})\right]^2 + \left[\frac{\partial \Delta T_{wj}}{\partial T_{w,out}} u(T_{w,out})\right]^2} \tag{B.12}$$

with $u(T_{w,in})$ and $u(T_{w,out})$ the measurement uncertainties of the water inlet and outlet temperature respectively. The partial derivatives shown in Equation (B.12) were specified as:

$$\frac{\partial \Delta T_{wj}}{\partial T_{w,in}} = -1 \tag{B.13}$$

$$\frac{\partial \Delta T_{wj}}{\partial T_{w,out}} = 1 \tag{B.14}$$

The second component of the bed heat transfer uncertainty was the uncertainty of the total heat loss through the insulation walls described by Equation (B.15):

$$u(Q_{totLoss}) = \sqrt{u(Q_{totLoss,top})^2 + u(Q_{totLoss,bottom})^2 + 2 \cdot u(Q_{totLoss,side})^2} \tag{B.15}$$

The uncertainty of the total heat loss through each of the insulation walls were calculated as the combined uncertainty of the incremental heat losses for each of the insulation walls:

$$u(Q_{totLoss,top/bottom/side}) = \sqrt{u(Q_{1,totLoss,top/bottom/side})^2 + \cdots + u(Q_{56,totLoss,top/bottom/side})^2} \tag{B.16}$$

For a single increment the uncertainty of the heat loss was calculated using Equation (B.17).

$$u(Q_{i,loss,top/bottom/side}) = \sqrt{\left[\frac{\partial Q_{i,loss}}{\partial T_{bed}} u(T_{bed})\right]^2 + \left[\frac{\partial Q_{i,loss}}{\partial \Delta T_{env}} u(T_{env})\right]^2} \tag{B.17}$$

The uncertainty of the bed temperature $u(T_{bed})$ was a combination of the maximum measurement uncertainty and scatter uncertainty for level A and C in the packed pebble bed, shown in Equation (B.18). The definition of the scatter uncertainty is given in Equation (B.19) and it describes the distribution of the measured temperature data around the fitted curve for the bed temperatures. The maximum values of both uncertainties were used in the calculations

to be more conservative. The measurement uncertainty values of the measured environmental temperatures were used for the uncertainty of the environmental temperature, $u(T_{env})$.

$$u(T_{bed}) = \sqrt{u_{meas}(T_{bed})^2 + u_{scatter}(T_{bed})^2} \tag{B.18}$$

$$u_{scatter}(T_{bed}) = \sqrt{\frac{\sum_{i=1}^{N}(T_{i,bed,experimental} - T_{i,bed,fittedCurve})^2}{N}} \tag{B.19}$$

B.3 Effective thermal conductivity results

A summary of the effective thermal conductivity results together with the associated uncertainties are provided in this section. The calculated values of the temperature distribution function and the effective thermal conductivity for a specific position from the heated wall are listed in Table B.9 to Table B.13 for the various test cases.

Table B.9: Calculated effective thermal conductivity values for the 800°C test case.

Position [m]	Sphere diameter	$T_{poly}(y)$ [°C]	$u(T_{poly})$ [°C]	$k_{eff}(y)$ [W/m-°C]	$u(k_{eff})$ [W/m-°C]
0.020	0.000	805.969	7.092	12.167	3.592
0.050	0.500	783.853	7.222	18.668	1.501
0.110	1.500	747.329	2.073	14.907	0.682
0.110	1.500	747.329	1.812	14.907	0.668
0.165	2.417	697.577	3.142	9.817	0.425
0.185	2.750	675.302	1.862	9.008	0.392
0.235	3.583	615.451	3.081	8.369	0.374
0.280	4.333	562.170	2.746	8.500	0.390
0.280	4.333	562.170	1.207	8.500	0.388
0.350	5.500	472.029	2.873	5.929	0.279
0.360	5.667	454.850	6.783	5.251	0.253
0.410	6.500	321.672	5.394	2.475	0.119

Table B.10: Calculated effective thermal conductivity values for the 700°C test case.

Position [m]	Sphere diameter	$T_{poly}(y)$ [°C]	$u(T_{poly})$ [°C]	$k_{eff}(y)$ [W/m-°C]	$u(k_{eff})$ [W/m-°C]
0.020	0.000	703.785	2.913	10.960	1.676
0.020	0.000	703.785	2.908	10.960	1.673
0.050	0.500	684.246	2.121	14.087	0.572
0.050	0.500	684.246	3.202	14.087	0.694
0.105	1.417	650.659	1.247	11.285	0.409
0.110	1.500	647.100	1.354	10.878	0.392
0.110	1.500	647.100	1.209	10.878	0.387
0.150	2.167	614.229	0.815	8.368	0.289
0.165	2.417	600.025	1.694	7.780	0.271
0.170	2.500	595.102	1.500	7.621	0.266
0.185	2.750	579.867	0.984	7.237	0.255
0.225	3.417	537.166	1.511	6.746	0.245
0.230	3.500	531.742	0.934	6.723	0.244
0.235	3.583	526.317	0.962	6.705	0.244
0.265	4.083	493.885	0.577	6.637	0.245
0.280	4.333	477.699	0.562	6.557	0.244
0.280	4.333	477.699	0.568	6.557	0.244
0.285	4.417	472.277	0.618	6.511	0.243
0.315	4.917	438.628	0.487	5.927	0.225
0.350	5.500	392.491	1.861	4.539	0.175
0.360	5.667	376.541	3.671	4.074	0.159
0.360	5.667	376.541	0.628	4.074	0.157
0.405	6.417	274.875	2.731	2.239	0.088
0.410	6.500	259.237	1.963	2.082	0.082

Table B.11: Calculated effective thermal conductivity values for the 600°C test case.

Position [m]	Sphere diameter	$T_{poly}(y)$ [°C]	$u(T_{poly})$ [°C]	$k_{eff}(y)$ [W/m-°C]	$u(k_{eff})$ [W/m-°C]
0.020	0.000	603.007	2.702	7.934	1.285
0.020	0.000	603.007	2.697	7.934	1.283
0.050	0.500	584.939	1.465	9.035	0.295
0.050	0.500	584.939	3.942	9.035	0.493
0.105	1.417	551.840	1.943	7.265	0.266
0.110	1.500	548.429	1.726	7.049	0.239
0.110	1.500	548.429	1.597	7.049	0.234
0.150	2.167	517.893	1.229	5.651	0.171
0.165	2.417	505.042	2.198	5.293	0.162
0.170	2.500	500.614	0.911	5.192	0.159
0.185	2.750	486.957	1.416	4.936	0.153
0.225	3.417	448.621	1.791	4.524	0.146
0.230	3.500	443.709	1.142	4.492	0.144
0.235	3.583	438.780	0.453	4.461	0.144
0.265	4.083	408.932	0.704	4.296	0.141
0.280	4.333	393.781	0.626	4.192	0.139
0.280	4.333	393.781	1.106	4.192	0.140
0.285	4.417	388.673	0.873	4.149	0.138
0.315	4.917	356.851	0.724	3.762	0.128
0.350	5.500	314.185	1.950	3.005	0.104
0.360	5.667	299.967	3.170	2.751	0.097
0.360	5.667	299.967	0.765	2.751	0.096
0.405	6.417	215.209	2.474	1.670	0.060
0.410	6.500	202.830	1.299	1.569	0.056

Table B.12: Calculated effective thermal conductivity values for the 500°C test case.

Position [m]	Sphere diameter	$T_{poly}(y)$ [°C]	$u(T_{poly})$ [°C]	$k_{eff}(y)$ [W/m-°C]	$u(k_{eff})$ [W/m-°C]
0.020	0.000	501.584	2.429	5.112	0.717
0.020	0.000	501.584	2.430	5.112	0.717
0.050	0.500	481.816	1.822	5.525	0.230
0.050	0.500	481.816	3.172	5.525	0.276
0.105	1.417	446.517	2.150	4.892	0.224
0.110	1.500	443.109	1.468	4.801	0.200
0.110	1.500	443.109	1.458	4.801	0.200
0.150	2.167	414.012	1.381	4.133	0.167
0.165	2.417	402.269	2.226	3.933	0.161
0.170	2.500	398.264	0.848	3.873	0.159
0.185	2.750	386.001	1.527	3.715	0.155
0.225	3.417	351.886	1.591	3.413	0.147
0.230	3.500	347.512	1.234	3.384	0.146
0.235	3.583	343.120	0.420	3.356	0.145
0.265	4.083	316.376	0.796	3.198	0.142
0.280	4.333	302.717	1.039	3.111	0.140
0.280	4.333	302.717	1.551	3.111	0.140
0.285	4.417	298.106	1.148	3.078	0.139
0.315	4.917	269.505	1.179	2.824	0.129
0.350	5.500	232.390	1.940	2.378	0.111
0.360	5.667	220.514	2.717	2.226	0.105
0.360	5.667	220.514	1.470	2.226	0.105
0.405	6.417	154.632	2.259	1.513	0.073
0.410	6.500	145.568	0.546	1.440	0.069

Table B.13: Calculated effective thermal conductivity values for the 400°C test case.

Position [m]	Sphere diameter	$T_{poly}(y)$ [°C]	$u(T_{poly})$ [°C]	$k_{eff}(y)$ [W/m-°C]	$u(k_{eff})$ [W/m-°C]
0.020	0.000	400.764	2.342	3.213	0.471
0.020	0.000	400.764	2.344	3.213	0.471
0.050	0.500	382.251	2.274	3.380	0.158
0.050	0.500	382.251	2.864	3.380	0.172
0.105	1.417	349.863	2.314	3.153	0.162
0.110	1.500	346.864	1.408	3.115	0.140
0.110	1.500	346.864	1.398	3.115	0.140
0.150	2.167	322.083	1.572	2.805	0.123
0.165	2.417	312.394	2.323	2.698	0.120
0.170	2.500	309.117	0.914	2.665	0.119
0.185	2.750	299.149	1.612	2.570	0.117
0.225	3.417	271.676	1.546	2.360	0.113
0.230	3.500	268.159	1.055	2.336	0.111
0.235	3.583	264.625	0.486	2.313	0.111
0.265	4.083	243.030	0.794	2.178	0.107
0.280	4.333	231.940	1.218	2.106	0.105
0.280	4.333	231.940	1.669	2.106	0.106
0.285	4.417	228.189	1.239	2.080	0.104
0.315	4.917	204.906	1.350	1.903	0.098
0.350	5.500	175.075	1.841	1.637	0.086
0.360	5.667	165.732	2.248	1.549	0.083
0.360	5.667	165.732	1.734	1.549	0.082
0.405	6.417	116.242	1.941	1.136	0.062
0.410	6.500	109.732	0.655	1.091	0.059

C. CFD simulation setup and results

The position coordinates of the probe points used for the temperature measurements in the CFD simulations are given in the following section.

C.1 Position coordinates of probe points in numerical pebble bed

The coordinates of the centroids of the spheres where the probe points were placed for the temperature measurements in the numerical packed pebble bed of the CFD simulation are given in Table C.1. The positions for level A, B and C in the packed pebble bed correspond to the instrumented spheres in the experimental packed pebble bed, listed in Table A.1. For the measurement of the positions of the spheres the origin was placed in the centre of the bottom surface of the numerical packed pebble bed.

Table C.1: Coordinates of positions of point probes in numerical packed pebble bed.

Thermocouple tag	Coordinates [m]		
	x	y	z
Level A			
TT 311	-0.00686	-0.00125	0.03000
TT 312	-0.01247	0.18001	0.03000
Level B			
TT 301	-0.06048	-0.18000	0.18850
TT 302	-0.02674	-0.12899	0.18400
TT 303	-0.05939	-0.07926	0.19580
TT 304	-0.01199	-0.04346	0.18741
TT 305	-0.05994	-0.02326	0.21729
TT 313	0.05892	0.06596	0.19123
TT 314	-0.05121	0.02220	0.17911
TT 315	0.04615	0.12577	0.19106
TT 316	-0.03948	0.06610	0.21829
TT 317	0.02171	0.18000	0.18323
TT 318	-0.01262	0.13376	0.20005
TT 320	0.00845	0.18000	0.24174
Level C			
TT 319	0.02065	0.03772	0.33617
TT 321	-0.02584	0.18000	0.33141